Progressive-Failure Analysis of Steel Building Structures under Abnormal Loads

by

Yuxin Liu

A thesis
presented to the University of Waterloo
in fulfillment of the
thesis requirement for the degree of
Doctor of Philosophy
in
Civil Engineering

Waterloo, Ontario, Canada, 2007

I hereby declare that I am the sole author of this thesis. This is a true copy of the thesis, including any required final revisions, as accepted by my examiners.

I understand that my thesis may be made electronically available to the public.

Abstract

Engineered structures are designed to resist all expected loadings without failure. However, structural failures do occasionally occur due to inadequate design and construction, especially for extreme and abnormal loads. This thesis concerns the progressive collapse of structures due to abnormal loading events, and develops a method of advanced analysis for predicting the progressive collapse behaviour of building structures in the plastic limit state.

A new procedure for progressive-failure analysis is developed that computes structural responses accounting for geometric/material nonlinearities and axial/flexural/shear deformations. The nonlinear behaviour of materials is discussed in detail. Combined-stress failure states and stiffness degradation models are proposed to simulate plastic deformation of structural members. Elliptic force-deformation relationships are employed to model the nonlinear material behaviour of members, and corresponding model parameters are determined from published experimental data.

Having the proposed nonlinear model, a generic member stiffness matrix is derived taking into account elastic-plastic bending, shearing and axial deformations. A modified moment distribution method is employed to obtain the stiffness coefficients. A computer-based incremental-load nonlinear analysis procedure is developed that progressively updates member stiffness using reduction factors that simulate degraded stiffness behaviour. Studies are conducted to demonstrate the effectiveness of the proposed method in predicting the progressive failure of structures under abnormal loading.

A general model of a compound element is proposed to consider the influence of semirigid connections on the progressive failure of steel frameworks. The stiffness degradation of semirigid connections is modeled by a moment-rotation relationship with four parameters. The stiffness degradation of a compound element resulting from the combined influence of member plasticity and nonlinear connection behaviour is modeled by a moment-rotation relationship with three parameters. The results from the proposed analysis method involving semirigid connection behaviour are compared with the results of other methods.

The proposed progressive-failure analysis method is threat-independent, in the sense that it is initially assumed that some type of short-duration abnormal loading has caused local damage represented by the removal of one (or more) critical member(s). The degree of damage to connections due to member-end disengagement is accounted for by a so-called health index factor. Three types of localized damage modes are investigated to identify different damage scenarios for the structure. Account can be taken of the connection damage that occurs when members disengage from the

structure. Account is taken of any debris loading that occurs when disengaged structural components fall onto lower parts of the structure. The associated dynamic effect is taken into account for the quasi-static analysis by utilizing an impact amplification factor. Any progressive collapse occurring thereafter involves a series of failure events associated with topological changes.

The progressive-failure analysis procedure is based on the alternate-load-path method suggested in the design and analysis guidelines of the General Services of Administration (GSA, 2003) and the Department of Defense (DoD, 2005). The residual load carrying capacity of the damaged framework is analyzed by incrementally applying prevailing long-term loads and impact debris loads. The deterioration of structural strength is progressively traced to the state at which either global stability is reached or progressive collapse to ground level occurs for part or all of the structure. The analysis procedure is extensively illustrated for several planar steel moment frames, including rigid and semirigid frames designed with and without consideration of seismic loading. The results obtained demonstrate that the proposed method is potentially an effective tool for the analysis of steel building structures under normal and abnormal loads.

Finally, with a view to improve modeling, the failure of a member cross-section under combined bending moment, shearing force and axial force is modeled by an Euler-Lagrange energy functional defining the three-dimensional stress distribution at failure. A corresponding combined-stress failure surface is developed for bi-symmetrical cross-sections, and a related model is proposed to simulate stiffness degradation. The interactive influence of bending moment, shear force and axial force is investigated for rectangular and W-shape cross-sections, and the results are compared with test results to demonstrate the significance of strain hardening and the contribution of the flange to shear strength. In future extensions of the research work, it is envisioned that the 3-dimensional M-V-P failure criterion will replace the 2-dimensional M-V and M-P failure criteria employed herein for progressive-failure analysis.

Acknowledgements

I would like to acknowledge the enthusiastic and meticulous supervision of Professors Donald E. Grierson and Lei Xu, and their insightful discussions, comments and suggestions during my Ph.D studies. Without their wisdom, guidance and patience, this thesis would have been impossible to complete.

I greatly appreciate Professors Marianna Polak, Gord Savage, G. Wayne Brodland, and Sriram Narasimhan for their comments and constructive suggestions, and to Professors S. T. Ariaratnam, Reinhold M. Schuster, Roger Green, Wei-Chau Xie, Mahesh Pandey and Stanislav Potapenko for their help.

Special thanks to Professor Bruce R. Ellingwood, of Georgia Institute of Technology, Atlanta, USA, for serving as the external examiner and for improving the quality of my thesis.

I thank my colleagues, Yanglin Gong, Joel Martinez, Xianxun Yuan, Mohammad Safi, Ying An and Hongtao Liu for their valuable discussions and help. In particular, I would like to acknowledge the help of Ignac Zajac, Gloria Rose, Joyce King, and Clayton Morgan towards revising the draft of this thesis.

Since a researcher cannot live on ideas and analyses alone, I cordially express my gratitude for the generous financial support I have received: the research assistantships provided by the Natural Sciences and Engineering Research Council of Canada; the graduate scholarships provided through the Ontario Graduate Scholarship Program; the University of Waterloo Faculty of Engineering Graduate Scholarships; the University of Waterloo President's Graduate Scholarship for 2005-2006; and the Teaching Assistantships granted by the Department of Civil Engineering.

Finally, I dedicate this thesis to my wife Hua Wang and my daughter Suya Liu. I am forever indebted to them for their understanding, endless patience, encouragement, support, and sacrifice when it was most required.

Table of Contents

List of Figures

List of Tables

Nomenclature

A	Cross-sectional area
AISC	American Institute of Steel Construction
a, a_j	Arbitrary constants
A_k	Abnormal load
AP	Alternate (Load) Path
A_s	Equivalent shear cross-sectional area
ASCE	American Society of Civil Engineers
b	Conventional stability function
b_f	Width of the flange
c	Conventional carryover function
CISC	Canadian Institute of Steel Construction
C_{ij}	Carryover factor in nonlinear analysis
c_{pm}	Plastic modulus coefficient
c_{sa}	Cross-section area coefficient
C_1	Coefficient accounting for M+V interaction
c_1 , c_2	Non-dimensional cross section parameters
d	Depth of the cross section
D	Deformation/deflection
$\boldsymbol{D}_i$	Total joint displacement vector at the end of the ith increment
$\Delta\boldsymbol{D}_i$	Incremental joint displacement vector
d_j	Local-axis member-end deformations/displacements
D_L, L_L, S_L,W_L	Nominal dead, live, snow and wind loads
DoD	Department of Defense (of the United States)
DWA	Double web-angle connection
E, E_h	Material Young's modulus, hardening modulus
EEP	Extended end-plate connection
e_j	Exponents in the inelastic force-deformation model
f_{ij}, f_{imj}, f_{ijs}	Total, bending, and shearing flexibility coefficients
f_s	Cross-section plastic shape factor
F	Internal force

$\boldsymbol{F}$	Equivalent joint load vector
$\Delta\boldsymbol{F}$	Incremental equivalent joint load vector
FEMA	Federal Emergency Management Agency (of the U.S.)
FEP	Flush end-plate connection
$(FES)_j$	Fixed-end shear/transverse force at end j
$\boldsymbol{f}_i$	Total member-end force vector at the end of the ith increment
$\Delta\boldsymbol{f}_i$	Incremental member-end force vector at the end of the ith increment
f_j	Local-axis member-end forces
G	Material shear modulus
g	Gravity constant
GSA	General Services Administration (of the United States)
h	Health condition index, health stiffness
i	Index of increment or member
I	Moment of inertia of cross section
I_{af}	Impact amplification factor
I_p, I_v, I_m	Integrals for axial force, shear force, and bending moment
j	Index of member ends, or other sequential indices
K_e	Effective length factor
k	Stiffness coefficient
$\boldsymbol{k}$	Member stiffness matrix in local coordinate system
$\boldsymbol{K}$	Structure stiffness matrix in global coordinate system
$\boldsymbol{K}_i$	Structure stiffness matrix for the ith incremental analysis
k_{ij}	General stiffness coefficient with both geometric and material nonlinearities
k^g_{ij}	Stiffness coefficient with geometric nonlinearity
k^r_{ij}	Stiffness coefficient with rotational stiffness degradation
L, l, l_0	Member length, instantaneous length, gage-length distance
m	Normalized bending moment
M, M_j	Bending moment, and moment at member end j
$m_j(x)$	Moment due to unit end moment
$m_{jv}(x)$	Virtual moment due to unit end moment
M_h	Fully-plastic moment capacity involving strain hardening
M_n	Nominal moment capacity of connection

M_p	Fully-plastic moment capacity
M_y	Initial yield moment of a section
M_0	Reference moment of connection
NRCC	National Research Council of Canada
N_j, n_j	Axial inelastic stiffness, corresponding degradation factor at end j
P, p	Axial force, normalized axial force
P_{cr}, P_e	Critical load, Euler buckling load
P_y, P_p	Initial and full yield axial forces
Q	The first moment of specified area
R, r	Rotational stiffness, and corresponding degradation factor
R_c, R_n,	Rotational connection stiffness, and nominal stiffness
r_c, r_p	Rotational stiffness degradation factors of connection and member plasticity
R_{ce}, R_{cp}	Initial rotational stiffness, strain-hardening/softening stiffness of connection
R_e, R_p	Elastic and inelastic rotational stiffnesses
R_{ij}	Rotational stiffness coefficient for member ij
r_s, r_z	Shear radius of gyration and cross-sectional radius of gyration
sdf	Stiffness degradation factor
s_{ij}	Stiffness coefficient
s_{sf}	Shearing shape factor
S_z, Z_z	Elastic, plastic moduli of the cross section about strong axis z
T, t	Transverse shear stiffness of a cross section, corresponding degradation factor
t_f	Thickness of the flange
t_w	Thickness of the cross section, or web
V, V_j	Shear force, shear force at member end j
v	Normalized shear force
$v_j(x)$	Shear force due to unit end moment
$v_{jv}(x)$	Virtual shear force due to unit end moment
$w(x)$ and W	Distributed load and concentrated load
W_{fd}	Weight of falling debris
WTC	World Trade Center (in New York City)
x	Coordinate distance along member
y, y_b, y_s	Total, bending, shearing deflections

α	Impact loading factor for progressive collapse analysis
α_v, α_h	Effective shear factor accounting for flanges, strain-hardening factor
β	Modified deflection stiffness factor
χ_j	Factors accounting for axial and shear stiffness degradation
δ	Axial deformation, or deflection
δ_p	Axial plastic limit deformation
δ_s	Transverse shear deflection
Δ_i	End deflection
ε	Normal strain or axial deformation
ϕ	Curvature or rotation of a member end in the plastic range
ϕ_p	Full-yield rotation of a section corresponding to full plastification
ϕ_y	Initial flexural yield rotation at which inelasticity starts
Γ	Density of energy functional
γ	Shear strain/plastic shear deformation or shape parameter of connections
γ_y, γ_p	Initial and full yield shear strains
γ_0	Average shear strain of a cross section
η	Exponent introduced in the internal loading interaction equation
η_i	Coefficients accounting for shear deformation
φ	Parameter used in 3D interactive analysis
κ	Parameter for different yield criteria, von Mises or Tresca
λ	Load factor/multiplier
λ_f	Load factor used to identify the failure behavior of the structure
λ_j	Increment/load scale factor/multiplier
$\Delta\lambda^*_J$	Initially specified incremental load factor for the *J*th stage
$\Delta\lambda_i$	The *i*th increment load factor
$\Delta\lambda_J$	Total increment load factor of the *J*th stage
$\Delta\lambda_{Ji}$	The *i*th increment load factor within the *J*th stage
λ_J	Total load factor at the end of the *J*th stage
μ	Shape parameter of moment-axial force interaction locus
μ_{ej}, μ_{sj}	Distribution factors in modified Hardy Cross method
ν	Poisson's ratio

Π_i, Π_e	Internal (strain) energy, external energy/work
θ	Rotation at member end, or an angle
θ_c	Rotational angle of semirigid connection
θ_j	Rotational angle at member end *j*
θ_M	Flexural-failure domain due to M+P interaction
θ_P	Axial-failure domain due to M+P interaction
θ_{MP}	Combined flexural-axial failure domain due to M+P interaction
θ_u	Ultimate rotation of connections
Θ	Angle used to determine failure domain due to M+V interaction
Θ_M	Flexural-failure domain due to M+V interaction
θ_V	Shear-failure domain due to M+V interaction
θ_{MV}	Combined flexural-shear failure domain due to M+V interaction
ϑ	Angle used to indicate loading path
ρ	Nondimensional size parameter
ρ_e, ρ_s	Ratio P/P_e, axial-shear influence factor
σ	Normal stress
σ_r	Residual normal stress
σ_{ry}	Initial-yield normal stress accounting for residual stress
σ_y	Specified yield stress
σ_u	Ultimate stress
τ	Shear stress
τ_y, τ_p	Initial yield and full yield shear stresses
τ_{yr}	Initial-yield shear stress accounting for residual stress
Ω	Stiffness coefficient denominator
ξ	Exponent
ψ	Interactive stiffness parameter
ζ	Ratio of normal strain to shear strain
$\aleph$	An arbitrary normal stress distribution

Chapter 1
Introduction

For some time now, building structures have been designed to resist normal loads such as those due to self-weight, occupancy and climatic or seismic effects. However, since the 1968 chain-reaction failure of the Ronan Point Apartment Block in London, UK, triggered by a gas explosion, abnormal loading and progressive collapse have become increasingly recognized as important phenomena to be accounted for in engineering design practice worldwide. Indeed, the complete structural collapse of the twin towers of the World Trade Centre (WTC) in New York City on September 11, 2001, has significantly increased the concern for these phenomena. Motivated by such abnormal loading events, this research addresses the topic of progressive-failure analysis of building structures.

1.1 Project Failure

In the structural engineering community, engineers apply their knowledge to design and construct buildings and infrastructure to meet the requirements of our society. Structures are designed to resist normal loads such as those due to self-weight, occupancy, wind, earthquake and other loading scenarios stipulated in building codes (e.g., ASCE, 2002; NRCC, 1995). In principle, any failure must be precluded by the structural design. Sometimes, however, failure does occur in the process of construction and ongoing operations due to unanticipated factors. The definition of failure is difficult to precisely express because of the many different types and severity of damage that can occur in structural systems. It might be appropriate to employ the following definition by Leonards (1982): *failure is an unacceptable difference between expected and observed performance*, which is suggested by the Technical Council on Forensic Engineering of the American Society of Civil Engineers. This thesis focuses on catastrophic structural failure, including partial and complete structural collapse.

1.1.1 Foreseen Project Failure

Foreseen structural failure may be avoidable because the causes are known. Such failure can be eliminated in the process of design, as well as during construction or operation, by preventing mistakes. To achieve this goal, professionals in different specialized disciplines must learn from their mistakes, and those of others. Fortunately, practitioners in many countries are strictly governed by laws to protect the public's welfare and safety. In Canada, for example, the practice of professional engineering is governed by local Professional Engineer Acts and other by-laws.

Flawed designs have contributed substantially to the failure of many structures. Avoidable problems include inappropriate site selection, misuse of structural systems, incompetence in selecting materials, ignorance of a load or a combination of loads, inaccurate analyses and computations, and unclear communication of the design and construction intent (Feld & Carper, 1996). For instance, the parking roof deck of a Save-On-Food store in Burnaby, British Columbia, Canada, on the opening day, April 23, 1988, partially fell into the store along with 20 cars, as illustrated in Figure 1.1. The collapse was primarily caused by design deficiencies, where the self-weight of the joists and beams supporting the roof were not accounted for, and excessive unbraced length of the beams over the collapsed area led to lateral-torsional buckling failure (Jones & Nathan, 1990; Essa & Kennedy, 1994).

Construction work can be a dangerous occupation, and structures can collapse during the process of erection. Construction errors include non-conformance to the design intent, excavation and equipment accidents, improper sequencing, inadequate temporary support, excessive construction loads, and premature removal of shoring or formwork (Feld & Carper, 1996). For example, a historic collapse is that of the University of Washington's Husky Stadium, depicted in Figure 1.2, on February 25, 1987. During construction, six of the nine guylines used to temporarily support the structure were removed prematurely, causing 250 tons of steel framework to sway and eventually topple.

Other causes, such as material deficiencies and operational errors, contribute to project failure. Designers should be able to rely on modern structural materials, but manufacturing or fabrication defects exist in the most reliable structural materials, including structural steel or mixed concrete. Such material defects might not be discovered and eliminated during the design or construction stages. Most problems with materials are the result of human error, inadequate understanding of the materials, or the use of incompatible materials. Regarding operational error, project failure can occur after a facility is occupied because of the owner/occupant's misuse or inadequate maintenance.

Case studies concerning project failures help professionals to recognize the nature of failure and, in turn, avoid making the same mistakes (Feld & Carper, 1996). Nevertheless, facilities can fail due to a myriad of errors in the process of design, construction, and operation. To protect facilities against such failures, in addition to educating engineers and other professionals about design requirements and construction regulations, innovative methods of design and analysis are required to address unforeseen problems so as to ensure the reliability and durability of engineered structures.

1.1.2 Unforeseen Project Failure

Unforeseen structural failure may be inevitable because the causes are unknown. Such failure concerns projects built according to the design code, but some unexpected loads occur in the process of construction or during operation. Since the 1968 gas explosion-triggered chain-reaction collapse of the Ronan Point Apartment Block in London, UK, depicted in Fig. 1.3, engineers worldwide are required to design buildings to meet specified levels of safety for protection against progressive collapse under unexpected abnormal loading events (Grierson, 2003).

Typically, structures are exposed to interior loading such as self-weight and occupancy weight, and to exterior loading such as wind and seismic loads. Foreseen or normal loads are directly or indirectly considered in the design process through existing codes and standards. Despite the potential for loading to lead to catastrophic progressive collapse, unforeseen or abnormal loads are presently not explicitly considered in general design codes, and they are rarely considered in design practice. Burnett (1975) identified three types of abnormal loading: pressure loading, impact loading, and other loading. Usually, pressure loading results from explosions of a service system (e.g., natural gas and steam), stored gas and liquid (butane, propane, oxygen, gasoline, etc.), hazardous material in transit, or bombing due to civil or criminal action. Sometimes, sonic booms lead to pressure loading on structures. In nature, pressure loading includes wind-induced localized effects such as a tornadoes and hurricanes. Impact loading may result from ground vehicle collisions, aircraft crashes, missile or military weapons, and failure of adjacent buildings or falling debris. Other loading may occur due to the malfunction of a water system or other service system, or debris from other incidents (e.g., flooding and tornado). Errors in design and construction can also result in structurally significant abnormal loadings (Fintel & Schultz, 1979).

The Ronan Point accident (Griffiths et al., 1968) involved the partial collapse of a 22-storey building constructed of precast concrete panels, as pictured in Figure 1.3. A natural gas explosion in the kitchen of an apartment on the 18th floor blew out an exterior wall panel. The reduced support due to the ejected panel resulted in a chain reaction that led to a collapsed roof. The falling debris caused the floors to successively tumble, almost to ground level. The pressure loading was designated as being abnormal because its cause was an explosion, which is generally not considered in the structural design process. According to Breen and Siess (1979), progressive collapse and abnormal loading are closely related. However, although progressive collapse may be related to abnormal loading, such loading does not necessarily induce progressive collapse.

Progressive collapse is characterized as a chain-reaction failure, due to abnormal loading (Ellingwood, 2006). According to Allen and Schriever (1973), Taylor (1975), and Eldukair and

Ayyub (1991), progressive collapse events comprise 16% of all the collapse incidents in Canada and the United State of America (USA). This low percentage suggests that local damage does not always induce progressive collapse. For the aforementioned collapse events, 52%, 40%, and 8% occurred during construction, service, and demolition, respectively. These results indicate that progressive collapse is a critical problem not only during construction but throughout the service life of a structure. Eldukair and Ayyub (1991) have presented similar results based on information published in the *Engineering News Record* from 1976 to 1986.

In terms of abnormal loading, terrorist attacks elicit the most concern because buildings and other infrastructure are the most vulnerable to terrorists whose intent is deliberate destruction. The robust design of building structures and infrastructures to effectively prevent such progressive failure is difficult to achieve. Since the 1990s, car-bomb events have become the norm for terrorists to damage public and private structures. For example, two major vehicle bomb attacks occurred in the USA within a two-year period: the WTC building in New York in 1993 (Figure 1.4), and the Alfred P. Murrah Federal Building in Oklahoma in 1995 (Figure 1.5). Both events have been compared and analyzed to identify the capacity of building structures to resist progressive collapse against such attacks (Longinow & Mniszewski, 1996).

Certainly, the collapse of the WTC twin towers has alerted the structural engineering community to the importance of preventing such catastrophic destruction in the future. After seven months of extensive investigation of the specific causes of the collapse, the United States Federal Emergency Management Agency (FEMA, 2002) has issued a report that attributes the collapse to three related but discrete loading events: (1) the Boeing aircraft crashed into the buildings and cut through their exterior superstructure, thereby causing substantial localized damage; (2) the subsequent fire, fed by the jet fuel and office furniture and material, weakened the damaged structures; and (3) the overwhelming falling debris caused by the progressive collapse itself. For event (1), the impact of the plane did not cause on immediate building collapse, because the structural systems were sufficiently redundant to offset the localized damage. According to the report (FEMA, 2002), most of the load supported by the damaged columns was transferred to the adjacent perimeter columns through the exterior wall frame, which served as an alternate loading path. The intense fire, event (2), relentlessly heated and weakened the structural systems, increasing the stress on the damaged structure. As the large mass of collapsing floors dropped, event (3), the floors below were directly impacted. The FEMA report stresses the need for further research on the progressive collapse of building structures, exposed to abnormal loading.

Natural disasters, including earthquakes, hurricanes, floods, tornadoes and fires, are usually much stronger than those associated with human activity. Figure 1.7 shows one of the severely damaged buildings resulting from Hurricane Katrina in New Orleans in 2005. According to Tapia (2001) and Hartwig (2004), the man-made disasters caused by the 1992 Los Angeles riots, the 1993 WTC bombing, the 1995 Oklahoma City bombing, and the 2001 WTC attack, resulted in $775 million, $510 million, $125 million, and $40 billion in losses, respectively. According to the Congressional Budget Office (CBO, 2002) and Holtz-Eakin (2005), the natural disasters due to the 1992 Hurricane Andrew, the 1994 Northridge earthquake, the 1995 Kobe earthquake, and the 2005 Hurricane Katrina, resulted in $34 billion, $43 billion, $110 billion, and $140 billion in losses, respectively. To mitigate the losses caused by earthquakes, FEMA has contracted out project ATC-58 to the Applied Technology Council (ATC) to develop the next generation of seismic performance-based design guidelines for buildings. Such philosophy of design and analysis can also be applied to man-made or natural hazards (Whittaker et al., 2005).

1.2 Design Considerations for Unforeseen Failures

General design strategies to counteract progressive collapse include three aspects: providing members to resist specific abnormal loading, adding vertical and horizontal ties to increase resiliency to local damage, and designing alternate loading paths to ensure an adequate residual load-carrying capacity of the damaged structure (Ellingwood & Leyendecker, 1978; Gross & McGuire, 1983; Zalka & Armer, 1992; ASCE, 2002). To implement the last two design strategies, alternate loading paths should be provided to transfer the loads from the damaged regions to the remaining structure, and progressive collapse analysis should be conducted for the structure. The September 11, 2001, photo of the Pentagon building collapse shown in Figure 1.8 is a vivid indication that the alternate loading path method is effective in practice. Even though the supporting columns were destroyed by abnormal loading, an alternate loading path was provided when the remaining upper reinforced-concrete frame with masonry-filled walls compensated for the column loss by acting as a transfer girder or vertical diaphragm (Mlakar et al., 2003).

Current design codes deal with progressive collapse failure problems in various ways. For instance, Eurocode 1 provides a general analysis and design principle that invokes designers to prevent structural damage that is disproportionate to the localized damage due to abnormal loading events (CEN, 1994). The American ASCE 7-05 non-mandatory commentary offers several general approaches in design for progressive collapse (ASCE, 2005; Ellingwood, 2006). The Canadian code requires buildings to be designed with structural integrity so that they can effectively withstand

abnormal loading that can occur during the service life of a structure (NRCC, 1995). Some research work has been conducted to quantify abnormal loading and mitigate its effects. For example, Ellingwood and Dusenberry (2005) have summarized the information in technical design codes and research papers on progressive collapse under abnormal loading, and Ellingwood (2005) has proposed a probabilistic basis for establishing appropriate load combinations to facilitate the design of structures under extreme fire loading. Marjanishvili (2004) concluded that little detailed information was available to enable engineers to confidently perform a systematic progressive collapse analysis. Later, with the view to counteract this conclusion, Marjanishvili and Agnew (2006) provided clear conceptual descriptions of various procedures for progressive-collapse analyses based on step-by-step computer computation. The quasi-static nonlinear pushover analysis method, suggested in seismic engineering (FEMA, 1997), has been considered applicable for dealing with other extreme events such as blast loads and tornado winds (Hamburger et al., 2002). As well, a non-linear dynamic analysis method has been proposed for tracking the dynamic behaviour of progressive collapse (Kaewkulchai & Williamson, 2004), with account for impact loading (Kaewkulchai & Williamson, 2006).

Section 2.5 of the ASCE Standard-7 (ASCE, 2005) states that stability and strength should be checked to ensure that structures have the capacity to withstand the effects of abnormal loads. Both the USA Department of Defense (DoD, 2005) and General Services Administration (GSA, 2003) have promulgated analysis and design guidelines for dealing with progressive collapse hazards. These guidelines provide methods to protect existing or new facilities against potential progressive collapse under abnormal loading events. To satisfy requirements, the design methods suggested in the guidelines include: (1) structural integrity design, (2) local resistance specification, and (3) alternative loading path design, as described in the following.

1.2.1 Structural Integrity Design

Structural integrity design requires designers to add vertical and horizontal ties to increase load-path redundancy in the event of localized damage. This strategy comes from the lesson learned from the 1968 progressive collapse of the Ronan Point apartment building, composed of large bearing-wall panels (Griffiths et al., 1968). Considerable research has been conducted concerning structural integrity and resistance to progressive collapse, such as that by Haseltine and Thomas (1969), Redland Bricks Ltd. (1971), Taylor (1975), and Fintel and Schultz (1979).

The ASCE-7-05 (2005) guideline for the provision of general structural integrity requires designers to do the following:

- select proper plan layouts; for example, to reduce the spans of long wall sections;
- add short returns on walls to enhance structural stability;
- design strong joints to transfer the loads through alternate loading paths;
- arrange two-way floor systems to supply alternate loading paths;
- enhance interior partitions to redistribute the loads among other walls when a wall fails;
- use catenary action to change a slab/beam into a catenary element
- design walls as transfer beams with ability to span openings.

If the previous requirements are satisfied, a designed building structure can sustain localized damage and still remain intact and stable. Thoughtful determination of minimum levels of strength, continuity and ductility during the design process can lead to structures that are able to resist progressive collapse. However, if minimum requirements (e.g., related to tie forces) are not specifically provided in design codes, a designer might overlook having concern for considering progressive collapse (Ellingwood & Leyendecker, 1978).

The general integrity design strategy (DoD, 2005) is suitable both for normal and abnormal loading. Similar to current design practice concerning normal loads (e.g., where the requirements of structural integrity are considered for horizontal seismic and wind loads), general integrity design against progressive collapse caused by abnormal loading should focus on strengthening the transverse, longitudinal, vertical and peripheral connections of a building.

1.2.2 Specifying Localized Resistance

A localized resistance design strategy requires checking the strength of members subjected to specific abnormal loading (e.g., the 34 kN/m^2 pressure load for gas related explosions specified in the United Kingdom).

Based on the work of Galambos et al. (1982) and Ellingwood et al. (1982), Commentary C2.5 of ASCE Standard 7 provides load combination formulae for checking structural demands (ASCE, 2005). Although some code authorities might specify abnormal loads (Burnett, 1975), limited data are available to determine the magnitude and distribution of such loads. To date, little information about localized resistant strength is provided in design codes to aid designers in designing buildings to resist abnormal loading events. A localized resistance strategy can lead to ‘hard spots’ within a structure in the areas where abnormal loading events are prone to occur (Ellingwood & Dusenberry, 2005). Designing a structure to only resist one specific abnormal load can be both costly and impractical (Taylor, 1975).

1.2.3 Alternate Load Paths

The Alternate-load Path (AP) design strategy (DoD, 2005) is attractive in design practice. The principle feature of this strategy is the removal of critical member(s) to simulate the consequences of an abnormal loading event, without specifically identifying the nature of the loading.

The AP design strategy requires a structure to be checked for its residual load-carrying capacity when one or more load-bearing member/s is/are notionally removed (DoD, 2005). This calls for an alternate path to be available in the structure to transfer the loads away from the damaged area to other parts of the structure so as to avoid a chain-reaction failure. For example, the damaged Pentagon building in Figure 1.8 illustrates how the damaged area was bridged by an alternate path, saving lives above the floor of destruction. This demonstrates that the AP strategy can be a practical and appropriate way to protect a structure from progressive collapse. Based on this strategy, a computer-based plastic-hinge method has been developed to predict the plastic collapse of framed structures related to selectively removed member/s (Gross & McGuire, 1983).

The AP strategy is treated as a principal method in design guidelines for protecting new and existing buildings from progressive collapse (GSA, 2003; DoD, 2005). If a vehicular collision or car-bombing occurs at a building's ground level, the localized damage caused by the abnormal loading event is assumed to be the removal of one of the following critical members: an exterior column near the middle of the long side of the building; an exterior column near the middle of the short side of the building; or a column located at the corner of the building. If the building has underground parking and/or uncontrolled public ground floor areas, a column in the perimeter column lines of each area is removed to begin the AP analysis. More detailed requirements for removing a member (column or wall) are provided in the DoD document (2005).

Design guidelines provided by GSA (2003) and DoD (2005) for the prevention of progressive collapse of government and military facilities address the AP strategy. However, the strategy can be applied to any kind of building and infrastructure to mitigate against progressive collapse and thereby save lives and reduce property losses. In general, the AP strategy has been accepted as an effective means to estimate the robustness and redundancy of structures (Wada et al., 2006; Vlassis et al., 2006).

1.3 Structural Analysis for Abnormal Loading

The current AP method involves conventional plastic limit analysis of a structure with one or more removed member(s). Little work has been conducted on developing rigorous analysis procedures to trace the complete process of progressive collapse under abnormal loads, primarily because the

modelling of corresponding structural damage patterns is very complicated. This subsection reviews static methods of structural analysis as a basis to investigate the progressive collapse of framed structures.

1.3.1 Structural Analysis Methods

The most common methods of analytical structural analysis have been presented and implemented for statically loaded frames (e.g., McGuire et al., 2000; Chen et al., 1996). There are four types of analytical methods: linear elastic analysis, elastic stability analysis, plastic collapse analysis, and nonlinear inelastic collapse analysis.

Linear elastic analysis is a basic method that is effectively used in serviceability level design. In spite of some errors compared to nonlinear analysis, the simplicity of linear elastic analysis aids designers to quickly and conceptually grasp structural behaviour. Therefore, this method is still popular in structural analysis and design.

Elastic stability analysis is adopted to calculate the critical load multiplier that corresponds to the elastic limit state of a structure. A common way of obtaining the load multiplier at the limit state bifurcation point is to conduct a generalized eigenvalue analysis based on an idealized structural model. An alternate way is to conduct a nonlinear elastic analysis. Although the same load multiplier is found for both analyses, a nonlinear analysis can be used to trace a nonlinear process and to predict nonlinear responses.

Plastic collapse analysis is more complicated than linear elastic analysis due to material stiffness degradation and strength deterioration. Different methods of plastic limit analysis can be developed by using different material constitutive laws to characterize the degradation and deterioration. To this end, ‘plastic-hinge’ and ‘spread-of-plasticity’ methods are commonly applied in the plastic collapse analysis of framed structures. With the plastic-hinge approach, member plasticity is assumed to be concentrated in zero-length regions (e.g., plastic hinges form at member ends). Also, to account for stiffness degradation, it is assumed that the material property changes from pure elasticity to full plasticity once the corresponding moment reaches a level that satisfies the predefined yield criterion. (Orbison et al., 1982). By these assumptions, the load factor of a structure at the limit plastic state can be found by employing the static or kinematical theorem (Grierson, 2002). Alternatively, a computer-based incremental-plastic method can be used to find the plastic load factor and the load-deflection responses. Because of the simplicity of the plastic-hinge method, it has been applied extensively in the plastic collapse analysis of framed structures (Chen et al., 1996). A FORTRAN-based program,

called PHINGE (Plastic HINGE), has been developed by Chen et al. (1996) to conduct nonlinear analysis of semi-rigid frameworks.

However, some assumptions regarding the plastic-hinge method might not be realistic. For instance, the idealization of material behaviour that can abruptly change from perfect elasticity to perfect plasticity ignores the gradual stiffness degradation effect taking place from initial yield to full plasticity. Moreover, the evolution of plasticity along a member is not taken into account in the structural analysis. Consequently, the spread-of-plasticity approach has been introduced to address these shortcomings. The gradual stiffness degradation of materials from initial to full yield is accounted for in the nonlinear analysis, depending on the different degradation models. For instance, the spread of plasticity along a member can be modeled either by a tapered element attached to the member end (Acroyd, 1979), or by viewing the entire member as a collection of segments with variable flexural stiffness *EI* along the member's length (Cook, 1983). Plasticity can also be gradually traced by including higher-order displacement fields in the member stiffness formulation (Espion, 1986). More accurately, a fibre-element method can track the gradual spread of plasticity in discrete fibre elements along the length and through the cross-section depth of a member (Powell & Chen, 1986).

Nonlinear geometric effects were not addressed by the plastic collapse analysis methods discussed previously. In fact, a structural collapse can involve the combined actions of geometric and material nonlinearities. For this reason, nonlinear inelastic analysis simultaneously accounts for the interactive effect of geometric nonlinearity and material nonlinearity. When conventional plastic-hinge assumptions are made without accounting for gradual stiffness degradation behaviour, a second-order inelastic analysis can lead to an overestimate of structural strength (King et al., 1992). The spread-of-plasticity approach has been introduced to address this shortcoming. For example, in the quasi-plastic-hinge method, an integration technique is available to find the flexibility coefficients that permit the formation of an incremental member stiffness matrix that accounts for gradual plasticity evolution and the P-delta effect (Attalla et al., 1994). This method gives a reasonable description of the gradually degraded change in member stiffness. Another approach is to combine the plastic hinge and spread-of-plasticity methods by using an inelastic hinge to efficiently model the evolution of member plasticity through the use of gradually degraded plastic stiffness factors (Hasan et al., 2002; Gong 2003; Grierson et al., 2005; Xu et al., 2005).

If the member stiffness matrix used in nonlinear inelastic analysis is expanded as a Taylor series with respect to the member axial force and the higher-order terms are omitted, a second-order inelastic analysis approach is achieved. By truncating the higher-order terms, however, the structural

responses are significantly affected when the framework approaches the buckling state. Consequently, so as to improve response prediction accuracy, this thesis focuses on nonlinear inelastic analysis without truncating higher-order terms. Specifically, the analysis method involves employing a more accurate structure stiffness matrix in the incremental-load procedure employed to identify plastic collapse limit states.

1.3.2 Progressive Collapse Analysis

Identifying all the possible abnormal loads for a structure is difficult. Providing adequate resistance to one abnormal loading condition does not necessarily ensure sufficient strength to resist other abnormal loading events. Also, the additional cost required to prevent failure against abnormal loads is often not justifiable because of the low probability of abnormal loading events. Since the principal dangers are fire, degradation, impact and explosion, and since the research on complex structural response to these events is sparse, specifying local resistance for a structure without dependable data is unproductive and potentially dangerous (Zalka & Armer, 1992). In many cases, the AP method is an appropriate basis for progressive collapse analysis (Ellingwood & Leyendecker, 1978).

In the AP-based progressive-collapse analysis method proposed by Gross and McGuire (1983), the behaviour of a framed structure to plastic collapse is traced by the second-order plastic-hinge approach. In the analysis procedure, the abnormal loading is not explicitly considered. Rather, its effect is accounted for by removing selected member(s). In an analysis of the partial collapse of the Bankers Trust Building in the WTC complex (FEMA, 2002), the nonlinear analysis was performed using ANSYS software (ANSYS, 2005) to account for large-deflection geometric nonlinearities. The inelastic responses at the connections were simulated by nonlinear springs and localized inelastic material properties. Following the concept of AP design, the gravitational loading was applied first. The damaged or missing members were then removed sequentially to track the partial progressive collapse. The computed results demonstrated that the connections played an important role by enabling the beams to develop some membrane catenary action to hold the damaged structure in place so as to limit overall structural damage.

Shear failure is another contributing factor in the progressive collapse of concrete and steel structures. Regarding the collapse of concrete flat plate structures, Hawkins and Mitchell (1979) have concluded that the most likely mechanism to trigger progressive collapse is punching-shear failure occurring at interior columns. They analyzed four possible defences against progressive collapse, and concluded that designing for high live loads is unsatisfactory, integral beam stirrup reinforcement is impractical, and continuous bottom reinforcement and tensile membrane action for slabs is beneficial.

Abrupt shear failure can result from short-duration dynamic load impact (Conrath et al., 1999). Evidently, then, shear failure due to impacting debris loads must be considered by any progressive collapse analysis.

High-tension axial forces will appear in slabs or beams acting as catenary members as a result of the failure of columns or walls. The effect of axial force on the progressive collapse of truss structural systems has been extensively studied since the failure of the Hartford Coliseum space truss roof in 1978 (Blandford, 1996). Axial failure can also be one of the crucial factors in the progressive collapse of flexural frameworks. However, the combined shear plus axial failure model is not included in the current nonlinear inelastic analysis methods for analyzing flexural framed structures.

Probabilistic-based methods should be applied to help mitigate against progressive collapse due to abnormal loads. It is important to note that even though the occurrence of abnormal loading has low probability, the resulting consequences can be devastating (Ellingwood, 2006). Probabilistic risk analysis method can provide an efficient tool to quantify the uncertainty of abnormal loading for decision making (Ellingwood, 2005; Ellingwood & Wen, 2005; Ellingwood, 2001; Ellingwood, 2000). Although this study focuses on the development of fundamental concepts for deterministic progressive-collapse analysis, it is also important to conduct work concerning reliability-based progressive-failure analyses (Ellingwood et al., 2004; Ellingwood & Tekie, 2001; Ellingwood, 2000).

1.4 Objectives and Scope

The primary objective of this thesis is to establish new fundamental and physical insights into the progressive-collapse behaviour of steel building structures under abnormal loads. An analysis tool is developed for identifying possible collapse mechanisms and for predicting progressive-collapse behaviour of framed structures under extreme loading events. The specific objectives of this thesis are:

- Develop a multi-stage method of analysis to trace the process of progressive collapse of frameworks as characterized by the change of structural topology
- Identify progressive-failure characteristics, including member plastic deformation, connection damage, local collapse mechanisms, and residual capacity of the damaged structure
- Derive stiffness expressions for structural analysis involving geometric nonlinearities and member shear deformations
- Introduce stiffness degradation factors to characterize the degree of damage to members and connections of a structure loaded into the post-elastic response range

- Develop a compound-element model that effectively simulates the interactive behavior of members and connections
- Introduce an impact amplification factor to consider the dynamic effects of impact debris loading
- Develop a health index to model connection damage conditions

This scope of this research is the quasi-static progressive collapse analysis of planar steel frame structures subjected to event-independent abnormal loading and debris loading, to predict structural instability and corresponding failure states.

1.5 Assumptions and Idealizations

The investigation described in this thesis is based on the following assumptions and idealizations:

- Structural steel materials are homogenous and isotropic;
- The spread of plasticity along a member is modelled by inelastic springs, concentrated at member ends;
- Compared to member lengths defined by centre-to-centre dimensions, the lengths of connection and inelastic spring elements are assumed to be negligible;
- The effects of local buckling, lateral buckling, and panel-zone shear failure are assumed to be precluded by lateral bracings;
- The damage caused by abnormal loads is simulated by the removal of critical members of the structure under consideration;
- The dynamic effect of falling debris loads is accounted for through an impact amplification factor; and
- After an abnormal loading event causing damage has happened, the damaged structure is analyzed under the prevailing gravity loads alone, and potential debris loads.

1.6 Thesis Organization

This thesis involves the development of an analytical tool for predicting the failure behaviour of steel building structures that are exposed to abnormal loading events. The thesis is organized into seven chapters, as follows:

- Chapter 2 provides a discussion of geometric and material nonlinearity for structural members. Member force-deformation relationships are investigated to account for geometric nonlinearity and shear deformation in the elastic range. Stiffness coefficients are derived to serve as a basis for inelastic nonlinear analysis. Post-elastic moment-rotation, shear force-

deflection, and axial force-deformation relationships are investigated to determine stiffness degradation factors.

- Chapter 3 presents the derivation of a generalized stiffness matrix for a hybrid beam-column member accounting for geometric and material nonlinearities. A proposed nonlinear procedure is developed for the analysis of frameworks, and illustrated by two examples.
- Chapter 4 describes an effective method for the inelastic analysis of semi-rigid planar steel frameworks. The nonlinear characteristics of a member with both inelastic material behaviour and semi-rigid connections are discussed. Three semi-rigid steel frameworks are analyzed by proposed nonlinear analysis method to illustrate the influence of semi-rigid connections on post-elastic structural response. The results are also compared with those obtained from experiments and applying other methods.
- A progressive-failure analysis technique is developed in Chapter 5. Three types of localized failure models are developed to investigate member-end disengagement scenarios and subsequent impact debris loading. A health index is developed to account for connection damage due to the disengagement of members during progressive collapse. Semi-rigid connection behaviour is considered. A procedure based on the AP method for progressive-failure analysis is investigated.
- With a view to future improvement of the progressive-failure analysis method, Chapter 6 models the post-elastic behaviour of member sections under combined bending moment, shearing force and axial force using an Euler-Lagrange energy functional to define the three-dimensional stress distribution constituting the yield failure surface. The results predicted by the M-V-P failure model are compared with those obtained from experiments and other analytical methods.
- Chapter 7 discusses conclusions drawn from the study, and identifies future research work concerning progressive collapse from the viewpoints of both analysis and design.

Figure 1.1 Save-on-Foods Grocery Store failure, Canada (Closkey, 1988)

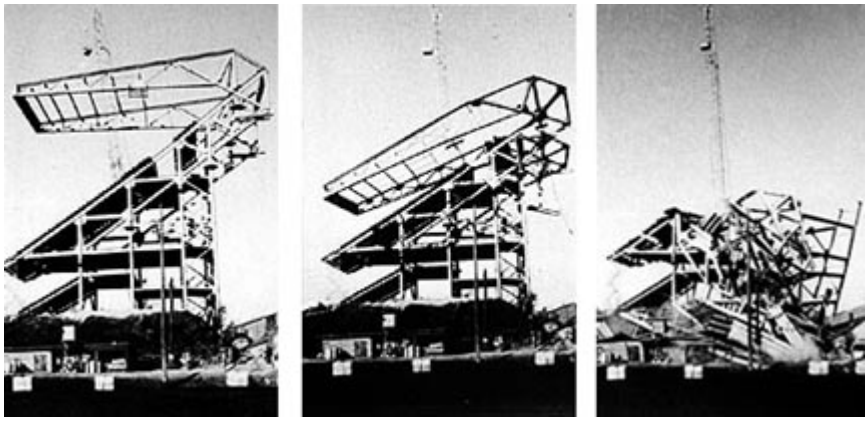

Figure 1.2 Progressive collapse of Husky Stadium, USA (© John Stamets, 1987)

Figure 1.3 Progressive collapse of Ronan Point Flats, UK (Griffiths et al., 1968)

Figure 1.4 Local damage of World Trade Centre building, New York (Bureau of ATF, 1993)

Figure 1.5 Progressive collapse of Murrah Office Building, Oklahoma (Hinman, 1997)

Figure 1.6 Progressive collapse of World Trade Centre tower, New York (FEMA , 2002)

Figure 1.7 Damaged building due to Hurricane Katrina, New Orleans (CNN, 2005)

Figure 1.8 Walls as transfer girders compensating for column loss, Pentagon, USA (SEI, 2003)

Chapter 2
Geometrical and Material Nonlinearity

This chapter provides a discussion of geometric and material nonlinearity for structural members. Member stiffness coefficients are derived to account for geometrical nonlinearity and member shear deformation. Axial, shearing and bending force-deformation relationships are obtained from typical experimental results, and corresponding stiffness degradation factors are established to quantify the extent of member plasticity (Grierson et al., 2005; Xu et al., 2005).

2.1 Geometrical Nonlinearity Associated with Shear Deformation

The local force-deformation relationship of members is fundamental to the formulation of computer-based structural analysis procedures for framed structures (McGuire et al., 2000). In geometrical nonlinear problems, even though the materials behave in a linear-elastic manner, the relationships between the external loads and structural responses are nonlinear. Although the effect of shear deformation is typically insignificant in the analysis of conventional framed structures, shear effects do contribute to nonlinear structure response in cases of heavy transverse loading. The effect of shear deformation on structural deflection has been previously studied (Timoshenko, 1955). For instance, consider a simply supported beam with a uniformly distributed transverse load. When shear deformation is taken into account, the maximum deflection increases by 9.5% when the member span-to-section depth ratio is 10. If the ratio decreases to 6, the deflection increases by 26.5%. In another example, investigation of a two-bay by two-storey frame supported by an elastic foundation beam (Aydogan, 1995) found that the maximum vertical deflection and bending moment for the foundation beam increase by 12.8% and 4.8%, respectively, when the shear deformation is accounted for. Timoshenko beam theory has been extensively investigated and applied in structural analysis (Wang, 1996). However, the combined action of shear deformation and P-delta effect associated with flexural deformation has been little studied.

Two key areas of geometric nonlinearity related to the interaction between axial load and shear deformation have been investigated in the literature. The first concerns how shear deformation affects the elastic buckling of columns. For an example cantilever column, an expression for the elastic buckling load accounting for shear deformation has been given by Timoshenko and Gere (1961). Recently, more comprehensive solutions for elastic buckling loads of columns with different end constraints have been found that account for the effect of shear deformation (Aristizabal-Ochoa, 2004). The second area concerns beams on elastic foundations, where the influence of shear

deformation is significant (Aydogan, 1995; Areiza-Hurtado et al., 2005). This chapter focuses on the interactive effect of shear deformation on geometrical nonlinear responses of structural systems in the elastic range.

2.1.1 Governing Differential Equation

Consider the prismatic planar beam-column member in Figure 2.1, where L = member length, E = material Young's modulus, G = material shear modulus, I = cross-section moment of inertia, A = cross-sectional area, and A_s = equivalent cross-sectional shear area. The objective is to find end moments M_1 and M_2 when the member is subjected to constant axial force P_1 and rotation θ_1 imposed at member end 1. Once the moments are determined, the corresponding end shear reactions V_1 and V_2 are found from the equilibrium conditions. For geometric nonlinear problems, equilibrium is established for the deformed profile of the member. Here, it is required that the differential equation of equilibrium that governs geometric nonlinearity includes shear deformation. It is assumed that the member cross-section area has biaxial x-y symmetry, where x and y define the horizontal and vertical neutral axes of the cross-section, respectively.

The internal moment, shear and axial forces M, V and P are found by referring to the free body diagram in Figure 2.1(b), where the forces and associated deformations y and θ are presented in their positive directions. The forces at any position x along the member can be found from equilibrium to be,

$$M = M_1 - P_1 y - V_1 x \tag{2.1.1}$$

$$V = -V_1 \cos\theta - P_1 \sin\theta \tag{2.1.2}$$

$$P = P_1 \cos\theta - V_1 \sin\theta \tag{2.1.3}$$

where θ is a rotation due to flexural deformation. Equation (2.1.1) indicates that moment M relates linearly to end moment M_1 and shear force V_1, but nonlinearly to the product of axial force P_1 and deflection y.

When shear deformation is taken into account, deflection y in Eq. (2.1.1) includes the combined contribution of both the bending and the shearing deformations. It remains to determine deflection y in Figure 2.2(a) for a differential segment of the beam. Assume total deflection y is equal to the summation of deflection y_b due to the bending deformation in Figure 2.2(b) and deflection y_s due to the shear deformation in Figure 2.2(c), i.e., the total deflection is expressed as (Aydogan, 1995; Areiza-Hurtado et al., 2005)

$$y = y_b + y_s \tag{2.1.4}$$

Note that Eqs. (2.1.1), (2.1.2), and (2.1.3) define only the member equilibrium conditions, whereas the equilibrium of a deformed differential segment of the member is governed by a differential equation involving deflections y_b and y_s. For the deformation model in Figure 2.2(b), it is well known that the bending moment-versus-deflection relationship is defined by the following differential equation (Hibbeler, 2004),

$$\frac{d^2 y_b / dx^2}{[1+(dy_b / dx)^2]^{1.5}} = \frac{M}{EI} \tag{2.1.5}$$

which is the moment-curvature relationship for pure bending. As well, the shear force-versus-deflection relationship is defined by the following differential equation (Timoshenko, 1955),

$$\frac{dy_s}{dx} = \gamma = \frac{s_{sf} V}{GA} \tag{2.1.6}$$

in which γ is the average shear strain, and s_{sf} is a shearing shape factor that accounts for the non-uniform shear stress distribution over the cross-section depth. For example, if the maximum shear strain is utilized to establish the shear deflection, then $s_{sf} = 1.5$ for a rectangular section. However, the use of maximum shear strain to determine shear deflection might be too conservative. Another approach that is more reasonable requires a value for the factor s_{sf} to be found by using the principle of virtual work. To this end, Appendix 2.A derives the following expression for the shearing shape factor,

$$s_{sf} = \frac{A}{I^2} \int_A \frac{Q^2}{t^2} dA \tag{2.1.7}$$

in which t is the width of the cross section at the point where the shear stress is measured, and Q is the first moment about the neutral axis of the portion of the section area defined by where γ is measured. For a rectangular section, for example, Eq. (2.1.7) determines the factor $s_{sf} = 1.2$, a value closer to that obtained when warping is taken into account (Timoshenko, 1955). Typically, by using the s_{sf} value from Eq. (2.1.7) in Eq. (2.1.6), smaller shear deflections are yielded than those found using the maximum shear strain criterion. For a W-shaped cross-section, the expression for the shear shape factor can be expressed as

$$\begin{aligned} s_{sf} &= \frac{2A}{I^2}\left[\int_0^{d/2-t_f} \frac{Q^2}{t_w} dy + \int_{d/2-t_f}^{d/2} \frac{Q^2}{b_f} dy \right] \\ &= \frac{3[8c_2 + 15c_1(1-c_2) + 30c_1^3(3c_2-1) + c_1^5(15-83c_2+128c_2^2)]}{20c_2[1-(1-c_2)c_1^3]^2/(1-c_1+c_1c_2)}. \end{aligned} \tag{2.1.7a}$$

where parameters c_1 and c_2 are:

$$c_1 = 1 - 2t_f / d \tag{2.1.7b}$$

$$c_2 = t_w / b_f \tag{2.1.7c}$$

in which d = depth, b_f = width of the flange, t_f = thickness of the flange, and t_w = thickness of the web. For W920X253 beam section with c_1 = 0.9434 and c_2 = 0.0541, the shearing shape factor s_{sf} = 5.997 from Eq. (2.1.7a). For W360X382 column section with c_1 = 0.7692 and c_2 = 0.0734, the factor s_{sf} =5.645 from Eq. (2.1.7a). Thus, it can be assumed $s_{sf} \approx 6$ for practical W-sections. Finally, from Eq. (2.1.7a), note when c_1 = 0 ($t_f = d/2$) and c_2 = 1 ($t_w = b_f$) that the factor s_{sf} = 1.2 for rectangular cross sections.

Once the shearing shape factor s_{sf} is estimated by Eq. (2.1.7) for a specified cross-section, the shear deflection y_s can be determined. To this end, differentiating Eq. (2.1.4) twice yields, from Eqs. (2.1.5) and (2.1.6),

$$\frac{d^2y}{dx^2} = \frac{d^2y_b}{dx^2} + \frac{d^2y_s}{dx^2} = \frac{M}{EI}\left[1 + \left(\frac{dy_b}{dx}\right)^2\right]^{1.5} + \frac{s_{sf}}{GA}\frac{dV}{dx} \tag{2.1.8}$$

which is the differential equation that relates total deflection y (accounting for combined bending and shearing deformations) to moment M and shear force V. The first derivative of the shear force in Eq. (2.1.8) is obtained by differentiating Eq. (2.1.2) once with respect to x, to obtain,

$$\frac{dV}{dx} = V_1 \sin\theta \frac{d\theta}{dx} - P_1 \cos\theta \frac{d\theta}{dx} = \cos\theta \frac{d\theta}{dx}(V_1 \tan\theta - P_1) = \frac{M}{EI}\left(V_1 \frac{dy_b}{dx} - P_1\right) \tag{2.1.9}$$

where the following relationships are employed,

$$\cos\theta \frac{d\theta}{dx} = \frac{M}{EI} \tag{2.1.10a}$$

$$\tan\theta = \frac{dy_b}{dx} \tag{2.1.10b}$$

By substituting Eq. (2.1.9) into (2.1.8), the general differential equilibrium equation involving the total deflection becomes

$$\frac{d^2y}{dx^2} = \frac{M}{EI}\left\{\left[1 + \left(\frac{dy_b}{dx}\right)^2\right]^{1.5} + \frac{s_{sf}}{GA}\left(V_1 \frac{dy_b}{dx} - P_1\right)\right\} \tag{2.1.11}$$

If the shearing deformation can be ignored (i.e., $1/GA = 0$ and $y = y_b$), Eq. (2.1.11) reduces to the differential equation Eq. (2.1.5) that accounts for the bending deformation only.

Note that the differential equation Eq. (2.1.11) does not account for external transverse load distributed along the length of the member. In circumstances where distributed transverse loads are applied over the member span, the expression on the right-hand side of Eq. (2.1.11) needs to be modified. For instance, in the analysis of beams on elastic foundations, the shearing effect is considered by modifying the right-hand side of Eq. (2.1.11) to account for the reaction due to the elastic foundation (Aydogan, 1995). The effect of shear deformation due to transverse loads on fixed-end reactions of a fix-fix member is investigated in Section 2.2.2.

Typically, a direct analytical solution of Eq. (2.1.11) cannot be found due to the presence of geometric nonlinearities. Adopting the conventional assumption of small strain, the squared term of the first derivative of y_b is dropped such that Eq. (2.1.11) is rewritten as,

$$\frac{EI}{1-P_1 s_{sf}/GA}\frac{d^2y}{dx^2} = M + \frac{MV_1}{GA/s_{sf} - P_1}\frac{dy_b}{dx} \tag{2.1.12}$$

Equation (2.1.12) still cannot be directly solved because the term dy_b/dx remains unknown. However, it is possible to solve Eq. (2.1.12) for the flexibility coefficients associated with bending deformation alone. Then, the principle of virtual work can be utilized to find the corresponding member stiffness coefficients accounting for geometrical nonlinearity and member shear deformation, as discussed in the following.

2.1.2 Derivation of Elastic Stiffness Coefficients

2.1.2.1 Rotational Stiffness Coefficients

Consider the simply supported member in Figure 2.3 (a), where moments M_1 and M_2, induced by rotation θ_1 are to be determined. By employing the principle of virtual work (the unit-force method), the flexibility coefficients in Figures 2.3 (b) and (c) are expressed as,

$$f_{11} = f_{11m} + f_{11s} = \int_0^L \frac{m_1(x)m_{1v}(x)}{EI}dx + s_{sf}\int_0^L \frac{v_1(x)v_{1v}(x)}{GA}dx = f_{22} \tag{2.1.13a}$$

and

$$f_{21} = f_{21m} + f_{21s} = \int_0^L \frac{m_1(x)m_{2v}(x)}{EI}dx + s_{sf}\int_0^L \frac{v_1(x)v_{2v}(x)}{GA}dx = f_{12} \tag{2.1.13b}$$

where moment $m_j(x)$ and shear force $v_j(x)$ are induced by unit moment $M_j = 1$ ($j = 1, 2$) and axial force P_1, whereas virtual moment $m_{jv}(x)$ and shear force $v_{jv}(x)$ are induced only by unit moment $M_j = 1$ ($j = 1, 2$). From member equilibrium in Figures 2.3 (b) and 2.3 (c), it follows that,

$$m_1(x) = 1 - P_1 y_1(x) - x/L \tag{2.1.14a}$$

$$v_1(x) = 1/L + P_1 dy_1/dx \tag{2.1.14b}$$

$$m_2(x) = -P_1 y_2(x) - x/L \tag{2.1.14c}$$

$$v_2(x) = 1/L + P_1 dy_2/dx \tag{2.1.14d}$$

$$m_{1v}(x) = 1 - x/L \tag{2.1.14e}$$

$$m_{2v}(x) = -x/L \tag{2.1.14f}$$

$$v_{1v}(x) = v_{2v}(x) = 1/L \tag{2.1.14g}$$

where $y_1(x)$ and $y_2(x)$ are the deflection curves of the primary structure due to the applied end moments $M_1 = 1$ and $M_2 = 1$, respectively, accounting for axial force P_1 and shear deformation. The flexibility coefficients f_{11m} and f_{21m} in Eqs. (2.1.13) cannot be computed from the integrals because both $y_1(x)$ and $y_2(x)$ in Eqs. (2.1.14) remain unknown. Without consideration of shear deformation caused by shear force, however, coefficients f_{11m} and f_{21m} are the rotations at end 1 and end 2 due to imposing $M_1 = 1$; i.e., these two coefficients are determined by Eq. (2.1.12) when the second term on the right-hand side involving shear force V_1 is ignored. When moment M in Eq. (2.1.12) is replaced by moment m_1 from Eq. (2.1.14a), coefficients f_{11m} and f_{21m} are found by solving the differential equation, to find (see Appendix 2.B),

$$f_{11m} = \begin{cases} \dfrac{(1 - P/GA_s)L}{EI\psi^2}\left(1 - \dfrac{\psi}{\tan\psi}\right) & P \le 0 \\ \dfrac{(1 - P/GA_s)L}{EI\psi^2}\left(\dfrac{\psi}{\tanh\psi} - 1\right) & P > 0 \end{cases} \tag{2.1.15a}$$

$$f_{21m} = \begin{cases} \dfrac{(1 - P/GA_s)L}{EI\psi^2}\left(1 - \dfrac{\psi}{\sin\psi}\right) & P \le 0 \\ \dfrac{(1 - P/GA_s)L}{EI\psi^2}\left(\dfrac{\psi}{\sinh\psi} - 1\right) & P > 0 \end{cases} \tag{2.1.15b}$$

in which

$$\psi = L\sqrt{\frac{|P|(1 - P/GA_s)}{EI}} \tag{2.1.15c}$$

where A_s (= A/f_{sf}) represents the equivalent shear cross-sectional area. Thus, the flexibility coefficients in Eqs. (2.1.13) related to moment have been determined.

To consider the contribution of shear deformation due to shear force in Eqs. (2.1.13), the shear forces $v_j(x)$ and virtual shear forces $v_{jv}(x)$ (j = 1, 2) given in Eqs. (2.1.14) are substituted into the relevant terms in Eqs. (2.1.13), to yield the following flexibility coefficients,

$$f_{11s} = f_{12s} = \int_0^L \frac{v_1 v_{1v}}{GA_s} dx = \int_0^L \frac{1/L + P_1 dy_1/dx}{LGA_s} dx = \frac{1}{LGA_s} \tag{2.1.16}$$

where boundary conditions $y_1(0) = y_1(L) = 0$ are applied to evaluate the integrals.

Upon evaluating Eqs. (2.1.15a, b) and Eq. (2.1.16), flexibility coefficients f_{ij} (i, j = 1, 2) are found through Eqs. (2.1.13) to obtain the flexibility matrix for the primary structure in Figure 2.3 (a) accounting for the axial force and shearing deformation. The bending moment-rotation deformation compatibility conditions for the member are expressed in the following matrix form,

$$\begin{bmatrix} f_{11} & f_{12} \\ f_{21} & f_{22} \end{bmatrix} \begin{Bmatrix} M_1 \\ M_2 \end{Bmatrix} = \begin{Bmatrix} \theta_1 \\ 0 \end{Bmatrix} \tag{2.1.17}$$

from which the relationships between the end moments and rotation are obtained as,

$$M_1 = kb\eta_1\theta_1 = k_{33}^g\theta_1 \tag{2.1.18a}$$

$$M_2 = c\eta_2 kb\eta_1\theta_1 = k_{63}^g\theta_1 = c\eta_2 M_1 \tag{2.1.18b}$$

where superscript g implies the involvement of geometric nonlinearity, and subscripts "33" and "63" correspond to the numbering system indicated in Figure 2.3(d) for the end displacements and forces for the member. The two stiffness coefficients in Eqs. (2.1.18) are given by,

$$k_{33}^g = kb\eta_1 \tag{2.1.19}$$

$$k_{63}^g = c\eta_2 kb\eta_1 \tag{2.1.20}$$

where coefficient $k = EI/L$. Parameters $kb\eta_1$ and $c\eta_2$ in Eqs. (2.1.18a) and (2.1.18b) define the modified rotation stiffness coefficient and carryover factor, respectively. Parameters b and c are defined by the following expressions (Chen et al., 1996),

$$b = \begin{cases} \dfrac{1 - \psi/\tan\psi}{\tan(\psi/2)/(\psi/2) - 1} & P \le 0 \\ \dfrac{1 - \psi/\tanh\psi}{\tanh(\psi/2)/(\psi/2) - 1} & P > 0 \end{cases} \tag{2.1.21}$$

$$c = \begin{cases} \dfrac{\psi - \sin\psi}{\sin\psi - \psi\cos\psi} & P \le 0 \\ \dfrac{\psi - \sinh\psi}{\sinh\psi - \psi\cosh\psi} & P > 0 \end{cases} \tag{2.1.22}$$

where the subscript of P_1 has been dropped to simplify the notation, and the parameter ψ is defined in Eq. (2.1.15c). Equations (2.1.21) and (2.1.22) are referred to in the literature as stability functions (Chen et al., 1996), but should probably be called geometrical stiffness coefficients, since they are applied not only in stability analysis but also in any geometrical nonlinear analysis. Parameters η_i (i

=1, 2) in Eqs. (2.1.18) or (2.1.19) are referred to as geometrical shearing coefficients, and are expressed as,

$$\eta_1 = \frac{1+\eta_3\eta_4}{(1-P/GA_s)(1+\eta_3\eta_5)} \tag{2.1.23}$$

$$\eta_2 = \frac{1+\eta_3\eta_6}{1+\eta_3\eta_4} \tag{2.1.24}$$

where parameters η_3, η_4, η_5, and η_6 are given by,

$$\eta_3 = \frac{EI}{(1-P/GA_s)GA_sL^2} \tag{2.1.25}$$

$$\eta_4 = \begin{cases} \psi^2/(1-\psi/\tan\psi) & P \le 0 \\ -\psi^2/(1-\psi/\tanh\psi) & P > 0 \end{cases} \tag{2.1.26a}$$

$$\eta_5 = \begin{cases} \psi^2\tan(\psi/2)/[\tan(\psi/2)-\psi/2] & P \le 0 \\ -\psi^2\tanh(\psi/2)/[\tanh(\psi/2)-\psi/2] & P > 0 \end{cases} \tag{2.1.26b}$$

$$\eta_6 = \begin{cases} \psi^2/(1-\psi/\sin\psi) & P \le 0 \\ -\psi^2/(1-\psi/\sinh\psi) & P > 0 \end{cases} \tag{2.1.26c}$$

2.1.2.2 Transverse Stiffness Coefficients

Following the same procedure as that used to derive the rotational stiffness coefficients in the previous section, the transverse stiffness coefficients are readily found accounting for axial force and member shearing deformation. To that end, consider the deformed profile of the beam-column member in Figure 2.4 (a) due to deflection Δ_1 imposed at end 1. When deflection Δ_1 is imposed on the simply-supported primary beam in Figure 2.4 (b), the rotation at both ends is equivalently expressed as $-\Delta_1/L$. The bending moment-rotation deformation compatibility condition Eq. (2.1.17) need only be changed on the right-hand side to establish the shear force-deflection deformation compatibility condition as,

$$\begin{bmatrix} f_{11} & f_{12} \\ f_{21} & f_{22} \end{bmatrix} \begin{Bmatrix} M_1 \\ M_2 \end{Bmatrix} = -\frac{\Delta_1}{L} \begin{Bmatrix} 1 \\ 1 \end{Bmatrix} \tag{2.1.27}$$

Upon solving Eq. (2.1.27), the relationship between the end moments and the deflection is found as,

$$M_1 = M_2 = kb\eta_1(1+c\eta_2)\Delta_1/L = k_{32}^g\Delta_1 \tag{2.1.28}$$

By setting deflection $\Delta_1 = 1$ in Eq. (2.1.28), the stiffness coefficient is given by,

$$k_{32}^g = kb\eta_1(1+c\eta_2)/L = k_{62}^g \tag{2.1.29}$$

which is depicted in Figure 2.4 (c), where the subscripts "32" and "62" refer to the end force/deformation numbering scheme in Figure 2.3 (d). From Eq. (2.1.28) and the equilibrium conditions for the member, the transverse end reactions are found as

$$V_1 = -V_2 = kb\eta_1[2(1+c\eta_2) + PL/(kb\eta_1)]\Delta_1 / L^2 = k^g_{22}\Delta_1 \tag{2.1.30}$$

By setting deflection $\Delta_1 = 1$ in Eq. (2.1.30), the stiffness coefficient is given by,

$$k^g_{22} = kb\eta_1[2(1+c\eta_2) + PL/(kb\eta_1)]/L^2 = -k^g_{52} \tag{2.1.31}$$

Similar to the discussion in the previous subsection, when deflection Δ_1 is set to unity, Eqs. (2.1.28) and (2.1.30), respectively, represent the rotational and translational stiffness coefficients due to a unit end deflection. The same stiffness coefficient expressions as in Eqs. (2.1.29) and (2.1.31) are obtained if the deflection is imposed at end 2 rather than end 1 of the member in Figure 2.4 (a); i.e., $k^g_{65} = k^g_{32}$ and $k^g_{55} = k^g_{22.}$ The stiffness coefficients are applied for monotonic incremental-load analysis, where, for each increment, the structure is essentially treated as being linear elastic, for which Maxwell's reciprocal theorem holds. Therefore, all stiffness coefficients k^g_{ij} accounting for geometric nonlinearity and member shear deformation have been determined; i.e., $k^g_{25} = k^g_{52}$, $k^g_{23} = k^g_{32}$, $k^g_{56} = k^g_{65}$ and $k^g_{26} = k^g_{62}$.

2.2 Effects of Shear Deformation on Structural Response

This section investigates the effects of shear deformation on elastic stability and fixed-end reactions using the formulas derived in the previous section. To facilitate the discussion, the Euler buckling load,

$$P_e = \pi^2 EI / L^2 \tag{2.2.1}$$

is introduced as a baseline reference. In addition, the ratio of axial force P to Euler buckling load P_e, and the ratio of Euler buckling load P_e to shearing stiffness GA_s are represented by the following parameters,

$$\rho_e = P / P_e \tag{2.2.2a}$$

$$\rho_s = \frac{P_e}{GA_s} = \frac{\pi^2 EI}{GA_s L^2} = \frac{\pi^2 E}{G}\left(\frac{r_s}{L}\right)^2 \tag{2.2.2b}$$

where the parameter ρ_s is the so-called axial-shear influence factor that depends on the geometric and material properties of the member, in which the parameter r_s is defined as,

$$r_s = \sqrt{I / A_s} = \sqrt{s_{sf} I / A} = \sqrt{s_{sf}}\sqrt{I / A} = r_z\sqrt{s_{sf}} \tag{2.2.3a}$$

where

$$s_{sf} > 1.0 \tag{2.2.3b}$$

is a shearing shape factor, discussed in Appendix 2.A, and r_s is the shear-radius of gyration modified from the conventional bending-radius of gyration r_z. From Eqs. (2.2.1) and (2.2.2), the parameter ψ given in Eq. (2.1.15c) is rewritten as,

$$\psi = \pi\sqrt{|P|(1 - P/GA_s)/P_e} = \pi\sqrt{|\rho_e|(1 - \rho_e\rho_s)} \tag{2.2.4}$$

When $\rho_s = 0$ and $\rho_e < 0$, Eq. (2.2.4) reduces to a parameter in elastic buckling analysis (Xu & Liu, 2002). By using the parameters ρ_s and ρ_e from Eqs. (2.2.2), the parameter η_3 in Eq. (2.1.25) is expressed as,

$$\eta_3 = \frac{1}{1 - \rho_e\rho_s}\frac{E}{G}\left(\frac{r_s}{L}\right)^2 \tag{2.2.5}$$

The effect of shear deformation on buckling stability and fixed-end reactions for a beam-column member is discussed in the following.

2.2.1 Effect of Shear Deformation on Elastic Buckling

The buckling of a beam-column member with the various boundary conditions in Figure 2.5 is discussed here to illustrate the effect of shear deformation on elastic stability. The notations in the figure are similar to those in Figure 2.1(a), except that rotational-constraining stiffnesses R_1, R_2 and translational-constraining stiffness R_3 are introduced to reflect the different types of end constraints. Buckling is defined by an instability condition where the axial load reaches such an extent that the structure stiffness matrix becomes singular (i.e., the corresponding determinant of the matrix vanishes).

Because tensile force has the tendency to increase the geometrical stiffness of a structural member, only a compressive axial force (assumed to be positive in this subsection) is here considered. Four types of end constraints are investigated: free-clamped cantilever column with $R_2 = R_3 = 0$ and $R_1 = \infty$ (free-fix); simply supported column with $R_1 = R_2 = 0$ and $R_3 = \infty$ (pin-pin); pin-clamped supported column with $R_2 = 0$ and $R_3 = R_1 = \infty$ (pin-fix); and clamped-clamped supported column with $R_1 = R_2 = R_3 = \infty$ (fix-fix).

Once a stability function is obtained with respect to axial-force parameter ρ_e, given in Eq. (2.2.2a), minimum root ρ_{ecr} can be solved from the stability function so that critical load P_{cr} is given by

$$P_{cr} = \rho_{ecr} P_e \tag{2.2.6}$$

The cantilever column (free-fix) has been previously studied by a number of researchers (Timoshenko & Gere, 1961; Chugh, 1977; Aristizabal-Ochoa, 2004). From Eqs. (2.1.19), (2.1.29), and (2.1.31), the stability function obtained by zeroing the determinant of the geometric stiffness matrix for the cantilever column is expressed as,

$$\begin{vmatrix} k_{22}^g & k_{23}^g \\ k_{32}^g & k_{33}^g \end{vmatrix} = k^2 b\eta_1 [b\eta_1 (1 - c^2\eta_2^2) - \pi^2 \rho_e] = 0 \tag{2.2.7}$$

Of all the possible solutions of Eq. (2.2.7) for parameter ρ_e, only the minimum solution value ρ_{ecr} yields the elastic buckling load of the column, i.e., from Eq. (2.2.2a), $P_{cr} = \rho_{ecr} P_e$.

To demonstrate the effect of member shear deformation on the elastic buckling load of a structural steel cantilever beam-column with $E = 2\times10^5$ MPa, $G = 77\times10^3$ MPa, and specified slenderness ratio $L/r_s = 20$, the parameter $\rho_s = 0.0641$ from Eq. (2.2.2b), and parameters ψ and η_3 are computed as, from Eqs. (2.2.4) and (2.2.5),

$$\psi = \pi\sqrt{\rho_e (1 + 0.0641\rho_e)} \tag{2.2.8a}$$

$$\eta_3 = 0.0065/(1 + 0.0641\rho_e) \tag{2.2.8b}$$

By substituting Eqs. (2.2.8) into the expressions for b, c, η_1, and η_2 in Eqs. (2.1.20) through (2.1.24), and then substituting b, c, η_1, and η_2 into Eq. (2.2.7), a complicated buckling function in terms of variable ρ_e results, for which it is difficult to solve for the minimum root ρ_{ecr}. Alternatively, instead of obtaining the exact stability function, this study input all the expressions related to Eq. (2.2.7) into a Microsoft Excel spread sheet, and then used the *Goal Seek* tool (Microsoft, 2000) for solution. This approach determines the non-dimensional buckling load $\rho_{ecr} = 0.243$, which corresponds to buckling load $P_{cr} = 0.243P_e$.

The theoretical value of the buckling load for a cantilever column without considering shear deformation is $P_{cr0} = P_e/4$. When shear deformation is taken into account, the relative difference is calculated as $(P_{cr}/P_{cr0} - 1) = (0.243\times4 - 1) = -0.028$. This indicates that when $L/r_s = 20$, the critical buckling load is decreased by 2.8% when shear deformation is accounted for. For the various slenderness ratios and end conditions with $L/r_s = 10$, 20, 30, 40, 50, and 60, the relative differences between critical buckling loads found when shear deformation is and is not accounted for are summarized in Table 2.1.

To demonstrate the effect of the shearing shape factor s_{sf}, the relative differences between actual critical loads and those found neglecting shear deformation are plotted in Figure 2.6 for slenderness

ratios KL/r_z = 50, 70 and 90. Parameter K is an effective-length factor that accounts for different end constraints. It is evident that for a given member with a specified KL/r_z value, the shearing shape factor s_{sf} decreases the critical buckling load as it increases in value.

2.2.2 Effect of Shear Deformation on Fixed-End Reactions

This section discusses how shear deformation affects the end reactions of beam-column members under transverse loads. The fixed-end reactions for a fix-fix beam with specified transverse loads are well established when the shearing effect is not accounted for (McGuire et al., 2000). In the following, these reactions are taken as the basis for expressing member-end reactions when shearing deformation is accounted for.

For the fix-fix beam with arbitrary transverse load $w(x)$ shown in Figure 2.7, the Force Method of analysis is utilized to obtain the fixed-end reactions. To this end, the primary structure is selected as the simply supported beam in Figure 2.3 (a). The deformation compatibility conditions taking into account shear deformation are expressed in compact matrix form as,

$$\begin{bmatrix} \dfrac{L}{3EI}+\dfrac{1}{GA_sL} & \dfrac{-L}{6EI}+\dfrac{1}{GA_sL} \\ \dfrac{-L}{6EI}+\dfrac{1}{GA_sL} & \dfrac{L}{3EI}+\dfrac{1}{GA_sL} \end{bmatrix} \begin{Bmatrix} M_1 \\ M_2 \end{Bmatrix} = -\begin{Bmatrix} \theta_{1l} \\ \theta_{2l} \end{Bmatrix} \tag{2.2.9}$$

where θ_{jl} (j = 1, 2) are the member-end rotations caused by the transverse load $w(x)$.

It is well known that shear force does not contribute to member-end rotations of a simply supported beam subjected to transverse loads, i.e., for shear force V the rotation is,

$$\theta_{jlv} = \int_0^L \frac{VV_v}{GA_s}dx = \int_0^L \frac{dM/dx}{LGA_s}dx = 0 \tag{2.1.10}$$

where M is the member moment distribution having boundary conditions $M(0) = M(L) = 0$, and $V_v = 1/L$ is virtual shear force due to a unit moment applied at the member end.

Solve Eq. (2.2.9) for the fixed-end moments to find,

$$\begin{Bmatrix} M_1 \\ M_2 \end{Bmatrix} = \frac{-2k}{1+12\rho_s/\pi^2} \begin{Bmatrix} 2\theta_{1l}+\theta_{2l}+6\rho_s(\theta_{1l}-\theta_{2l})/\pi^2 \\ \theta_{1l}+2\theta_{2l}+6\rho_s(\theta_{2l}-v_{1l})/\pi^2 \end{Bmatrix} \tag{2.2.11}$$

where parameter ρ_s is defined in Eq. (2.2.2b) and $k = EI/L$. If shear deformation is neglected, i.e., ρ_s = 0, the moment-rotation relationship in Eq. (2.2.11) reduces to the conventional expression,

$$\begin{Bmatrix} M_{10} \\ M_{20} \end{Bmatrix} = -2k \begin{Bmatrix} 2\theta_{1l} + \theta_{2l} \\ \theta_{1l} + 2\theta_{2l} \end{Bmatrix} \tag{2.2.12}$$

where the subscript "0" denotes the fixed-end moments without account for shear deformation. Note that Eq. (2.2.12) can be inversely expressed as

$$\begin{Bmatrix} \theta_{1l} \\ \theta_{2l} \end{Bmatrix} = \frac{-1}{6k} \begin{Bmatrix} 2M_{10} - M_{20} \\ 2M_{20} - M_{10} \end{Bmatrix} \tag{2.2.13}$$

Substitute Eq. (2.2.13) into Eq. (2.2.11) to find,

$$\begin{Bmatrix} M_1 \\ M_2 \end{Bmatrix} = \begin{Bmatrix} M_{10} \\ M_{20} \end{Bmatrix} - \frac{6\rho_s / \pi^2}{1 + 12\rho_s / \pi^2} \begin{bmatrix} 1 & 1 \\ 1 & 1 \end{bmatrix} \begin{Bmatrix} M_{10} \\ M_{20} \end{Bmatrix} \tag{2.2.14}$$

which transforms the conventional fixed-end moments M_{10} and M_{20} into moments M_1 and M_2 that account for shear deformation. From Eq. (2.2.14) and the equilibrium conditions for the member, the transverse end reactions found as

$$\begin{Bmatrix} V_1 \\ V_2 \end{Bmatrix} = \begin{Bmatrix} V_{10} \\ V_{20} \end{Bmatrix} + \frac{12\rho_s / \pi^2}{(1 + 12\rho_s / \pi^2)L} \begin{bmatrix} -1 & -1 \\ 1 & 1 \end{bmatrix} \begin{Bmatrix} M_{10} \\ M_{20} \end{Bmatrix} \tag{2.2.15}$$

which transforms the conventional fixed-end reactions V_{10} and V_{20} into reactions V_1 and V_2 that account for shear deformation.

It is interesting to observe from Eqs. (2.2.14) and (2.2.15) that if the external transverse load $w(x)$ is applied symmetrically to cover the span of the member, the shear deformation does not affect the fixed-end reactions because, then, $M_{20} = -M_{10}$ and the second term on the RHS of each of Eqs. (2.2.14) and (2.2.15) is zero valued. However, in such cases, the shear deformation does affect the member deflection.

2.3 Stiffness Degradation

The performance of any engineered structure under external loads depends not only on its geometric properties, but also, to a large extent, on the properties of the materials used to construct the structure. Although a slender framed structure can fail due to elastic buckling, most failures in commonly engineered structures are due to the advent of nonlinear material behaviour, referred to as post-elastic or plastic behaviour. Thus, structural failure or collapse generally involves both geometric and material nonlinearities. Material properties such as yield strength, ultimate strength, and ductility are crucial design indices that guide designers in their quest to ensure the safety of engineered structures. To facilitate the material-nonlinear analysis of a framed structure, the next Section introduces an appropriate model for the failure behaviour of a member cross-section.

2.3.1 Force-Deformation Model

The variation of the post-elastic (bending, shearing or axial) stiffness of a member section can be uniquely characterized by a force-deformation (F–D) curve of the form in Figure 2.8. In this figure, F_y is the specified initial-yield (M_y, V_y or P_y) capacity of the section and F_p is the corresponding full-yield (M_p, V_p or P_p) capacity, with the consideration of both primary and residual stresses (Heyman & Dutton 1954; Huber & Beedle 1954; Beedle, 1958). Also, D_p is the known magnitude of plastic deformation (rotation ϕ, transverse deflection γ or axial displacement δ) beyond initial yielding at which the section fully yields. Finally, for force $F = M$, V or P, the quantity $dF/dD = R$, T or N is the post-elastic (bending, shearing or axial) stiffness of the section, respectively. For most section shapes commonly used in steel building frameworks, the continuous nonlinear portion of the F–D curve in Figure 2.8 can be reasonably modeled as an elliptical shape defined by the following function (Grierson et al., 2005; Xu et al., 2005),

$$F = F_y + (F_p - F_y)\left[1 - \left(1 - \frac{D}{D_p}\right)^{e_0}\right]^{1/e_0} \quad 0 \le \frac{D}{D_p} < 1\ , \quad \frac{F_y}{F_p} \le \frac{F}{F_p} \le 1 \tag{2.3.1}$$

where exponent $e_0 > 1$ has different values, depending on whether force $F = M$, V or P. If $F \le F_y$ the post-elastic deformation $D = 0$, whereas if $F_y \le F \le F_p$ the post-elastic deformation is, from Eq. (2.3.1),

$$D = D_p - D_p\left\{1 - \left[\frac{F - F_y}{F_p - F_y}\right]^{e_0}\right\}^{1/e_0} \quad 0 \le \frac{D}{D_p} \le 1, \quad \frac{F_y}{F_p} \le \frac{F}{F_p} \le 1 \tag{2.3.2}$$

By differentiating Eq. (2.3.1) with respect to post-elastic deformation D, the post-elastic (bending, shearing or axial) stiffness is,

$$\frac{dF}{dD} = \frac{(F_p - F_y)}{D_p}\left(1 - \frac{D}{D_p}\right)^{e_0 - 1}\left[1 - \left(1 - \frac{D}{D_p}\right)^{e_0}\right]^{\frac{1-e_0}{e_0}} \quad 0 \le \frac{D}{D_p} \le 1\ , \ \frac{F_y}{F_p} \le \frac{F}{F_p} \le 1 \tag{2.3.3}$$

where, as shown in Figure 2.8, $dF/dD = \infty$ if post-elastic deformation $D = 0$ and $dF/dD = 0$ if $D \ge D_p$.

To identify the extent of the plasticity, so-called the stiffness degradation factors are defined by the ratio of the elastic deformation to the elastic-plus-plastic deformation at a member section. For a beam-column member with post-elastic bending, shearing, or axial stiffness R, T or N, respectively, the corresponding stiffness degradation factor $sdf = r$, t or n. As indicated in Figure 2.8, $sdf = 1$, if post-elastic stiffness $dF/dD = \infty$ (i.e., fully elastic behaviour), whereas $sdf = 0$, if post-elastic stiffness

dF/dD = 0 (i.e., idealized plastic behaviour). It is observed that when 0 < *sdf* < 1, the physical meaning of the value is a measure of the extent of the plasticity at a critical section. The determination of parameters F_y, F_p, D_p and e_0 and stiffnesses *R*, *T*, *N* is discussed in Appendix 2.C through consideration of test results from bending, shearing and axial experiments presented in the literature (Kusuda & Thurlimann, 1958; Hall & Newmark, 1957; Huber & Beedle, 1954). The next section introduces so-called stiffness degradation factors as a means to account for the degradation of post-elastic *R*, *T* and *N* stiffness beyond first yield.

2.3.2 Determination of Stiffness Degradation Factors

Stiffness degradation factors are introduced to identify the influence of plasticity on member stiffness (Grierson et al., 2005; Xu et al., 2005). A stiffness degradation factor is characterized by the ratio of *elastic* deformation to *elastic-plus-plastic* deformation of a member section. For a beam-column member with post-elastic bending, shearing or axial stiffness *R*, *T* or *N*, respectively, the corresponding stiffness degradation factor *sdf* = *r*, *t* or *n*. As indicated in Figure 2.8, *sdf* = 1 if post-elastic stiffness *dF/dD* = ∞ (i.e., fully elastic behavior), whereas *sdf* = 0 if post-elastic stiffness *dF/dD* = 0 (i.e., idealized plastic behaviour). It is observed that when 0 < *sdf* < 1, the physical meaning of the value is a measure of the extent of the plasticity at a critical section. In the following, the bending, shearing and axial stiffness degradation factors *r, t* and *n*, respectively, are derived assuming plastic deformation to be concentrated at a member section such that the elastic deformation of the immediately adjacent section occurs for the same magnitude of force *M*, *V* or *P*.

2.3.2.1 Bending Stiffness Degradation Factor *r*

Consider the simplified member model in Figure 2.9, which has a pin release at the right end and accounts for rotational bending deformation alone at the left end (i.e., no shear or axial deformation). Under the action of bending moment *M* applied at the left end, elastic bending deformation ϕ_e = *ML*/3*EI* and post-elastic bending deformation ϕ = *M/R*, and the bending stiffness degradation factor is,

$$r = \frac{\phi_e}{\phi_e + \phi} = \frac{1}{1 + 3EI / RL} \tag{2.3.4}$$

From Figure 2.8 and Eq. (2.3.4), for idealized elastic behavior, *R* = ∞ and *r* = 1 (i.e., no bending stiffness degradation), whereas for idealized plastic behavior, *R* = 0 and *r* = 0 (i.e., complete bending stiffness degradation).

2.3.2.2 Shear Stiffness Degradation Factor *t*

Consider the simplified member model in Figure 2.10, which has a pin release at the right end and accounts for transverse shear deformation alone at the left end (i.e., no bending or axial deformation). Under the action of shear force V applied at the left end, elastic shear deformation $\gamma_e = VL^3/3EI$ and post-elastic shear deformation $\gamma = V/T$, and the shear stiffness degradation factor is,

$$t = \frac{\gamma_e}{\gamma_e + \gamma} = \frac{1}{1 + 3EI / TL^3} \tag{2.3.5}$$

From Figure 2.8 and Eq. (2.3.5), for perfectly elastic behavior, $T = \infty$ and $t = 1$ (i.e., no shear stiffness degradation), whereas for perfectly plastic behavior, $T = 0$ and $t = 0$ (i.e., complete shear stiffness degradation).

2.3.2.3 Axial Stiffness Degradation Factor *n*

Consider the simplified member model in Figure 2.11, which accounts for normal axial deformation alone at the left end (i.e., no bending or shear deformation). Under the action of axial force P, elastic axial deformation $\delta_e = PL/EA$ and post-elastic axial deformation $\delta = P/N$, and the axial stiffness degradation factor,

$$n = \frac{\delta_e}{\delta_e + \delta} = \frac{1}{1 + AE / NL} \tag{2.3.6}$$

From Figure 2.8 and Eq. (2.3.6), for perfectly elastic behavior, $N = \infty$ and $n = 1$ (i.e., no axial stiffness degradation), whereas for perfectly plastic behavior, $N = 0$ and $n = 0$ (i.e., complete axial stiffness degradation).

Appendix 2.A Derivation of Flexibility Coefficients

This section derives the flexibility coefficients f_{m11} and f_{m21} for the simply supported beam in Figure 2.12accounting for the contribution of bending moment M and axial force P (note the subscript of P_1 is dropped for simplicity). When the second term involving shear force V_1 on the right-hand side of Eq. (2.1.12) is ignored (i.e., no shear force contribution), and the moment M is replaced by $Py+x/L$-1 from Figure 2.14, the differential equation Eq. (2.1.12) becomes,

$$\frac{EI}{1 - P / GA_s} \frac{d^2 y}{dx^2} - Py = \frac{x}{L} - 1 \tag{2.A.1}$$

Coefficients f_{m11} and f_{m21} indicated in Figure 2.12are determined from the solution of Eq. (2.A.1), which depends on whether the value of axial force P is positive, negative or zero. Only the derivation

for case where $P < 0$ is detailed here (the results for the two other cases are similarly derived, but only the results are given here). When $P < 0$,

$$\vartheta^2 = \frac{-P(1-P/GA_s)}{EI} \tag{2.A.2}$$

and Eq. (2.A.1) is rewritten as,

$$\frac{d^2y}{dx^2} + \vartheta^2 y = \frac{1-P/GA_s}{EI}\left(\frac{x}{L}-1\right) \tag{2.A.3}$$

The particular solution of Eq. (2.A.3) is given by,

$$y_p = \frac{1}{P}\left(1-\frac{x}{L}\right) \tag{2.A.4}$$

The general solution of Eq. (2.A.3) is,

$$y = a_1\cos(\vartheta x) + a_2\sin(\vartheta x) + (1-x/L)/P \tag{2.A.5}$$

where a_1 and a_2 are two arbitrary constants determined from the following two boundary conditions,

$$y(0) = 0 \tag{2.A.6a}$$

$$y(L) = 0 \tag{2.A.6b}$$

By applying the boundary condition Eq. (2.A.6a) in Eq. (2.A.5), the constant a_1 is found as below,

$$y(0) = a_1 + 1/P = 0 \rightarrow a_1 = -1/P \tag{2.A.7}$$

Similarly, apply the boundary condition Eq. (2.A.6a) to find a_2 as below,

$$y(L) = a_1\cos\psi + a_2\sin\psi = 0 \rightarrow a_2 = 1/(P\tan\psi) \tag{2.A.8}$$

in which,

$$\psi = \vartheta L = L\sqrt{\frac{-P(1-P/GA_s)}{EI}} \tag{2.A.9}$$

To find the slope of the deflection curve, differentiate Eq. (2.A.5) with respect to x to get,

$$\frac{dy}{dx} = -a_1\vartheta\sin(\vartheta x) + a_2\vartheta\cos(\vartheta x) - 1/(LP)$$

which, upon substituting for a_1, a_2 and ψ from Eqs. (2.A.7), (2.A.8) and (2.A.9), becomes,

$$\frac{dy}{dx} = \frac{\vartheta\sin(\vartheta x)}{P} + \frac{\vartheta\cos(\vartheta x)}{P\tan\psi} - \frac{1}{PL} = \frac{-1}{PL}\left[1 - \psi\sin(\vartheta x) - \frac{\psi\cos(\vartheta x)}{\tan\psi}\right] \tag{2.A.10}$$

From Eq. (2.A.10), the rotational flexibility coefficient at end 1 is expressed as,

$$f_{11m} = \left.\frac{dy_1}{dx}\right|_{x=0} = \frac{-1}{PL}\left(1 - \frac{\psi}{\tan\psi}\right) = \frac{L(1-P/GA_s)}{EI\psi^2}\left(1 - \frac{\psi}{\tan\psi}\right) \tag{2.A.11}$$

Similarly, the rotational flexibility coefficient at end 2 is given by,

$$f_{21m} = \left.\frac{dy_1}{dx}\right|_{x=L} = \frac{-1}{PL}\left(1 - \frac{\psi}{\sin\psi}\right) = \frac{L(1-P/GA_s)}{EI\psi^2}\left(1 - \frac{\psi}{\sin\psi}\right) \tag{2.A.12}$$

In the same manner as for the previous case where $P < 0$, the rotational flexibility coefficients are also readily found when $P \geq 0$. The complete set of flexibility coefficients f_{11m} and f_{21m} for axial force P less than, greater than or equal to zero are,

$$f_{11m} = \begin{cases} \dfrac{(1-P/GA_s)L}{EI\psi^2}\left(1 - \dfrac{\psi}{\tan\psi}\right) & P \leq 0 \\ \dfrac{(1-P/GA_s)L}{EI\psi^2}\left(\dfrac{\psi}{\tanh\psi} - 1\right) & P > 0 \end{cases} \tag{2.A.13}$$

$$f_{21m} = \begin{cases} \dfrac{(1-P/GA_s)L}{EI\psi^2}\left(1 - \dfrac{\psi}{\sin\psi}\right) & P \leq 0 \\ \dfrac{(1-P/GA_s)L}{EI\psi^2}\left(\dfrac{\psi}{\sinh\psi} - 1\right) & P > 0 \end{cases} \tag{2.A.14}$$

where,

$$\psi = L\sqrt{\frac{|P|(1-P/GA_s)}{EI}}\,. \tag{2.A.15}$$

Appendix 2.B Post-Elastic Stiffness Degradation

The general force-deformation model in the post-elastic range has been discussed in Section 2.3.1. This section presents an approach to determine the degraded stiffness of member sections as a consequence of post-elastic flexural, shearing and axial deformations. Corresponding bending, shearing and axial force-deformation relationships M-ϕ, V-γ and P-δ, respectively, are based on related experimental results.

2.B.1 Bending Stiffness Degradation

To analyze structures with substantial plastic deformations, an inelastic bending moment-rotation relationship is required to assess the bending stiffness degradation. The force-deformation relationship can be derived from a point-failure criterion such as the von Mises yield condition, or from an empirical relationship calibrated by experimental results. This latter approach is adopted

herein to determine the parameters for the elliptic moment-rotation model defined in Section 2.3.1. Specifically, the test results for a stub beam (Kusuda & Thurlimann, 1958) are used to determine the moment-rotation relation for typical steel W-shaped cross-sections. The simply supported stub beam with a W10×29 cross-section with English units is portrayed in Figure 2.13, where the small open circles indicate pairs of the moment-rotation test values in the central pure bending segment of the beam span. The fully plastic moment capacity M_p from the experiment is 140.12 kN-m (1240 kips-in). Plasticity theory defines the shape factor $f_s = M_p/M_y = 1.13$ for the W10×29 cross-section. However, it is clear from the test results in Figure 2.13 that the initial-yield moment M_y = 80.6 kN-m $\neq M_p/1.13$ = 140.12 /1.13 = 124 kN-m. To correct this discrepancy, residual stress $\sigma_r = 0.3\sigma_y$ is assumed present such that the initial-yield moment is calculated as $M_y \approx (1\text{-}0.3)\times M_p/1.13$ = 0.7 x 140.12/1.13 = 86.8 kN-m. A curve-fitting procedure is applied to determine the M-ϕ solid-line curve drawn in Figure 2.13. This M-ϕ relationship is discussed in detail in the following.

Upon excluding elastic deformation $\phi < \phi_y$ in Figure 2.13, the M-ϕ relationship in the inelastic range between M_y and M_p can be modeled by the following nonlinear function that expresses post-elastic rotation as,

$$\phi = \phi_p \left\{ 1 - \left[1 - \left(\frac{M - M_y}{M_p - M_y} \right)^{e_0} \right]^{1/e_0} \right\} \quad \left\{ \phi_y \le \phi \; ; \quad \frac{M_y}{M_p} \le \frac{M}{M_p} \le 1 \right\} \tag{2.B.1}$$

where parameters e_0 and ϕ_p are, respectively, defined as the *shape parameter* and the *full-yield rotation* for the section. From the experimental data in Figure 2.13 for the W10X29 section, the rotation at initial-yield of the outer fiber of the beam is ϕ_y = 0.00017 radians per unit length, whereas the initial-yield moment taking into account residual stress is M_y = 86.8 kN-m (768 kips-in). From Eq. (2.B.1), the full-yield rotation ϕ_p is defined as the rotation level at which the idealized full-yield moment $M = M_p$ is initially achieved. From the experimental results in Figure 2.13, the full-yield moment M_p can correspond to many different ϕ_p values because it remains almost constant for rotations ranging from 0.002 to 0.003 radians per unit length. It is assumed in this study that the full-yield rotation is the average value ϕ_p = 0.0025 radians per unit length (Grierson et al., 2005; Xu & Liu, 2006). Based on the values of M_y, M_p and ϕ_p discussed in the foregoing, the exponent $e_0 = 4$ is derived from the curve-fitting procedure.

Finally, differentiate curvature ϕ in Eq. (2.B.1) with respect to moment M to find,

$$\frac{d\phi}{dM}=\frac{\phi_p}{M_p-M_y}\left(\frac{M-M_y}{M_p-M_y}\right)^{e_0-1}\left[1-\left(\frac{M-M_y}{M_p-M_y}\right)^{e_0}\right]^{1/e_0-1} \tag{2.B.2}$$

from which post-elastic rotational stiffness R_p is found as,

$$R_p=\frac{dM}{d\phi}=\frac{M_p-M_y}{\phi_p}\left(\frac{M-M_y}{M_p-M_y}\right)^{1-e_0}\left[1-\left(\frac{M-M_y}{M_p-M_y}\right)^{e_0}\right]^{1-1/e_0} \quad M_y\le M\le M_p \tag{2.B.3}$$

It is noted that $R_p=\infty$ when post-elastic deformation $\phi=0$, whereas $R_p=0$ when $\phi\ge\phi_p$

2.B.2 Shearing Stiffness Degradation

The transverse shear stiffness of an inelastic segment can be found from the relationship between the shear force and the transverse deflection. Similar to the discussion for the moment-rotation relationship of section, the transverse force-deformation relationship is modeled by the following elliptic function,

$$\frac{\gamma}{\gamma_p}=1-\left[1-\left(\frac{V-V_y}{V_p-V_y}\right)^{e_0}\right]^{1/e_0} \qquad \left\{0\le\ \frac{\gamma}{\gamma_p}<1\ ;\ \ \frac{V_y}{V_p}\le\frac{V}{V_p}<1\right\} \tag{2.B.4}$$

which is interpreted as the relationship between the shear force and the transverse deflection at a critical section in the post-elastic range (i.e., excluding the elastic deflection). In Eq. (2.B.4), shear deformation γ = inelastic deflection = the difference between the total and initial-yield transverse deflections, γ_p = the plastic limit deflection = the difference between the total plastic and initial-yield deflections, and V_y and V_p are the initial-yield shear force and plastic-limit shear force, respectively. The initial and full-yield shear forces V_y and V_p are determined by the properties of the cross-section, whereas the full-yield transverse deflection γ_p and shape parameter e_0 are determined by the experimental results. This subsection illustrates how the parameters in Eq. (2.B.4) are determined from test results. Then, the transverse shear stiffness T is derived using the V-γ relationship Eq. (2.B.4). To this end, the following experimental-based shear stress-strain relationships (Hall & Newmark, 1957) are used,

$$\gamma=\begin{cases}\tau/G & (0\le\gamma<0.00143\ \text{mm/mm};\ 0\le\tau<113.685\ \text{MPa})\\ \dfrac{\tau-110.653}{2115.23} & (0.00143\le\gamma<0.02\ ;113.685\le\tau<152.958\text{MPa})\\ (\tau/482.3)^{3.4} & (0.02\le\gamma<0.3\ ;152.958\le\tau<338.299\text{MPa}\ )\end{cases} \tag{2.B.5a, b, c}$$

where γ and τ are the shear strain and shear stress, respectively. Although Eqs. (2.B.5) are obtained from a limited number of specimens, these shear stress-strain relations have been long used for estimating the shear deflections of mild-steel, wide-flange sections (Hall & Newmark, 1957). It can be seen from Eqs. (2.B.5) that initial-yield stress τ_y = 113.685 MPa corresponds to shear strain γ_y = 0.00143 mm/mm, and that the fully-plastic stress and strain are τ_p = 338.299 MPa and γ_p = 0.3 mm/mm, respectively.

For the effective shear area $A_s = t_w(d\text{-}t_f)$, where t_w = web thickness, d = beam depth, t_f = flange thickness, the shear force on the cross-section can be expressed as $V = \tau A_s$. The average transverse shear deflection can be evaluated as $\delta_s = \gamma l_s$, where l_s is the length of the inelastic zone of the member. Hereinafter, the experiment-based Eqs. (2.B.5) are used to determine the exponent e_0 in the elliptic model of Eq. (2.B.4). As a result, the non-dimensional V-δ_s expressions of Eqs. (2.B.5) are written as

$$\frac{\delta_s}{\delta_{sp}} = \frac{\gamma}{\gamma_p} = \begin{cases} \dfrac{0.0142V}{V_p}, & \left(0 \le \dfrac{\gamma}{\gamma_p} < 0.00477,\ 0 \le \dfrac{V}{V_p} < 0.336\right) \\ \dfrac{0.533V}{V_p} - 0.174, & \left(0.00477 \le \dfrac{\gamma}{\gamma_p} < 0.067,\ 0.336 \le \dfrac{V}{V_p} < 0.452\right) \\ \left(\dfrac{V}{V_p}\right)^{3.4}, & \left(0.067 \le \dfrac{\gamma}{\gamma_p} < 1,\ 0.452 \le \dfrac{V}{V_p} < 1\right) \end{cases} \quad \text{(2.B.6a, b, c)}$$

where shear force capacity $V_p = \tau_y A_s$. Equation (2.B.6a) represents the linear elastic V-γ relation, and Eq. (2.B.6c) represents the nonlinear inelastic V-γ relation, whereas Eq. (2.B.6b) is the linear transition between them. It can be seen from Eqs. (2.B.6) that both the elastic deflection limit γ/γ_p = 0.00477 and transition limit = 0.067 are negligibly small, compared to the value of 1.0 at the plastic limit state. Based on the experimental results given in Eqs. (2.B.6), it is found that γ_p = 0.3-0.00143 ≈ 0.3 and $V_p \approx 3V_y$.

The nonlinear regression analysis using the experiment-based datum pairs from Eqs. (2.B.6) as observations, determines for the curve defined by Eq. (2.B.4) that the exponent $e_0 \approx 1.5$. The non-dimensional V-γ relationship Eq. (2.B.4) is plotted in Figure 2.14 as the solid curve. For the purpose of comparison, Eqs. (2.B.6) are graphically shown in the figure as the dashed curve. It is evident from Figure 2.14 that Eq. (2.B.4) is in good agreement with the experiment-based expression in Eqs. (2.B.6). As such, this study adopts Eq. (2.B.4) and the parameter values discussed in the foregoing to model the shear deflection V-γ relationship from the initial-yield state to the fully-plastic state.

In the range between the initial-yield and fully plastic states, the transverse shear stiffness T is derived by using the shear force-deflection relationship Eq. (2.B.4). To this end, upon differentiating Eq. (2.B.4) with respect to γ, the transverse shear stiffness T of a cross-section is found to be,

$$T = \frac{dV}{d\gamma} = \frac{V_p - V_y}{\gamma_p} \sqrt{\frac{V_p - V_y}{V - V_y}} \left[1 - \left(\frac{V_p - V_y}{V - V_y} \right)^{e_0} \right]^{1/e_0} \tag{2.B.7}$$

For exponent $e_0 = 1.5$, Eq. (2.B.7) yields transverse shear stiffness values that match with preceding experiment-based results (Hall & Newmark, 1957). It can be seen from Eqs. (2.B.7) that the cross-section of the member remains elastic (i.e., $T = \infty$) until the applied shear force reaches V_y, whereas the section becomes fully plastic and the shear stiffness degrades to zero (i.e., $T = 0$) when $V = V_p$.

2.B.3 Axial Stiffness Degradation

The axial stiffness of an inelastic segment is derived from the axial force-deformation relationship in the post-elastic range. As discussed in Section 2.B.1 and 2.B.2, the axial force-deformation relationship is modeled by the following elliptic function,

$$\frac{\delta}{\delta_p} = 1 - \left[1 - \left(\frac{P - P_y}{P_p - P_y} \right)^{e_0} \right]^{1/e_0} \qquad \left\{ 0 \le \frac{\delta}{\delta_p} < 1 \; ; \quad \frac{P_y}{P_p} \le \frac{P}{P_p} \le 1 \right\} \tag{2.B.8}$$

where the axial force = P, initial yield axial force $P_y = (\sigma_y - \sigma_r)A$ (where σ_r is the axial residual stress), the full-yield axial force $P_p = \sigma_y A$, the post-elastic axial deformation δ = the difference between the inelastic and initial-yield axial deformations, and the plastic limit deformation δ_p = the difference between the limit plastic and initial-yield deformations. This section presents an approach to determine deformation δ_p and exponent e_0 using on the experimental results.

The experimental results for a stub column (Huber & Beedle, 1954) are employed to determine the parameters in the axial force-deformation model Eq. (2.B.8). The stub column has length of 83.82 cm (33″) and W8×31 section with yield-stress σ_y = 248 MPa (36 ksi), as shown in Figure 2.15, where the small open circles indicate the axial load-deformation test values. Initial yielding is observed at a strain of 0.0015, and local buckling of the flange occurs at a strain of 0.0047. From nonlinear regression analysis based on the data in the range between initial-yielding and full-yielding, the exponent value $e_0 = 2.5$ is found for the normalized axial force-deformation relation Eq. (2.B.8).

When elastic limit strain δ_y/33″ = 0.0015 and plastic limit strain δ_p/33″ = 0.0047, axial force-displacement P-δ relation Eq. (2.B.8) is plotted in Figure 2.15 as the solid-line curve; it is clear from the figure that Eq. (2.B.8) is in good agreement with the experimental results. Equation (2.B.8) is

employed in this study to model the P-δ transition curve from initial-yield state to the full-plastic state.

The axial stiffness N of a member is found by differentiating Eq. (2.B.8) with respect to δ to get,

$$N = \frac{dP}{d\delta} = \frac{P_p - P_y}{\delta_p} \sqrt{\frac{P_p - P_y}{P - P_y}} \left[1 - \left(\frac{P_p - P_y}{P - P_y} \right)^{e_0} \right]^{1/e_0} \tag{2.B.9}$$

where δ_p and P_y are determined from the experimental results. For example, δ_p = (0.0047-0.0015) (33×25.4 mm) = 0.2268 mm, and P_y = 0.7 P_p are determined from the experimental results of Huber and Beedle (1954). Recall also that the exponent e_0 = 2.5 has been previously determined from the experimental results.

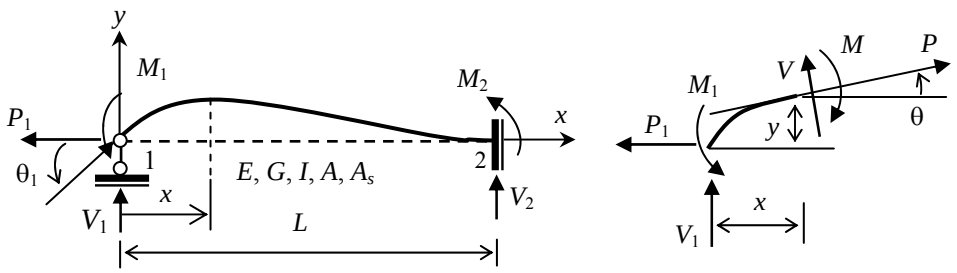

(a) Deformed profile (b) Free body diagram

Figure 2-1 Force-deformation due to end rotation

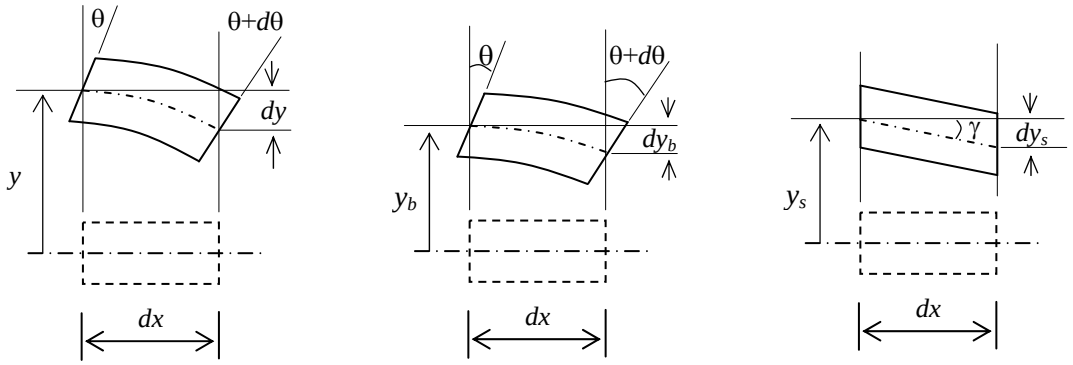

(a) Total (b) Flexural (c) Shearing

Figure 2-2 Deformations of a differential segment

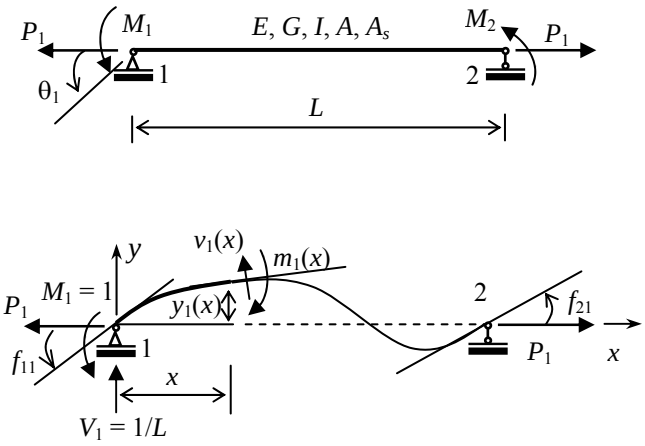

(a) Primary structure

(b) Moment and shear force, where M_1 =1

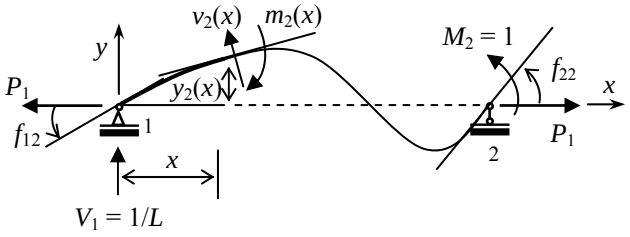

(c) Moment and shear force, where $M_2 = 1$

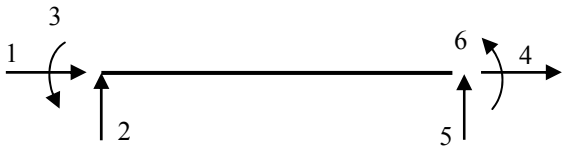

(d) End forces/deformation numbering for a member

Figure 2-3 Flexibility coefficients and member-end numbering

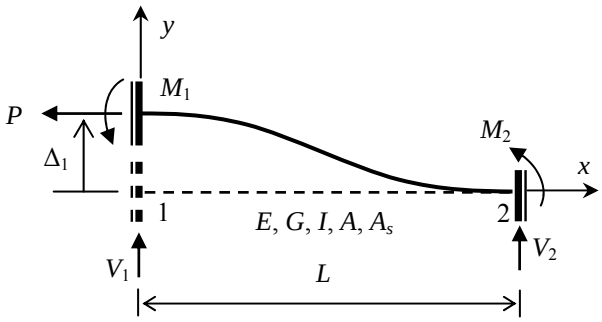

(a) Deformed profile

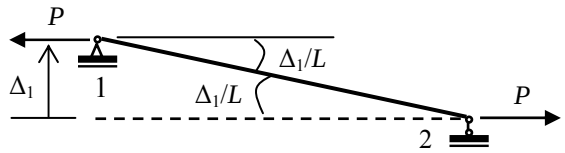

(b) Equivalent rotation

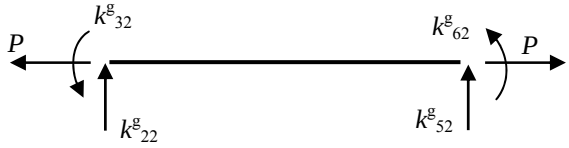

(c) Stiffness coefficients

Figure 2-4 Force-deformation due to end translation

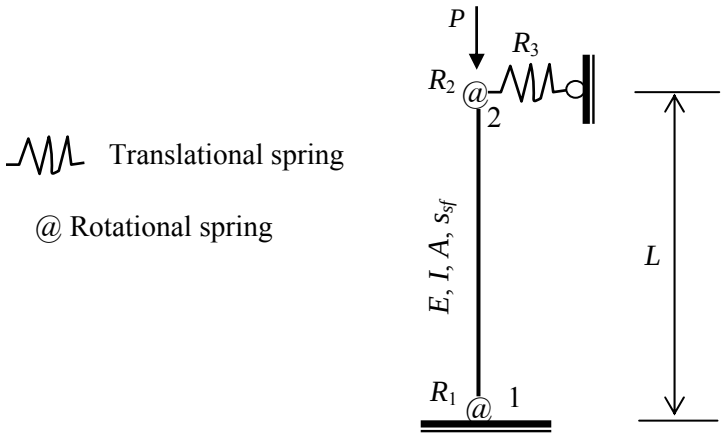

Figure 2-5 Column with different end constraints

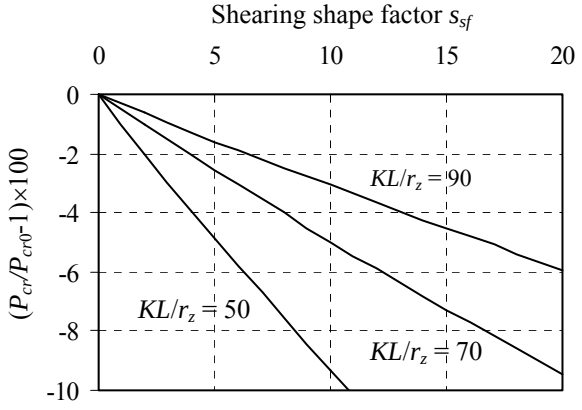

Figure 2-6 Relative difference of critical load due to shear deformation

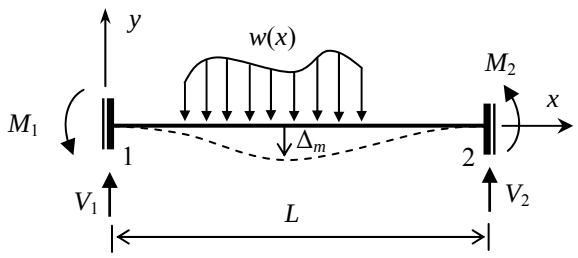

Figure 2-7 Fixed-end reactions and deflections due to transverse loading

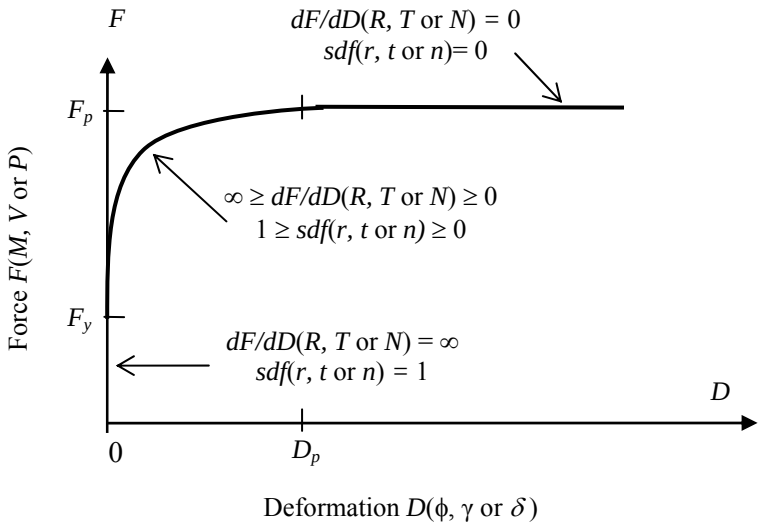

Figure 2-8 Force-deformation relationship in the post-elastic range

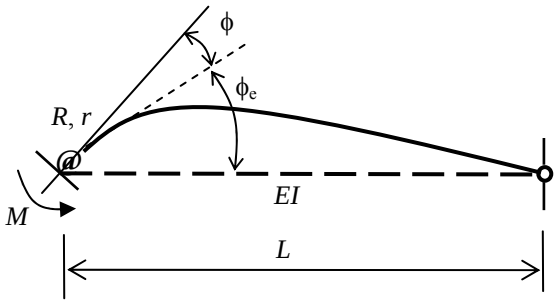

Figure 2-9 Bending member model

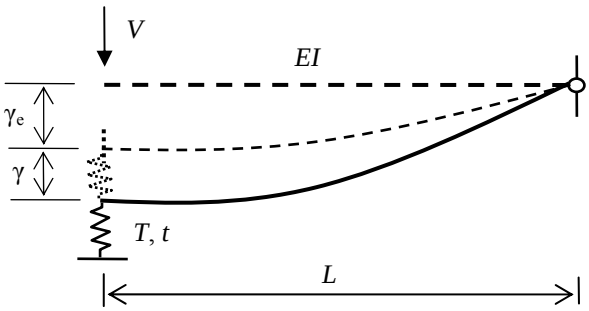

Figure 2-10 Shearing member model

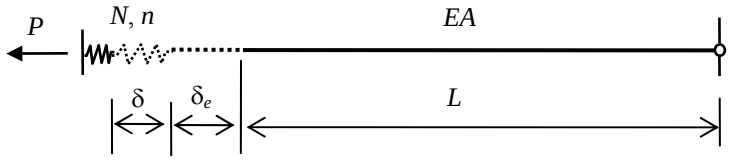

Figure 2-11 Axial member model

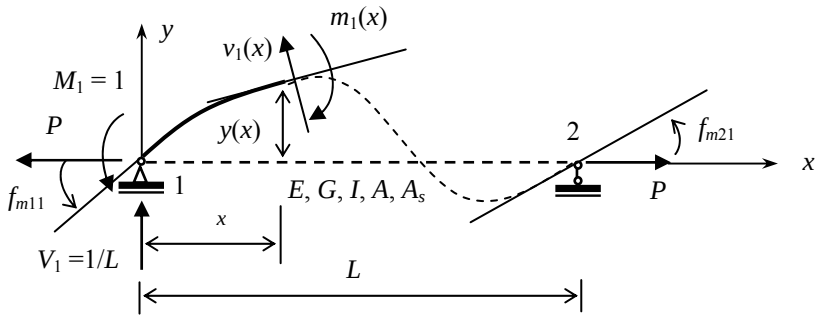

Figure 2-12 Flexibility coefficients due to unit end moment

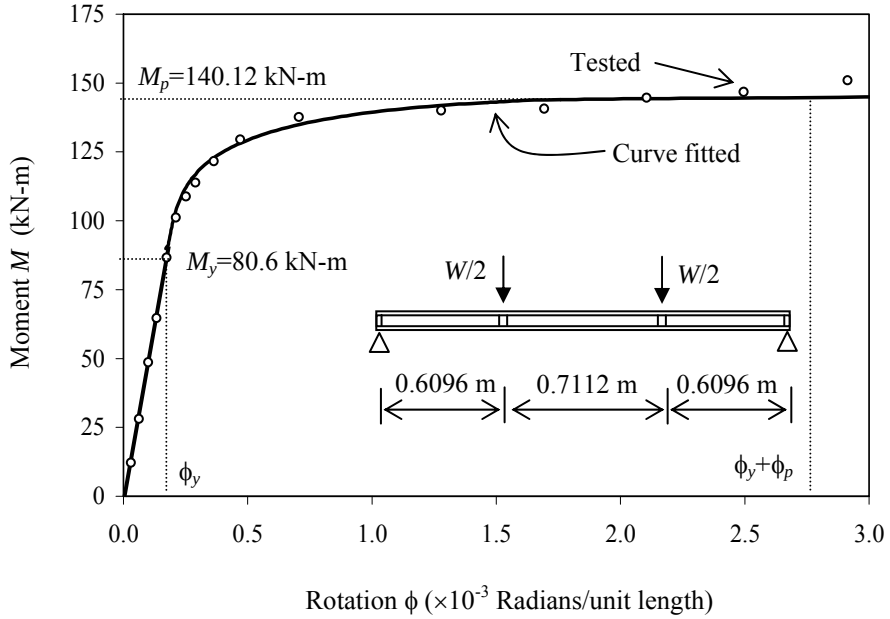

Figure 2-13 Experimental-based moment-rotation curve (Kusuda & Thurlimann, 1958)

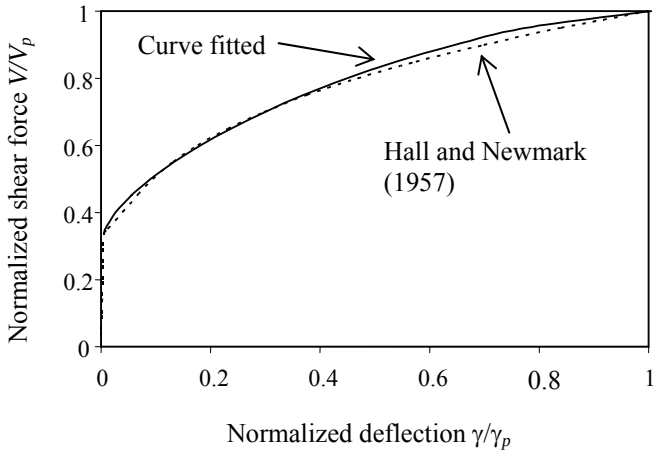

Figure 2-14 Experimental-based shear force-transverse deflection curve

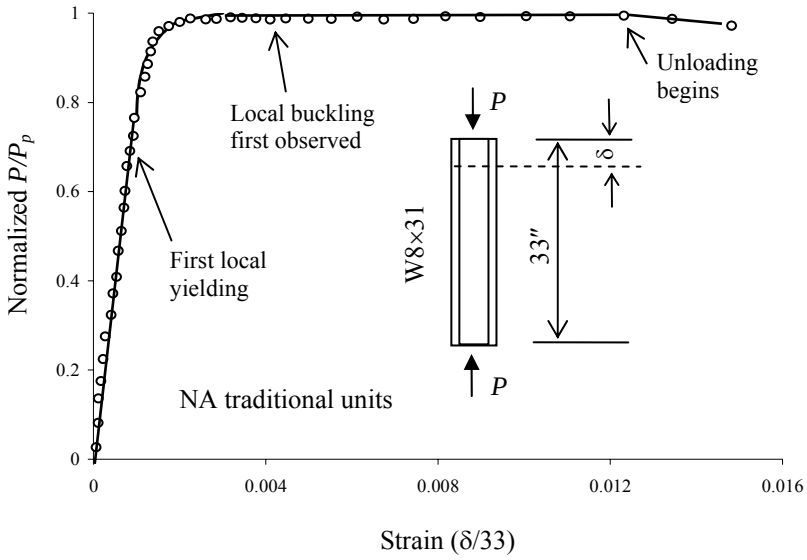

Figure 2-15 Experimental-based axial force-deformation curve (Huber & Beedle, 1954)

Table 2.1 Effect of shear deformation on critical loads (%)

L/r_s	Free-fix	Pin-pin	Pin-fix	Fix-fix
10	-9.92	-17.46	-29.43	-57.38
20	-2.77	-5.71	-11.22	-28.52
30	-1.26	-2.63	-5.50	-15.96
40	-0.72	-1.55	-3.14	-9.93
50	-0.46	-1.01	-1.97	-6.70
60	-0.32	-0.70	-1.32	-4.79

Chapter 3
Nonlinear Analysis of Steel Frameworks

This chapter presents the derivation of a generalized member stiffness matrix for nonlinear analysis. Stiffness degradation under combined stress states is investigated using a nonlinear analysis procedure based on the Euler incremental method with a gradually decreasing step size. The nonlinear method of analysis is illustrated for two benchmark planar steel structures that have been studied in the literature (Driscoll & Beedle, 1957; Clarke, 1994; Attalla et al., 1994; Iffland & Birnstiel, 1982).

3.1 Nonlinear Member Stiffness Matrix

Consider a planar steel framework that is discretized as an assembly of beam-column members with compact sections, for which plastic deformation is not precluded by local buckling (AISC, 2001). The effect of the out-of-plane torsion of a member is ignored in the analysis. Plastic bending, shearing or axial deformation D (= ϕ, γ or δ) related to moment, shear or axial force F (= M, V or P) is assumed to be concentrated at member sections. From the conventional matrix Displacement Method of analysis (McGuire, 2000), the end force-displacement relationship for the hybrid beam-column member in Figure 3.1 is symbolically expressed as in compact matrix form as,

$$\boldsymbol{f} = \boldsymbol{k}\boldsymbol{d} \tag{3.1.1}$$

where $\boldsymbol{d} = [d_1\ d_2\ d_3\ d_4\ d_5\ d_6]^T$ is the nodal displacement vector corresponding to end-force vector $\boldsymbol{f} = [f_1\ f_2\ f_3\ f_4\ f_5\ f_6]^T$. The member stiffness matrix $\boldsymbol{k}$ is represented in general form as,

$$\boldsymbol{k} = \begin{bmatrix} k_{11} & 0 & 0 & k_{14} & 0 & 0 \\ & k_{22} & k_{23} & 0 & k_{25} & k_{26} \\ & & k_{33} & 0 & k_{35} & k_{36} \\ & & & k_{44} & 0 & 0 \\ & Sym & & & k_{55} & k_{56} \\ & & & & & k_{66} \end{bmatrix} \tag{3.1.2}$$

In Figure 3.1, L = member length, E = material Young's modulus, G = material shear modulus, I = cross-section moment of inertia, A = cross-section area, and A_s = equivalent shear area. Furthermore, from Chapter 2, R_j, T_j and N_j (j =1, 2) are the post-elastic rotational bending, transverse shearing and normal axial stiffnesses at the two member-end sections, respectively, while r_j, t_j and n_j (j =1, 2) are the corresponding bending, shearing and axial stiffness degradation factors.

3.2 Derivation of Member Stiffness Coefficients

The non-zero stiffness coefficients k_{ij} (i, j = 1, 2,…, 6) in Eq. (3.1.2) are derived in the following, with account for geometrical nonlinearity, shear deformation, and flexural, shear and axial stiffness degradation.

3.2.1 Stiffness Coefficients due to End Rotations

Figure 3.2 (a) indicates stiffness coefficients k_{ij} that account for the influence of axial load P along with rotational and transverse stiffness degradation due to plasticity. Rotational bending stiffness R_j and transverse shearing stiffness T_j (j = 1, 2), and corresponding flexural and shearing degradation factors r_j and t_j, are also shown in the figure. The Displacement Method is applied in the following to find the stiffness coefficients.

Consider the primary structure in Figure 3.2 (b). Quantities $(FES)_j$, (j = 1, 2) denote fixed-end shearing forces due to unit rotation $d_3 = 1$ is imposed at end 1, and are given by

$$(FES)_1 = -(FES)_2 = k^r_{23} \tag{3.2.1}$$

where k^r_{23} is defined by Eq. (3.A.16) in Appendix 3.A. When the vertical unit deflection $Y_1 = 1$ is imposed at joint 1 in Figure 3.2 (c), the transverse stiffness coefficients s_{11} and s_{21} are given by,

$$s_{11} = k^r_{22} + T_1 \tag{3.2.2a}$$

$$s_{21} = s_{12} = -k^r_{22} \tag{3.2.2b}$$

where k^r_{22} is given by Eq. (3.A.20) in Appendix 3.A. Similarly, when $Y_2 = 1$ is imposed at end 2 as shown in Figure 3.2(d), the stiffness coefficient s_{22} is given by,

$$s_{22} = k^r_{22} + T_2 \tag{3.2.3}$$

Having Eqs. (3.2.1), (3.2.2) and (3.2.3), the equilibrium equations related to joint displacements Y_1 and Y_2 in Figure 3.2(a) can be written as,

$$\begin{bmatrix} T_1 + k^r_{22} & -k^r_{22} \\ -k^r_{22} & T_2 + k^r_{22} \end{bmatrix} \begin{Bmatrix} Y_1 \\ Y_2 \end{Bmatrix} = k^r_{23} \begin{Bmatrix} -1 \\ 1 \end{Bmatrix} \tag{3.2.4}$$

and solved to find the joint displacements,

$$\begin{Bmatrix} Y_1 \\ Y_2 \end{Bmatrix} = \frac{k^r_{23}}{(T_1 + T_2)k^r_{22} + T_1 T_2} \begin{Bmatrix} -T_2 \\ T_1 \end{Bmatrix} \tag{3.2.5}$$

Having Y_1 and Y_2, the stiffness coefficient k_{33} is given by,

$$k_{33} = k_{33}^r + k_{32}^r Y_1 + k_{35}^r Y_2 = k_{33}^r \left[1 - \frac{k_{23}^r k_{23}^r}{k_{33}^r k_{22}^r} \frac{(T_1 + T_2) k_{22}^r}{(T_1 + T_2) k_{22}^r + T_1 T_2} \right] \tag{3.2.6}$$

which accounts for geometric and material nonlinearities associated with member shear deformation. It is noted that when there is no post-elastic transverse shear stiffness degradation ($T_1 = T_2 = \infty$), Eq. (3.2.6) reduces to the k^r_{33} coefficient given by Eq. (3.A.13) in Appendix 3.A.

To further simplify Eq. (3.2.6), from Eqs. (3.A.13), (3.A.16) and (3.A.20) in Appendix 3.A it can be shown that,

$$\frac{k_{23}^r k_{23}^r}{k_{33}^r k_{22}^r} = \frac{b\eta_1 r_1}{4\Omega\beta} \frac{(1 + c\eta_2)^2 [b\eta_1 (1 - r_2)(1 - c\eta_2) + 3r_2]^2}{b\eta_1 (1 - r_2)[1 - (c\eta_2)^2] + 3r_2} \tag{3.2.7}$$

and

$$\frac{(T_1 + T_2) k_{22}^r}{(T_1 + T_2) k_{22}^r + T_1 T_2} = 1 - \frac{1}{(1/T_1 + 1/T_2) k_{22}^r + 1} = 1 - \chi_1 \tag{3.2.8}$$

where

$$\chi_1 = \frac{t_1 t_2}{t_1 t_2 + 4\beta(t_1 + t_2 - 2t_1 t_2)} \tag{3.2.9}$$

is a factor accounting for the effect of the degraded transverse shear stiffness. Parameter β is a modified deflection stiffness factor, introduced for the storey-based analysis of frameworks (Xu & Liu, 2002; Liu & Xu, 2005), and is defined as,

$$\beta = \frac{L^3}{12EI} k_{22}^r \tag{3.2.10}$$

Other parameters are defined in Chapter 2 and Appendix 3.A.

By substituting Eqs. (3.2.7) and (3.2.8) into Eq. (3.2.6), the stiffness coefficient k_{33} is concisely written as,

$$k_{33} = k_{33}^r \chi_2 \tag{3.2.11}$$

where

$$\chi_2 = 1 - \frac{b\eta_1 r_1}{4\Omega\beta} \frac{(1 + c\eta_2)^2 [b\eta_1 (1 - r_2)(1 - c\eta_2) + 3r_2]^2}{b\eta_1 (1 - r_2)[1 - (c\eta_2)^2] + 3r_2} (1 - \chi_1) \tag{3.2.12}$$

is a modifying factor that accounts for the effect of shear stiffness degradation. It is noteworthy that $\chi_2 = 1$ when $\chi_1 = 1$, thereby indicating no shear stiffness degradation.

In a similar manner to the derivation of Eq. (3.2.11), the stiffness coefficient k_{63} at end 2 is found as,

$$k_{63} = k^r_{63} + k^r_{62} Y_1 + k^r_{65} Y_2 = k^r_{63} \chi_3 \tag{3.2.13}$$

where k^r_{63} and k^r_{65} are given by Eqs. (3.A.19) and (3.A.18), and the parameter χ_3 is given by,

$$\begin{aligned} \chi_3 &= 1 - \frac{b\eta_1 (1 + c\eta_2)^2 (1 - \chi_1)}{12\Omega c\eta_2 \beta} \\ &\times [b\eta_1 (1 - r_1)(1 - c\eta_2) + 3r_1][b\eta_1 (1 - r_2)(1 - c\eta_2) + 3r_2] \end{aligned} \tag{3.2.14}$$

which is a modification factor that accounts for the interaction between flexural bending and transverse shearing stiffness degradations.

From transverse equilibrium at end 1 in Figure 3.2 (a), the transverse stiffness coefficients associated with end-rotation $d_3 = 1$ are,

$$k_{23} = -T_1 Y_1 = \frac{T_1 T_2 k^r_{23}}{(T_1 + T_2) k^r_{22} + T_1 T_2} = k^r_{23} \chi_1 = -k_{53} \tag{3.2.15}$$

Having the stiffness coefficients associated with rotation $d_3 = 1$ at end 1 of the member, the stiffness coefficients associated with rotation $d_6 = 1$ at end 2 are obtained analogically. From Eq. (3.2.11),

$$k_{66} = k^r_{66} \chi_4 \tag{3.2.16}$$

where k^r_{66} is defined by Eq. (3.A.17) in Appendix 3.A, and by exchanging subscripts 1 and 2 of the flexural degradation factors r in Eq. (3.2.12) the modification factor χ_4 is given by,

$$\chi_4 = 1 - \frac{b\eta_1 r_2}{4\Omega\beta} \frac{(1 + c\eta_2)^2 [b\eta_1 (1 - r_1)(1 - c\eta_2) + 3r_1]^2}{b\eta_1 (1 - r_1)(1 - c^2 \eta_2^2) + 3r_1} (1 - \chi_1) \tag{3.2.17}$$

Similar to that for Eq. (3.2.15), the transverse stiffness coefficients due to rotation $d_6 = 1$ at end 2 are given by,

$$k_{26} = k^r_{26} \chi_1 = -k_{56} \tag{3.2.18}$$

3.2.2 Stiffness Coefficients due to End Translations

When unit translation $d_2 = 1$ is imposed at end 1 of the member as indicated in Figure 3.3 (a), the corresponding stiffness coefficients can be found by the Displacement Method of analysis. To this end, the corresponding primary structure with two unknown transverse displacements Y_1 and Y_2 is taken to be as shown in Figure 3.3 (b). The fixed-end transverse forces are written as,

$$(FES)_1 = T_1 \tag{3.2.19a}$$

$$(FES)_2 = 0 \tag{3.2.19b}$$

where $(FES)_j$ (j = 1, 2) is the transverse reaction of end j due to unit displacement Y_1, while T_1 is the corresponding post-elastic shear stiffness of the spring.

Note that the stiffness coefficients associated with unit translations $Y_1 = 1$ and $Y_2 = 1$ are the same as those in Figures 3.2 (c) and (d), respectively. Therefore, the equilibrium condition Eq. (3.2.4) can be directly applied upon replacing the right-hand side by Eqs. (3.2.19) to get,

$$\begin{bmatrix} T_1 + k_{22}^r & -k_{22}^r \\ -k_{22}^r & T_2 + k_{22}^r \end{bmatrix} \begin{Bmatrix} Y_1 \\ Y_2 \end{Bmatrix} = T_1 \begin{Bmatrix} 1 \\ 0 \end{Bmatrix} \tag{3.2.19c}$$

which can then be solved to find the transverse deflections,

$$\begin{Bmatrix} Y_1 \\ Y_2 \end{Bmatrix} = \frac{1}{(1/T_1 + 1/T_2)k_{22}^r + 1} \begin{Bmatrix} 1 + k_{22}^r / T_2 \\ k_{22}^r / T_2 \end{Bmatrix} \tag{3.2.20}$$

From Figures 3.2 (c, d) and 3.3 (b), the stiffness coefficient k_{22} is expressed as,

$$k_{22} = T_1 - T_1 Y_1 + 0 Y_2 = \frac{k_{22}^r}{1 + k_{22}^r / T_1 + k_{22}^r / T_2} = k_{22}^r \chi_1 \tag{3.2.21}$$

Similarly, it is shown that stiffness coefficient $k_{52} = -k_{22}$. Also, from the Maxwell reciprocal theorem, $k_{32} = k_{23}$ and $k_{62} = k_{26}$ (all of which have been defined in the preceding section). Finally, the stiffness coefficients associated with unit translation $d_5 = 1$ alone imposed at the beam right end in Figure 3.3 are analogically determined. For example, $k_{55} = k_{22}$ from Eq. (3.2.21) since T_1 and T_2 are in a symmetric position. The rest of the stiffness coefficients are readily determined through the Maxwell reciprocal theorem.

3.2.3 Stiffness Coefficients due to Axial Displacement

In the preceding sections, member stiffness coefficients have been derived accounting for the effects of flexural bending and transverse shearing stiffness degradations due to inelastic behaviour. As post-elastic axial stiffness degradation can sometimes also be significant under heavy axial loading, the effect is taken into account in this section.

The analytical member model is represented in Figure 3.4 (a), where N_j (j = 1, 2) are normal axial stiffness in the inelastic range, and n_j (j = 1, 2) are corresponding axial-stiffness degradation factors. The problem under consideration is to find the axial stiffness coefficient (end reaction) k_{11} when end 1 is displaced a unit distance along the member axis, as shown in Figure 3.4 (a). The Force Method of

analysis is employed to this end, for which the primary structure is selected as shown in Figure 3.4 (b). Displacement f_{11} under unit force $F = 1$ is expressed as,

$$f_{11} = \frac{1}{N_1} + \frac{L}{EA} + \frac{1}{N_2} \tag{3.2.22a}$$

where L/EA is elastic deformation, and $1/N_i$ (i = 1, 2) are plastic deformations. From Eq. (2.3.6) in Chapter 2, Eq. (3.2.22a) can be rewritten as,

$$f_{11} = \frac{2 + n_1 n_2 - n_1 - n_2}{n_1 n_2} \frac{L}{EA} \tag{3.2.22b}$$

Therefore, from Eq. (3.2.22b), the axial stiffness at member end 1 is,

$$k_{11} = \frac{1}{f_{11}} = \chi_0 \frac{EA}{L} \tag{3.2.23}$$

where,

$$\chi_0 = \frac{n_1 n_2}{2 + n_1 n_2 - n_1 - n_2} \tag{3.2.24}$$

is referred to as an axial stiffness-reduction coefficient. If $\chi_0 = 1$ there is no axial stiffness reduction, while if $\chi_0 = 0$ the axial stiffness is reduced to zero. Due to symmetry, the same axial stiffness coefficient as in Eq. (3.2.23) is obtained when a unit displacement is alternatively imposed at end 2 of the beam in Figure 3.4.

3.2.4 Summary of Stiffness Coefficients

In the foregoing, all of the non-zero stiffness coefficients k_{ij} (i, j = 1, 2,…, 6) in the member stiffness matrix Eq. (3.1.2) have been derived accounting for geometrical nonlinearity, shear deformation, and flexural, shear and axial stiffness degradation;i.e., as given by Eqs. (3.2.11), (3.2.13), (3.2.15), (3.2.16), (3.2.18), (3.2.21), and (3.2.23). A summary listing of the coefficients is given in the following.

$$k_{11} = k_{11}^a \chi_0 = k_{44} = -k_{14} = -k_{41} \tag{3.2.25a}$$

$$k_{22} = k_{22}^r \chi_1 = k_{55} = -k_{25} = -k_{52} \tag{3.2.25b}$$

$$k_{23} = k_{23}^r \chi_1 = k_{32} = -k_{35} = -k_{53} \tag{3.2.25c}$$

$$k_{26} = k_{26}^r \chi_1 = k_{62} = -k_{56} = -k_{65} \tag{3.2.25d}$$

$$k_{33} = k_{33}^r \chi_2 \tag{3.2.25e}$$

$$k_{36} = k_{36}^{r}\chi_3 = k_{63} \tag{3.2.25f}$$

$$k_{66} = k_{66}^{r}\chi_4 \tag{3.2.25g}$$

where,

$$k_{11}^{a} = AE/L \tag{3.2.26a}$$

$$k_{22}^{r} = \frac{f_2}{d_2} = \frac{EI}{L^3\Omega}\left\{3b\eta_1(1+c\eta_2)[6r_1r_2 + b\eta_1(1-c\eta_2)(r_1+r_2-2r_1r_2)] + P\frac{L^2\Omega}{EI}\right\} \tag{3.2.26b}$$

$$k_{23}^{r} = \frac{k_{33}^{r}+k_{63}^{r}}{L} = \frac{3b\eta_1 kr_1(1+c\eta_2)[b\eta_1(1-r_2)(1-c\eta_2)+3r_2]}{\Omega L} \tag{3.2.26c}$$

$$k_{26}^{r} = \frac{3b\eta_1 kr_2(1+c\eta_2)[b\eta_1(1-r_1)(1-c\eta_2)+3r_1]}{\Omega L} = -k_{56}^{r} \tag{3.2.26d}$$

$$k_{33}^{r} = \frac{3r_1 b\eta_1 k[b\eta_1(1-r_2)(1-c^2\eta_2^2)+3r_2]}{\Omega} \tag{3.2.26e}$$

$$k_{36}^{r} = 9kbc\eta_2\eta_1 r_2 r_1/\Omega \tag{3.2.26f}$$

$$k_{66}^{r} = 3r_2 b\eta_1 k[b\eta_1(1-r_1)(1-c^2\eta_2^2)+3r_1]/\Omega \tag{3.2.26g}$$

$$\chi_0 = \frac{n_1 n_2}{2+n_1 n_2 - n_1 - n_2} \tag{3.2.26h}$$

$$\chi_1 = \frac{t_1 t_2}{t_1 t_2 + 4\beta(t_1+t_2-2t_1t_2)} \tag{3.2.26i}$$

$$\chi_2 = 1 - \frac{b\eta_1 r_1}{4\Omega\beta}\frac{(1+c\eta_2)^2[b\eta_1(1-r_2)(1-c\eta_2)+3r_2]^2}{b\eta_1(1-r_2)[1-(c\eta_2)^2]+3r_2}(1-\chi_1) \tag{3.2.26j}$$

$$\chi_3 = 1 - \frac{b\eta_1(1+c\eta_2)^2(1-\chi_1)}{12\Omega c\eta_2\beta} \times [b\eta_1(1-r_1)(1-c\eta_2)+3r_1][b\eta_1(1-r_2)(1-c\eta_2)+3r_2] \tag{3.2.26k}$$

$$\chi_4 = 1 - \frac{b\eta_1 r_2}{4\Omega\beta}\frac{(1+c\eta_2)^2[b\eta_1(1-r_1)(1-c\eta_2)+3r_1]^2}{b\eta_1(1-r_1)(1-c^2\eta_2^2)+3r_1}(1-\chi_1) \tag{3.2.26h}$$

in which,

$$b = \begin{cases} \dfrac{1-\psi/\tan\psi}{\tan(\psi/2)/(\psi/2)-1} & P \le 0 \\ \dfrac{1-\psi/\tanh\psi}{\tanh(\psi/2)/(\psi/2)-1} & P > 0 \end{cases} \tag{3.2.27a}$$

$$c = \begin{cases} \dfrac{\psi - \sin\psi}{\sin\psi - \psi\cos\psi} & P \le 0 \\ \dfrac{\psi - \sinh\psi}{\sinh\psi - \psi\cosh\psi} & P > 0, \end{cases} \tag{3.2.27b}$$

$$\psi = L\sqrt{\frac{|P|(1 - P/GA_s)}{EI}} \tag{3.2.27c}$$

$$\eta_1 = \frac{1 + \eta_3\eta_4}{(1 - P/GA_s)(1 + \eta_3\eta_5)} \tag{3.2.27d}$$

$$\eta_2 = \frac{1 + \eta_3\eta_6}{1 + \eta_3\eta_4} \tag{3.2.27e}$$

$$\eta_3 = \frac{EI}{(1 - P/GA_s)GA_sL^2} \tag{3.2.27f}$$

$$\eta_4 = \begin{cases} \psi^2/(1 - \psi/\tan\psi) & P \le 0 \\ -\psi^2/(1 - \psi/\tanh\psi) & P > 0 \end{cases} \tag{3.2.27g}$$

$$\eta_5 = \begin{cases} \psi^2\tan(\psi/2)/[\tan(\psi/2) - \psi/2] & P \le 0 \\ -\psi^2\tanh(\psi/2)/[\tanh(\psi/2) - \psi/2] & P > 0 \end{cases} \tag{3.2.27h}$$

$$\eta_6 = \begin{cases} \psi^2/(1 - \psi/\sin\psi) & P \le 0 \\ -\psi^2/(1 - \psi/\sinh\psi) & P > 0 \end{cases} \tag{3.2.27i}$$

$$\Omega = 9r_1r_2 + 3r_2b\eta_1(1 - r_1) + 3r_1b\eta_1(1 - r_2) + b^2\eta_1^2(1 - r_1)(1 - r_2)(1 - c^2\eta_2^2) \tag{3.2.27j}$$

$$\beta = \frac{L^3}{12EI}k_{22}^r \tag{3.2.27k}$$

3.3 Combined Stress States

For the analysis model presented so far, a steel beam-column member that experiences post-elastic behaviour due to individual moment, shear or axial force effects has alone been examined. For a steel building frame, however, column members are often subjected to significant bending moment plus axial force effects, while beam members may experience significant moment and shear force effects. Accordingly, the proposed analysis model is extended in this section to account for post-elastic behaviour due to combined flexural + axial and flexural + shear stress states.

3.3.1 Bending Moment plus Axial Force

Under some combination of applied bending moment M and axial force P, the initial yielding of a member section is governed by the normalized initial-yield criterion,

$$\frac{M}{M_y}+\frac{P}{P_y}=1 \tag{3.3.1}$$

Residual stresses due to cooling, rolling, welding, punching, etc., can significantly affect the initial yield of materials. Specifically, residual stresses can cause member yielding at loads lower than those predicted by usual stress analysis. The stresses can also lower the ultimate capacity by inducing premature local or global buckling of compressive members (Huber & Beedle, 1954). Generally, residual stress σ_r is about 68.9 MPa (10 ksi) for a steel cross section. The yield stress σ_y for hot-rolled shapes considered in this study is in the range of 248 MPa (36ksi) to 345 MPa (50 ksi). Thus, residual stress σ_r = (68.9/248~68.9/345)σ_y = 20%~30%σ_y. In this study, residual stress σ_r is taken as approximately 30%σ_y. For compressive residual stress in the flanges of W-shaped sections, the LRFD-05 specification (AISC, 2005) requires σ_r = 68.9 MPa (10 ksi) for rolled shapes, and σ_r = 113.7 MPa (16.5 ksi) for welded shapes. Following current code practices, this study assumes the residual normal stress is $\sigma_r = 0.3\sigma_y$, such that the initial-yield normal stress becomes $\sigma_{yr} = \sigma_y - \sigma_r = 0.7\sigma_y$. Consequently, the initial-yield moment in Eq. (3.3.1) is $M_y = 0.7\sigma_y S_z$, where S_z is the elastic modulus of the cross-section, while the initial-yield axial force is $P_y = 0.7\sigma_y A$ in tension or compression, where A is the cross-section area.

If the effect of strain hardening is neglected, residual stress does not affect the plastic limit capacity (Huber & Beedle, 1954). Thus, the moment and axial force full-yield capacities are $M_p = \sigma_y Z_z$ and $P_p = \sigma_y A$, respectively, where Z_z is the plastic section modulus.

Based on experimental and theoretical results, the full yielding of a cross-section is assumed to be governed by the following normalized full-yield criterion,

$$\frac{M}{M_P}+\left(\frac{P}{P_P}\right)^{\eta}=1 \tag{3.3.2}$$

where the exponent η in Eq. (3.3.2) depends on the shape of the member section; for example, η = 1.3 for a steel wide-flange section (Duan & Chen, 1990). The post-elastic response domain for the member section is indicated as the shaded area in Figure 3.5, bounded by Eq. (3.3.1) plotted as the linear initial-yield line, and by Eq. (3.3.2) plotted as the nonlinear full-yield line (for specified exponent η). It remains to establish the influence that combined bending moment M plus axial force P have on the post-elastic bending and axial stiffnesses of the member. To this end, the post-elastic response domain in Figure 3.5 is divided into the three regions defined in Figure 3.6 by the following three angles,

$$\theta_M = \tan^{-1}\left[\frac{(1-M_y/M_p)^{1/\eta}}{M_y/M_p}\right] \tag{3.3.3a}$$

$$\theta_P = \tan^{-1}\left[\frac{1-(P_y/P_p)^{\eta}}{P_y/P_p}\right] \tag{3.3.3b}$$

$$\theta_{MP} = 90^{\circ} - \theta_M - \theta_P \tag{3.3.3c}$$

where, as indicated in Figure 3.6: the region defined by angle θ_M is assumed to correspond to combinations of M plus P that influence only post-elastic bending stiffness (since full yielding of the section in this region of the response domain occurs for $M \geq M_y$ while $P < P_y$); the region defined by angle θ_P is assumed to correspond to combinations of M plus P that influence only post-elastic axial stiffness (since full yielding in this region occurs for $P \geq P_y$ while $M < M_y$); finally, the region defined by angle θ_{MP} is assumed to correspond to combinations of M plus P that influence both post-elastic bending stiffness and post-elastic axial stiffness (since full yielding in this region occurs for $M \leq M_y$ and $P \leq P_y$).

As seen in Figure 3.5, the region of influence in the post-elastic response domain for a particular combination of moment M plus axial force P is defined by the angle of inclination θ of the straight line that passes through origin point O_o, and points O_y and O_p corresponding to the initial yield and full yield of the section, respectively. The straight line between initial-yield point O_y and full-yield point O_p is used to approximately determine the parameters M_{pr} and P_{pr} in the stiffness degradation model. Figure 3.5 indicates that point O_y corresponds to the reduced initial-yield moment and axial force capacities M_{yr} and P_{yr}, respectively. Whereas point O_p corresponds to the reduced full-yield moment and axial force capacities M_{pr} and P_{pr}, respectively. The angle of inclination of line O_o-O_y-O_p in Figure 3.5 is readily found as,

$$\theta = \tan^{-1}\left[\frac{P_{yr}/M_p}{M_{yr}P_p}\right] \tag{3.3.4}$$

Depending on the value of angle θ from Eq. (3.3.4), and the values of angles θ_M, θ_P and θ_{MP} from Eqs. (3.3.3), the bending or/and axial stiffness degradation factor/s (see Appendix 3.A) for the member-end section is/are evaluated as follows: a) if $0 \leq \theta < \theta_M$, set $F = M$, $F_y = M_{yr}$, $F_p = M_{pr}$, $D = \phi$, $D_p = \phi_p$ and $e_0 = 2$ in Eqs. (2.3.2)-(2.3.3) to find bending stiffness degradation factor $sdf = r \leq 1$; b) if $90^{\circ} - \theta_P < \theta \leq 90^{\circ}$, set $F = P$, $F_y = P_{yr}$, $F_p = P_{pr}$, $D = \delta$, $D_p = \delta_p$, $e_0 = 2.5$ in Eqs. (2.3.2)-(2.3.3) to find axial stiffness degradation factor $sdf = n \leq 1$; and 3) if $\theta_M \leq \theta \leq \theta_M + \theta_{MP}$, proceed as in the foregoing to find both bending stiffness degradation factor $sdf = r \leq 1$ and axial stiffness degradation factor sdf

= $n \leq 1$. Finally, the calculated r or/and n value/s is/are substituted into the relevant stiffness coefficient expressions derived in the previous section, thereby modifying the member stiffness matrix $\boldsymbol{k}$ defined by Eq. (3.1.2) to account for the influence that the combination of bending moment M plus axial force P has on the post-elastic stiffness of the member.

3.3.2 Bending Moment plus Shear Force

Under some combination of applied bending moment M and shear force V, the initial-yielding of a member section is approximately governed by the normalized first-yield criterion,

$$\frac{M}{M_y}+\frac{V}{V_y}=1 \tag{3.3.5}$$

where the initial-yield moment M_y is the same as that for the case of moment-axial force interaction discussed in the previous section. It is assumed that the residual shear stress $\tau_r = 0.05\tau_y$, such that the initial-yield shear stress $\tau_{ry} = 0.95\tau_y$. The full yielding of the cross section is considered to be governed by the normalized full-yield criterion (Heyman & Dutton 1954),

$$M/M_P + C_1\left[1-\sqrt{1-(V/V_P)^2}\right]=1 \tag{3.3.6}$$

where the moment and shear force initial-yield and full-yield capacities (M_y, V_y) and (M_p, V_p), respectively, account for residual stresses. In Eq. (3.3.6), the coefficient $C_1=A_w/(2A - A_w)$ for a wide-flange section with total area A and web area A_w (e.g., $C_1 = 0.2$ when $A_w = A/3$). The post-elastic response domain for the member section is the shaded area in Figure 3.7, bounded by Eq. (3.3.5) plotted as the linear first-yield line, Eq. (3.3.6) plotted as the nonlinear full-yield line (for specified coefficient C_1), and the linear full-yield in shear line $V/V_p=1$.

It remains to establish the influence that combined bending moment M plus shear force V have on the post-elastic bending and shear stiffnesses of the member. To this end, the post-elastic response domain in Figure 3.7 is divided into the three regions defined in Figure 3.8 by the following three angles,

$$\Theta_M = \tan^{-1}\left[\frac{V_y/V_p}{1-C_1\{1-\sqrt{1-(V_y/V_p)^2}\}}\right] \tag{3.3.7a}$$

$$\Theta_V = \tan^{-1}(M_y/M_p) \tag{3.3.7b}$$

$$\Theta_{MV} = 90^\circ - \Theta_M - \Theta_V \tag{3.3.7c}$$

The region defined by angle Θ_M is assumed to correspond to combinations of M plus V that influence only the post-elastic bending stiffness (since full yielding of the section in this region of the response domain occurs for $M > M_y$ while $V \le V_y$); the region defined by angle Θ_V is assumed to correspond to combinations of M plus V that influence only the post-elastic shearing stiffness (since full yielding in this region occurs for $V = V_p$ while $M \le M_y$); finally, the region defined by angle Θ_{MV} is assumed to correspond to combinations of M plus V that influence both the post-elastic bending stiffness and the post-elastic shearing stiffness (since full yielding in this region occurs for $M \ge M_y$ and $V \ge V_y$).

As shown in Figure 3.7, the region of influence in the post-elastic response domain for a particular combination of moment M plus shear force V is defined by the angle of inclination Θ of the straight line that passes through origin point O_o, and points O_y and O_p corresponding to initial yield and full yield of the section, respectively. Figure 3.7 indicates that point O_y corresponds to reduced initial-yield moment and shear force capacities M_{yr} and V_{yr}, respectively, and point O_p corresponds to reduced full-yield moment and shear force capacities M_{pr} and V_{pr}, respectively. The angle of inclination of line O_o-O_y-O_p in Figure 3.7 is found to be,

$$\Theta = \tan^{-1}\left[\frac{V_{yr}M_p}{M_{yr}V_p}\right] \tag{3.3.8}$$

Depending on the value of angle Θ from Eq. (3.3.8), and the values of angles Θ_M , Θ_V and Θ_{MV} from Eqs. (3.3.7), the bending or/and shearing stiffness degradation factor/s (see Appendix 3.A) for the member end-section is/are evaluated as follows: a) if $0 \le \Theta < \Theta_M$, set $F = M$, $F_y = M_{yr}$, $F_p = M_{pr}$, $D = \phi$, $D_p = \phi_p$ and $e_0 = 2$ in Eqs. (2.3.2)-(2.3.3) to find bending stiffness degradation factor $sdf = r \le 1$; b) if $90^\circ - \Theta_V < \Theta \le 90^\circ$, set $F = V$, $F_y = V_{yr}$, $F_p = V_{pr}$, $D = \gamma$, $D_p = \gamma_p$ and $e_0 = 1.5$ in Eqs. (2.3.2) and (2.3.3) to find shearing stiffness degradation factor $sdf = t \le 1$; and c) if $\Theta_M \le \Theta \le \Theta_M + \Theta_{MV}$, proceed as in the foregoing to find both bending stiffness degradation factor $sdf = r \le 1$ and shearing stiffness degradation factor $sdf = t \le 1$. Finally, the calculated r or/and t value/s is/are substituted into the corresponding stiffness coefficient expressions derived in the previous section, thereby modifying the member stiffness matrix $\boldsymbol{k}$ defined by Eq. (3.1.2) to account for the influence that the combination of bending moment M plus shear force V has on the post-elastic stiffness of the member. (Note that the smaller of the two r values calculated for the M+P and M+V combinations should be adopted so as to conservatively account for the maximum degradation of the member stiffness).

3.4 Nonlinear Analysis Procedure

Having the local-axis stiffness matrix $\boldsymbol{k}$ for each framework member from Sections 3.1 and 3.2, the corresponding global member stiffness matrix is readily obtained using conventional matrix transformation techniques (McGuire et al., 2000). Then, the structural stiffness matrix $\boldsymbol{K}$ is assembled by direct summation of the global member stiffness matrices. The incremental (tangent-stiffness) equilibrium equation for any load increment of the nonlinear analysis procedure is expressed as,

$$\boldsymbol{K}\Delta\boldsymbol{D} = \Delta\boldsymbol{F} \tag{3.4.1}$$

where $\boldsymbol{K}$, $\Delta\boldsymbol{D}$ and $\Delta\boldsymbol{F}$ are the tangent stiffness matrix, incremental displacement vector and incremental equivalent-joint-load vector, respectively. The Euler incremental method is employed to solve Eqs. (3.4.1).

The single-step Euler method is computationally simple and efficient, but a drift-off error may occur in the nonlinear analysis procedure. To reduce this error, a strategy for gradually reducing the increment-step size is adopted. A load-factor increment $\Delta\lambda_i$ is introduced to facilitate the formation of the equivalent joint load vector $\Delta\boldsymbol{F}_i$ applied to the structure at the ith incremental-step of the analysis. A load-factor increment $\Delta\lambda$ is introduced to facilitate the identification of the load levels at which the plastic deformation of the members is initiated. While the single-step Euler method is computationally simple and efficient, a drift-off error may occur over the incremental load history. To reduce this error, a strategy for gradually reducing the increment-step size is adopted. The magnitude of the load-factor increment is decreased over the loading history whereby the initial step size is specified to be,

$$\Delta\lambda_1 = \Delta\lambda^* \tag{3.4.2a}$$

while, thereafter,

$$\Delta\lambda_i = \Delta\lambda_{i-1}(1 - \Delta\lambda^*) \quad (i = 2, 3 \ldots) \tag{3.4.2b}$$

where $\Delta\lambda^* < 1$ is an initially specified small value (say 0.05), selected to ensure first-order linear-elastic behaviour of the structure for the first load increment. If the structure stiffness matrix $\boldsymbol{K}_i$ is non-singular for the ith load increment, Eq. (3.4.1) is solved for the incremental nodal displacements $\Delta\boldsymbol{D}_i$. Incremental member-end forces $\Delta\boldsymbol{f}_i$ for each member are then determined. Total nodal displacements $\boldsymbol{D}_i$ at the end of the ith load increment are found as,

$$\boldsymbol{D}_i = \boldsymbol{D}_{i-1} + \Delta\boldsymbol{D}_i \tag{3.4.3}$$

while the corresponding internal member forces $\boldsymbol{f}_i$ are,

$$\boldsymbol{f}_i = \boldsymbol{f}_{i-1} + \Delta\boldsymbol{f}_i \tag{3.4.4}$$

The initial-yield and full-yield conditions for each member-end section are checked to detect plastic behaviour and, if occurring, the corresponding bending, shearing and axial stiffness degradation factors (*r, t, n*) are found and applied to modify member stiffness matrices $\boldsymbol{k}$ and, consequently, the structure stiffness matrix $\boldsymbol{K_i}$ at loading level *i* for the analysis.

The incremental load factor $\Delta\lambda_i$ is accumulatively recorded to identify the loading level λ_f for the corresponding total loads, i.e.,

$$\lambda_f = \sum_{i=1} \Delta\lambda_i = \Delta\lambda^*[1 + (1-\Delta\lambda^*) + (1-\Delta\lambda^*)^2 + ...(1-\Delta\lambda^*)^i + ...] \tag{3.4.5}$$

The incremental-load analysis procedure continues until either a specified load level λ_f is reached (i.e., final $\lambda_f = \Sigma\Delta\lambda_i = 1$) without structural collapse, or the structure stiffness matrix $\boldsymbol{K_i}$, at some step becomes singular as a consequence of the failure of part or all the structure at a lower load level (i.e., $\lambda_f = \Sigma\Delta\lambda_i < 1$). Typically, the specified load level at $\lambda_f = 1$ is dictated by design code requirements. If the structure does not fail at load level $\lambda_f = 1$, and if required, the analysis can be continued to a higher load level (i.e., $\lambda_f > 1$) until failure of the structure occurs (see Examples in the next section).

The nonlinear analysis procedure is illustrated by the flowchart in Figure 3.9. The analysis results include the values of bending, shearing and axial post-elastic stiffness degradation factors *r*, *t* and *n*, respectively, indicating the extent of plastic deformation of the members. Further computational details are provided by the analysis examples presented in the following section.

3.5 Example Studies

The incremental-load procedure of nonlinear analysis is illustrated in the following for two example structures consisting of steel beam-column members with wide-flange cross-sections. The first example is a two-span continuous beam, for which the analytical results found by using Timoshenko beam theory are compared with known experimental test results (Driscoll & Beedle, 1957) and other analytical results that are found by applying Euler-Bernoulli beam theory (McGuire et al., 2000). The second example is a low-rise steel building framework, the nonlinear analysis of which has been extensively studied in the literature (Clarke, 1994; Ziemian et al., 1992; Attalla et al., 1994).

For both examples, the exponent in Eq. (2.4.1) is taken as $e_0 = 2$, 1.5 or 2.5 when force $F = M$, V or P, respectively, values that were obtained by curve-fitting test results reported by several experimental investigations (Lay & Galambos, 1964; Kusuda & Thurlimann, 1958; Hall & Newmark, 1957). Plastic deformation D_p in Eq. (2.4.1) is taken as $\phi_p = 0.0025$ radians (Attalla et al., 1994; Kusuda & Thurlimann, 1958), parameter $\gamma_p = 0.3$ when force $F = V$ (Hall & Newmark 1957), and

parameter δ_p= 0.0032 *x* member length when force $F = P$ (Lay & Galambos, 1964). In Eq. (3.3.2) the exponent is taken as η =1.3 (Duan & Chen, 1990). The material normal-yield stress σ_y = 247.3 MPa (35.9 ksi) for the beam, as determined by experiments (Lay & Galambos 1964), and σ_y = 248 MPa (36 ksi) for the two-bay by two-storey frame, while the material shear-yield stress $\tau_y = 0.5\sigma_y$ (Tresca criterion). The residual stresses are taken as $\sigma_{rc} = 0.3\sigma_y$ for compressive normal stress, $\sigma_{rt} = 0.15\sigma_y$ for tensile normal stress (AISC, 2001; Huber & Beedle, 1954), and $\tau_r = 0.05\tau_y$ for shear stress (See Appendix 6.B).

The nonlinear analysis results include the values of the bending, shearing and axial post-elastic stiffness degradation factors *r*, *t* and *n* for the member sections at which plastic deformation occurs. If the plastic deformation is related to degraded bending, shearing or axial stiffness, the member section is designated by a circle, triangle or square symbol (O, ∇, or □), respectively. Otherwise, the section is designated by a circle inscribed in a triangle if the plasticity is associated with both degraded bending and shearing stiffness, or by a circle inscribed in a square if associated with degraded bending and axial stiffness. For a member section that experiences plastic deformation over its entire surface area, the designation symbol has a black infill to indicate that the section has reached a state of zero post-elastic stiffness (i.e., $r = 0$, and/or $t = 0$, and/or $n = 0$); for example, if $r = 0$ where $t = n = 1$, the section is designated by a black-infill circle (the classic representation of a *plastic-hinge* section). Contrarily, if a section has experienced only partial plasticity over its surface area, the designation symbol is left open with a number inscribed in it that indicates the percentage of plastic deformation, calculated as *%Plasticity* = 100 (1– *r, t* or *n*). For example, if $r = t = 1$, while $n < 1$, the section is designated by 100(1– *n*), inscribed in an open square (e.g., see Example 2).

3.5.1 Two-Span Continuous Beam

Consider the two-span continuous beam subjected to the pattern of concentrated point loading in Figure 3.10 (Driscoll & Beedle 1957). For the purpose of this illustration, the total target load is taken as W = 1000 kN. The steel beam has a wide-flange W12×36 section (NA traditional) with the following properties: section depth d = 312.42 mm (12.30 in), flange width b_f = 168.275 mm (4.625 in), flange thickness t_f = 13.056 mm (0.514 in), web thickness t_w = 8.560 mm (0.337 in), section area A = 6954.82 mm^2 (10.78 in^2), moment of inertia $I = 117.42 \times 10^6$ mm^4 (282.1 in^4), plastic modulus $Z = 848.69 \times 10^3$ mm^3 (51.79 in^3), and shape factor f = 1.13. The moment and shear capacities are $M_p = Z\sigma_y$ = 210 MPa and $V_p = A_w\sigma_y/1.732$ = 351 kN, respectively, and the axial force $P = 0$ for the beam. Plastic deformation can occur at each load point B, C, E and F, and at central support point D (i.e., the

beam is modeled by six elements). The results from the nonlinear analysis method are illustrated in Figure 3.11, and compared with the results of other studies in Figures 3.12 and 3.13.

The nonlinear incremental-load analysis terminates when the beam fails at load factor level λ_f = 0.996 (i.e., at total load level $\lambda_f \times W = 0.996 \times 1000 = 996$ kN). The analysis results are illustrated in Figure 3.11 where, in view of symmetry, the information for the right span of the symmetrical beam is alone shown. From the loading history up to failure, the beam develops two fully-plastic sections at points D and F (designated by the black infill symbols in Figure 3.11 (a)) at load-factor levels λ = 0.992 and 0.996, respectively. The plastic deformation of plastic-hinge section D is associated with both fully degraded bending stiffness and fully degraded shear stiffness (i.e., $r = t = 0$ and $n = 1$), because the *M*-*V* stress state for the section (see Figures 3.11 (b) and (c)) lies in the region defined by angle Θ_{MV} in Figure 3.8. The plastic deformation of plastic-hinge section F is associated with fully degraded bending stiffness alone (i.e., $r = 0$ and $t = n = 1$), because the *M*-*V* stress state for the section (see Figures 3.11 (b) and (c)) exists in the region defined by angle Θ_M in Figure 3.8. As a consequence of the combined *M*-*V* influence on plastic behaviour at point F (see Eq.(3.3.6)), note from Figure 3.11 that a 100% fully-plastic flexural hinge forms to the right of point F where the larger shear force is, while a 93% partially-plastic flexural hinge forms to the left of the point (i.e., $r = 0.07$ and $t = n = 1$). Note that section E also experiences two types of plastic behaviour as a result of the abrupt change in shear there; i.e., the *M*-*V* stress states to the right and left of point E lie in the regions defined by angles Θ_M and Θ_V in Figure 3.8, respectively, such that a 59% partially-plastic flexural hinge forms to the right (i.e., $r = 0.41$ and $t = n = 1$) while a 77% partially-plastic shear hinge forms to the left (i.e., $t = 0.23$, and $r = n = 1$). As indicated in Figure 3.11(d), the vertical deflection of point F reaches a value of δ_F = 12.42 mm at the instance of incipient failure of the beam (i.e., the incipient formation of a classic rigid-body mechanism involving plastic hinges at sections D and F).

The variation in the vertical deflection of point F of the beam during the incremental loading process is defined by the solid line in Figure 3.12. The beam remains stable until 99.6% of total load W =1000 kN is applied, at which point, δ_F begins to increase indefinitely without any further increase in load (numerically, this failure event is characterized by the beam stiffness matrix $\boldsymbol{K}$ becoming singular as the stiffness coefficient associated with vertical deflection of point F tends to zero at load-factor level λ_f = 0.996). Also shown in Figure 3.12 are experimental test results found for the same beam by Driscoll and Beedle (1957). It is observed that vertical deflections δ_F predicted by the proposed analysis method over the loading history are in good agreement with those obtained from the experimental measurements.

The experimental tests conducted by Driscoll and Beedle (1957) determined that shear had a significant influence on both the elastic and plastic behaviour of the beam. They observed that beam deflections related to transverse shear deformations were of the same order of magnitude as those associated with flexural deformations. The experimentalists also reported that a shear yielding stress was observed near the centre support D at a load level which was less than that causing flexural yielding. Presented in the following are analytical results found by this study that demonstrate the influence that shear has on the behaviour of the beam.

The analytical results in Figures 3.11 and 3.12 reflect the combined influence that bending and shearing have on plastic behaviour, and are found by using Timoshenko beam theory to account for the effect that shear deformation has on elastic behaviour. The corresponding results in Figure 3.12 are reproduced in Figure 3.13 (i.e., the lowest curve). It is readily possible to conduct the same analysis according to Euler-Bernoulli beam theory by setting the beam shear stiffness $GA_s = \infty$, thereby effectively eliminating the effect of shear deformation on elastic behaviour. The corresponding analytical results are shown in Figure 3.13, along with those found for the pure bending case which also ignores the influence that shear has on plastic behaviour. From Figure 3.13, it is observed that the predicted failure load level for the beam increases from 996 kN to 1036 kN when the influence of shear on elastic behaviour is ignored, and further increases to 1104 kN when the influence of shear on the plastic behaviour is also ignored. It is evident from Figure 3.12 that the experimentally determined failure load level is no more than 996 kN and, therefore, it can be concluded that ignoring shear effects leads to an over-estimation of load capacity (by as much as approximately 10% for this particular case).

3.5.2 Low-Rise Steel Building Framework

Consider the two-bay by two-storey steel framework subjected to uniformly distributed service-level design gravity loads shown in Figure 3.14. The structure is a building perimeter frame that supports a load intensity of 109.5 N/mm on floor members 4-5 and 5-6, and 51.1 N/mm on roof members 7-8 and 8-9. All the members have W-shape sections (CISC, 2004) that are oriented such that their webs are in the plane of the framework, and are assumed to be fully restrained against out-of-plane behaviour. If plastic deformation occurs, it is assumed to be confined to the end sections of each of the six column members, and to the end and midspan sections of each of the four beam members (i.e., 14 elements in all). The framework has 13 nodes and 33 degrees-of-freedom (*dof*) for nodal displacement (i.e., rotation *dof* at each of the three pin-support nodes 1-3, plus lateral and vertical translation and rotation *dof* at each of the ten free nodes 4-13).

The ultimate design (target) load level for the incremental-load analysis is 1.4 times that of the service gravity loads in Figure 3.14 (AISC, 2001). In fact, to facilitate a comparison with other published results for this example (Clarke, 1994; Ziemian et al., 1992; Attalla et al., 1994), the loads are increased beyond this load level until failure of the frame occurs. The analysis results found by this study are illustrated in Figure 3.15, and compared with the results of other studies in Figure 3.16.

The incremental-load analysis terminates when the frame fails at load factor level λ_f = 1.08 (i.e., at 108% of the specified ultimate design load level). Over the loading history up to failure, the frame develops five full-plastic sections (designated by the black infill symbols in Figure 3.15) that sequentially reach their full-yield capacities at load-factor levels λ = 0.827, 0.895, 0.902, 0.931 and 1.058, respectively. Also, there are nine sections that become 2, 3, 8, 23, 28, 30, 32, 38, 40, 69 and 88% partially plastic (designated by the open symbols in Figure 3.15) after reaching their initial-yield capacities at load-factor levels λ = 0.637, 0.567, 0.845, 1.043, 0.405, 0.571, 0.827, 0.441, 0.535, 0.947 and 0.722, respectively, over the loading history.

The plastic deformation of each of the first four fully-plastic sections is associated with fully degraded bending stiffness alone (i.e., each section behaves like a classic plastic hinge with stiffness degradation factors r = 0 and t = n = 1, because the *M-V-P* stress state for the section lies in the regions defined by angles θ_M and Θ_M in Figures 3.6 and 3.8). The plastic deformation of the fifth fully-plastic section is related to fully degraded bending stiffness and fully degraded axial stiffness (i.e., r = n = 0 and t = 1, because the *M-V-P* stress state for the section exists in the regions defined by angles θ_{MP} and Θ_M in Figures 3.6 and 3.8). For the seven sections for which bending stiffness alone is partially degraded by 2, 3, 8, 28, 30, 32, 38, 40, and 88% (i.e., the sections designated by the open circles in Figure 3.15), the stiffness degradation factors are t = n = 1, and r = 0.98, 0.97, 0.92, 0.72, 0.70, 0.68, 0.62, 0.60 and 0.12, respectively (i.e., the *M-V-P* stress state for each section lies in the regions defined by angles θ_M and Θ_M in Figures 3.6 and 3.8). Finally, for the two sections for which axial stiffness alone is partially degraded by 23% and 69% (i.e., the sections designated by the open squares in Figure 3.15), the stiffness degradation factors are r = t = 1, and n = 0.77 and 0.31, respectively (i.e., the *M-V-P* stress state for each section lies in the regions defined by angles θ_P and Θ_M in Figures 3.6 and 3.8).

The lateral translation of the top right corner (joint node 9) of the frame over the incremental loading history is defined by the solid line in Figure 3.16. It can be seen that the frame initially translates laterally to the left until approximately 90% of the factored gravity loads are applied, at which point the top storey begins to translate to the right, until it suddenly lurches to the left again as it loses its lateral stability at 108% of the specified ultimate design load level, due to a combination of

plastic deformation and nonlinear geometric effects. Numerically, this event is characterized by the structure stiffness matrix becoming singular as the stiffness coefficient associated with the lateral translation of node 9 tends to zero at load-factor level $\lambda_f = 1.08$. Note that the failure of the frame is due to system instability of the right bay in a lateral sway mode, and not the formation of a rigid-body plastic collapse mechanism.

This example frame originally appeared in an *America Institute of Steel Construction* report on frame stability (Iffland & Birnstiel, 1982) and, since then, its nonlinear behaviour has been studied by a number of researchers from a variety of computational viewpoints. Ziemian et al. (1992) have conducted a plastic-hinge analysis (with 28 elements) and a plastic-zone analysis (with 540 elements having 80 fibers each). Clarke (1994) has also conducted a plastic-zone analysis of the frame (with 240 elements having 256 fibers each). Attalla et al. (1994) have analyzed the frame by using a quasi-plastic hinge approach (with 28 beam and column elements). The lateral displacement behaviour and failure load level λ_f found by these various analyses are depicted in Figure 3.16. It is evident that the results found by the method proposed herein are in good agreement with those reported for the other methods. The slight discrepancies between the results are likely due to the different ways in which residual stresses and strain hardening were considered. It is worth noting that the structural model for the proposed method has significantly fewer beam and column elements (14 in total) than the other methods.

Appendix 3.A Accounting for Bending Stiffness Degradation

This Appendix uses the moment-rotation relationships derived in Chapter 2 to derive member stiffness coefficients accounting for post-elastic bending stiffness degradation, geometric nonlinearity and shear deformation. To this end, the moment distribution method (Cross, 1932) is extended to account for both geometric and material nonlinearities through modified distribution and carry-over factors.

3.A.1 Modified Moment Distribution Method

To obtain the modified rotational stiffness coefficient and carry-over factor, consider the beam-column in Figure 3.17, at the right end of which there is an inelastic zone located between nodes *e* and 2. From Eq. (2.4.4) in Chapter 2, the relation between flexural-degradation factor r_2 and rotational bending stiffness R_2 at end 2 is given by,

$$r_2 = \frac{1}{1 + 3EI / LR_2} \tag{3.A.1}$$

In the conventional moment distribution method, the degradation factor r_2 is equal to 1 or 0 for a fixed or pinned support, respectively. A modified method of moment distribution is developed in the following to account for r_2 ranging from 0 to 1; specifically, the modified rotational stiffness distribution and carryover factors are derived from the moment-rotation relationships expressed in Eqs. (2.1.17) in Chapter 2; that is, end moments M_1 and M_2 caused by rotation θ_1 are found by employing the moment distribution method for the beam in Figure 3.17. As a result, the member 1-2 is divided into two elements at intermediate node *e*, where 1-*e* represents an elastic element, and *e*-2 denotes a inelastic element associated with post-elastic rotational stiffness R_2.

First, determine the distribution factors for the member's axial force and shear deformation. The member ends in Table 3.1 are defined in such a way that the first character represents the near end, and the second one identifies the far end. Only the rotation at node *e* is unknown. Following the principles of the moment-distribution method, the distribution factor at end *e*1 (or *e*2) is defined as the ratio of the member-end rotational stiffness to the total rotational stiffness of the joint. For instance, the stiffness distribution factor at end *e*1 of member 1-*e* is given by,

$$\mu_{e1} = \frac{kb\eta_1}{R_2 + kb\eta_1} = \frac{b\eta_1(1-r_2)}{b\eta_1(1-r_2)+3r_2} \tag{3.A.2}$$

where the term $kb\eta_1$ is defined for Eq. (2.1.18) in Chapter 2 and represents the rotational stiffness coefficient at end *e* of member 1-*e*, while $R_2 + kb\eta_1$ is the total rotational stiffness at joint *e*. Similarly, the distribution factor at end *e* of member *e*-2 is given by,

$$\mu_{e2} = \frac{R_2}{R_2 + kb\eta_1} = \frac{3r_2}{b\eta_1(1-r_2)+3r_2} \tag{3.A.3}$$

The distribution factors defined by Eqs. (3.A.2) and (3.A.3) are listed in Table 3.1. Note that for the member 1-*e* with axial load *P* in Figure 3.17, the carry-over factor is equal to $c\eta_2$ defined by Eq. (2.1.17b) in Chapter 2.

Secondly, determine the fixed-end moments due to rotation θ_1 imposed at end 1. When node *e* is fixed by a virtual rotational constraint, the fixed-end moments for member 1-*e* are $M_{1e} = kb\eta_1\theta_1$ and $M_{e1} = kcb\eta_1\eta_2\theta_1$ from Eqs. (2.1.17a, b) in Chapter 2, as indicated in the 4th row of Table 3.1.

Thirdly, distribute the unbalanced moment at node *e* and carry over the distributed moments to the corresponding far ends. Note that for the spring element modeling rotational inelasticity, the mutual carry-over factor = -1 since the length of the element is negligible and the moments at the two ends are equal in magnitude but opposite in sense. After the moment distribution operation based on the

modified distribution and carrying-over factors is completed, the distributed and carry-over moments are found to be those in the 5th and 6th rows of Table 3.1, respectively.

Finally, find the final end-moments M_1 and M_2 by summing the fixed, distributed and carry-over moments in the corresponding column of Table 3.1, i.e., from the second column of the table,

$$M_1 = b\eta_1 k(1-\mu_{e1}c^2\eta_2^2)\theta_1 = R_{11}\theta_1 \tag{3.A.4}$$

while from the last column of the table 3.1,

$$M_2 = b\eta_1 k\mu_{e2}c\eta_2\theta_1 = R_{21}\theta_1 \tag{3.A.5}$$

The modified rotational stiffness coefficient and carry-over factor accounting for the effects of both geometric and material nonlinearities can be defined through Eqs. (3.A.4) and (3.A.5). To that end, substitute the distribution factor μ_{e1} from Eq. (3.A.2) into Eq. (3.A.4) to obtain the following expression for post-elastic rotational stiffness,

$$R_{11} = \frac{M_1}{\theta_1} = kb\eta_1 \frac{3r_2 + b\eta_1(1-r_2)(1-c^2\eta_2^2)}{b\eta_1(1-r_2)+3r_2} \tag{3.A.6}$$

If r_2 tends to unity, then Eq.(3.A.6) reduces to the rotational stiffness coefficient $kb\eta_1$ involving both geometrical nonlinearity and shear deformation in the elastic range. If the shear deformation is ignored (i.e., $\eta_1 = 1$), the term kb in Eq. (3.A.6) becomes the stiffness coefficient in elastic stability analysis. Furthermore, if geometrical nonlinearity is ignored the term $kb = 4EI/L$, the conventional stiffness coefficient in the moment distribution method (Cross, 1932).

By substituting the distribution factors μ_{e1} and μ_{e2} from Eqs. (3.A.2) and (3.A.3) into Eqs. (3.A.4) and (3.A.5), respectively, the modified carryover factor is,

$$C_{12} = \frac{M_2}{M_1} = \frac{R_{21}}{R_{11}} = \frac{3r_2 c\eta_2}{3r_2 + b\eta_1(1-r_2)(1-c^2\eta_2^2)} \tag{3.A.7}$$

If the far end is fixed with $r_2 = 1$ (i.e., end 2 remains in the elastic range), the carryover factor becomes $C_{12} = c\eta_2$. If shear deformation is further ignored then the coefficient $\eta_2 = 1$ and the carryover factor becomes $C_{12} = c$. If the geometrical nonlinearity is neglected as well, the parameter $c = 0.5$ so that the carryover factor C_{12} reduces to the well-known value of 0.5. Note that if $r_2 = 0$ (i.e., the rotational stiffness has degraded to zero at end 2), the carryover factor becomes $C_{12} = 0$, which is the conventional case when the far end of the member is pin supported.

By following the same procedure for deriving Eqs. (3.A.6) and (3.A.7), the modified rotational stiffness coefficient and carryover factor are readily found for the case where the unit rotation is imposed at end 2 and plasticity occurs at end 1 rather than at end 2. These results are directly obtained

by exchanging the subscripts 1 and 2 for the degradation factor r in Eqs. (3.A.6) and (3.A.7), to achieve the two corresponding expressions,

$$R_{22} = \frac{M_2}{\theta_2} = kb\eta_1 \frac{3r_1 + b\eta_1(1-r_1)(1-c^2\eta_2^2)}{b\eta_1(1-r_1)+3r_1} \tag{3.A.8}$$

$$C_{21} = \frac{3r_1 c\eta_2}{3r_1 + b\eta_1(1-r_1)(1-c^2\eta_2^2)} \tag{3.A.9}$$

It is observed by comparison of Eq. (3.A.6) with Eq. (3.A.8), and Eq. (3.A.7) with Eq. (3.A.9), that the modified rotational stiffness coefficients and carryover factors differ when the post-elastic degradation factors r_1 and r_2 have different values, which is unlike the case in the elastic range.

3.A.2 Member Stiffness Coefficients

To illustrate the modified moment distribution method developed in the previous section, the stiffness coefficients are derived for a member with flexural stiffness degradations at both ends. The calculation procedure is the same as that in the conventional moment distribution method.

3.A.2.1 Stiffness Coefficients due to End Rotations

As shown in Figure 3.18, assume the inelastic zones at the two member ends have flexural stiffness R_j (j = 1, 2) associated with stiffness degradation factors r_j (j = 1, 2). The member is comprised of two parts: inelastic spring element 1-s and element s-2 that includes elastic member s-e and inelastic spring e-2. Since the modified rotational stiffness and carry-over factor element s-2 are known from the previous section, joint e is alone considered in the following.

The distribution factors at ends 1s and 2e are unity, as indicated in Table 3.2 and explained in the previous section. The distribution factor μ_{s2} at end s2 of member s-2 is expressed by the use of the modified rotational stiffness of Eq. (3.A.6) as,

$$\begin{aligned}\mu_{s2} &= \frac{R_{11}}{R_{11}+R_1} \\ &= \frac{3kb\eta_1 r_1[b\eta_1(1-r_2)(1-b^2\eta_1^2)+3r_2]/R_1}{3r_1[b\eta_1(1-r_2)+3r_2]+(1-r_1)b\eta_1[b\eta_1(1-r_2)(1-c^2\eta_2^2)+3r_2]}\end{aligned} \tag{3.A.10}$$

It is not necessary to find distribution factor μ_{s1} because it is known that the moments at ends se and 1s have the same value due to the negligible length of inelastic spring element 1-s. The carryover factor given by Eq. (3.A.7) can be directly applied because the moment-rotation relationship for member s-2 is the same as that discussed in the previous section for member 1-2 in Figure 3.17.

When node *s* is locked and rotation θ_1 is imposed at end 1, the fixed-end moments at end 1 and end *s* of member 1-*s* are $R_1\theta_1$ and $-R_1\theta_1$, respectively (as given in Table 3.2). By employing the modified distribution factor to distribute the unbalanced moment $R_1\theta_1$ at node *s* to ends *s*1 and *se*, the carry over of these moments to the corresponding far ends yields the results given in rows 5 and 6 of Table 3.2, respectively. From the last two columns in Table 3.2, the bending moments at ends 1 and 2 of the member 1-2 in Figure 3.18 are,

$$M_1 = \mu_{s2} R_1 \theta_1 \tag{3.A.11}$$

$$M_2 = C_{12} \mu_{s2} R_1 \theta_1 \tag{3.A.12}$$

These two moment expressions can be used to find the relevant stiffness coefficients associated with unit rotation θ_1. To that end, substitute Eq. (3.A.10) into Eq. (3.A.11) to find the rotational stiffness coefficient end 1,

$$k^r_{33} = \frac{M_1}{\theta_1} = \frac{3r_1 b\eta_1 k[b\eta_1(1-r_2)(1-c^2\eta_2^2)+3r_2]}{\Omega} \tag{3.A.13}$$

The parameter Ω in Eq. (3.A.13) is given by,

$$\Omega = 9r_1r_2 + 3r_2 b\eta_1(1-r_1) + 3r_1 b\eta_1(1-r_2) + b^2\eta_1^2(1-r_1)(1-r_2)(1-c^2\eta_2^2) \tag{3.A.14}$$

When $r_1 = r_2 = 1$ in Eq. (3.A.14), $\Omega = 9$ and the rotational stiffness coefficient $k^r_{33} = kb\eta_1$ as in Eqs. (2.1.17) of Chapter 2. By substituting into Eq. (3.A.12) the carryover factor C_{12} defined by Eq. (3.A.7) and the distribution factor μ_{s2} defined by Eq. (3.A.10), the rotational stiffness coefficient at end 2 is found as,

$$k^r_{63} = M_2/\theta_1 = 9kbc\eta_1\eta_2 r_1 r_2/\Omega \tag{3.A.15}$$

After k^r_{33} and k^r_{36} are obtained, the transverse shear stiffness coefficient for the member is determined from the moment equilibrium condition about end 2 as,

$$k^r_{23} = \frac{k^r_{33}+k^r_{63}}{L} = \frac{3b\eta_1 kr_1(1+c\eta_2)[b\eta_1(1-r_2)(1-c\eta_2)+3r_2]}{\Omega L} \tag{3.A.16}$$

From the transverse equilibrium condition, it is found that stiffness coefficient $k^r_{53} = -k^r_{23}$.

Following the same procedure as that used to find the stiffness coefficients when $\theta_1 = 1$, similar stiffness coefficient expressions are found when $\theta_2 = 1$ alone is imposed at end 2 of the beam in Figure 3.18. Thus, the rotational stiffness coefficient at End 2 is given by,

$$k^r_{66} = 3r_2 b\eta_1 k[b\eta_1(1-r_1)(1-c^2\eta_2^2)+3r_1]/\Omega \tag{3.A.17}$$

which can alternatively be found from Eq. (3.A.13) by simply exchanging the subscripts 1 and 2 of the rotational degradation factors r_j (j = 1, 2). In the same way, the transverse stiffness coefficient can be found from Eq. (3.A.16) to be,

$$k_{26}^r = \frac{3b\eta_1 kr_2(1+c\eta_2)[b\eta_1(1-r_1)(1-c\eta_2)+3r_1]}{\Omega L} = -k_{56}^r \tag{3.A.18}$$

It can be demonstrated that the Maxwell reciprocal theorem is satisfied for the post-elastic stiffness coefficients when the inelasticity is assumed to be concentrated at the member ends. For instance, for θ_2 = 1or θ_1 = 1 it can be shown that the related rotational stiffness coefficients at end 1 or 2 are equal (see Eq. (3.A.15)), i.e.,

$$k_{36}^r = 9kbc\eta_2\eta_1 r_2 r_1/\Omega = k_{63}^r \tag{3.A.19}$$

The Maxwell reciprocal theorem can then be directly employed to obtain the stiffness coefficients k^r_{32} = k^r_{23}, k^r_{35} = k^r_{53}, k^r_{62} = k^r_{26}, and k^r_{65} = k^r_{56}.

3.A.2.2 Stiffness Coefficients due to End Translations

In principle, the modified moment distribution method in the preceding subsection can be utilized to find the stiffness coefficients associated with translation at any member end, e.g., d_2 = 1 shown in Figure 3.19. However, it might be quite tedious to do so because two rounds of distributing and carrying over moments need to be conducted. Alternatively, the stiffness coefficients can be determined on the basis of the results found in the previous section by using the Maxwell reciprocal theorem.

From the Maxwell reciprocal theorem, k^r_{32} = k^r_{23} and k^r_{62} = k^r_{26}, where k^r_{23} and k^r_{26} are defined by Eqs. (3.A.16) and (3.A.18), respectively. Thus, the rotational stiffness coefficients are known at both ends of the member. The remaining work is to find transverse stiffness coefficients k^r_{22} and k^r_{52}. To that end, from moment equilibrium about end 2 the transverse stiffness coefficient k^r_{22} is found as,

$$k_{22}^r = \frac{f_2}{d_2} = \frac{EI}{L^3\Omega}\left\{3b\eta_1(1+c\eta_2)[6r_1r_2 + b\eta_1(1-c\eta_2)(r_1+r_2-2r_1r_2)] + P\frac{L^2\Omega}{EI}\right\} \tag{3.A.20}$$

where f_2 is the transverse force induced by unit deflection d_2. It is then readily found that k^r_{52} = –k^r_{22}.

It is observed from Eqs. (3.A.14) and (3.A.20) that degradation factors r_1 and r_2 are in symmetrical positions in the expression for k^r_{22}. This implies that if a unit deflection is imposed at end 2 instead of end 1, the transverse stiffness coefficient found is k^r_{55} = k^r_{22}. By the reciprocal theorem, k^r_{25} = –k^r_{55} and k^r_{35} = k^r_{53} are readily found.

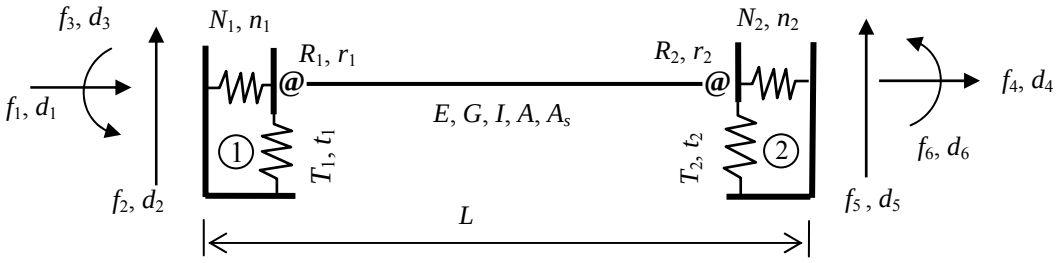

Figure 3.1 Hybrid beam-column member

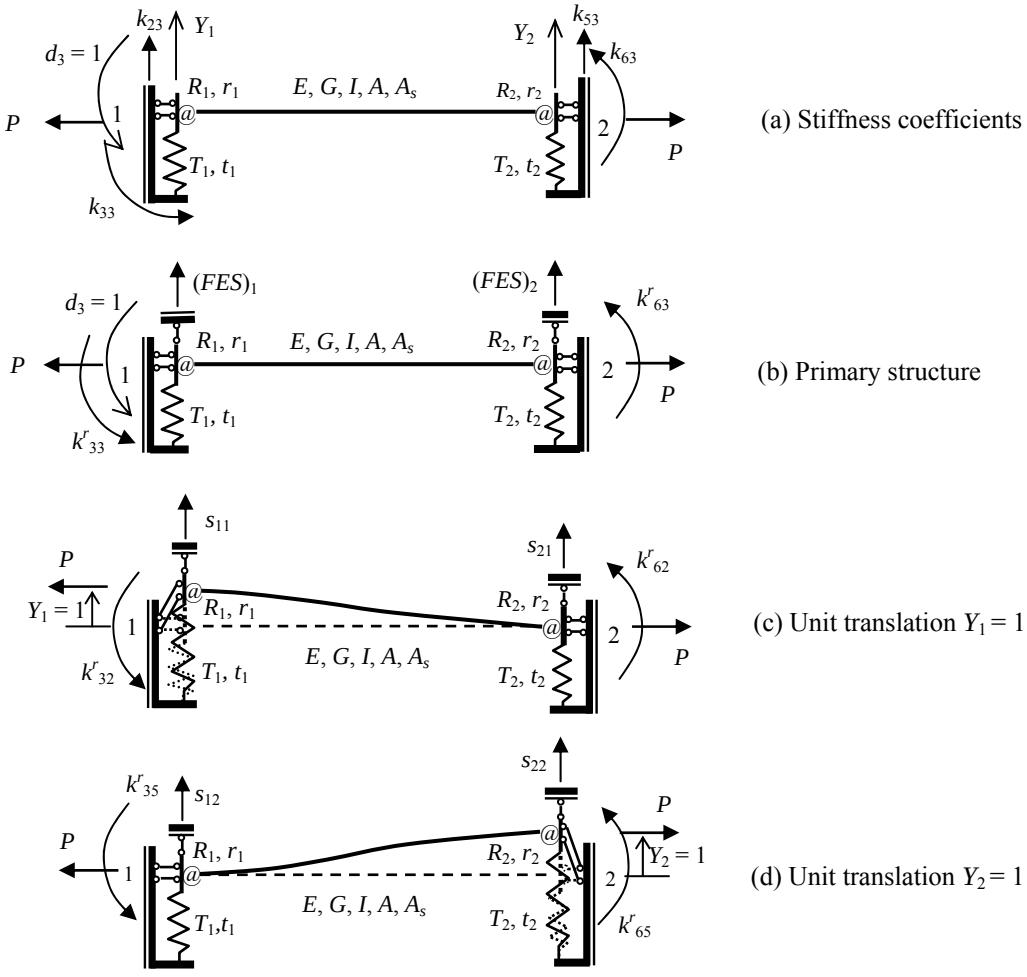

Figure 3.2 Stiffness coefficients due to rotation

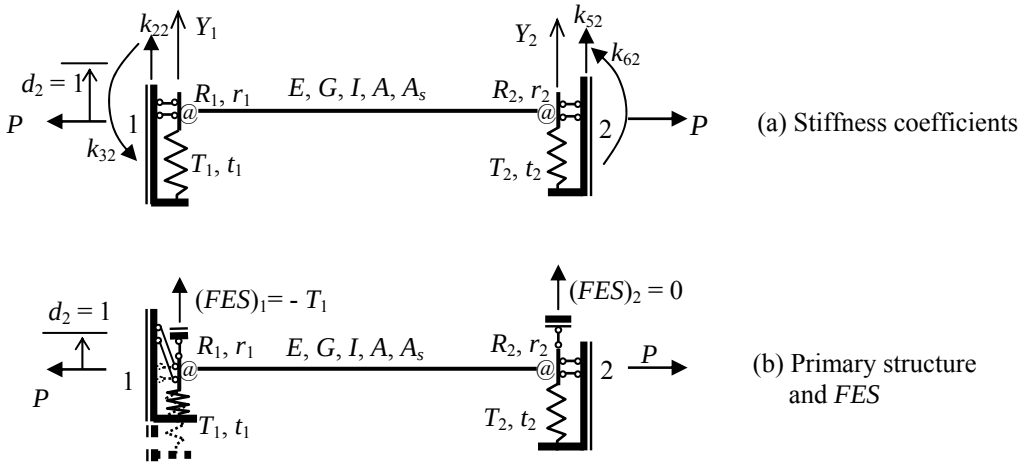

Figure 3.3 Stiffness coefficients due to translation

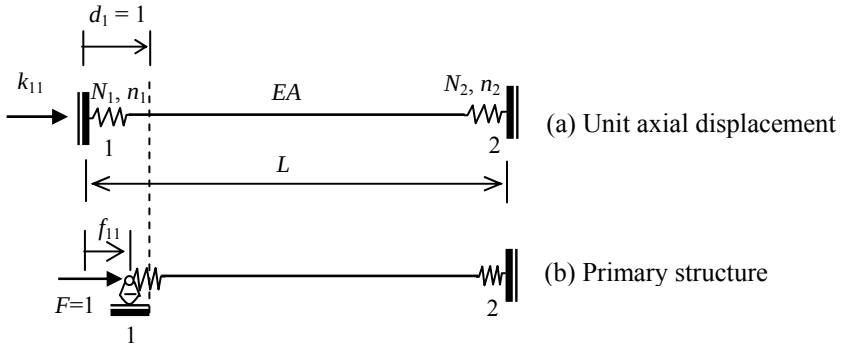

Figure 3.4 Axial force and deformation

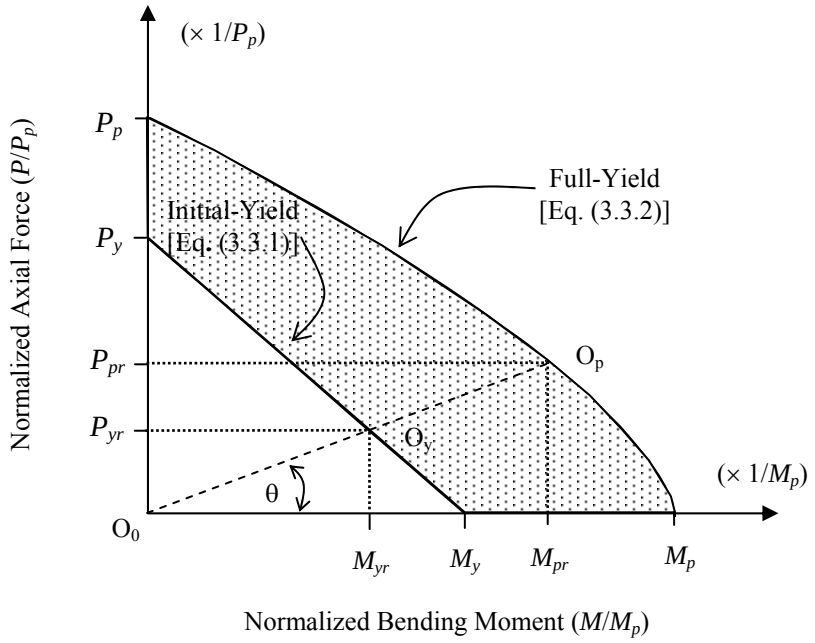

Figure 3.5 *M+P* first-yield and full-yield capacities

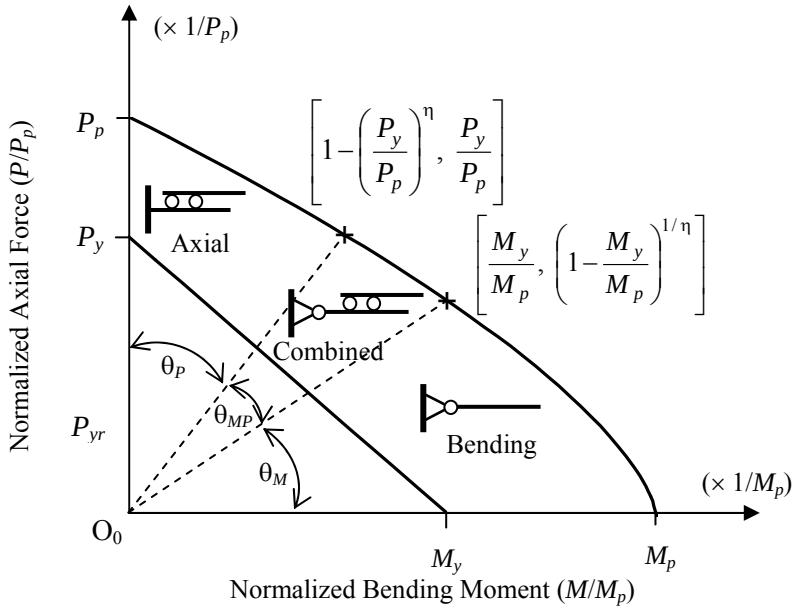

Figure 3.6 *M+P* stiffness degradation

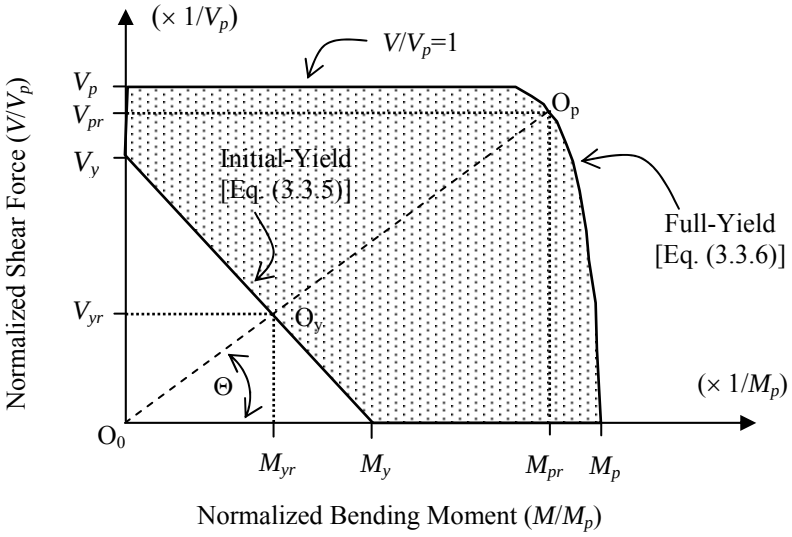

Figure 3.7 *M+V* first-yield and full-yield capacities

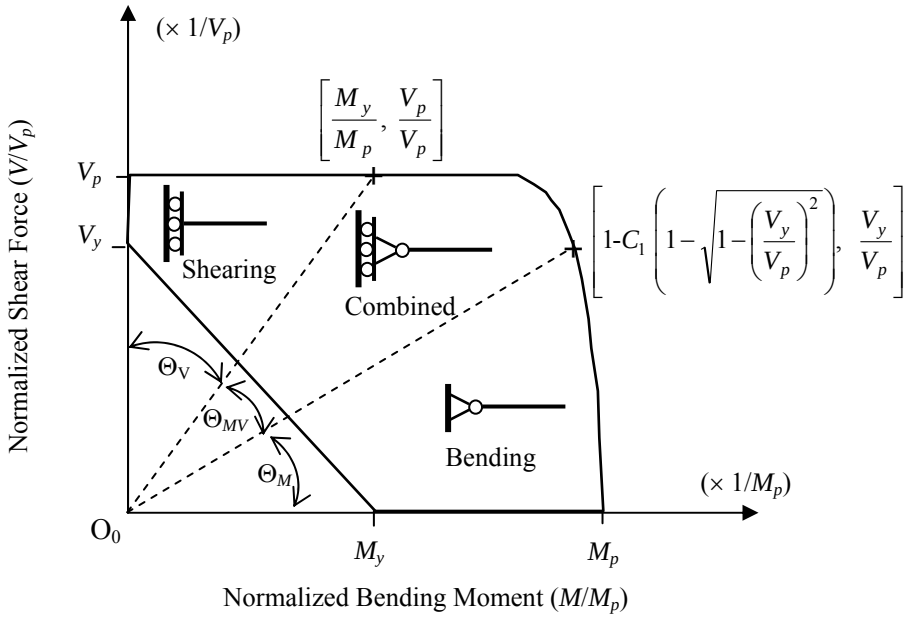

Figure 3.8 *M+V* stiffness degradation

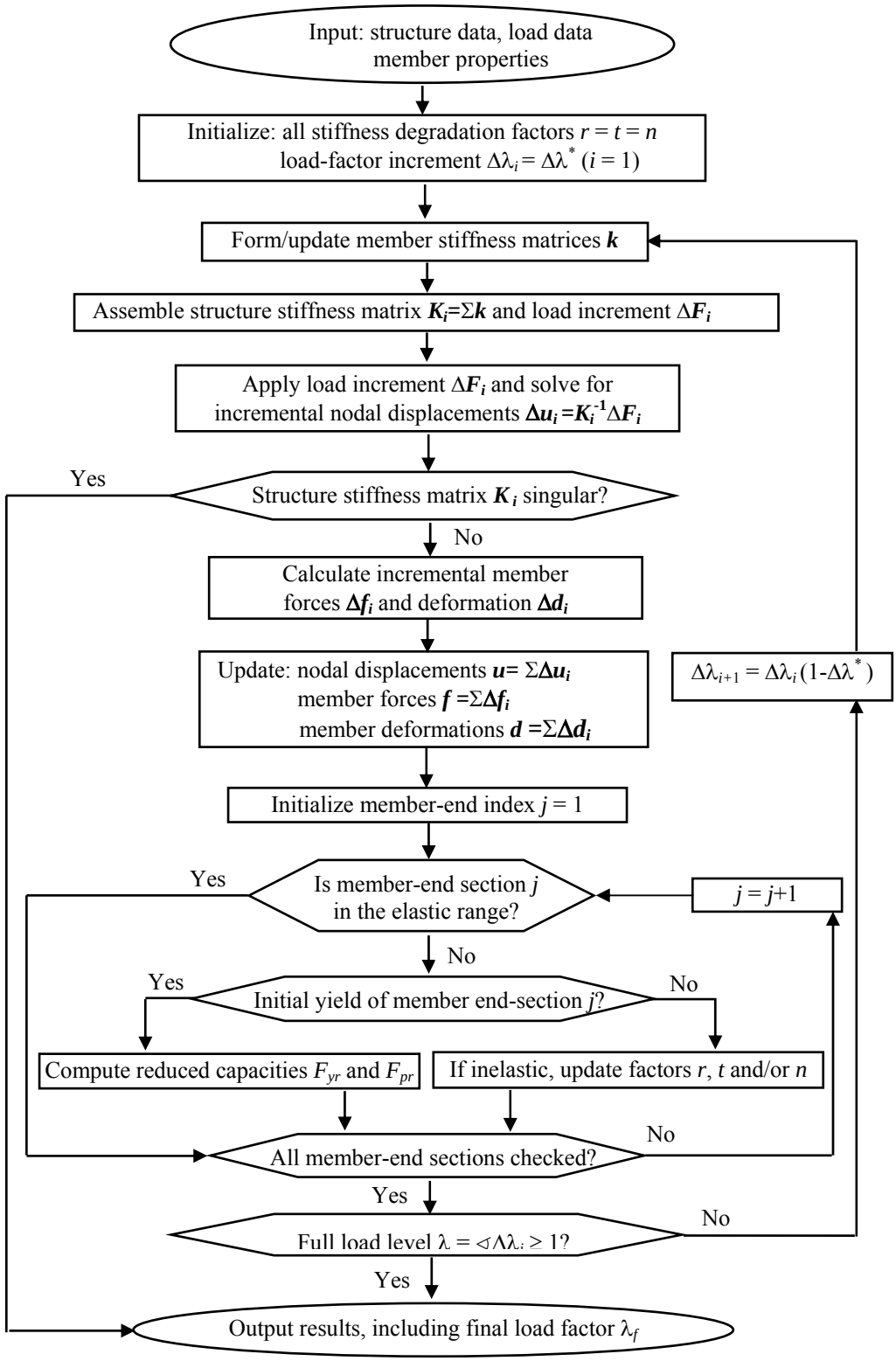

Figure 3.9 Flow chart for nonlinear analysis

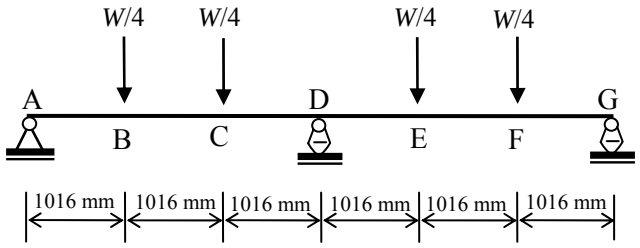

Figure 3.10 Two-span beam with point loading

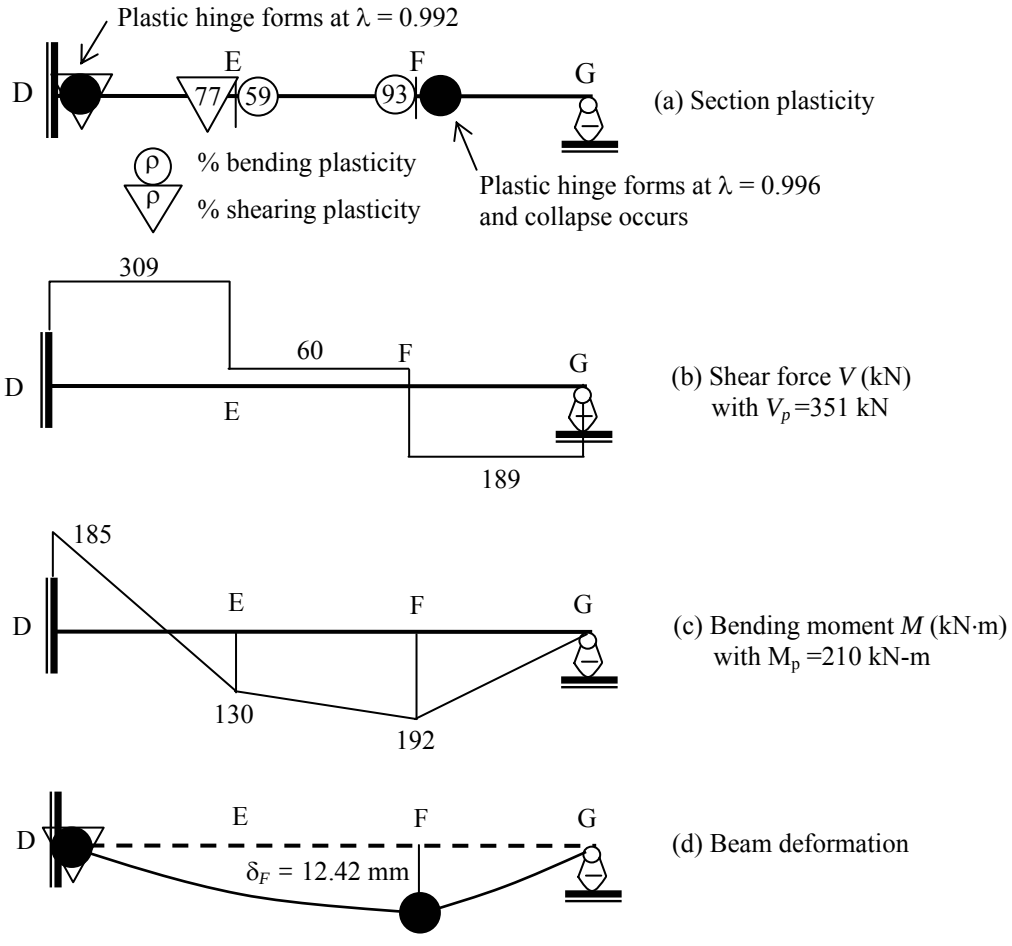

Figure 3.11 Example 1: Post-elastic behaviour at incipient beam failure

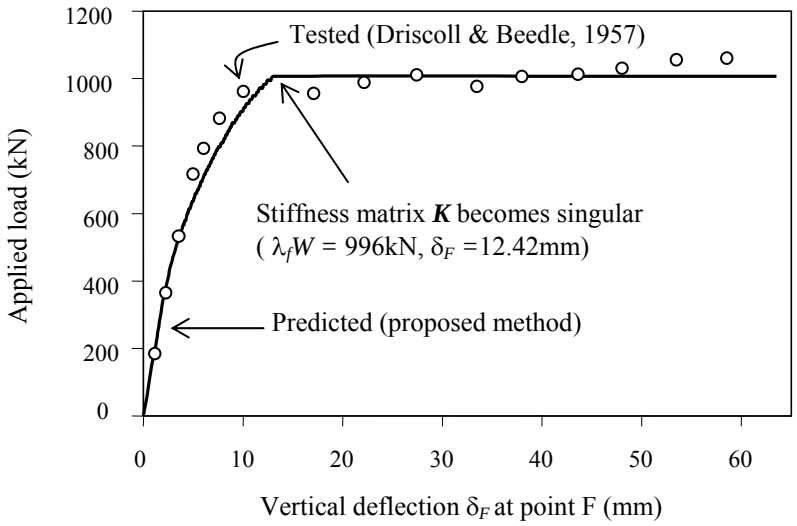

Figure 3.12 Example 1: Comparison of analytical and test results

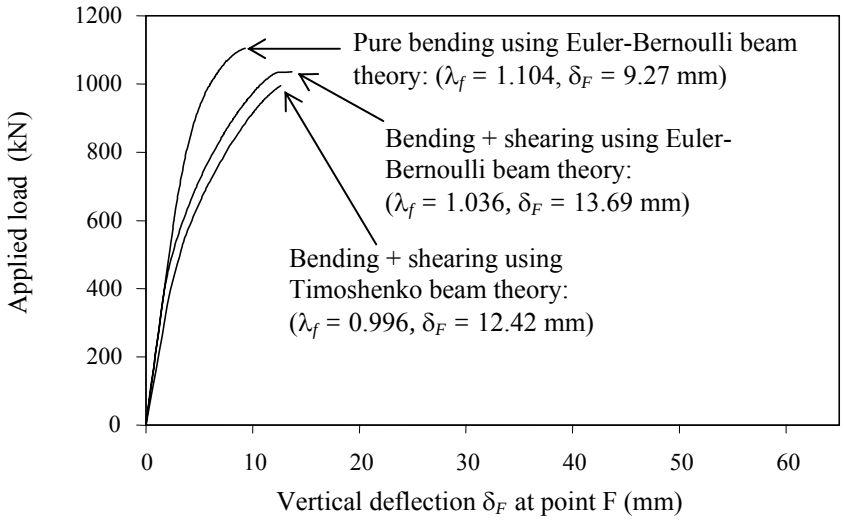

Figure 3.13 Example 1: Analytical results for different beam models

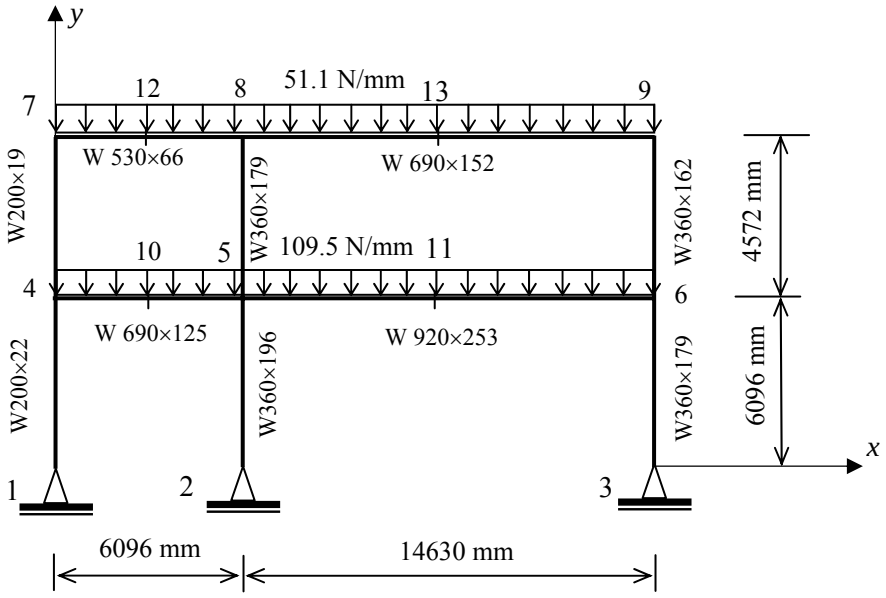

Figure 3.14 Frame and service-level design gravity loading

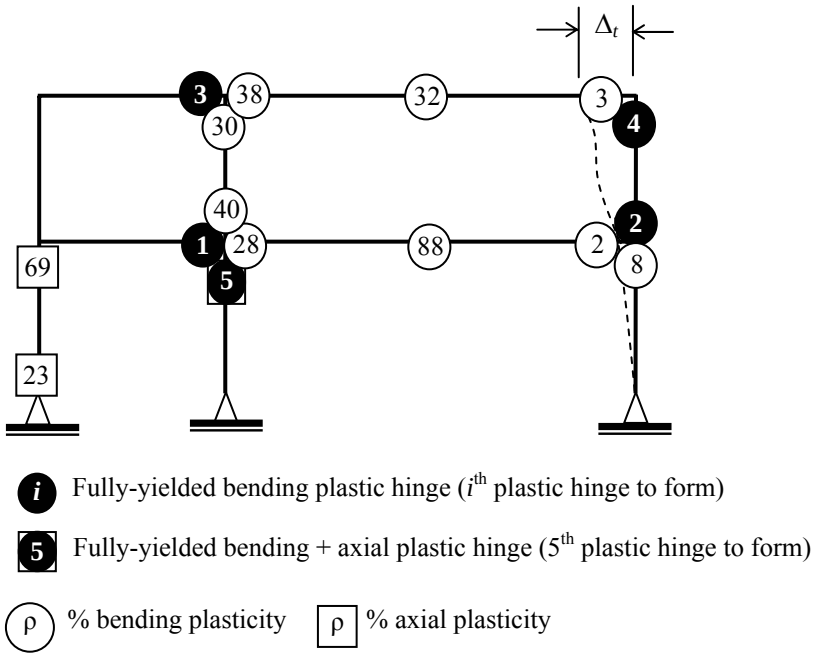

Figure 3.15 Plasticity at frame failure load-factor level $\lambda_f = 1.08$

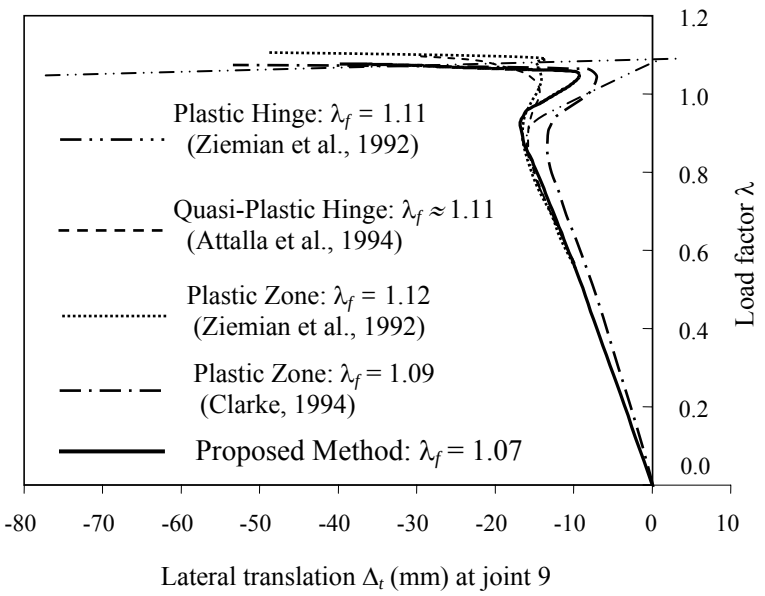

Figure 3.16 Comparison with other analyses

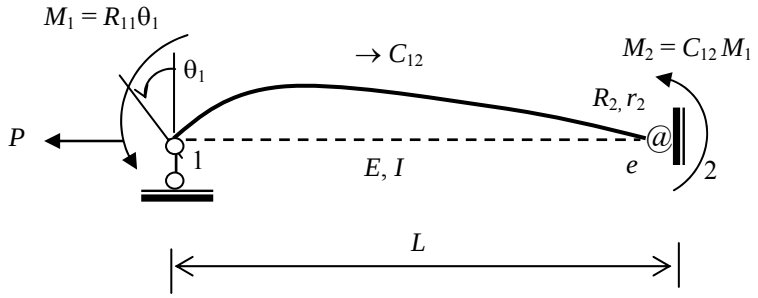

Figure 3.17 End moments due to rotation θ_1

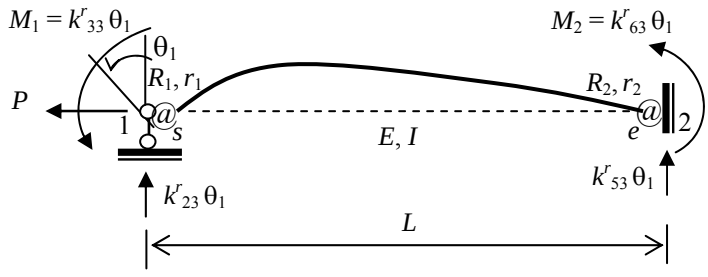

Figure 3.18 Stiffness coefficients due to rotation θ_1

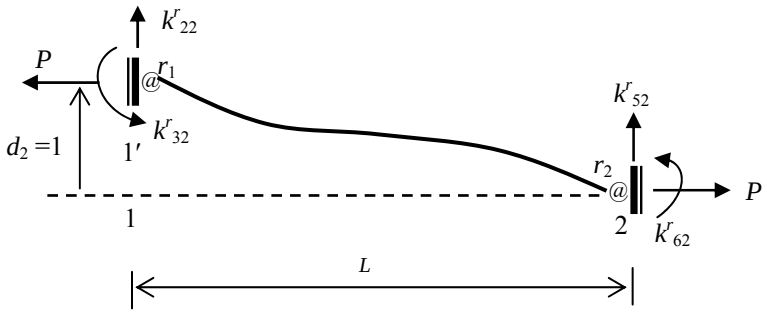

Figure 3.19 Stiffness coefficients due to deflection

Table 3.1 Rotation stiffness and carry-over factor for extended Cross method

Node	1		*e*	2
Member end	1*e*	*e*1	*e*2	2*e*
Distribution Factor	1	μ_{e1}	μ_{e2}	1
Fixed-end moment	$kb\eta_1\theta_1$	$kcb\eta_1\eta_2\theta_1$	0	
Distribution		$-\mu_{e1}kcb\eta_1\eta_2\theta_1$	$-\mu_{e2}\,kcb\eta_1\eta_2\theta_1$	
Carry-over	$\mu_{e1}kbc^2\eta_1\eta^2{}_1\theta_1$			$\mu_{e2}\,kcb\eta_1\eta_2\theta_1$
Final end moment *M*	$M_1= R_{11}\theta_1$	M_2	$-M_2$	$M_2= R_{21}\theta_1$
Stiffness coefficient	$R_{11}=$ $b\eta_1k(1-\mu_{e1}c^2\eta_2{}^2)$	-	-	$R_{21}=C_{12}\,R_{11}=$ $b\eta_1k\mu_{e2}\,c\eta_2$

Table 3.2. End moments due to end rotation θ_1

Node	1		*s*	2
Member end	1*s*	*s*1	*se*	2*e*
Distribution Factor	1	μ_{s1}	μ_{s2}	1
Fixed-end moment	$R_1\theta_1$	$-R_1\theta_1$	0	0
Distribution		$\mu_{s1}\,R_1\theta_1$	$\mu_{s2}\,R_1\theta_1$	
Carry-over	$-\mu_{s1}\,R_1\theta_1$			$\mu_{s2}\,C_{12}\,R_1\theta_1$
Final end moment *M*	$M_1=$ $\mu_{s2}\,R_1\theta_1$	$-M_1$	M_1	$M_2=$ $\mu_{s2}\,C_{12}\,R_1\theta_1$

Chapter 4
Frameworks with Semi-rigid Connections

This chapter describes an efficient method for the inelastic analysis of semi-rigid planar steel frameworks. A compound element, comprised of a plastic-hinge element and a semi-rigid connection element, is located at member ends that may undergo inelastic deformation. Nonlinear inelastic flexural behaviour of the member is modeled by an empirical relationship between moment and rotation, for which the parameters are available from experimental results. A four-parameter model is employed to simulate the nonlinear moment-rotation behaviour of the semi-rigid connections. The member stiffness matrix for the compound element is expressed in terms of stiffness degradation factors that vary according to the loading level. This permits direct account for the combined influence of member plasticity and semi-rigid connection behaviour on the structure stiffness. Three steel frameworks are analyzed to illustrate the proposed analysis method. The results are compared with those obtained from experiments and applying other methods.

4.1 Introduction

Many studies have been devoted to developing practical methods of nonlinear analysis of frameworks accounting for semi-rigid behaviour of the connections and/or plastic behaviour of the members (Chen et al., 1994; Chen et al., 1996; Faella et al., 2000; Chan & Zhou, 2004). However, little has been done to investigate the interaction between the behaviour of semi-rigid connections and that of member plasticity, as well as transverse-shear and axial stiffness degradations. This thesis focuses on such interaction by applying a planar-compound-element concept. A member plastic zone forms at the beam end due to internal forces (e.g., moment, shear force, and axial force). The characteristics of the interaction between a flexural semi-rigid connection and the flexural plastic zone of its connected member are discussed and illustrated in detail.

Figure 4.1(a) exhibits a typical beam-to-column connection joint, where there is member plasticity due to bending. Typically, the connection is semi-rigid, and can include bolts, welds and angles. To facilitate a nonlinear analysis, the model in Figure 4.1(a) is replaced by the analytical model in Figure 4.1(b). Here, one of the two springs represents the plasticity formed at the member end, while the other spring represents the semi-rigid connection.

An incremental-load method of analysis has been recently developed to deal with material and geometric nonlinearities (Grierson et al., 2005; Xu et al., 2005). The goal of this chapter is to extend this method to account as well for semi-rigid connections. Each stage of the analysis accounts for

stiffness degradation due to semi-rigid connection behaviour combined with member plasticity, geometric nonlinearity and shear deformation when updating the corresponding tangent stiffness matrix for the structure. The incremental-load process ends when the specified external loads have been completely applied to the structure, or a limit failure loading state is reached.

4.2 Rotational Compound Element

This section employs an assembly of springs, connected in series, to develop a compound element representing the combined rotational stiffness behaviour of a semi-rigid connection and a member-end plastic hinge. The determination of the stiffness of semi-rigid connections is discussed in detail, while that for member-end plasticity is adopted directly from previous research (Grierson et al., 2005; Xu et al., 2005).

4.2.1 Series Element Model

The series element model consists of a semi-rigid connection spring, an inelastic spring and an elastic member, all connected in series. Herein, an inelastic spring is defined as a spring that characterizes the inelastic behaviour of a cross section from initial yield to full yield. The nature of the compound element is indicated in Figure 4.2, where parameters R_c, R_p, and R_e denote the rotational stiffnesses of the semi-rigid connection spring, the member plasticity spring and the elastic member end, respectively. Only end 1 of the member is considered (end 2 may or may not have the exact same nature as end 1).

The case in Figure 4.2(a) is conventionally used in structural analysis, where a beam-to-column connection at node 1 is assumed as either a pinned connection ($R_c = 0$) or fixed connection ($R_c = \infty$). This assumption simplifies the analysis for both hand and computer-based analyses. However, if the effect of the actual connections on structural response is significant, the model including a semi-rigid connection represented by a spring symbol @ in Figure 4.2(b) should be accounted for in the analysis and design of the structure. Another model popular in rigid-plastic analysis assumes that a member plastic hinge abruptly forms, i.e., rather than gradually forming from initial yield to full yield. To improve the accuracy in this case, the inelastic-spring model in Figure 4.2(c) is suitable for simulating gradual stiffness degradation due to increasing extent of plastic behaviour. Finally, if both semi-rigid connection and plastic member behaviour occur at the same time, the series-element model shown in Figure 4.2(d) should be introduced in the analysis. Although Yau and Chan (1994) previously considered the latter model, the influences of member plasticity and semi-rigid connections were considered separately.

The rotational deformations of the semi-rigid connection and inelastic member end, indicated in Figure 4.2(d), are graphically represented in Figure 4.3(a). It is readily shown that the two series-connected springs can be substituted for by the compound element in Figure 4.3(b) having only one spring. It remains to derive the expression for compound stiffness R representing the combined effect of stiffnesses R_c and R_p. To that end, for applied moment M in Figure 4.3(a), the rotations θ_c and θ_p caused by semi-rigid connection behaviour member plastic behaviour, respectively, are found as,

$$\theta_c = M / R_c \tag{4.2.1a}$$

$$\theta_p = M / R_p \tag{4.2.1b}$$

Then, the total rotation θ between the joint and the elastic member end is, from Eqs. (4.2.1),

$$\theta = \theta_c + \theta_p = M / R_c + M / R_p = M / R \tag{4.2.2}$$

from which it is observed that the compound rotational stiffness accounting for semi-rigid connection and member plastic behaviour is,

$$R = \frac{1}{1/R_c + 1/R_p} = \frac{R_c R_p}{R_c + R_p} \tag{4.2.3}$$

4.2.2 Determining Connection Stiffness R_c

It remains to determine the stiffness of the compound element defined by Eq. (4.2.3). To that end, member plasticity stiffness R_p is directly given by Eq. (2.3.3) or (2.C.3) in Chapter 2, and semi-rigid connection stiffness R_c alone needs to be established in the following.

Several semi-rigid connection models have been investigated by Xu (1994). A four-parameter power model, originally proposed for modeling post-elastic stress-strain behaviour (Richard & Abbott, 1975), has been commonly adopted in analysis. Recently, experimental data for extended-end-plate and flush-end-plate connections has further confirmed this model to be effective and accurate for predicting the behaviour of end-plate connections (Kishi et al., 2004). The following four-parameter model is employed in this study to simulate the behaviour of semi-rigid connections,

$$M = \frac{(R_{ce} - R_{cp})\theta_c}{\{1 + [(R_{ce} - R_{cp})\theta_c / M_0]^{\gamma}\}^{1/\gamma}} + R_{cp}\theta_c \tag{4.2.4}$$

In Eq. (4.2.4), θ_c denotes the rotation of the semi-rigid connection, and the four parameters R_{ce}, R_{cp}, M_0 and γ are the elastic rotation stiffness, strain-hardening/softening stiffness, reference moment and shape parameter for the connection, respectively. The elastic stiffness $R_{ce} = M_{cy}/\theta_{cy}$, where M_{cy} and θ_{cy} are the initial yield moment and corresponding rotation. The shape of the moment-rotation curve is

defined by the parameter γ, whose magnitude is related to the strain hardening and softening behaviour of the connection (the value γ used in the model is found by curve fitting experimental data). The four parameters in Eq. (4.2.4) can be found for different types of connections from an existing database of experimental results (Xu, 1994). The reference moment M_0, strain-hardening or softening stiffness R_{cp}, and nominal rotation θ_n determine the nominal maximum moment or moment capacity of the connection to be,

$$M_n = M_0 + \theta_n R_{cp} \tag{4.2.5}$$

where θ_n depends on the connection type and is determined from published research results; e.g., Bjorhovde et al., (1990). It is noteworthy that when the moment-rotation response does not have a humped point, the nominal moment capacity is determined by the moment at which $\theta_n = 0.02$, as suggested in the AISC(2005) design specifications.

By differentiating Eq. (4.2.4) with respect to rotation θ_c, the tangent stiffness of the connection is given by (Richard & Abbott, 1975),

$$R_c = \frac{dM}{d\theta_c} = R_{cp} + \frac{R_{ce} - R_{cp}}{\{1 + [(R_{ce} - R_{cp})\theta_c / M_0]^{\gamma}\}^{1+1/\gamma}} \tag{4.2.6}$$

where R_{ce} is the elastic rotational stiffness at the initial condition $\theta_c = 0$, and R_{cp} is the strain-hardening and softening stiffness when rotation θ_c tends to infinity. For practical analysis of steel structures, the rotation θ_c is at most equal to the limiting nominal rotation value when connection fracture occurs (Bjorhovde et al., 1990).

It is seen from Eqs. (4.2.4) and (4.2.6) that the four-parameter model reduces to a linear model with $R_c = R_{ce}$ when R_{cp} tends to R_{ce}. A bi-linear model is realized when the shape parameter γ approaches infinity; i.e., when $\theta_c < M_0/(R_{ce}-R_{cp})$, the term $[(R_{ce}-R_{cp})\theta_c/M_0]^{\gamma}$ tends to zero and Eq. (4.2.6) reduces to $R_c = R_{ce}$, while when $\theta_c > M_0/(R_{ce}-R_{cp})$, the term $[(R_{ce}-R_{cp})\theta_c/M_0]^{\gamma}$ tends to infinity and Eq. (4.2.6) reduces to $R_c = R_{cp}$. If R_{cp} is set to zero (i.e., strain-hardening and softening is ignored), Eq. (4.2.4) reduces to the following three-parameter model, suggested by Kishi and Chen (1987),

$$M = \frac{R_{ce}\theta_c}{[1 + (R_{ce}\theta_c / M_0)^{\gamma}]^{1/\gamma}} \tag{4.2.7}$$

where reference moment M_0 is equal to nominal moment capacity M_n. Note that rotation θ_c can be explicitly obtained from Eq. (4.2.7) as,

$$\theta_c = \frac{M}{R_{ce}[1 - (M / M_0)^{\gamma}]^{1/\gamma}} \tag{4.2.8a}$$

As given by Eq. (2.3.2) or (2.C.1) in Chapter 2 (Grierson et al. (2005) and Xu et al. (2005)), the post-elastic rotation of the connecting member is taken by this study to be,

$$\phi = \phi_p \left\{ 1 - \left[1 - \left(\frac{M - M_y}{M_p - M_y} \right)^{e_0} \right]^{1/e_0} \right\} \qquad \frac{M_y}{M_p} \le \frac{M}{M_p} \le 1 \tag{4.2.8b}$$

Therefore, from Eqs. (4.2.8a, b), the total rotation $\theta = \theta_c + \phi$ of the compound element can be explicitly expressed as,

$$\theta = \frac{M}{R_{ce}[1-(M/M_u)^{\gamma}]^{1/\gamma}} + \phi_p \left\{ 1 - \left[1 - \left(\frac{M - M_y}{M_p - M_y} \right)^{e_0} \right]^{1/e_0} \right\} \qquad \frac{M_y}{M_p} \le \frac{M}{M_p} \le 1 \tag{4.2.9}$$

which represents the moment-rotation relationship of the compound element. The benefit of using the three-parameter model Eq. (4.2.7) is that rotation θ_c of the connection is directly obtained from Eq. (4.2.8a) given moment M found by the non-linear analysis; the disadvantage is that the strain-hardening or softening nature of the connection is omitted. In contrast, although strain hardening and softening is accounted for in the four-parameter model, an iterative procedure is needed to find the rotation θ_c of the connection. Both connection models are considered for the verification analysis presented in Section 4.5.

4.2.3 Stiffness Degradation Factors

The flexural stiffness degradation factor associated with semi-rigid stiffness R_c is given by (Monforton et al., 1963),

$$r_c = \frac{1}{1 + 3EI / LR_c} \tag{4.2.10}$$

where EI/L is the flexural stiffness of the elastic member. The factor r_c is interpreted as the ratio of the end rotation of the elastic member to the combined rotation of the elastic member and the semi-rigid connection due to unit end-moment (Xu 1994). Similarly, the stiffness degradation factor associated with the inelastic member stiffness R_p is given by (Grierson et al., 2005),

$$r_p = \frac{1}{1 + 3EI / LR_p} \tag{4.2.11}$$

where the factor r_p is interpreted as the ratio of the inelastic rotation M/R_p to the total elastic and inelastic rotation $ML/3EI + M/R_p$ due to bending moment M applied at the end connected to the compound element, where the far end of the elastic member is simply supported (Xu et al., 2005).

To evaluate the combined stiffness effect, a stiffness degradation factor for the compound stiffness R defined by Eq. (4.2.3) is introduced and similarly expressed as,

$$r = \frac{1}{1 + 3EI / LR} \tag{4.2.12}$$

which is Eq. (2.3.4) in Chapter 2. The factor r is the ratio of the rotation of the compound element to the sum total rotation of the compound element and the rotation of the elastic member, when it is simply supported at the far end. From Eqs. (4.2.3), (4.2.10), (4.2.11) and (4.2.12), the compound stiffness degradation factor is expressed as,

$$r = \frac{1}{1 + 3EI / LR_c + 3EI / LR_p} = \frac{r_c r_p}{r_c + r_p - r_c r_p} \tag{4.2.13}$$

which maps $R \in [0, \infty]$ to $r \in [0, 1]$. From Eq. (4.2.13), the stiffness degradation factor for the compound element is a function of the degradation factors of the semi-rigid connection and member inelasticity such that, if any of these factors degrades to zero, the stiffness of the compound element degrades to zero as well.

4.3 Characteristics of Compound Rotational Element

The behaviour of the compound rotational element is dependent upon the strength capacities of the connection and the connected beam members. For the current study, the effect of shear deformation of the panel zone on the behaviour of the beam-column connection is ignored. Connection strength is important in the inelastic analysis of frameworks. The strength behaviour of the compound element is analyzed in the following.

If only the effect of the member plasticity is considered, the moment-rotation relation in the post-elastic range is that shown in Figure 4.5 (a). Alternatively, if the effect of the semi-rigid connection is accounted for, the moment-rotation relationship is as shown in Figure 4.5 (b). In Figure 4.5, the nominal maximum moment M_n defined by Eq. (4.2.5) is the moment capacity of the connection, while M_y and M_p are the initial-yield and fully-plastic moment capacities of the connected member, respectively. Depending on the interaction between member inelasticity and semi-rigid connection behaviour, three types of connections are characterized by the compound element, as described in the following

Under-Strength Connections: $M_n \leq M_y$

In this situation, the performance of the compound element is governed only by the semi-rigid connection, and no plasticity occurs in the vicinity of the member end. This can occur for Single

Web-Angle (SWA) connections with $M_n = M_n^{SWA}$. Since the member end does not undergo any plasticity, the nonlinear moment-rotation behaviour of the compound element is determined by the behaviour of the semi-rigid connection alone; i.e., the moment-rotation relationship defined by the lowest solid curve in Figure 4.6 is the same as that given in Figure 4.5(b) for a SWA connection. This kind of connection is referred to as under-strength connection, since the strength capacity of the compound element is less than the yield strength capacity of the connected member. If M_n is small enough, this type of connection is categorized as a conventional simple or pinned connection (AISC, 2001; CISC, 2004). (Note that the definition of under-strength connections in this study is based on there being no plasticity at the member end, whereas the flexible connections defined in AISC-LRFD (AISC, 2001) are based on $M_n \leq 0.2M_p$).

Partial-Strength Connections: $M_y < M_n < M_p$

In this second case, both semi-rigid connection behaviour and member inelasticity govern the behaviour of the compound element, but the limit strength is determined by the nature of the connection. In other words, the connected member does not reach its moment capacity M_p, while the compound element achieves nominal moment capacity M_n. Such behaviour for a Flush End-Plate (FEP) connection is illustrated by the middle solid curve in Figure 4.6 (the corresponding dotted curve refers to the middle solid curve in Figure 4.5(b)). Although this type of semi-rigid connection is here referred to as a partial-strength connection, it is somewhat different from the definition in the design codes (AISC, 2001), where the inelasticity of the member is not accounted for.

Full-Strength Connections; $M_n \geq M_p$

Finally, when the nominal moment capacity of the connection M_n is equal or greater than the plastic moment capacity M_p of the connected member, the member inelasticity dominates the behaviour of the compound element (even though the connection influences the stiffness degradation of the compound element due to its non-linear behaviour). Such behaviour for an Extended End-Plate (EEP) connection is illustrated in Figures 4.5 and 4.6 (where the dotted moment-rotation curve refers to the EEP connection alone). It is evident in Figure 4.6 that the moment-rotation behaviour of the compound element (solid curve) is dominated by the plastic behaviour of the member. This kind of connection is referred to as a full-strength connection, which is defined the same way in the design codes (e.g., AISC, 2001).

It can be concluded from the preceding discussions that when the nominal capacity of a connection is much lower than that of the connected member, the connection dominates the behaviour of the compound element; however, if the nominal capacity of a connection is much greater than the capacity of the connected member, the member plasticity dominates the compound element

behaviour. In practice, a flexible connection with low connection capacity ($M_n << M_y$) can be employed in the design of braced frames. In the design of moment-resisting frames, however, excessive deformation can occur if the connection capacity M_n is far less than the capacity M_p of the connected member (see Example 3 in this chapter). A satisfactory design is achieved if both the connection and the corresponding connected member have approximately the same strength capacity (i.e., $M_p \approx M_n$). It is prudent to avoid over-strength connections (i.e., $M_n >> M_p$), since this results in over-costly construction because excess connection capacity is not utilized.

Besides the strength of connections, connection stiffness is another important factor characterizing the behaviour of connections, especially in serviceability design concerning initial elastic stiffness R_{ce}. According to Eurocode 3 (CEN, 2002; Jaspart, 2002), for example, a beam-to-column connection is assumed to be rigid if its elastic stiffness satisfies the following condition,

$$\frac{LR_{ce}}{EI} \geq 25 \quad (\text{or } r_c \geq 0.893 \text{ for an unbraced frame}) \tag{4.3.1}$$

or

$$\frac{R_{ce}L}{EI} \geq 8 \quad (\text{or } r_c \geq 0.727 \text{ for a braced frame}) \tag{4.3.2}$$

where the notations are the same as those defined in Eq. (4.2.10), except that R_c is replaced by elastic stiffness R_{ce}. Conversely, a connection is assumed to be flexible if the following condition is satisfied,

$$\frac{R_{ce}L}{EI} \leq 0.5 \quad (\text{or } r_c \leq 0.143 \text{ for either a braced or an unbraced frame}) \tag{4.3.3}$$

When elastic stiffness R_{ce} or corresponding stiffness factor r_c is located between the values defined by Eq. (4.3.1) or (4.3.2) and (4.3.3), a semi-rigid connection is attained. Note that the stiffness criteria defined in Eqs. (4.3.1) through (4.3.3) are related to member length L. If only the member length changes, the connection category changes according to the stiffness criteria. For instance, if $R_{ce}L/EI = 9$ for a braced frame, then the connection is rigid; however, when member length L changes to $0.5L$, the corresponding stiffness ratio becomes $0.5R_{ce}L/EI = 4.5$, and the same connection becomes semi-rigid. Such a paradox challenges the current classification systems for beam-to-column connections and further research is needed. For the time being, Eqs. (4.3.2) and (4.3.3) are used as the criteria in this study to characterize connection behaviour.

Contrary to that for connection stiffness, connection strength criteria are based on member moment capacities M_y and M_p, as well as nominal connection capacity M_n, and are independent of any length variation of the connected member. It is noteworthy that conventional rigid connections are recognized as having full strength ($M_n \geq M_p$) and rigid stiffness ($R_{ce} = \infty$). So, if the behaviour of a

connection is considered according to the strength and stiffness classification criteria, a rigid connection with full strength is not equivalent to the conventional rigid connection because R_{ce} satisfies Eq. (4.3.1) or (4.3.2) but is less than infinity. To distinguish from a conventional rigid connection, a full-strength connection with $R_{ce} < \infty$ is referred to as a fullly-rigid connection in this study.

The characteristics of stiffness degradation of a compound element are further examined in the following. The relationships between the compound degradation factor r and the connection and plasticity factors r_c, r_p, given in Eq. (4.2.13) are graphed in Figure 4.7. It is observed that for the common pinned-connection case when $r_c = 0$, the compound element has zero rotational stiffness for any value of r_p and the connected member exhibits no plasticity. For the other extreme case when $r_c = 1$, the compound element behaviour is governed by the plastic behaviour of the member ($r = r_p$). For the two cases, it is evident from Figure 4.7 that when the plasticity factor is less than unity (e.g., $r_p = 0.7$), the r value of the compound element is approximately the value of r_c. This means that even when the member end has undergone some degree of plasticity (e.g., 30% = 1.0 – 0.7), the stiffness of the compound element is dominated by that of the connection. In other words, the level of member plasticity has little effect on the stiffness degradation of the compound element.

To numerically demonstrate the interaction between semi-rigid connections and member plasticity, an illustration is presented the following for a beam member with three different connections. As shown in Figure 4.8, the member has span length L = 4m and a W310×33 cross-section (with the following properties: elastic and plastic moduli $S = 0.415\times10^6$ mm^3 and $Z = 0.48\times10^6$ mm^3, moment of inertia $I = 65\times10^6$ mm^4, Young's modulus E = 200000 MPa, yield stress $\sigma_y = 248$ MPa). The residual stress is assumed to be $\sigma_r = 0.3\sigma_y$, such that the initial and full-yield moments $M_y = 0.7S\sigma_y = 0.7\times0.415\times10^{-3}\times248\times10^3 = 72$ kN-m and $M_p = Z\sigma_y = 119$ kN-m, respectively. The parameters for the three typical connections listed in Table 4.1 are taken from a published databank (Xu, 1994). Illustrated in Figure 4.8(b) are the moment-rotation curves found for the connections using the four-parameter connection model defined by Eq. (4.2.4). It is seen from Figure 4.8(b) that the Double Web-Angle (DWA) is an under-strength connection, the Flush End-Plate (FEP) is a partial-strength connection, and the Extended End-Plate (EEP) is a full-strength connection.

Since no plasticity occurs at the member end when the DWA connection is employed, only the stiffness degradation behaviour of the beams with FEP and EEP connections are investigated in the following. The variations of stiffnesses predicted by Eqs. (4.2.6) for EEP and FEP connections are plotted in Figure 4.9 versus applied moment M. The corresponding values of the stiffness of these two connections are listed in Tables 4.2 and 4.3. It is seen from Figure 4.9 for both the EEP and FEP

connections that connection stiffness R_c and compound stiffness R are equal before member yielding takes place, and that compound stiffness R degrades to zero after member yielding occurs. The corresponding degradation factors r_p, r_c, and r in Tables 4.2 and 4.3 demonstrate that the member-section plastic behaviour dominates the stiffness degradation of the compound element.

4.4 Nonlinear Analysis of Frameworks with Semi-rigid Connections

Once the stiffness degradation factor of a compound element is determined, as discussed in the previous sections, the structural analysis is conducted. This study focuses on planar semi-rigid steel frameworks comprised of beam-column members with compact sections, for which plastic deformation is not precluded by local buckling (AISC, 2001). Plastic bending, shearing or axial deformation (ϕ, γ or δ) of a member under the action of moment, shear or axial force M, V or P, respectively, is assumed concentrated at the member-end sections (Xu et al., 2005). Figure 4.10(a) represents a general member with Young's modulus E, shear modulus G, member length L, cross-section moment of inertia I, sectional area A, and equivalent shear area A_s. Parameters R_{pj}, T_{pj} and N_{pj} are, respectively, the post-elastic rotational bending, transverse shearing and normal axial stiffness of the member at the two end sections j =1, 2, while R_{cj}, T_{cj} and N_{cj} are, respectively, the rotational bending, transverse shearing and normal axial stiffness of the connections at the two end sections. By adopting the compound element developed previously in this chapter, the simplified member model in Figure 4.10(b) is obtained, the corresponding parameters for which are discussed in the following.

The evaluation of connection and member rotational stiffnesses R_{cj} and R_{pj} in Figure 4.10(a), and corresponding stiffness degradation factors r_{cj} and r_{pj}, have been discussed in detail in Section 4.2. The member transverse shear and normal axial stiffnesses T_{pj} and N_{pj} have also been determined in previous research (Grierson et al., 2005; Xu et al., 2005), where corresponding stiffness degradation factors t_{pj} and n_{pj} for member end j are given by,

$$t_{pj} = \frac{1}{1 + 3EI / L^3 T_{pj}} \tag{4.4.1a}$$

$$n_{pj} = \frac{1}{1 + EA / LN_{pj}} \tag{4.4.1b}$$

which map T_{pj} or $N_{pj} \in [0, \infty]$ into t_{pj} or $n_{pj} \in [0, 1]$. Similarly, the transverse and normal stiffness degradation factors for the connection are expressed as,

$$t_{cj} = \frac{1}{1 + 3EI / L^3 T_{cj}} \tag{4.4.2a}$$

$$n_{cj} = \frac{1}{1 + EA/LN_{cj}} \tag{4.4.2b}$$

where T_{cj} and N_{cj} are the transverse shear and normal axial stiffnesses of the connection.

When the connection is in the elastic range, it is assumed that stiffness T_{cj} or N_{cj} is infinite and corresponding degradation factor t_{cj} or n_{cj} in Eqs. (4.4.2) is unity. Conversely, when the connection is in the plastic range, it is assumed that stiffness T_{cj} or N_{cj} is zero and corresponding degradation factor t_{cj} or n_{cj} is zero. Such idealized elastic-plastic models are depicted in Figure 4.11.

For the general planar compound member in Figure 4.10 (b), the bending stiffness degradation factor r_j is found through Eq. (4.2.13), while the shearing and axial stiffness degradation factors t_j and n_j are similarly found as,

$$t_j = \frac{t_{cj} t_{pj}}{t_{cj} + t_{pj} - t_{cj} t_{pj}} \tag{4.4.3a}$$

$$n_j = \frac{n_{cj} n_{pj}}{n_{cj} + n_{pj} - n_{cj} n_{pj}} \tag{4.4.3b}$$

Also in Figure 4.10(b), f_i and d_i (i =1, 2,..., 6) are respectively the local-axis joint forces and deformations corresponding to the local stiffness matrix $\boldsymbol{k}$ for the compound frame element, with account for the effects of shear deformation and geometrical nonlinearity. The local-axis stiffness matrices for all elements are transformed into the global coordinate system and then assembled as the structure stiffness matrix $\boldsymbol{K_i}$, where subscript i refers to the i^{th} stage of the incremental-load analysis procedure. If $\boldsymbol{K_i}$ is non-singular at the end of the i^{th} load step, corresponding incremental nodal displacements $\Delta\boldsymbol{u_i}$ are solved for and incremental member-end forces $\Delta\boldsymbol{f_i}$ and deformations $\Delta\boldsymbol{d_i}$ are found. As well, total nodal displacements $\boldsymbol{u_i} = \Sigma\Delta\boldsymbol{u_i}$, member-end forces $\boldsymbol{f_i} = \Sigma\Delta\boldsymbol{f_i}$ and deformations $\boldsymbol{d_i} = \Sigma\Delta\boldsymbol{d_i}$ accumulated over the loading history are found. The initial-yield and full-yield conditions for each member-end section are checked to detect plastic behaviour, and the corresponding bending, shearing and axial stiffness degradation factors are found. Degraded stiffnesses R_c, T_c and/or N_c are determined based on the moment, shear and axial forces found by the analysis at the current loading level. Degradation factors (r_p, t_p, n_p, r_c, t_c, and n_c) are applied to modify each element stiffness matrices $\boldsymbol{k}$ and, hence, the structure stiffness matrix $\boldsymbol{K}$ before commencing the next load step. The incremental-load analysis procedure continues until either a specified load level $\boldsymbol{F}$ is reached or the structure stiffness matrix $\boldsymbol{K}$ becomes singular at a lower load level, as a consequence of failure of part or all of the structure. (If the structure has not failed at load level $\boldsymbol{F}$, the analysis can be continued beyond that level until failure of the structure does occur.)

The final analysis results include the values of the bending, shearing and axial stiffness degradation factors r, t and n indicating the extent of the combined member plasticity and semi-rigid connection deformation in the beam-to-column connection regions of the compound element. Further computational details are provided through the analysis example presented in the following section.

4.5 Example Studies

Three examples of semi-rigid structural steel frameworks are selected to illustrate the analysis method proposed in the foregoing. The objective of the first example concerning a semi-rigid portal frame is to compare results obtained by this study with those obtained from experimental testing (Liew et al., 1997). The second example illustrates a comparison study of a one-bay by two-storey semi-rigid frame designed by Chen et al. (1996). Finally, the two-bay by two-storey frame described in Chapter 3 is revisited to investigate the influence of semi-rigid connections on the analysis results. In all analyses, Young's modulus E = 200000 MPa and shear rigidity G = 77000 MPa. The residual stress for bending and axial behaviour is $\sigma_r = 0.3\sigma_y$, while for shearing behaviour it is $\tau_r = 0.05\tau_y$, where σ_y and τ_y are respectively the normal yield stress and shearing yield stress of the steel material for each example.

4.5.1 Example 1: Semi-rigid Portal Frame

For the semi-rigid portal frame in Figure 4.12, for which experimental test results are available in the literature (Liew et al., 1997), the properties of the beam are: area A = 4740 mm^2, moment of inertia I = 5547×10^4 mm^4, plastic modulus Z = 485×10^3 mm^3, normal yield stress σ_y = 345 MPa, and shear yield stress τ_y = 199 MPa (based on the von Mises criterion). The properties of the two columns are: area A = 7600 mm^2, moment of inertia I = 6103×10^4 mm^4, plastic modulus Z = 654×10^3 mm^3, and yield stresses σ_y = 336 MPa and τ_y = 194 MPa.

The semi-rigid connections are modeled by the four-parameter model in Figure 4.4 (Richard et al., 1975), for which the parameter values are obtained from the following pilot-test results. The moment-rotation test results for the beam-to-column connection C1 are traced in Figure 4.13(a) as the dotted curve. By applying a curve-fitting technique to the model parameters in Eq. (4.2.4), the four parameters are determined to be M_0 = 79 kN-m, R_{ce} = 7202 kN-m/rad, R_{cp} = 144 kN-m/rad and γ = 0.57. Similarly, for the column-to-base connection C2, whose pilot-test results shown in Figure 4.13 (b), the model parameters are determined to be M_0 = 148 kN-m, R_{ce} = 24721 kN-m/rad, R_{cp} = 151 kN-m/rad and γ = 0.78.

To match the experimental test setup, the loads for the analysis procedure in this study are monotonically increased up to the collapse load level by incrementally changing the horizontal load H, while the vertical loads remain fixed at those shown in Figure 4.12. The beam is divided into three elements, and each column is taken as one element. The analysis results concerning the load-deflection behaviour of joint 6 are given by the solid line in Figure 4.14(a). Also shown are the test results (Liew et al., 1997) and the computed results from a refined plastic hinge analysis method called PHINGE (Chen et al., 1996). It is obvious at lower loading levels (H < 35 kN) that the load-deflection results found by this study (heavy-solid curve) and the PHINGE method (dashed curve) are in good agreement with each other and the test results (dotted curve). At higher loading levels (H > 40 kN), the results of the current study are slightly less than those of the PHINGE method, most likely because the latter method does not account for the influence of elastic shear deformation.

As is shown in the following, the behaviour of the portal frame is such that semi-rigid connection behaviour rather than member inelasticity dominates. The proposed method predicts that the structure collapses at load level H_f = 74 kN, which is close to the value of 77 kN as predicted by the PHINGE method, but both values are considerably less than the 99 kN value found as the limit state by the experimental test. It likely that this discrepancy between experimental and analytical results is as a consequence of the analysis methods using connection behaviour data which were determined by separate pilot experiments (Liew et al., 1997), but which differ from that for the behaviour of the connections in the actual frame itself.

It is evident in Figure 4.14(b) that the development of plasticity at the member ends is not very significant. This occurs because connections C1 and C2 have nominal moment capacities M_n = 82 kN-m and M_n = 151 kN-m, respectively, which are not much greater than yield moment capacities M_y = 100 kN-m and M_y = 134 kN-m of the beam and columns, respectively. Upon referring to the regions defined in Figure 4.5 and discussed in Section 4.3, it is observed that connection C1 is an under-strength connection ($M_n < M_y$) while C2 is a partial-strength connection ($M_y < M_n < M_p$). This is consistent with the plasticity distribution indicated in Figure 4.14 (b), where 6% and 3% plasticity occurs at joints 4 and 5 of the beam, respectively, and only 1% plasticity occurs at the bottom end of the right column.

As summarized in Table 4.4, the C_{26} column base experiences r_p = 100(1-0.994) = 0.6% (≈ 1%) of plasticity. However, the values of connection stiffness degradation factor r_c at the bases of columns C_{13} and C_{26} reduce from their initial value of 0.671 to approximately 0.085; i.e., the degradation factors r_c decrease by about 87% (0.085/0.671–1 = –0.87) compared with their initial values. For the beam-to-column connections, the factor r_c varies from 0.168 to 0.012; i.e., a decrease of about 93%

(0.012/0.168−1 = −0.93). In essence, then, the stiffness degradation factors of the compound beam and column elements are the same as those of the connections, as shown in Table 4.4. These results indicate for a framework with low-strength semi-rigid connections that connection behaviour rather than member plasticity dominates the nonlinear response of the structure.

Also shown in Figure 4.14(a) are two special cases where it is assumed for the portal frame that some or all of the connections are rigid. When both the beam-to-column and beam-to-base connections are rigid, it is observed from the corresponding load-deflection behaviour that the deflection at limit load level H_f = 143.3 kN is only about one-fifth of that for semi-rigid connections. When the beam-to-column connections are assumed to be rigid while the column-to-base connections are pinned, a conventional situation in design, the corresponding load-deflection behaviour is close to that when the connections are semi-rigid, with frame limit load capacity H_f = 82.4 kN. The plasticity behaviour of the frame members at the limit state for the two cases is exhibited in Figure 4.15. From Figure 4.15(a), the case of all rigid connections, four plastic hinges (i.e., 100% plasticity) form in the beam and right column, while the left column base undergoes 52% plasticity under combined axial force and bending moment. The formation of the fourth plastic hinge at node 4 occurs when the horizontal load H_f = 143.3 kN, at which point the frame fails due to inelastic instability signalled by the horizontal displacement of node 6 becoming infinitely large (i.e., the corresponding stiffness coefficient tends to zero and causes the structure stiffness matrix to become singular). From Figure 4.15(b), the case of beam-to-column rigid connections and column-to-base pinned connections, the beam experiences more plastic deformation than the columns. The formation of the plastic hinge at the right end of the beam occurs when the horizontal load reaches H = 77.7 kN. At the limit load level H_f = 82.4 kN, the frame fails due to inelastic instability signalled by the horizontal displacement of node 6 becoming infinitely large (i.e., the same failure mode as for the rigid frame). Table 4.4 indicates the different degrees of member-end stiffness degradation for the case where all connections are semi-rigid, and the two cases where all or some of the connections are rigid.

4.5.2 Example 2: One-Bay Two-Storey Frame

Consider the one-bay two-storey frame with semi-rigid connections in Figure 4.16. This frame has been analyzed and designed previously by Chen et al. (1996) for the loads, member sizes and connections shown in the figure. The least weight frame design was achieved for the following two combinations of dead loads (D_L), live loads (L_L) and wind loads (W_L): $1.2D_L + 1.6L_L$ and $1.3W_L + 1.2D_L + 0.5L_L$ (AISC 2001). The latter load combination was found to govern the design (Chen et al. 1996) and, as such, is alone considered here.

In order to account for the imperfect geometry of the frame, it is assumed that all columns are initially out-of-plumb by $h/400$, where h is the storey height. Connections C1 and C2 have top and seat angles with double web angles, and are represented by a three-parameter model (i.e., $R_{cp} = 0$) using the M_n, R_{cp} and γ parameters given in Table 4.5, which also reports the values of the plastic moment M_p and initial yield moment M_y of the corresponding connected beams. The normalized moment-rotation curves of the two connections are presented in Figure 4.17, where a connection classification system proposed by Bjorhovde et al. (1990) is sketched to demonstrate that both connections are in the semi-rigid category. The rotational demands imposed on the connections by the factored gravity loads are smaller than the corresponding rotational capacity indicated in Figure 4.17 (Chen et al., 1996). That is, the connections have adequate ductility to allow for the full evolution of plasticity in the connection.. According to the discussion in Section 4.3 when the residual stress of a member section is ignored, and as shown in Figure 4.17, the non-dimensional yield stress $m_y = 0.61$ and C2 is an -strength connection while C1 is a partial-strength connection. When the residual stress distribution in the member is taken into account as $\sigma_r = 0.3\sigma_y$, the initial-yield stress $m_{yr} = 0.43$ and C1 and C2 are both partial-strength connections. As a result, in the pure bending case, the roof beam-ends at connections C2 and the floor member ends at connections C1 exhibit plasticity that depends on the residual stress levels.

Upon applying the compound-element analysis method proposed by this study, the lateral load-deflection relationship at node 8 of the frame up to load-factor level $\lambda_f = 1.10$ is found to be the solid-line curve shown in Figure 4.18. Two fully-plastic hinges form at the midspan of the beams. The member-end plasticity ranges between 9% and 22% at the column ends, and between 1% and 11% at the beam ends. To further see the behaviour of the compound connection-beam elements, corresponding stiffness degradation factors r_c, r_p, and r are listed in Table 4.6, as well as initial connection stiffness factors r_{c0}. From this table it is observed that that connection stiffness degrades significantly; e.g., the connection stiffness factor for end E5 of beam B_{45} drops 94% (0.045/0.766–1=–0.94) from its initial value $r_{c0} = 0.766$ to its final value $r_c = 0.045$ It is also observed from the fourth and sixth columns in Table 4.6 that although a beam end such as E5 undergoes 10.9% ($r_p = 0.891$) plasticity, the member stiffness degradation behaviour does not affect the stiffness degradation of the compound elements (i.e., $r_c = r$). This confirms that semi-rigid connections dominate compound-element behaviour when the connection moment capacity M_n is significantly less than the moment capacity M_p of the connected member, as is the case for this framework (see Table 4.5).

The formation of the second plastic hinge at node 7 in Figure 4.18 occurs when the load factor $\lambda = 1.04$. When $\lambda_f = 1.101$, the frame fails due to inelastic instability instigated by the horizontal

displacement of node 8 becoming extremely large. For the purpose of comparison, the dashed-curve in Figure 4.18 is obtained by the PHINGE analysis method (Chen et al., 1996), which finds the load factor $\lambda_f = 1.096$. Obviously, the results from this study and PHINGE are in good agreement.

To consider the difference between a semi-rigid connection design and a conventional rigid connection design, Figure 4.19 also includes the analysis results found by the method proposed in this study for the rigidly-connected frame. Note that the load factor λ_f at collapse increases 6.8% from 1.10 for the frame with semi-rigid connections to 1.18 for the frame with rigid connections. As well, the plasticity formation in the rigid frame is much different than that in the semi-rigid frame. Specifically, five plastic hinges form at the column ends in the rigid connected frame. This demonstrates that the rigid connections transmit substantial bending moments to the columns. Moreover, plasticity increases from about 10% to 100% at the upper column ends, while the plastic hinge section at node 7 in the semi-rigid frame experiences only 73% plasticity in the rigid frame. Similar to that for the semi-rigid frame, the rigid frame fails due to inelastic instability signalled by the horizontal displacement of node 8 becoming extremely large.

4.5.3 Example 3: Two-Bay Two-Storey Frame

The third example illustrated in Figure 4.20 is a two-bay by two-storey frame with semi-rigid connections, which was previously analyzed in Section 3.5.2 with rigid connections. The loads shown in Figure 4.20 are at the design load level for the frame. The frame is investigated here to demonstrate the effect of semi-rigid connections on structural response up to failure. Two connection cases are analyzed: (1) under-strength semi-rigid connections, and (2) fully-rigid connections.

In the first case, the two connection curves from Example 2 in Section 4.5.2 are applied to the frame in Figure 4.20. The connection model parameters for all floor beam-to-column connections C1 and C2 assume the values in the second row of Table 4.5, while the parameters for all roof beam-to-column connections C3 and C4 are those in the third row of Table 4.5. According to the member M_p moment values given in the second column of Table 4.7, and the connection M_n moment values given in the fourth column of Table 4.5, the frame has under-strength connections because $M_n < M_y$ (= 0.7 M_p/1.15, assuming residual stress $0.3\sigma_y$ and shape factor 1.15 for the W-section). From the stiffness criteria defined in Eqs. (4.3.1) and (4.3.3), and the r_{c0} values given in the third column of Table 4.8, all the connections are categorized as being semi-rigid because $0.143 < r_{c0} < 0.893$.

Upon applying the compound-element analysis method, the semi-rigid frame was found to collapse when the load factor reached $\lambda_f = 0.688$ (i.e., at 68.8% of the specified nominal design load level), as indicated by the heavy solid-line curve in Figure 4.21. To consider the difference between the semi-

rigid connection design and conventional rigid connection design, the analysis results obtained by other methods for rigid connections are also indicated in Figure 4.21. It is seen from the figure that the collapse-load factor λ_f decreases by 36.3% from 1.08 for the rigid frame to 0.688 for the semi-rigid frame, and that large lateral translation occurs for the semi-rigid frame. In addition to the significant changes in the loading capacity, the plasticity formation in Figure 4.22 for the semi-rigid frame varies substantially from that for the rigid frame (see Figure 3.15). Because of the under-strength semi-rigid connections, all of the member ends at the connections do not undergo any plasticity, as indicated in the fifth column of Table 4.8. However, the connection stiffness factors associated with the beams in the right large-span bay drop almost to zero, as shown in column four of Table 4.8. The factors relevant to the left short-span bay drop by about 24~63% when the r_c values in column four are compared with the r values in column six of Table 4.8, it is noted that the compound element behaviour is dominated by that of the under-strength connections. Similar to the failure mode of the frames in the previous two examples, the 2-bay by 2-storey frame fails at load factor level λ_f = 0.688 due to inelastic instability signalled by the horizontal displacement of node 9 becoming extremely large.

From the load-deflection response designated by the heavy solid-line curve in Figure 4.21, the flexibility of the frame increases considerably when the connections are semi-rigid. As such, serviceability design requirements might not be satisfied due to excessive deflections. To enhance the stiffness and strength of the frame, stiffer connections are now selected while maintaining all the same member properties. Specifically, the parameters of the moment-rotation connections in the last three columns of Table 4.7 are chosen for the structural analysis. (The four parameters for each connection in Table 4.7 are obtained from the research of Kishi et al. (2004) concerning extended end-plate connections). According to the member M_p and connection M_n values in the second and third columns of Table 4.7, the connections C1, C2, C3 and C4 are categorized as being full-strength. Also, from the r_{c0} values in column seven of Table 4.8, and the criteria in Eqs. (4.2.13), all of the connections are categorized as being fully-rigid.

After conducting the non-linear analysis for the fully-rigid frame, the plasticity distribution for the members, the lateral load-deflection curve at joint 9, and the degradation factors corresponding to the connections, are found to be as given in Figure 4.23, Figure 4.21 and Table 4.8, respectively. These results reveal the following structural behaviour. First, the loading capacity of the fully-rigid frame is the same λ_f = 1.08 value as for the conventional rigid frame, as indicated in Figure 4.21. Secondly, the structural stiffness of the fully-rigid frame is considerably greater than that of the semi-rigid frame, and approaches the stiffness of the conventional rigid frame. From Figure 4.21, the heavy

dotted-line load-deflection curve at joint 9 of the fully-rigid frame almost coincides with the curve of the rigid frame when the load factor λ is below 0.6. Unlike the load-deflection behaviour of the conventional rigid frame, however, there is no sudden kink transition as the external loading approaches the limit state. Thirdly, the plasticity distribution of the fully-rigid frame is much different from that of the semi-rigid frame in Figure 4.22, but close to that of the conventional rigid frame. For the fully-rigid frame, plastic hinges appear at the top end of column C_{25}, the top and bottom ends of column C_{69}, and the midspan of beam B_{56}, as indicated in Figure 4.23, while the three plastic hinges shown in Figure 4.22 for the semi-rigid frame no longer appear. More importantly, as indicated in Figure 4.23, plasticity now appears at the beam member ends linked to the stiffer fully-rigid connections. Upon comparing Figure 4.23 with Figure 3.15, it is observed that all the columns have similar plasticity behaviour except for the different order of the plastic hinge formation. However, a significant difference between the plasticity formation in these two figures is observed for the compound elements where plasticity occurs; more detailed information in this regard is shown by the r_p and r values in the ninth and last columns of Table 4.8. For instance, end E5 of beam B_{45} has a considerable difference in stiffness factors, ranging from $r_p = 0.392$ for the fully-rigid connection to $r = 0.00$ for the conventional rigid connection. Finally, after the formation of the fourth plastic hinge at the midspan of beam B_{56} occurs at load factor $\lambda_f = 1.08$, the frame fails due to inelastic instability without a sudden change of the force-deflection relation like that for the rigid frame in Figure 4.21.

4.6 Final commentary

The member-connection compound element developed in this chapter is used in Chapter 5 to investigate the influence that both damaged connections and semi-rigid connections have on the capacity of framework structures to resist progressive collapse failure under abnormal loading.

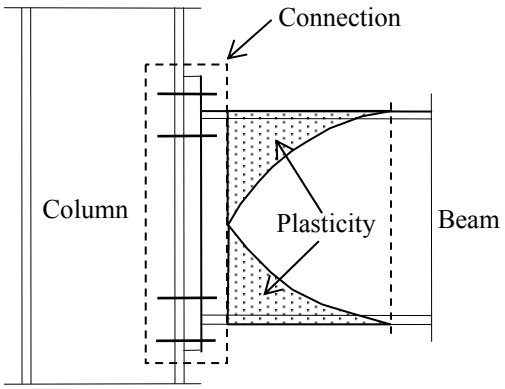

(a) Actual connection with member bending plasticity

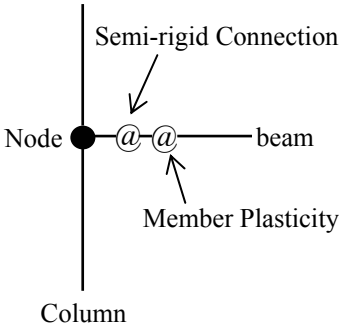

(b) Analytical model

Figure 4.1 Semi-rigid connection and member-inelasticity model

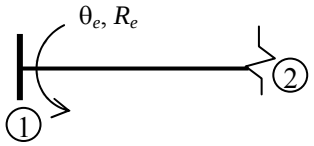

(a) Conventional end

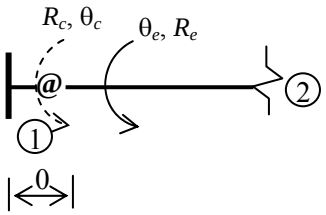

(b) Semi-rigid connection

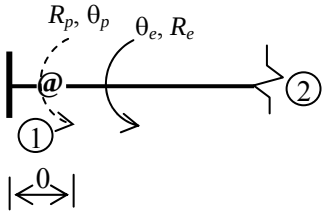

(c) Inelastic spring

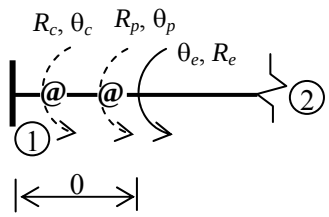

(d) Series elements

Figure 4.2 Four types of member ends and connection models

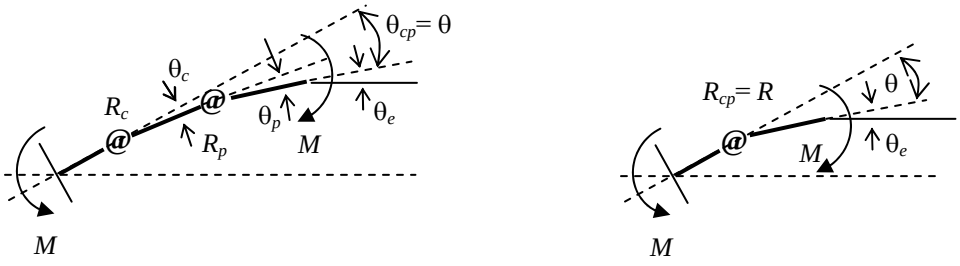

Figure 4.3 Compound element replaces the elements in series

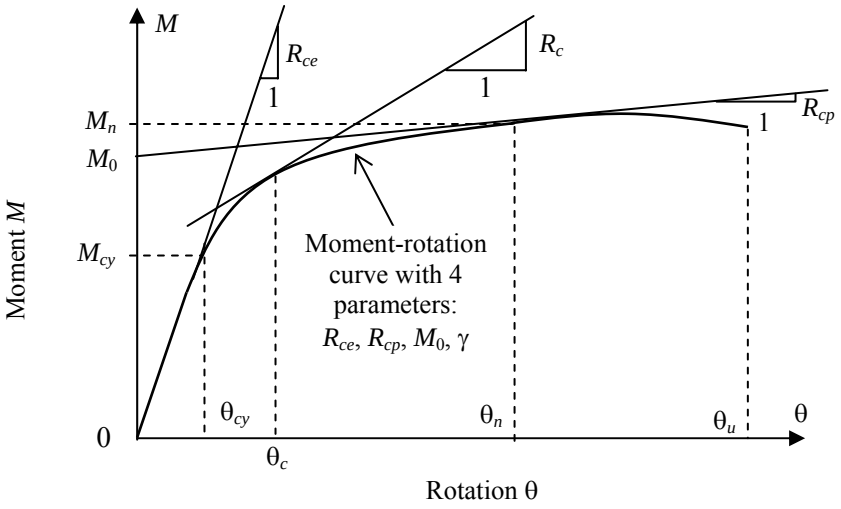

Figure 4.4 Four-parameter model of semi-rigid connections

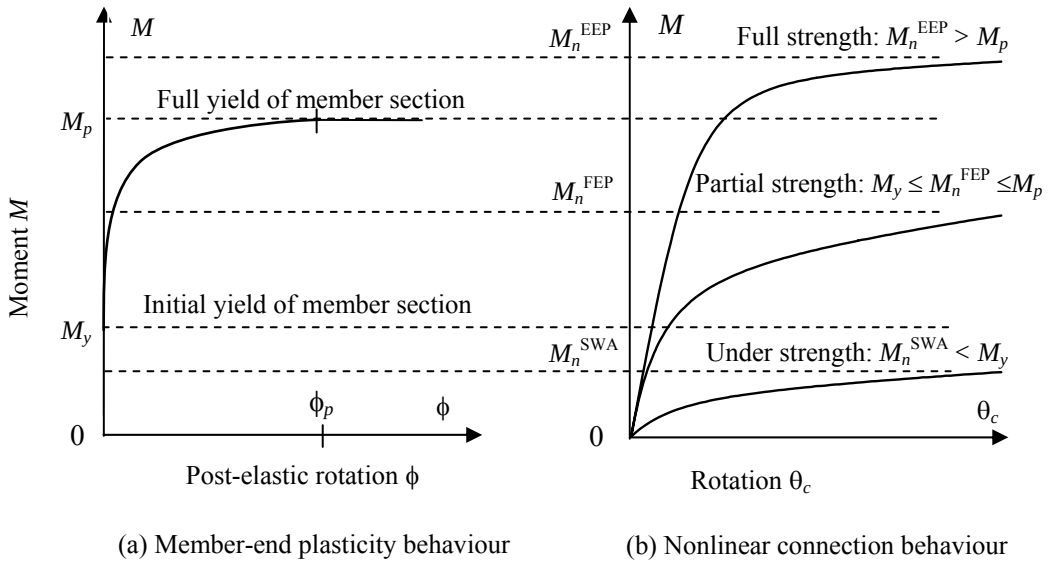

(a) Member-end plasticity behaviour (b) Nonlinear connection behaviour

Figure 4.5 Stiffness degradation relationships at a member end

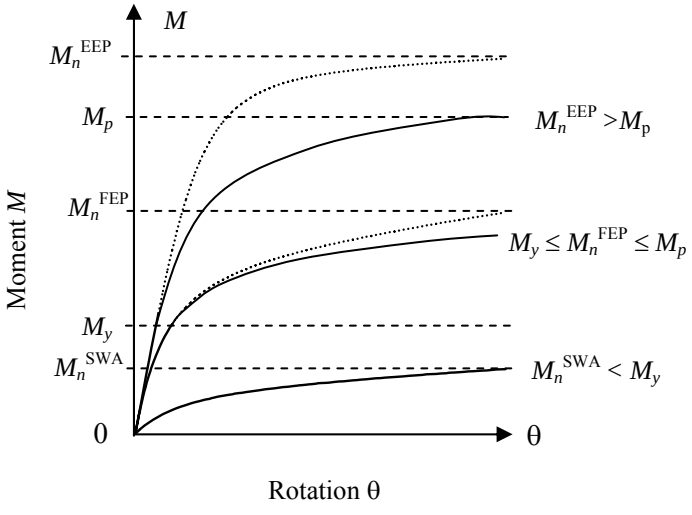

Figure 4.6 Combined moment-rotation relationships for a compound element

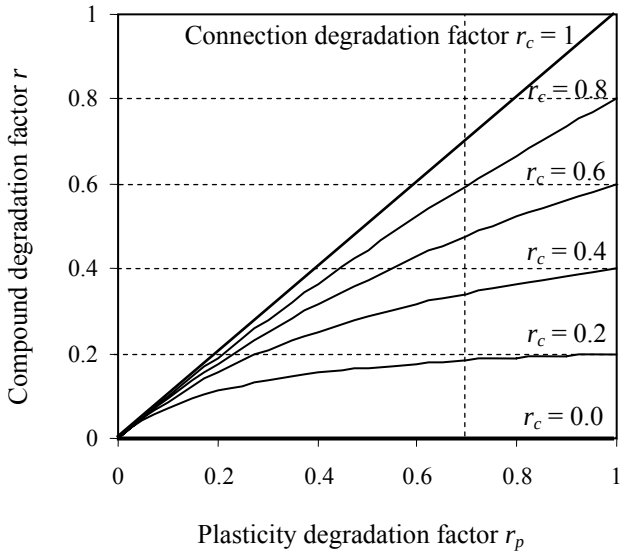

Figure 4.7 Relationship between the degradation factors for a compound element

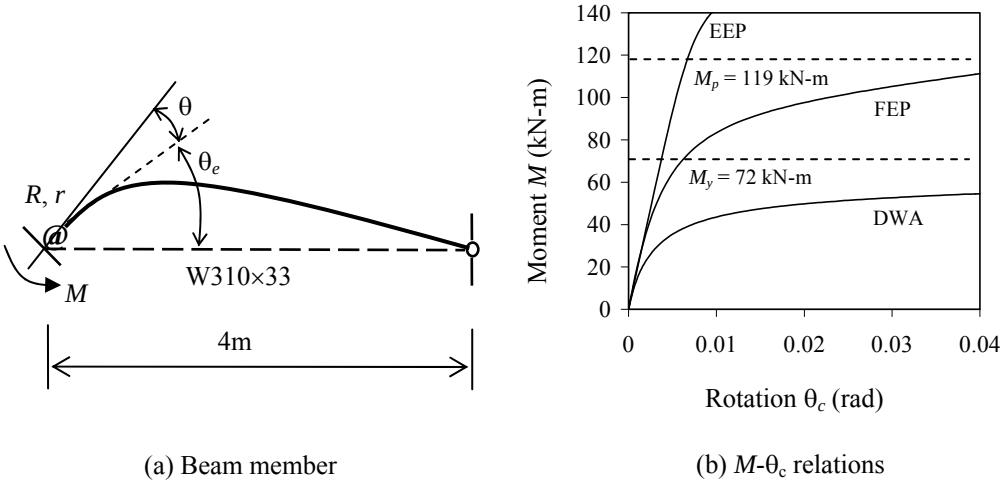

(a) Beam member

(b) M-θ_c relations

Figure 4.8 Simple beam structure with semi-rigid connections

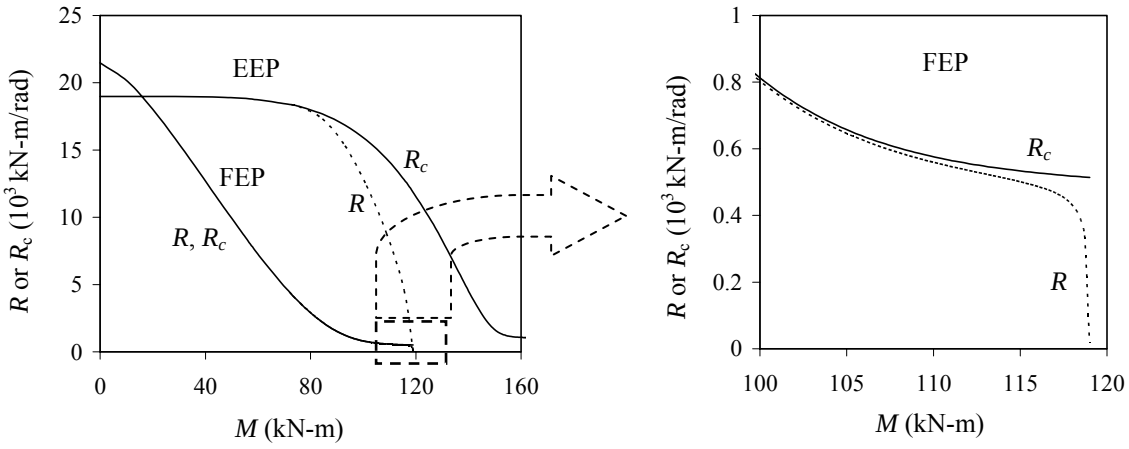

(a) Stiffness for EEP and FEP

(b) Enlarged portion for FEP

Figure 4.9 Stiffness degradation behaviour of different compound elements

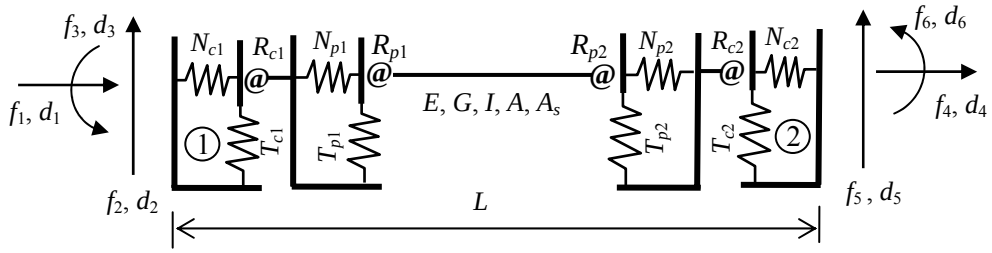

(a) Elements in series

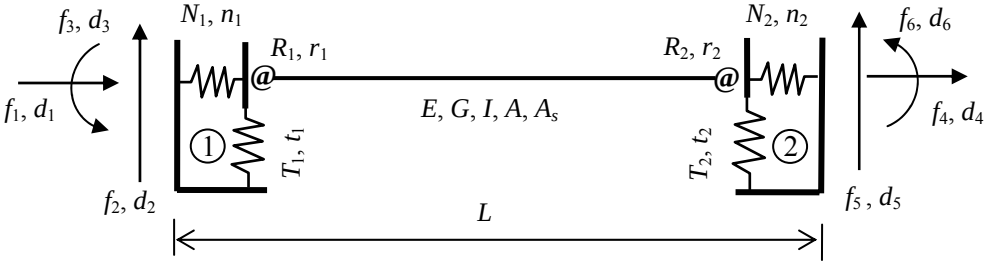

(b) Compound element

Figure 4.10 Compound model of beam-column member

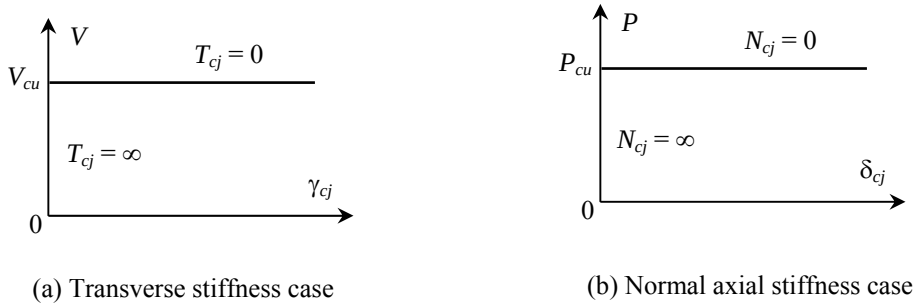

(a) Transverse stiffness case

(b) Normal axial stiffness case

Figure 4.11 Idealized force-displacement relations for transverse and axial connections

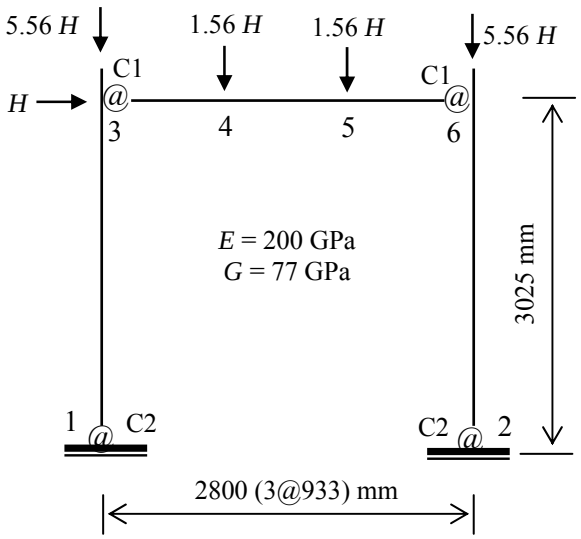

Figure 4.12 Example 1: Portal frame (Liew et al., 1997)

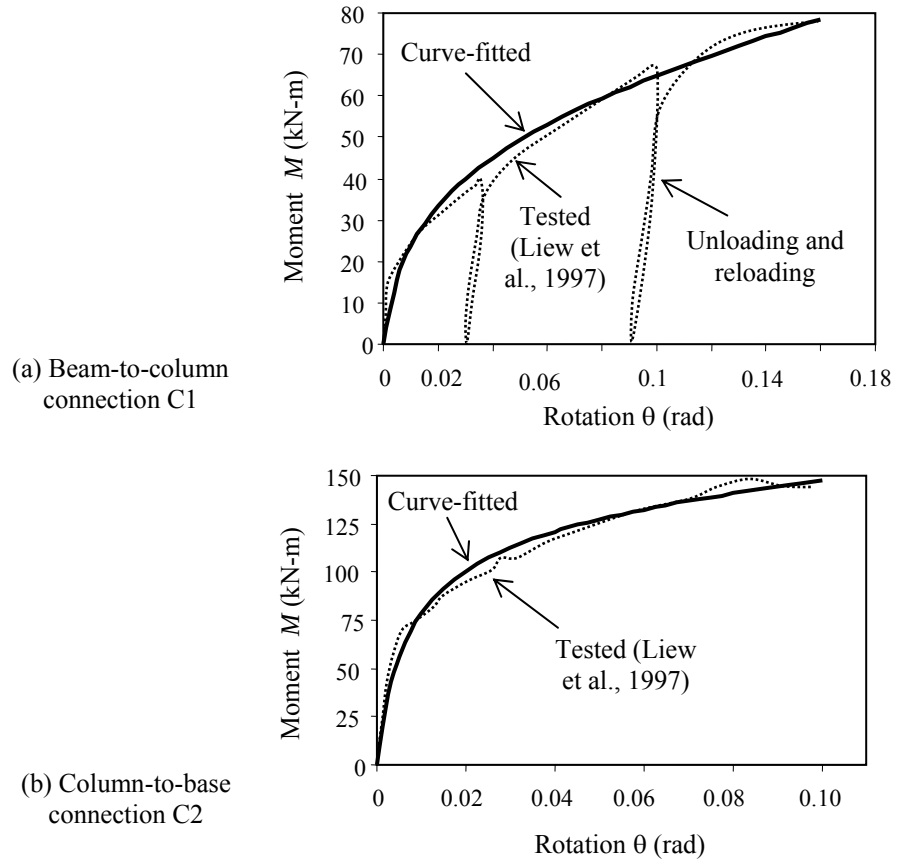

Figure 4.13 Example 1: Moment-rotation relations for connections

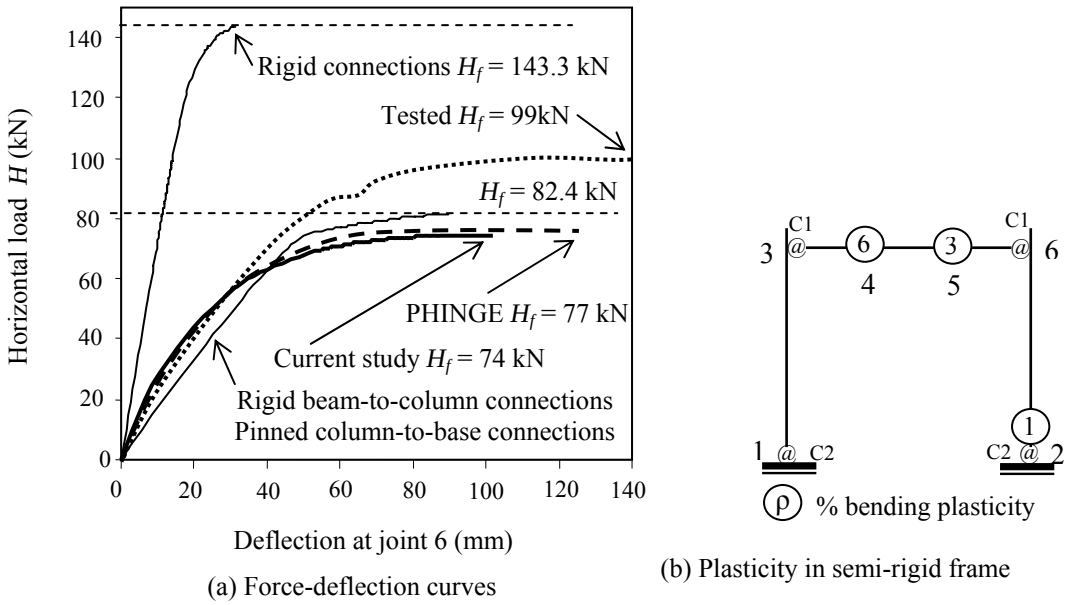

Figure 4.14 Example 1: Load-deflection responses and plasticity formation

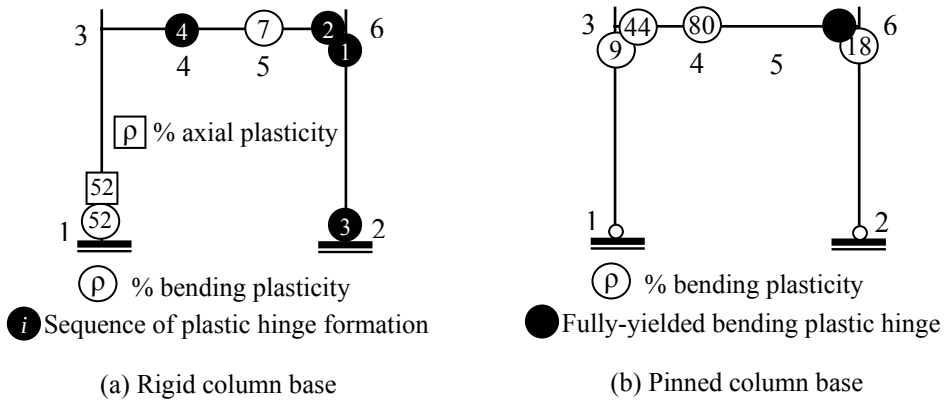

Figure 4.15 Plasticity behaviour of rigid frame with different supports

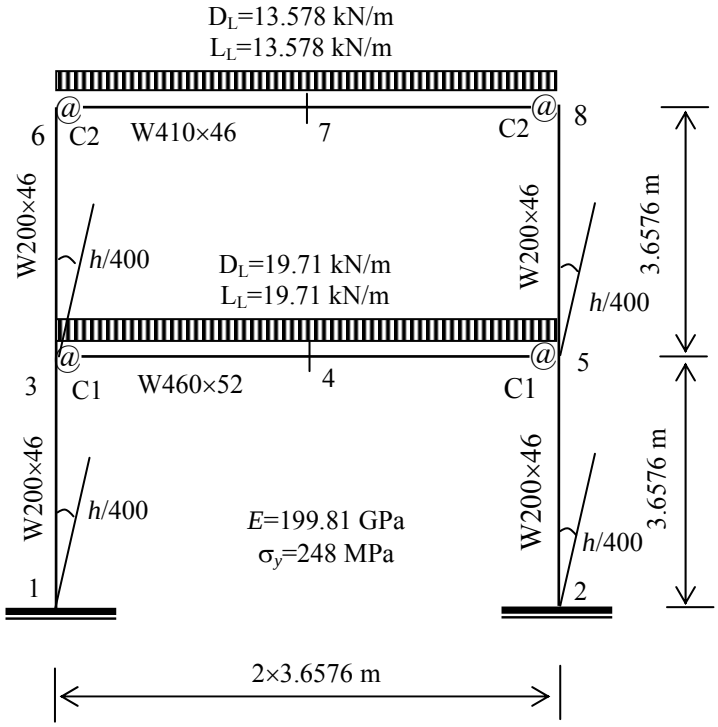

Figure 4.16 Example 2: One-bay by two-storey frame (Chen et al., 1996)

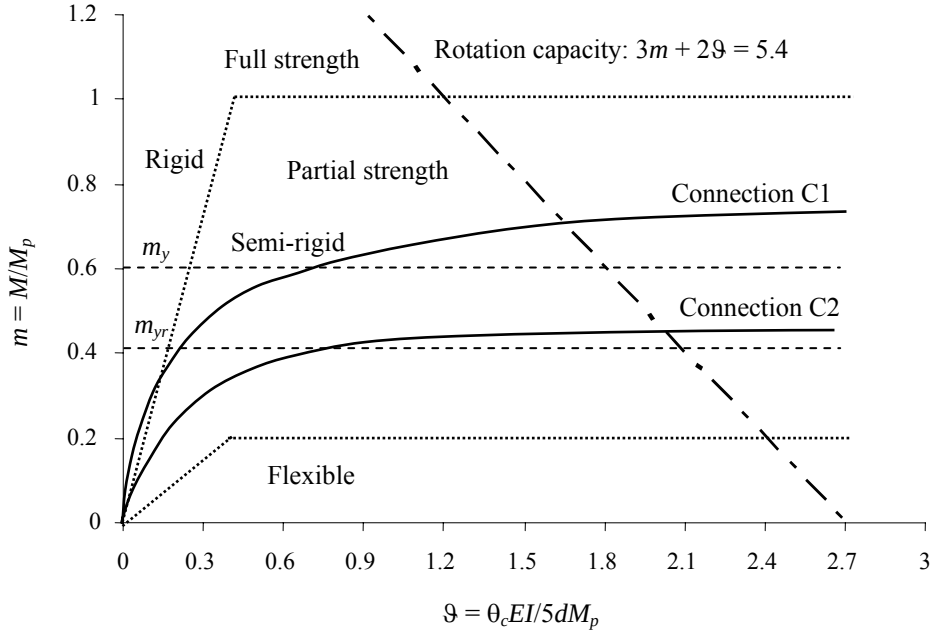

Figure 4.17 Example 2: Categories of connections

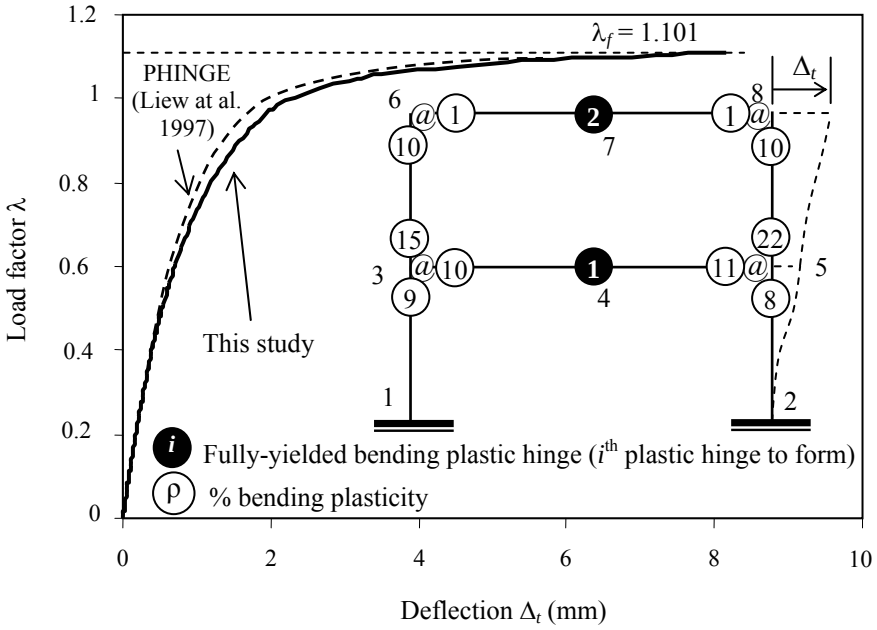

Figure 4.18 Example 2: Comparison with PHINGE (Liew at al. 1997)

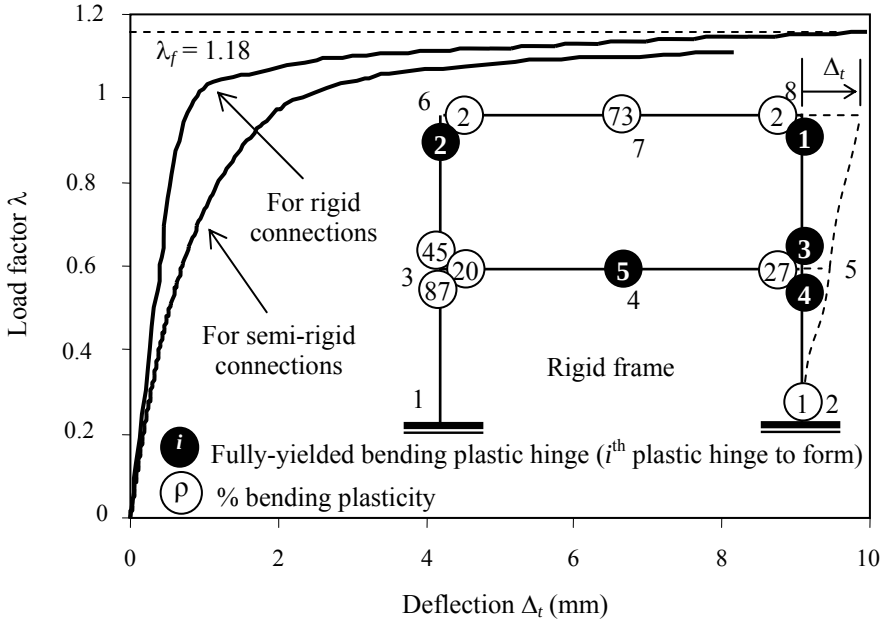

Figure 4.19 Example 2: Comparison with rigid connection analysis

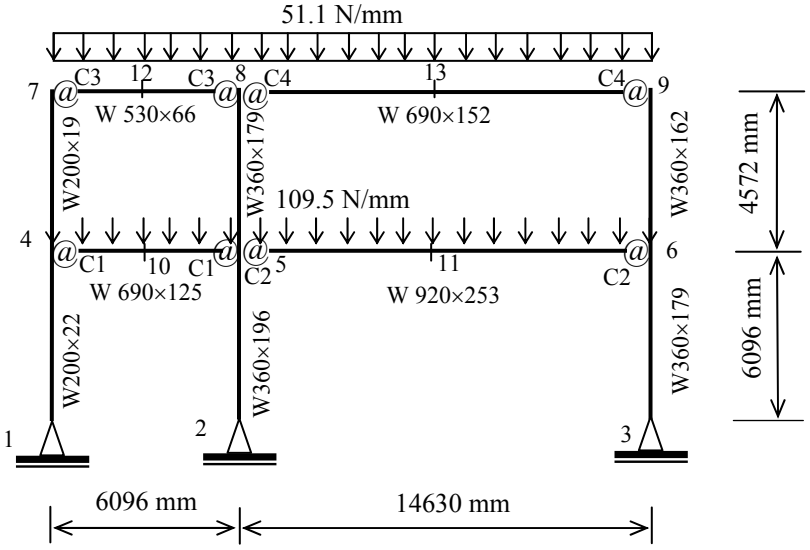

Figure 4.20 Example 3: Frame and service-level design gravity loading (Ziemian et al., 1992)

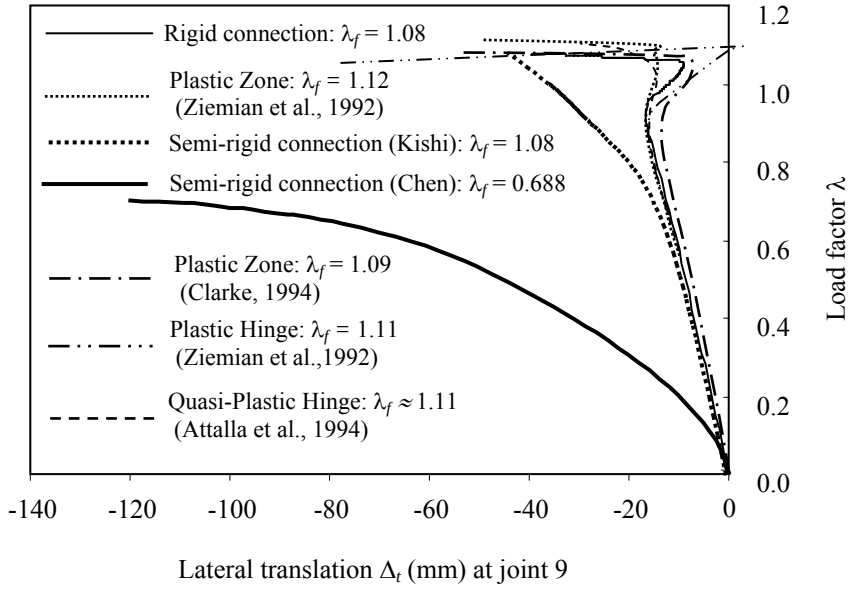

Figure 4.21 Example 3: Comparison with rigid-connection analysis

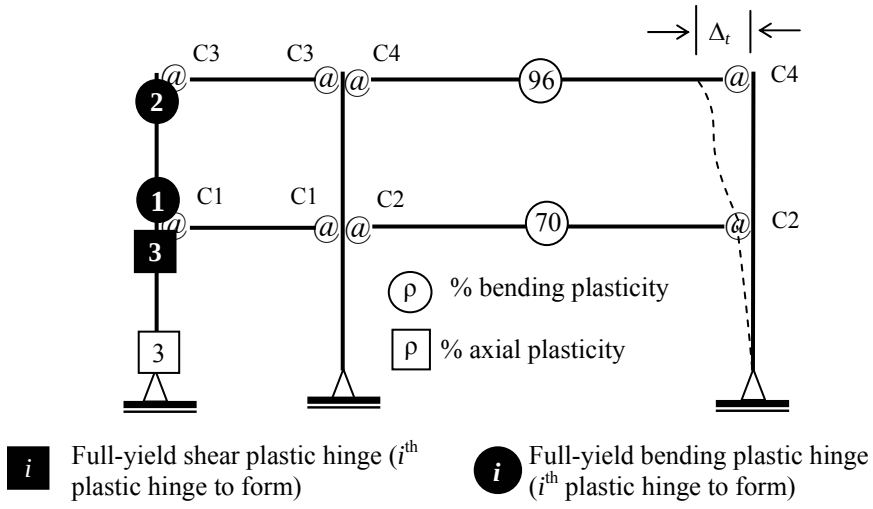

Figure 4.22 Example 3: Plasticity at failure load-factor level $\lambda_f = 0.694$

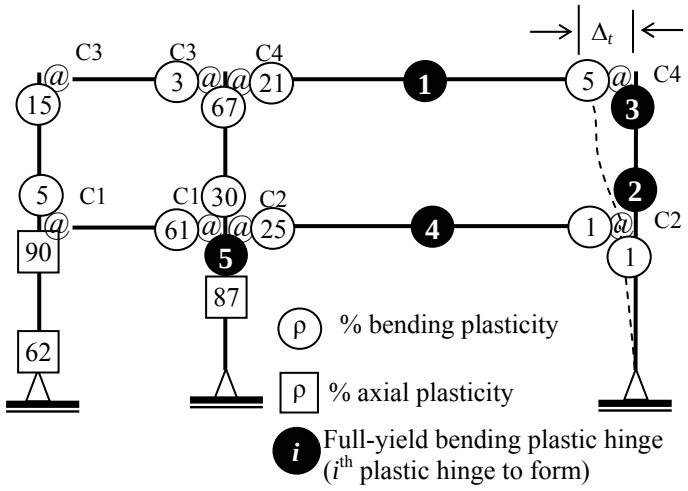

Figure 4.23 Example 3: Plasticity at failure load-factor level λ_f = 1.08

Table 4.1 Parameters for specified connections

Connection	M_0 (kN-m)	R_{ce} (kN-m/rad)	R_{cp} (kN-m/rad)	γ
DWA	55.935	20114	69.608	0.964
FEP	95.146	21470	468.95	1.45
EEP	137.86	18984	1041.86	5.11

Table 4.2 Results for EEP connection

M (kN)	R_p (kN-m/rad)	R_c (kN-m/rad)	R (kN-m/rad)	r_p	r_c	r
0		18984	18984		0.661	0.661
9		18984	18984		0.661	0.661
19		18983	18983		0.661	0.661
28		18979	18979		0.661	0.661
38		18962	18962		0.660	0.660
47		18915	18915		0.660	0.660
57		18810	18810		0.659	0.659
73	4732880719	18376	18375	1.000	0.653	0.653
75	39559835	18249	18241	1.000	0.652	0.652
84	838297	17683	17318	0.989	0.645	0.640
93	167474	16857	15315	0.945	0.634	0.611
101	57301	15745	12351	0.855	0.618	0.559
109	22861	14366	8822	0.701	0.596	0.475
116	7139	12786	4581	0.423	0.567	0.320
119	0	11861	0	0.000	0.549	0.000

Table 4.3 Results for FEP connection

M (kN)	R_p (kN-m/rad)	R_c (kN-m/rad)	R (kN-m/rad)	r_p	r_c	r
0		21470			0.688	0.688
10		20094			0.673	0.673
20		18026			0.649	0.649
28		15873			0.619	0.619
36		13853			0.587	0.587
42		12050			0.553	0.553
48		10483			0.518	0.518
56		8323			0.461	0.461
57		8000			0.451	0.451
61		7033			0.419	0.419
64		6214			0.389	0.389
67		5518			0.361	0.361
70		4926			0.336	0.336

72	Infinity	4420	4420	1.000	0.312	0.312
90	274191	1524	1516	0.966	0.135	0.135
95	125900	1082	1073	0.928	0.100	0.099
100	68670	822	813	0.876	0.078	0.077
105	38651	668	657	0.799	0.064	0.063
110	20013	579	562	0.672	0.056	0.055
115	9206	537	507	0.486	0.052	0.049
116	7157	530	494	0.423	0.052	0.048
117	5187	525	476	0.347	0.051	0.047
118	3213	520	447	0.248	0.051	0.044
119	0	514	0	0.000	0.050	0.000

Table 4.4 Example 1: Stiffness degradation factors

Member	End	Semi-rigid				Rigid	
		Initial: r_{c0}	r_c	r_p	r	Case 1: r	Case 2: r
C_{13}	E1	0.671	0.085	0.998	0.085	0.482	-
C_{26}	E2	0.671	0.084	0.994	0.084	0.000	-
B_{34}	E3	0.168	0.019	1.000	0.019	1.000	0.572
B_{56}	E6	0.168	0.012	1.000	0.012	0.000	0.000

Table 4.5 Example 2: Semi-rigid connection parameters (Chen et al., 1996)

Connection	M_p (kN-m)	M_y (kN-m)	M_n (kN-m)	R_{ce} (kN-m/rad)	R_{cp}	γ
C1	270	164	200	107804	0	0.81
C2	219	134	92	23269	0	1.27

Table 4.6 Example 2: Stiffness degradation factors

Beam	End	Semi-rigid				Rigid
		Initial r_{c0}	r_c	r_p	r	r
B_{34}	E3	0.766	0.055	0.901	0.054	0.798
B_{45}	E5	0.766	0.045	0.891	0.044	0.737
B_{67}	E6	0.490	0.005	0.991	0.005	0.982
B_{78}	E8	0.490	0.004	0.991	0.004	0.983

Table 4.7 Example 3: Semi-rigid connection parameters (Kishi et al. 2004)

Connection	M_p (kN-m)	M_n (kN-m)	R_{ce} (kN-m/rad)	R_{cp} (kN-m/rad)	γ
C1 (CF6-U12x96)	995	1736	1240000	56900	1.39
C2 (EP8 with shim)	2773	3252	15300000	81600	1.20
C3 (CF5-U10x49)	387	867	893000	30300	1.18
C4 (CF5-U10x68)	1240	1494	1020000	46100	1.69

Table 4.8 Example 3: Stiffness degradation factors

Beam	End	Semi-rigid				Fully-rigid				Rigid
		r_{c0}	r_c	r_p	r	r_{c0}	r_c	r_p	r	r
B_{45}	E4	0.315	0.131	1.000	0.131	0.914	0.837	1.000	0.837	1.000
B_{45}	E5	0.315	0.117	1.000	0.117	0.914	0.206	0.392	0.156	0.000
B_{56}	E5	0.231	0.002	1.000	0.002	0.988	0.200	0.752	0.188	0.847
B_{56}	E6	0.231	0.013	1.000	0.013	0.988	0.514	0.988	0.511	1.000
B_{78}	E7	0.252	0.134	1.000	0.134	0.963	0.834	1.000	0.834	1.000
B_{78}	E8	0.252	0.192	1.000	0.192	0.963	0.051	0.966	0.051	0.000
B_{89}	E8	0.158	0.001	1.000	0.001	0.943	0.197	0.792	0.187	0.891
B_{89}	E9	0.158	0.009	1.000	0.009	0.943	0.197	0.952	0.195	0.952

Chapter 5
Progressive-Failure Analysis

A method for progressive-failure analysis is presented in this chapter. The objective is to evaluate the performance of a building framework after it has been damaged by an abnormal loading event. These include an impact or blast load caused by a natural, accidental or deliberate event, or as a result of human errors in design and construction. To begin, it is assumed that some type of short-duration abnormal loading has already caused some form of local damage to the structure. The local damage is simulated by removing one or more critical member(s) as recommended by the Alternate-load Path (AP) analysis method suggested in published guidelines (GSA, 2003; DoD, 2005). The residual load-carrying capacity of the remaining framework is then analyzed by incrementally applying the prevailing long-term loads and any impact debris loads. Specifically, the strength deterioration of the structure is progressively traced until either a globally stable state is reached or progressive collapse occurs for part or all of the structure. A constitutive model for structural steel is adopted to account for elastic-plastic behaviour due to single or combined stress states. The progressive-failure analysis procedure is illustrated for four planar steel moment frameworks subjected to abnormal loading.

5.1 Local Failure Modes and Debris Loading

For analysis under normal loading, the focus is on determining the loading capacity of the structure corresponding to plastic collapse or instability, and not on the structural failure modes themselves. However, under abnormal loading, knowledge of any localized failure modes is critical to the progressive collapse analysis of the structure. For example, if the failure mode is a local mechanism, the damaged structure may be able to further carry loads, including debris loading resulting from the damage. This section investigates local failure modes associated with member removal and the creation of debris loading.

5.1.1 Failure Modes of Components

As discussed in Chapter 1, project failures can be categorized as foreseen and unforeseen. Typically, the causes are classified in three categories: faulty considerations during design, incorrect procedures or misinterpretation of design intention during construction, and misuse or sabotage during operation conditions. Whatever the causes are, structural failure can be a ductile collapse involving excessive deformation, brittle fracture with insignificant deformation, fatigue under cyclical loading, or creep due to high-temperature fire. From the structural perspective, two categories of failure have been

defined: instability and plastic collapse. Usually, instability failure is related to the geometrical deterioration of a structural system for which the material behaviour is either elastic or plastic, whereas plastic collapse is related to the post-elastic strength deterioration of members of the structure such as to create a movable mechanism. This subsection addresses the failure modes of structural components, including connections and members.

As described in Chapters 2 and 3, for this investigation the failure of a member at a critical section involves bending, shearing and axial stiffness degradation tracked along an elliptic curve from initial yield to full plasticity. Similar to section failure, and as described in Chapter 4, the rotational failure of a semi-rigid connection is modeled by a four-parameter model that accounts for strain hardening or softening.

Figure 5.1 illustrates the failure of connections recovered from the WTC 5 building that partially collapsed on September 11, 2001 (FEMA, 2002). Figure 5.1(a) shows a failed connection from the 7^{th} floor of the building. It is observed that the main failure feature is tear-out at the bolt locations in the web of the connected beam, and that substantial rotational, shearing and axial deformation occurs during the failure process. Figure 5.1(b) shows a second failed connection recovered from the 8^{th} floor of the WTC 5 building. The failure mode is different from that in Figure 5.1(a), and is due to shearing fracture caused by tear-out of the bolts for the single-angle web connection plate. It is observed that the failure also involves significant axial deformation. These samples of failed connections indicate that the failure model for semi-rigid connections proposed in Chapter 4 is conceptually appropriate.

Generally, connection or member section failure results in the formation of a local mechanism for a structural beam-column member. Three types of member failure modes are described in the following. The first local failure mode is the cantilever failure in Figure 5.2(a), where member-end section A undergoes ultimate rotation θ_u corresponding to the formation of a fully plastic hinge. Rigid-body displacement of the member occurs as the plastic hinge deforms. If member section A is perfectly ductile, the plastic hinge behaves like a common hinge and member AB does not separate from connection joint A. In this case, a point debris load may be generated when end B of the member impacts on the floor below. Even for a ductile structure, however, it is possible for fracture failure to occur when the rotational deformation becomes large to the point that the tension-side top fibers of the beam section are torn while the compression-side bottom fibres are crushed. When this occurs, member AB disengages from the structure at end A to create a distributed debris load that falls on the floor member immediately beneath it. (The dynamic effect of such debris loading is discussed later in this chapter).

When a member is separated from its connected joint, the disengagement condition depends on the ultimate rotation θ_u, which can be determined from the failure criteria for structural members adopted in design standards and guidelines (e.g., DoD, 2005; ASCE, 1997; TM5-1300, 1990). For instance, the document UFC-023-03 (DoD 2005) provides the deformation limits for structural steel given in Table 5.1. It is seen from the table, for example, that beams with seismic sections have ductility of 20 (ratio of full-yield to initial-yield deformations) and rotation capacity of 12° for low level of protection (LLOP), and 10 and 6° for both medium level of protection (MLOP) and high level of protection (HLOP). In this study, it is assumed that a member section disengages from the structure when it reaches its deformation limit listed in Table 5.1.

The second local failure mode considered by this study is the catenary failure shown in Figure 5.2(b). After the formation of the three plastic hinges at the end-sections and midspan of the beam, a mechanism involving significant transverse deformation is developed. Such catenary deformation causes increased axial force in the member. The catenary load-transfer function of the member is achieved if its axial strength offers sufficient resistance to this increased load. However, if the axial strength is insufficient the member will disengage from one or both of its connections at ends A and B, either by tearing-out fracture of the connections or by rupture of the member. In this study, it is assumed that after a local plastic-collapse mechanism forms and the plastic rotations at both member ends reach their deformation limits given in Table 5.1, the whole member disengages from the structure and falls as debris loading on the member just below it. In the progressive-failure analysis, catenary action is accounted for through the interaction between axial force and displacement.

The third local failure mode considered by this study is the shear failure shown in Figure 5.2(c). Punching shear failure is an important consideration in the design of concrete structures, while concern for shear failure in most steel structures is relatively unimportant. However, shear failure due to severe short-duration dynamic loads is recognized as a principle factor contributing to member collapse, regardless of the material type (Jones, 1995). Dynamic shear failure depends on the loading speed and intensity. It is important to consider dynamic shear failure as possible whenever there is blast or debris impact loading, because the corresponding shear force can be many times that for a member under static loading. It is assumed by this study that once the shear capacity at both ends of a member has been exceeded, the entire member disengages from its supports (as shown by the dashed line in Figure 5.2 (c)) and impacts as debris loading on the member beneath it.

5.1.2 Impact Debris Loading

When local collapse occurs as discussed in the previous subsection, the disengaged portions fall as debris loads on the remaining structure. Experiments confirm that with the increase of strain rate or loading speed, the material yield stress increases and approaches the ultimate stress state (Manjoine, 1944; ASCE, 1997). This implies that even a ductile material such as mild steel can experience brittle failure under high-velocity impact loading. Nonlinear dynamic analysis offers a reasonably accurate prediction of structural response under impact loading. However, a quasi-static analysis proves to be simpler and in good agreement with test results when the impact velocities do not exceed 12 m/s (Jones, 1995). In the current study, the impact velocities of the debris loads generally do not exceed this limit, and it is presumed reasonable to employ a quasi-static method of analysis to determine structural response under impact debris loading.

To account for the impact effect of debris loads, a dynamic amplification factor is introduced into the structural analysis. Existing design guidelines for dealing with impact debris loads suggest several methods to estimate impact forces. For instance: FEMA-259 (1995) suggests designers employ an impulse-momentum method; the Australian highway bridge design specification (NAASRA, 1990) suggests a work-energy method; and the American LRFD-specifications for bridge design (AASHTO, 1998) suggests a contact-stiffness method. In the design of shelter structures, the FEMA-361 (2000) guidelines include the effect of falling debris caused by extreme wind loads. Determining equivalent static design loads corresponding to free-falling debris is a complicated problem that is dependent on material properties, stiffness of impacted structure and impact angle between the debris and structure.

The effect of falling debris loading on the progressive collapse of structures is yet to be discussed in either analysis or design guidelines. Determining the impact effect of debris loading is a complicated process involving an inelastic dynamic analysis of the structure, which is beyond the scope of this study. Instead, the approach taken herein is to determine the magnitude of the impact amplification factor for which progressive collapse occurs.

5.2 Damage Degree due to Local Collapse

Once any one of the three types of local collapse discussed in the previous section occurs, severe local damage of the structure ensues due to the disengagement of failed member(s). Although recent design/analysis guidelines (DoD, 2005; GSA, 2003) suggest such local damage to the structure can be ignored for simplicity, the disengagement of failed member(s) can significantly affect further structural behaviour. To investigate the influence of the localized damage, an analytical approach is

proposed in this study for modeling damaged portions of a structure that experience member removal and associated connection damage.

To assess the residual strength of a structure damaged by excessive loading, test methods can be used to objectively identify the extent of damage. For instance, destructive and non-destructive test techniques are suggested in the FEMA-267 (1995) interim guidelines to evaluate moment-frame steel structures after extreme earthquakes. If there is no existing data regarding the material properties, sample elements taken from critical locations of the damaged structure should undergo laboratory testing to determine tensile/compressive strength, etc. Because such specimen extraction can conceivably further affect or even destroy the damaged structure, non-destructive test methods should be used if possible. For steel structures, the ultrasonic pulse velocity method is often adopted to determine the size, thickness, and material uniformity quickly and accurately (FEMA-267, 1995). The in-place Rockwell and Brinnell hardness testers can be utilized to identify tensile strength and grade of steel (Carden & Fanning, 2004). The radioactive method and the magnetic particle method can be used to inspect properties of the welds and connections (FEMA-267, 1995).

To augment the data obtained from local test methods, structure-based test methods can also be applied to obtain information about the damaged structure. Such methods quantify the stiffness of the structural components by applying input and output dynamic signals defined by a dynamic structural analysis. Diagnostic analysis focuses on identifying what is wrong in the system under consideration, whereas prognostic analysis focuses on predicting what is going to happen in the future due to some damage factors. Some state-of-the-art aspects of such analyses have been presented in the technical literature. For instance, a method illustrated for a cantilever beam can predict real-time remaining life by using non-linear dynamic analysis to track the damage evolution (Nataraju et al., 2005). A method which uses correlating numerical models to measure the modal properties of undamaged and damaged components can effectively predict the behaviour of aerospace and offshore structures (Carden & Fanning, 2004). To classify the damage behaviour of a system, experiments for a three-storey building frame model have been carried out to identify the extent of damage to steel connections (Adams & Farrar 2002). Much research in this area has focused on developing techniques for damage assessment through non-destructive evaluation of structural systems. A method of prognostics has been developed to predict the remaining useful life of a structure, with account for damage accumulation (Engel et al., 2000).

It should be pointed out that structural identification is an inverse problem that is quite complex in that both geometric and material nonlinearities must be taken into account. In this study, it is assumed that the initial stiffness degradation data for a locally damaged structure are known by using the

aforementioned diagnostics techniques, and that subsequent prognostics is investigated by progressive-failure analysis; that is, known information about the local damage state is utilized to estimate the remaining life or residual capacity of the damaged system.

5.2.1 Connection damage

Often, connection failures have been observed to trigger the progressive collapse of building structures (Griffiths et al., 1968; FEMA, 2002). That said, however, current analysis guidelines for conducting alternate-load path analysis (GSA 2003 and DoD 2005) assume that structural members fail without any damage to their end-joint connections. A more likely scenario is that a connection is also damaged when a member disengages from it, and that the connection damage influences the ensuing behaviour of the remaining structure. That being the case, a progressive-failure analysis should take connection damage into account if it is to reasonably predict the behaviour of structures subjected to abnormal loading. To that end, this study proposes in the following to employ connection stiffness as measure of connection damage. This is in keeping with conventional structural health monitoring, where the stiffness of a component is considered representative of its health condition (Wang & Haldar, 1997; Koh et al., 2003). Typically, a health condition index h equal to the ratio of damaged-to-undamaged stiffness is adopted as a measure of the severity of component damage (Kol et al., 2003); i.e., $h = 1$ signifies no damage, while at the other extreme $h = 0$ signifies complete damage.

As a member is removed, the two joints connected to the failed member are likely to undergo some damage caused by the removal. In fact, all member-ends connected to the two joints of the remaining structure are likely to undergo local damage. To take such local damage into account, two cases of stiffness deduction are considered in this study. For a fully-rigid joint, the level of connection damage is assumed to modify the plastic degradation factor for each member-end at the joint as,

$$r_{ph} = hr_p = \frac{h}{1 + 3EI / R_p L} \tag{5.2.1}$$

where r_p is the member-plasticity degradation factor defined in Eq. (2.3.4). The parameter h in Eq. (5.2.1) is a health index that characterizes the degree of local damage. When health index $h = 1$ the member-end is perfectly healthy, while $h = 0$ indicates it is completely damaged (i.e., has no stiffness).

In a similar manner, if a semi-rigid connection is at the joint relevant to the member removal, the health index h is assumed to modify the connection-stiffness degradation factor as,

$$r_{ch} = hr_c = \frac{h}{1 + 3EI / R_c L} \tag{5.2.2}$$

where r_c is the member-connection degradation factor defined in Eq. (4.2.10). As above, when $h = 1$ the semi-rigid connection is perfectly healthy, while $h = 0$ indicates it is completely damaged.

A parametric study of the health index h is presented in Example 1 of this chapter, where progressive-failure analysis of a frame structure is conducted for a range of h values to illustrate the influence that connection damage has on structural behaviour in the aftermath of an abnormal loading event. The study only considers damage that diminishes the rotational capacity of connections. However, by following similar reasoning as in the foregoing, it is readily possible to also account for diminished shear and axial connection capacity in the progressive-failure analysis.

5.3 Progressive-Failure Analysis Procedure

This section presents a computer-based procedure for progressive-failure analysis. The determination of the loading conditions is first considered. The nonlinear analysis procedure proposed in Chapter 3 is then extended to the analysis of a structure that has been locally damaged by abnormal loading to the extent that part of the structure has disengaged from the main structure and impacted as debris loading on the remaining structure below.

5.3.1 Load Combinations due to Abnormal Loading Events

A structure exposed to a natural environment is subjected to dead gravity loads due to the structure self weight, live gravity loads, wind loads, earthquakes, and so on. All the loads within a structure's lifetime may never achieve their maximum values at the same instant and, as such, the normal design loads applied to the structure are established by probabilistic analysis (Galambos et al., 1982). The specification of normal design loads is included in the design codes of many countries, but the stipulation of abnormal loads appears in only some specialized guidelines. For instance, after the progressive collapse of the Ronan Point Tower due to a gas explosion (Griffiths et al., 1968), a number of codes and standards in countries such as Canada, Western Europe, and the United States have implemented provisions to minimize the probability of progressive collapse. The Canadian Code (NRCC, 1995) requires structural designs to have sufficient structural redundancy and integrity against all abnormal effects within a building's service life; specifically, the structure is to have the capability to absorb local failure without widespread collapse.

In addition to the structural redundancy and integrity stipulations in the Canadian code, Eurocode-1 (CEN, 1994) implements an alternative design strategy that explicitly accounts for abnormal loads.

For example, account for a loading intensity of 34 kPa by a natural gas explosion is required for structures where explosions have high probability of occurring. If abnormal or accidental loads A_k are specified, the following design load combinations are routinely incorporated in design (CEN, 1994),

$$D_L + A_k + 0.5L_L \tag{5.3.1}$$

$$D_L + A_k + 0.2S_L + 0.3L_L \tag{5.3.2}$$

$$D_L + A_k + 0.5W_L + 0.3L_L \tag{5.3.3}$$

where D_L, L_L, S_L and W_L are specified dead load, live load, snow load and wind load, respectively.

In the United States, design requirements for progressive collapse were introduced in 1972 just after the 1968 Ronan Point event. In addition to the consideration of general structural integrity, a recent design code (ASCE-7, 2005) unofficially recommends that designers consider the following loading combination,

$$(0.9 \text{ or } 1.2)D_L + A_k + (0.5L_L \text{ or } 0.2S_L) \tag{5.3.4}$$

It is observed that the European and the American design codes adopt almost the same load combination style. Under the action of the combined loads of Eqs. (5.3.1) to (5.3.4), the loading capacities of certain key elements in a structural system are checked to meet the safety demands.

For a design having concern for an abnormal action A_k, it is difficult for designers to specify the magnitude of A_k due to considerable uncertainties. Even if possible, a structure designed to account for one hazard might not provide reasonable resistance to other hazards. At the other extreme, designing many "hard" portions within the structure is uneconomical (Ellingwood & Dusenberry, 2005). A more attractive approach may be to eliminate the hazard, or to control the consequence of local damage by providing alternate paths that safely transfer loads away from the damaged area (Breen & Siess, 1979).

The alternate load-path strategy is to design a structure that can bridge local damage due to any abnormal loading event. To achieve this objective, the ASCE-7 design code (2005) requires applying the following load combination,

$$(0.9 \text{ or } 1.2)D_L + (0.5L_L \text{ or } 0.2S_L) + 0.2W_L \tag{5.3.6}$$

to check the residual capacity of a locally damaged structure to maintain its overall stability for a sufficient period of time to evacuate the building or take any necessary measures to remedy the damage. Based on the discretion of designers, local damage is simulated by removing critical load-bearing component(s), and then the strength capacity of the damaged structure is checked under the load combination Eq. (5.3.6).

The foregoing procedure, however, creates a dilemma for designers since the local damage is not explicitly stipulated. In this regard, guidelines released by the General Services Administration of the United States (GSA 2003) address this issue for the design of new buildings or the assessment of existing office buildings subject to abnormal loading events. Specifically, to model the localized damage caused by abnormal loads, designers or assessors are required to remove the following critical members of the structure on the first floor: an exterior column near the centre of the short side of the structure, an exterior column close to the center of the long side of the structure, an exterior column at a corner, an interior column, an exterior bearing wall near the centre of the short side of the structure, an exterior bearing wall near the center of the long side of the structure, an exterior bearing wall that wraps around a corner, and an interior bearing wall. At the same time, to analyze each resulting damaged structure, the load combination,

$$2(D_L + 0.25L_L) \tag{5.3.7}$$

is employed in a linear static elastic analysis, while the load combination,

$$D_L + 0.25L_L \tag{5.3.8}$$

is employed in a linear elastic dynamic analysis. By comparing Eq. (5.3.7) with Eq. (5.3.8), it is observed that a dynamic amplification factor of 2 is accounted for in the static analysis. Typical and atypical structures are distinguished in the GSA guidelines. Atypical structures have the following features: plan irregularities, vertical discontinuities, combinations of structural systems, variations in bay size, extreme bay sizes, and closely spaced columns.

More recently, the Department of Defense of the United States has released the Unified Facilities Criteria (UFC) design guidelines to reduce the potential of progressive collapse for new and existing facilities (DoD, 2005). The guidance provides for an effective and uniform level of resistance to progressive collapse without expensive or radical changes to conventional design practice. As suggested in the GSA guidelines, the Alternate-load Path (AP) method is recommended for the static and dynamic analysis and design of structures, as follows: “The primary objective in a progressive collapse analysis is to check the structure for alternative load paths after some elements are potentially lost through some abnormal loading such as an explosive event. These alternative load paths will need to provide sufficient damage tolerance to minimize the loss of life that might otherwise occur and will allow the safe egress of occupants from the damaged structure.”

The following load combination provided in the DoD guidelines for a static analysis is based on the ASCE-7 (2005) load formulation given in Eq. (5.3.6), and the GSA formulation given in Eqs. (5.3.7) and (5.3.8):

$$2[(0.9 \text{ or } 1.2)D_L + (0.5L_L \text{ or } 0.2S_L)] + 0.2W_L \quad (5.3.9)$$

where the coefficient of 2 is a dynamic amplification factor that is applied only to the loads at the bays just above the removed column (see DoD, 2005).

This study assumes that the abnormal loading occurs jointly with the normal gravity loading for the building. Lateral loading is not considered because the probability of a simultaneous occurrence of an abnormal loading and a strong wind or seismic loading is considered negligible (Ellingwood & Leyendecker, 1978). If the structure and abnormal loading are symmetrical, the $0.2W_L$ term in Eq. (5.3.9) is used to ensure that the lateral deflection of the frame is involved in the analysis.

Following the published guidelines (GSA, 2003; DoD, 2005), this study models localized damage due to abnormal loading by removing one or more members to signify they abruptly break away from the structure. The analysis is quasi-dynamic in the sense that the gravity load on a failed member that has broken away is scaled by an impact factor, and applied as a debris load on the remaining structure immediately below. In view of the lack of research on the values of dynamic impact factors applicable for building structures, the objective of this study is to determine the magnitude of impact factors that initiate further debris loading and, if it happens, cause progressive collapse.

5.3.2 Incremental-Load Analysis

After the occurrence of local damage from an abnormal loading event, progressive-failure analysis traces the residual load carrying capacity of the remaining framework over a loading history involving proportionally applied increments of the prevailing gravity loads and any impact loads due to falling debris. The progressive collapse of a structure is divided into a series of failure stages. The first stage after the occurrence of abnormal loading is up to a local failure state signalled by the singularity of the structure stiffness matrix. To begin the second stage, the local failure mechanism is identified by the zero-valued stiffness coefficient(s) on the main diagonal of the stiffness matrix. The corresponding failed member(s) are removed from the structure, one-step elastic unloading analysis is conducted, and the internal forces and nodal displacements are upgraded accordingly. Debris loading from the failed member(s) is applied on the remaining structure, and the incremental-load procedure continues on to the next stage. The analysis procedure terminates either when progressive collapse occurs or the target design load level is reached, which happens first (see Example 1 in Section 5.4.1 for illustrative details).

Reaching each failure stage involves a number of load increments. After each such load increment, the stiffness matrix of each member is updated to account for bending, shear or axial stiffness degradation due to plastic behaviour under increasing applied loads. The computational model allows

the incremental analysis to proceed beyond loading levels at which structural instabilities occur, including members breaking away from the structure or the formation of local plastic collapse mechanisms. The analysis traces the behaviour of the building framework over the incremental load history, until either the full intensity of all gravity and debris loading is reached and the structure is still stable, or a structural instability occurs at a lower loading level that causes part or all of the structure to undergo progressive collapse to ground level.

For a structure that has been initially damaged due to an abnormal loading event, the progressive-failure analysis commences from the zero-load level identified by load factor $\lambda_0 = 0$. Thereafter, it proceeds by incrementally increasing the loading level over a succession of failure stages. Each such stage corresponds to a local or global failure state; i.e., formation of a rigid-body collapse mechanism, member disengagement and associated debris loading, or, if it happens, progressive collapse of part or all of the structure. To accurately identify the loading levels corresponding to the various failure stages, the magnitude of the load-factor increment is decreased over the loading history as follows,

$$\Delta\lambda_{J1} = \Delta\lambda^*_J; \quad \Delta\lambda_{Ji} = \Delta\lambda_{Ji-1}(1 - \Delta\lambda^*_J) \quad (i = 2, 3, \ldots) \tag{5.3.10}$$

where $\Delta\lambda^*_J < 1$ is the specified increment for the first stage of the analysis (e.g., $\Delta\lambda^*_J = 0.05$). Assume the structure is subjected to applied load W_0, as determined by either the GSA criterion Eq. (5.3.7) or the DoD criterion Eq. (5.3.9). The portion of the load applied at the end of stage J-1 is $(1-\lambda_{J-1})W_0$, where λ_{J-1} is the total recorded load factor over J-1 stages. Thus, for the i^{th} loading increment within stage J, the corresponding load increment is,

$$\Delta W_{Ji} = \Delta\lambda_{Ji}(1 - \lambda_{J-1})W_0 \quad (i = 1, 2, 3, \ldots) \tag{5.3.11}$$

If the structure stiffness matrix is non-singular at the end of the incremental load step defined by Eq. (5.3.11), the corresponding incremental nodal displacements and member forces are solved for and added to the total displacements and forces accumulated to date. The initial-yield and full-yield conditions for each member-end section are then evaluated and, if plastic behaviour is detected, the appropriate bending, shearing and axial stiffness degradation factors r, t and n are calculated, and the member stiffness matrix is updated accordingly. The computation proceeds until the end of the J^{th} stage, when either the target load level W_0 is reached or a further local/global failure state is detected. The total load applied on the damaged structure within the stage is,

$$\Delta W_J = \sum_i \Delta W_{Ji} = (1 - \lambda_{J-1})W_0 \sum_i \Delta\lambda_{Ji} = (1 - \lambda_{J-1})W_0\Delta\lambda_J \tag{5.3.12}$$

where parameter $\Delta\lambda_J$ is the sum load factor for the J^{th} stage. Thus, the total load factor for all J stages is

$$\lambda_J = \lambda_{J-1} + \Delta\lambda_J \tag{5.3.13}$$

From Eqs. (5.3.12) and (5.3.13), the load remaining at the end of the J^{th} stage that is yet to be applied commencing in the next stage J+1 of the analysis is,

$$W_{J+1} = (1-\lambda_{J-1})W_0 - \Delta W_J = (1-\lambda_J)W_0 \tag{5.3.14}$$

where $W_0 - W_{J+1} = \lambda_J W_0$ is the load magnitude already applied on the structure. The locally damaged structure does not experience further collapse.

It is evident from Eq. (5.3.14) that $W_{J+1} = 0$ when the load factor $\lambda_J = 1$, which indicates the target load level W_0 has been reached at the end of stage J. This means that the structure does not experience progressive collapse failure. On the other hand, if load factor $\lambda_J < 1$ then a local/global failure state has been detected at the end of the J^{th} loading stage. This failure is characterized by the structural stiffness matrix becoming singular, which indicates that the structure has become unstable in either a local or global sense. The first is a global instability, corresponding to part or all of the structure undergoing progressive collapse to ground level; here, the analysis is terminated at $\lambda_f = \lambda_J < 1$.

In the case of local instability, the structure still has residual capacity to resist further loads. Before commencing the next stage of the analysis, it is assumed that the affected member or subassembly of members abruptly break(s) away from the supporting connections, based on the criteria in Table 5.1. The corresponding gravity loading then falls as debris loading with magnitude $I_{af}W_{fd}$ on the remaining structure below, where I_{af} is a specified impact amplification factor and W_{fd} denotes the weight of the falling debris. At the instant that the debris loading is created, the remaining structure experiences an abrupt unloading phenomenon as the moment, shear and axial restraining forces decrease to zero at the node(s) where the member or subassembly of members breaks away. The corresponding "unloaded" member forces and nodal displacements for the remaining structure are found by applying the incremental-load analysis procedure for the affected node(s) loaded by the reverse of the member-end moment, shear and axial forces that existed immediately before the abrupt unloading occurs. The "unloaded" forces and displacements are then added to the member forces and nodal displacements that existed for the remaining structure just prior to the unloading event, to establish the starting basis for the next (J+1) stage of the analysis.

To commence the (J+1) analysis stage, any falling debris loading is applied with the remainder loads defined by Eq. (5.3.14), such that the remainder loads for any member(s) impacted by falling debris become,

$$W_{J+1} = (1-\lambda_J)W_0 + I_{af}W_{fd} \tag{5.3.15}$$

The corresponding load increment within stage (J+1) is then given by,

$$\Delta W_{(J+1)i} = \Delta\lambda_{(J+1)i} W_{J+1} = \Delta\lambda_{(J+1)i}[(1-\lambda_J)W_0 + I_{af} W_{fd}] \quad (i = 1, 2, 3, \ldots) \tag{5.3.16}$$

When the debris loading is included in the analysis process according to the loading scheme based on Eq. (5.3.16), the computer-based procedure becomes much more complicated. In current design-load-based analysis, the external loading vector, relevant to the design W_0, is taken as a reference in the entire progressive collapse process, whereas load factor λ characterizes the extent of which the structure carries the loading. The approach in the following is to deal with the debris loading without changing the loading basis that is used to identify the progressive collapse level of the structure. To this end, the increment load of Eq. (5.3.16) is rearranged as

$$\Delta W_{(J+1)i} = \Delta\lambda_{(J+1)i}(1-\lambda_J)\left(W_0 + \frac{I_{af}}{1-\lambda_J} W_{fd}\right) \quad (i = 1, 2, 3, \ldots) \tag{5.3.17}$$

Note from Eq. (5.3.17) that the weight W_{fd} of the falling debris is multiplied by the factor,

$$\alpha = \frac{I_{af}}{1-\lambda_J} \tag{5.3.18}$$

which is referred to herein an 'equivalent impact amplification factor'. This scale factor ensures that the entire debris (displaced gravity) loading is accounted for in succeeding stage(s) of the incremental analysis after load level J. Therefore, from Eqs. (5.3.17) and (5.3.18), the load-increment within stage (J+1) of the analysis is,

$$\Delta W_{(J+1)i} = \Delta\lambda_{(J+1)i}(1-\lambda_J)(W_0 + \alpha W_{fd}) \quad (i = 1, 2, 3, \ldots) \tag{5.3.19}$$

One benefit of this loading approach is that the original external load records (W_0) maintain unchanged in the entire nonlinear analysis process except that only limited new record(s), related to debris load(s) is added. From Eq. (5.3.19), load factor $\Delta\lambda_{J+1}$ in stage (J+1) is expressed as

$$\Delta\lambda_{J+1} = \sum_i \Delta\lambda_{(J+1)i}$$

which is similar to the expression in Eq. (5.3.12). As a result, load factor λ_{J+1} at the end of stage (J+1) is determined by Eq. (5.3.13) and the analysis continues until the progressive collapse halts.

In the previous analysis procedure, the unloading is conducted before applying the debris load, caused by the member-end disengagement. The axial force, shear force, and bending moment released from each disengaged member end are reversely applied on the remaining structure. One-step elastic analysis is carried out for the reversed loads alone and the internal forces and nodal displacements are added to the corresponding internal forces and nodal displacements existing just before the member disengaged. More detailed illustration of unloading is provided in the Example of Section 5.4.1. Then, after determining the scaled debris loads, the next stage of the progressive-failure

analysis is performed for the remaining structure under the specified incremental-loading scheme, defined in Eq. (5.3.19). The analysis continues from load level λ_{J+1}, and accounts for the remainder loads, including the remaining yet prevailing service-level gravity loading and the previously created new debris loading. The process of the multi-stage incremental-load analysis continues until either the remaining structure is found to be still stable at loading level $\lambda_f = 1$, albeit in a deteriorated state, or a progressive collapse to ground level occurs for part or all of the remaining structure at a lower loading level $\lambda_f < 1$. The computational steps of the progressive-failure analysis procedure are illustrated in the flowchart in Figure 5.3.

5.4 Example Case Studies

The procedure of progressive-failure analysis is illustrated in the following for three building frameworks, consisting of steel beam-column members with W-shape sections. Example 1 illustrates the details and results of the analysis procedure for a low-rise steel building framework, including how the results are affected by connection damage and semi-rigid connection behaviour. Example 2 is a mid-rise steel framework taken from the Los Angeles Model Building (FEMA 355C, 2000), referred to as the Los Angeles frame hereinafter, and serves to illustrate both the creation of different types of debris loading and the vulnerability of such frameworks to progressive collapse due to interior explosion. With the same Los Angeles frame and loading condition as employed in Example 2, Examples 3 and 4 investigate structural behaviour caused by car-bombing and aircraft crash events, respectively. Example 5 is a framework taken from the Boston Model Building (FEMA 355C, 2000), referred to as the Boston frame hereinafter, and serves to evaluate the progressive-collapse behaviour of a building in a non-seismic region.

For Example 1, the normal yield stress of material $\sigma_y = 36$ ksi (248 MPa) for all members, and the section properties are defined in the CISC handbook (CISC, 2004); for Examples 2, 3 and 4, the yield stress σ_y = 49.2 ksi (339 MPa) and 57.6 ksi (397 MPa) for the beam and column members, respectively, and section properties are defined in the AISC-LRFD manual (2001). For all four examples 1, the exponent in Eq. (3.3.2) is taken as $\eta = 1.37$ for all the members; the shear yield stress of the material is taken as $\tau_y = 0.5\sigma_y$ (Tresca criterion); residual stresses are taken as $\sigma_{rc} = 0.3\sigma_y$ for the compressive normal stress, $\sigma_{rt} = 0.15\sigma_y$ for tensile normal stress, and $\tau_r = 0.05\tau_y$ for the shear stress. The initial load factor increment in Eq. (5.3.10) is taken as $\Delta\lambda^*_J = 0.05$.

The progressive-failure analysis results include the values of the bending, shearing and axial post-elastic stiffness degradation factors *r*, *t* and *n*, respectively, for member sections at which plastic deformation occurs. If the plastic deformation is related to degraded bending, shearing or axial

stiffness, the member section is designated by a circle, triangle or square symbol (O, ∇ or □), respectively. Otherwise, the section is designated by a circle inscribed in a triangle if the plasticity is associated with both degraded bending and shearing stiffness, or by a circle inscribed in a square if related to degraded bending and axial stiffness. For a member exhibiting plastic deformation over its entire cross-section area, the designation symbol has a black infill to indicate that the section has reached a state of zero post-elastic stiffness (i.e., r=0 and/or t=0 and/or n=0); for example, if r=0 while t=n=1, the section is designated by a black-infill circle (the classic representation of a plastic-hinge section). On the other hand, if a member has experienced only partial plasticity over its cross-section area, the designation symbol is left open with a number inscribed in it that indicates the percentage of plastic deformation calculated as *%Plasticity* = 100 (1 – r, t *or* n); for example, if r = t = 1 while n < 1, the section is designated by the number 100(1 – n) inscribed in an open square (see Example 1). Primarily, the following is a presentation of the fundamental details of the proposed progressive-failure analysis procedure. A number of practical issues stemming from the four examples are subsequently commented upon and discussed at the end of the chapter.

5.4.1 Example 1: Low-Rise Steel Frame

Consider the two-bay by two-story steel framework subject to the uniformly distributed service-level design gravity loads in Figure 3.14 (Ziemian et al., 1992; Liu et al., 2003; Xu et al., 2005), or in Figure 4.20 with semirigid connections. The structure is a building perimeter frame that supports open-web-steel-joist floor and roof systems. The load intensity w_{45}= w_{56} = 109.5 N/mm on floor members 4-5 and 5-6 is due to the member self-weight and tributary floor loading; the load intensity w_{78}= w_{89} = 51.1 N/mm on roof members 7-8 and 8-9 is due to member self-weight and tributary roof loading. Here, all the applied loads are assumed to be determined according to the DoD (2005) guidelines. All the members are oriented with their webs in the plane of the framework, and are assumed to be fully restrained against out-of-plane behaviour. By virtue of the nature of the applied loading, plastic deformation can occur at the end sections of each of the six column members, and at the end and midspan sections of each of the four beam members. The framework has 13 nodes and 33 degrees-of-freedom for nodal displacement (i.e., rotation at each of the three pin-support nodes 1-3, plus lateral and vertical translation, and rotation at each of the ten free nodes 4-13).

As indicated in Figure 5.4, it is assumed that column C_{69} of the framework is initially subjected to an abnormal loading event that destroys the member, and causes it to be thrown outward from the structure so that the member does not impact as debris loading on the members below. The objective of the progressive-failure analysis conducted thereafter is to determine whether or not the remaining

part of the framework is capable of carrying the prevailing loads without progressive collapse occurring. Starting from the zero-load level defined by load factor $\lambda_0 = 0$, the target loading level for the incremental-load analysis is defined by the service-level gravity loads shown in Figure 5.4, since they are the loads prevailing on the frame at the time of the abnormal loading event. The analysis results found for the frame are discussed in the following and illustrated in Figures 5.4, 5.5 and 5.6.

As shown in Figure 5.4, the first stage of the progressive-failure analysis after column C_{69} is eliminated from the structure determines that four fully-plastic hinges ($r = 0$, $t = n = 1$) and three partially-plastic hinges ($r < 1$, $t = n = 1$) are developed over the incremental loading history up to load level $\lambda_{f1} = 0.227$ times the service-level gravity loads. At this point, the structure stiffness matrix becomes singular because the stiffness coefficient associated with the vertical displacement of node 9 tends to zero as a plastic hinge fully develops at the left end-section of cantilever beam B_{89}; i.e., the loads can be incrementally increased to only 22.7% of the service-load gravity loads shown in Figure 5.4 before beam B_{89} fails as a rigid-body cantilever collapse mechanism.

As the local collapse mechanism deforms, the beam B_{89} rotates through an angle great enough to cause it to disconnect from the frame at node 8 (see Table 5.1). It is assumed that its entire gravity load weight impacts as debris loading on the lower floor beam B_{56}. In addition, the structure also undergoes an unloading phenomenon as the moment and shear force restraining effects at node 8, related to beam B_{89}, abruptly decrease to zero. Member forces (M, V, P) and nodal displacements (u_x, u_y, u_z) for the remaining structure after the unloading takes place are found by applying the incremental-load analysis procedure for the loading shown in Figure 5.5, where the moment couple and vertical load applied at node 8 are equal to the bending moment and shear force that existed at the left end of member B_{89} immediately before breaking away from the frame at load level $\lambda_{f1} = 0.227$. The incremental-load 'unloading' analysis is conducted with account for geometric nonlinearity, but not material nonlinearity (i.e., a second-order elastic analysis). The starting basis for the 'unloading' analysis is the set of before-unloading member forces and nodal displacements previously found for the structure at load level $\lambda_{f1} = 0.227$, that are given in columns 2 to 4 of Tables 5.2 and 5.3, respectively. The after-unloading member forces and nodal displacements found by the unloading analysis are given in columns 5 to 7 of Tables 5.2 and 5.3.

As a progressive collapse to ground level has not yet occurred for any part of the structure, a second-stage progressive-failure analysis is conducted beginning from loading level $\lambda_{f1} = 0.227$, with account for the service-level gravity loading on members B_{45}, B_{56} and B_{78}, and the added debris loading that has fallen on member B_{56} as a result of the failure of beam B_{89}. The triangular distribution of debris loads on member 5-6 of the frame in Figure 5.6 (a) is due to tributary roof loads

that are presumed to be transferred to the beam by an open-web-steel-joist roof system. As the right end of beam B_{89} falls, and before the member disengages from the frame at its left end, it is assumed that the connections at the ends of the roof joists fail at their points of support on the beam. As a result, the tributary roof loads slide from left to right on beam B_{89}, and are mainly deposited as debris on the right half of beam B_{56}.

As shown in Figure 5.6(a), and discussed above, the debris loading on beam B_{56} is a triangular pattern (the mirror-image of the rigid-body displacement of collapsed beam B_{89}) with maximum intensity $w_d = 2\alpha w_{89} = 2\alpha(51.1) = 102.2\alpha$ N/mm at the right end of the beam. The load amplification factor α accounts for the dynamic load impact amplification factor I_{af} of the debris load and the load level λ_J at which the debris is created; i.e., from Eq. (5.3.18), for specified $I_{af} = 2$ and $\lambda_J = \lambda_{f1} = 0.227$, the factor $\alpha = 2/(1-0.227) = 2.59$. That is, from Figures 5.4 and 5.6 (a), the load intensity at the right end of beam 5-6 for the second-stage analysis is $w_{56} + w_d = 109.5 + (102.2)(2.59) = 374.2$ N/mm. The incremental member forces and nodal displacements found for each load increment of the second-stage analysis are added to the corresponding forces and nodal displacements accumulated over all previous load steps.

As shown in Figure 5.6, the second stage of the progressive-failure analysis determines that three more fully-plastic hinges ($r = 0$, $t = n = 1$) and three more partially-plastic hinges ($r < 1$, $t = n = 1$) are developed over the incremental loading history from load level $\lambda_{f1} = 0.227$ up to load level $\lambda_{f2} = 0.904$ (i.e., 90.4% of the gravity and debris loads). At this point, the framework becomes unstable as the horizontal and vertical displacements of both nodes 6 and 11 become excessively large (i.e., the corresponding stiffness coefficients tend to zero such that the structure stiffness matrix becomes singular). This is a global instability that indicates the lower-story right bay of the framework is undergoing progressive collapse to ground level at failure load level $\lambda_f = \lambda_{f2} = 0.904$. The member-end axial forces, shear forces and bending moments just before collapse are given in the last three columns of Table 5.2.

5.4.1.1 Example 1: Accounting for connection damage

It is important to note that the analysis results discussed in the foregoing are based on the assumption that connections remain perfectly healthy after members disengage from them. This coincides with current analysis guidelines when applying the AP strategy (GSA, 2003; DoD, 2005). However, such an assumption might not be realistic because a joint connection may experience severe damage due to member disengagement. Based on the discussion in Section 5.2.1 concerning the connection health condition index h, the rest of this Example 1 focuses on investigating structural behaviour when

connections are damaged such that their rotational capacity is diminished. Specifically, after the failure of column C_{69} due to the initial interior explosion, the ensuing structural behaviour is assessed when the connection at joint 6 is assigned a range of health index values $h_6 < 1$. Similarly, after the disengagement of beam B_{89} at load level $\lambda_{f1} = 0.227$, as shown in Figure 5.5, the influence of various health index values h_8 for the connection at joint 8 is investigated.

To begin, the effect of damage to connection 6 on structural behaviour is alone investigated by assuming there is no damage to connection 8 throughout the progressive-failure analysis process (i.e., $h_8 = 1$). For complete rotational damage at joint 6 (i.e., $h_6 = 0$), the analysis results are as follows: the load factor at the first stage is $\lambda_1 = \lambda_{f1} = 0.226$, which is close to the value 0.227 found when the connection is perfectly healthy (Figure 5.4). This result demonstrates that the health condition of joint connection 6 does not significantly affect the frame capacity for the first loading stage. This is due to the fact that the load on beam B_{89} is mostly transmitted to the left-hand bay of the frame after the failure of column C_{69}. However, for the second loading stage when $h_6 = 0$, the analysis determines that the framework undergoes progressive collapse to ground level at load-capacity level $\lambda_f = \lambda_{f2} = 0.726$, which is almost 20% less than the load-capacity level $\lambda_f = 0.904$ when $h_6 = 1$. The second row of Table 5.4 illustrates the variation in the load factor λ_f for values of h_6 from zero to one. It is seen that when the health index $h_6 = 0.5$ and 0.75, the failure load factor $\lambda_f = 0.884$ and 0.897, respectively. These values represent reductions of only 2.21% and 0.77%, respectively, compared to $\lambda_f = 0.904$ when $h_6 = 1$, which indicates that the influence of the health of joint connection 6 is significant only when it experiences severe flexural damage represented by $h_6 \leq 0.5$. This example serves to illustrate the importance of accurately assessing the health of connections from which members have disengaged, so as to more accurately predict the structural behaviour that ensues thereafter.

Results are similarly found when damage to joint connection 8 (i.e., $h_8 < 1$) is accounted for after beam B_{89} disengages from the structure. Table 5.4 lists the λ_f levels found by the progressive-failure analysis when $h_8 = 0.05$, 0.5 and 1, and $h_6 = 0.05$, 0.1, 0.2, 0.5, 0.75 and 1.0. The important fact to be observed from these results is that the health of joint connection 8 has no effect on the load level λ_f at which progressive collapse occurs, regardless of the health of joint 6.

To the effect of rigid connection damage on load capacity, Table 5.5 gives the plasticity degradation factors r values , and the internal forces at the first and second stages, respectively, when health index $h_6 = h_8 = h = 0.5$. It is seen from Table 5.5 that at the end of stage 1, plasticity factor $r =$

0.5 for the end E6 of both beam B_{56} and column C_{36}. In the second stage, the health index $h_8 = 0.5$ is applied to the damaged end E8 for both column C_{58} and beam B_{78}.

5.4.1.2 Example 1: Accounting for semi-rigid connection behaviour

The semirigid frame in Figure 4.20 is investigated in the following to illustrate the effect that semirigid connections have on progressive collapse. Two cases are investigated in this subsection: (1) connection damage is ignored in that the health indexes discussed in the previous section are all set at unity (i.e., $h_8 = h_6 = 1$); (2) connection damage is taken into account as $h_8 = h_6 = 0.5$. Parameters M_n, R_{ce}, R_{ce}, and γ for the four connections are selected from experimental results (Kishi et al., 2004) and shown in Table 5.6.

In principle, the progressive-failure analysis procedure for semirigid frames is similar to that for rigid frames, except that the stiffness degradation factor r for a rigid frame is replaced by the compound degradation factor r presented in Chapter 4, and the health index h is imposed on damaged semirigid connections from Eq. (5.2.2). The compound factor r is calculated as described in the following. First, semirigid connection stiffness R_c is calculated by Eq. (4.2.6) for the four-parameter model described in Figure 4.4 and Eq. (4.2.4). Secondly, upon substituting the value of R_c and the properties of the connected member into Eq. (4.2.10), the stiffness degradation factor r_c is found for the connection. Thirdly, the member plasticity factor r_p is found by Eq. (2.3.4) in Section 2.3.2 or Eq. (4.2.11) in Section 4.2.3. Finally, the two factors r_c and r_p are substituted into Eq. (4.2.13) to find the compound stiffness degradation factor r.

After column C_{69} is eliminated from the structure, the first stage of the progressive-failure analysis accounting for semi-rigid connection behaviour determines that member plasticity is developed in the semi-rigid frame, including three column-end plastic hinges and two beam-end plastic hinges as indicated in Table 5.7. Meanwhile, the connection stiffness degradation factors are changed from their initial r_{c0} values in column three of Table 5.7 to the r_c values shown in column four of the table. It is observed that the beam B_{89} of the semi-rigid frame fails in a cantilever mode. at load level $\lambda_{f1} = 0.226$, which is close to the first-stage load capacity $\lambda_{f1} = 0.227$ of the rigid frame shown in Figure 5.4. Note that $r_c = 0.197$ for the left-end of roof beam B_{89} is greater than $r_c = 0.046$ for the right-end of roof beam B_{87} because of the different connection properties. After conducting unloading analysis to account for the abrupt disengagement of beam B_{89} from the structure, the second stage of the progressive-failure analysis determines that only end E6 of column C_{36} becomes a plastic hinge while 68% plasticity is developed at end E5 of column C_{25}. On the other hand, the values of connection stiffness degradation factors of beam B_{56} degrade over 77%. Similar to the failure mode of the rigid

frame in Figure 5.6, the semi-rigid frame fails due to inelastic instability at loading level λ_{f1} = 0.863, which is 4.54% less than the collapse load factor 0.904 for the corresponding rigid frame.

When the effect of connection damage is taken into account for the semi-rigid frame, the corresponding plastic degradation factor r_p and connection stiffness degradation factor r_c are modified using Eqs. (5.2.1) and (5.2.2), respectively. The results of progressive-failure analysis for the semi-rigid frame with health index $h_6 = h_8 = 0.5$ are presented in Table 5.8. For the first stage of analysis, the significant changes of the results shown in Table 5.8 are the plastic degradation factor of E6 of column C_{36} and semi-rigid connection stiffness of E6 of beam B_{56}. Although the loading capacity of the frame is the same value of 0.226 as obtained for the frame without accounting for connection damage, some member-end moments change significantly. For instance, the moment at E6 of column C_{36} is 150.9 kN-m, which reduced 27.6% from the value 208.4 kN-m in Table 5.7 when the effect of connection damage is ignored. For the second stage of analysis, all the degradation factors just before collapse of the frame are shown in Table 5.8. It is seen that only the semi-rigid stiffness degradation factor value of 0.083 at end E6 of beam B_{56} differs significantly from the corresponding value 0.157 in Table 5.7, due to connection damage. When connection damage is taken into account, the loading capacity given in Table 5.8 is λ_f = 0.859, which is only 0.46% less than that obtained for the frame when not accounting for the effect of connection damage.

5.4.2 Example 2: Internal Explosion in Medium-Rise (Los Angeles) Frame

The steel moment-frame shown in Figure 5.7 has been previously explored for seismic loads (Gupta & Krawinkler, 1999; Hasan et al., 2002). The framework is a perimeter frame of a building located in Los Angeles that was designed in accordance with the earthquake provisions of the Uniform Building Code (UBC, 1994). The gravity load intensities indicated for the roof and floor beams include a tributary-area width of 15 feet. These design load intensities are taken as the target loading level for the incremental-load analysis. The dynamic load impact factor is taken as I_{af} = 4 for both concentrated and distributed debris loads.

The initial abnormal loading event is assumed to be an explosion that occurs in an interior bay on the eighth storey of the framework, as shown in Figure 5.7, such that beam B_{72} and columns C_{82} and C_{83} are destroyed. After the remaining structure is analyzed, the middle bay of the frame is found to undergo progressive collapse to ground level at failure load level λ_f = 0.997. The results of the progressive-failure analysis are summarized in Table 5.9 and illustrated in Figures 5.7 through 5.15. Although the overall analysis involves ten stages, the progressive collapse of the framework is essentially in progress after the second analysis stage at load level λ_{f2} = 0.934. In the progressive-

failure analysis, a similar assumption of triangular debris loading as in Example 1 in Section 5.4.1 is applied to the situations in Figures 5.9 to 5.15. On the other hand, the uniform distribution of the debris loads shown in Figure 5.15 indicates that both ends of the failed floor girders disconnect simultaneously such that their tributary floor loads fall directly downward as debris.

5.4.3 Example 3: Car/Truck Collision with Medium-Rise (Los Angeles) Frame

For the same Los Angeles frame as that in Figure 5.7, the abnormal loading is here taken to be a car-bombing event at ground level, as shown in Figure 5.16. When columns C_{11} and C_{12} fail due to the car collision and bomb explosion, the progressive-failure analysis results indicate that the locally damaged structure still has the carrying capacity to resist the applied dead and live loads without any member of the damaged structure experiencing plasticity. That there is no further failure (strength/stiffness deterioration) is due to the fact the damaged framework has alternative paths for bridging the loads over the missing two columns, as shown in Figure 5.16. It is observed that in addition to shear forces (V) induced by the resulting cantilever behaviour, the upper beams experience tensile forces (TF) while the lower beams experience compressive forces (CF). Such cantilever action over the local damaged region allows the applied loads to be transferred to ground without further inelastic distress. To achieve this cantilever action, rigid connections between the members play an important role in accommodating the load redistribution.

5.4.4 Example 4: Airplane Crash into Medium-Rise (Los Angeles) Frame

Consider again the Los Angeles frame in Figure 5.7. The abnormal loading event is here taken to be an aircraft crashing into the 8^{th} floor, as shown in Figure 5.17. The weight of the aircraft is not considered directly, but it may be included by the selected impact amplification factor. If only column C_{81} fails due to the impact, the results obtained using progressive-failure analysis of the damaged frame indicate that no further collapse occurs and the frame behaves elastically. If both columns C_{81} and C_{82} fail, the upper portion of the frame above the two column locations acts as a cantilever and forms four fully-plastic hinges, as shown in Figure 5.17. A cantilever plastic collapse mechanism occurs when the fourth plastic hinge forms at loading level $\lambda_1 = 0.608$ (i.e. after 60.8% of the gravity loads have been applied).

A large downward deformation leads to the disengagement of the cantilever portion from the main structure at the locations of plastic hinges 1 and 2, which falls as debris loading on the lower floor beams B_{71} and B_{72}, as depicted in Figure 5.18. The intensity of uniformly distributed debris load is evaluated as $L_d = I_{af}\, w_u$, where I_{af} is the impact amplification factor and w_u is the total weight density

of the falling portion. For I_{af} = 3, the progressive-failure analysis indicates that the damaged structure can carry all loads (gravity plus debris) without developing further plasticity. For I_{af} = 4, the results from the analysis indicate that the left end of beam B_{72},, and right ends of beams B_{71} and B_{72} develop three bending plastic hinges, respectively. For I_{af} = 10, local beam B_{71} fails and the beam disengages from its end joints at load factor level λ_{f2} = 0.796, and falls as debris loading on beam B_{61} below. For the next stage, beam B_{72} also experiences bending failure and disengages at load level λ_{f3} = 0.798, and falls as debris loading on beam B_{62} below. Thereafter, progressive collapse takes place like the cascading failure described in Example 2, beams progressively undergo bending plus shear failure until the collapse halts at ground level, as indicated in Figure 5.16, where the dashed column and members indicate that the entire left bay of the framework topples to the ground.

5.4.5 Example 5: Internal Explosion in Medium-Rise (Boston) Frame

Consider the frame in Figure 5.19, which was selected from the medium-rise Boston Model Building (FEMA 355C, 2000). Compared with the Los Angeles Model Building in Example 2 of Section 5.4.2, there are changes in the cross section sizes of beams and columns because the design of the Boston building is not controlled by seismic loading. The results of nonlinear analysis, based on the factored load 1.4 D_L (dead load) adopted in Example 2 of Section 3.5.2, are shown in Figure 5.20. It is observed from Figure 5.20(a) that the frame remains elastic when the factored loading is completely applied. As the loading is monotonically increased, the frame reaches plastic collapse at loading level λ_f = 2.34 of the factored loads; the formation of plasticity is shown in Figure 5.20(b) for the half-frame due to symmetry. It is seen that a local collapse mechanism occurs at the roof level because of the lower strength of the roof beam compared to that of the floor beams.

To estimate the progressive-collapse behaviour of the non-seismic resistant Boston building, the initial abnormal loading event is assumed to be the same explosion as for the Los Angeles frame Example 2 of Section 5.4.2. In this Boston building example, the effect of connection damage is taken into account using a health index h. When h = 1.0 there is no connection damage and the frame undergoes collapse in the first loading stage at level λ_{f1} = 0.598 after eight plastic hinges form, as shown in Figure 5.21(a). When h = 0.5 the connections are damaged to a certain extent, but the frame collapses in the first loading stage at almost the same level λ_{f1} = 0.593, as shown in Figure 5.22(a). However, the maximum vertical deflection at joint J_5 is 19.15″ when h = 0.5, which is 41% greater than that when h = 1.0. Furthermore, the corresponding moments shown in Figures 5.21(b) and 5.22(b) for the two cases are significantly different. These results show, therefore, that the effect of

connection damage significantly affects the internal force and joint displacement response of the Boston building.

Results of the subsequent stages of the progressive-failure analysis for the Boston frame with account for connection damage are summarized in Table 5.10 and illustrated in Figures 5.23 through 5.28. Compared to the progressive collapse results for the Los Angeles frame Example 2 in Section 5.4.2, the local collapse in stages 3 through 6 are different for the two buildings. In Stage 3, beam B_{63} fails due to the impact of beam B_{71} in the Boston frame; while beam B_{71} fails in the Los Angeles frame. In Stage 4, beam B_{71} fails due to local instability in the Boston frame; while beam B_{63} similarly fails in the Los Angeles frame. Note that at the end of the second stage, the load factor for Boston frame is $\lambda_{f1} = 0.707$, which is less than 24.3% of the value 0.934 for Los Angeles frame. This indicates that a seismic-resistant frame has more strength capacity to resist impact loading than a non-seismic-resistant frame. Similar inverse responses for the two building frames are observed in Stages 5 and 6 of the analysis. Note from Tables 5.9 and 5.10 that the final loading capacities for the Los Angeles and Boston frames differ by only 3.42%.

5.5 Commentary and Discussion

The proposed progressive-failure analysis procedure is developed to an almost fully-automated state. However, some user intervention is yet required when a local failure mechanism is identified by the singularity of the structure stiffness matrix. Specifically, the computer program provides information for the analyst to determine the failure mechanism or collapse mode, which member(s) should be removed, the corresponding loads, and which member(s) in the remaining structure should receive the debris loads.

The incremental-load analysis is a tangent-stiffness procedure for which nodal unbalanced-force errors can occur after each load iteration. For all four examples presented, however, it was not found necessary to employ an unbalanced-force correction routine. This is because at load levels when plasticity began to develop in each structure, the loading increments defined by Eqs. (5.3.11) became smaller and smaller to the point that any unbalanced forces were insignificant. However, this occurrence was achieved at the expense of many load increments, requiring excessive computational effort. The use of an unbalanced-force correction routine would allow for larger load increments, hence smaller computational effort.

As presented herein, the progressive-failure analysis is based on small deformation theory, for which equilibrium is referenced to the undeformed structure, and, at most, first- and second-order deformations are accounted for. A separate large-deformation analysis of the frame in Figure 5.4

reveals results that differ little from those reported for Example 1. However, this is not likely to be the case for larger structures such as that considered in Example 2. Here, to compensate for the influence of large displacements, the nodal coordinates of the structure should be updated after each incremental analysis.

The progressive-failure analysis procedure can be readily applied to planar steel frames having members with sections other than W-shape. For a given section type, it only remains to adopt the appropriate interaction relations governing cross-sectional post-elastic behaviour under various combinations of member forces. Such interaction relations are available in the literature for a number of conventional steel sections and, in many cases, do not differ much in their general forms from those introduced in this study for W-sections. For example, the post-elastic interaction relations for steel hollow-box, angle, tee and channel sections are available from the work of Chen and Atsuta (1977). For other material types and sections, it is necessary to establish the required relations experimentally, analytically, or numerically (Grierson & Abdel-Baset, 1977).

Although the proposed nonlinear analysis method assumes plasticity is confined to the critical sections of a member, the spread of plasticity along the member is somewhat accounted for by the fact that the stiffness degradation factors vary between unity (fully elastic) and zero (fully plastic).

The impact load factor values I_{af}, specified for the five examples were known from previous analyses to result in progressive collapse. For instance, the progressive collapse of the frame in Figure 5.6 at load level $\lambda_f = 0.904$ was known a priori to occur for specified dynamic load impact factor $I_{af} = 2$. This is a relatively small impact factor, indicative of significant damping of the dynamic effect of the debris loading. When the impact factor is specified by larger values of $I_{af} = 5$, 10 or 20, indicative of less dynamic damping, the incremental-load analysis determines that the progressive collapse of the frame occurs at the smaller load levels of $\lambda_f = 0.669$, 0.502 or 0.384, respectively. The overall conclusion from the analysis results for Example 1 is that any abnormal loading event that initially destroys column C_{69} is likely to trigger progressive collapse to ground level in the right bay of the frame, even if the dynamic impact factor for debris loads is small (e.g., $I_{af} = 2$). This is primarily because low-rise steel frameworks such as this one have a low load-path redundancy (Khajehpour & Grierson, 2003).

The dynamic load impact factor $I_{af} = 4$ specified for Example 2 is the smallest impact factor for which progressive collapse occurs precisely at load level $\lambda_f = 1.0$. This is a relatively small impact factor, indicative of significant dynamic damping. Further analysis for larger values of I_{af} determine that the progressive collapse of the frame occurs for smaller load levels $\lambda_f < 1.0$. When $I_{af} \geq 4.0$, it can

be concluded from the analysis of Example 2 that any abnormal loading event that initially destroys beam B_{72} and columns C_{82} and C_{83} will likely cause progressive collapse of the middle bay of the frame, characterized by cascading shear failure of the floor girders under falling debris loads.

The results for Example 3 shown in Figure 5.16 indicate that even if severe local damage takes place due to a car/truck collision, no progressive collapse occurs for the damaged structure. This indicates that local column damage at ground level can be accommodated if a frame has rigid beam-to-column connections. The results for Example 1 in Section 4.5.1 concerning semi-rigid connections suggest, however, that this might not be the case if the frame has flexible beam-to-column connections.

Example 4 in Section 5.4.4 shows the results when an external crash occurs at the upper level of the Los Angeles frame. When exterior column C_{81} fails due to the impact of the aircraft, there is no progressive collapse. This indicates that the loss of one exterior column in a storey will not lead to progressive collapse. However, when both columns C_{81} and C_{82} fail, the portion above the two failed columns will fall down due to the lack of redundancy. The progressive collapse behaviour of the remaining frame under debris loading depends on the magnitude of impact amplification factor I_{af}. If I_{af} is less than 4, there is no progressive collapse. Otherwise, when I_{af} = 6, partially progressive collapse occurs; while I_{af} = 10, the progressive collapse takes place to the ground level. The results for both Examples 3 and 4 of Section 5.4 indicate that progressive collapse is sensitive to the redundancy of the damaged structure and the magnitude of impact debris loading.

Comparison of the results for Example 2 with those for Example 5 in Section 5.4 indicates that the progressive collapse behaviour of a building frame significantly depends on whether or not its design accounts for seismic loading. The seismic-resistant Los Angeles frame and the non-seismic-resistant Boston frame have common configuration and loading parameters, but their beam and column cross-sections are different. Under the same abnormal loading, from Figure 5.8, the load factor λ_{f1}= 0.906 for the Los Angeles frame, which is 51% greater than the load factor λ_{f1}= 0.598 obtained for the Boston frame in Figure 5.21(a). The differences in load factors for the rest of the progressive collapse stages are also significant, as indicated in Tables 5.9 and 5.10. As well, unlike the Los Angeles frame, the Boston frame experiences local instability in Stage 4, as indicated in Figure 5.25 and Table 5.10. These results reveal that a building designed in a seismic region has a higher capacity against abnormal loading than a building with the same configuration but designed for a non-seismic region.

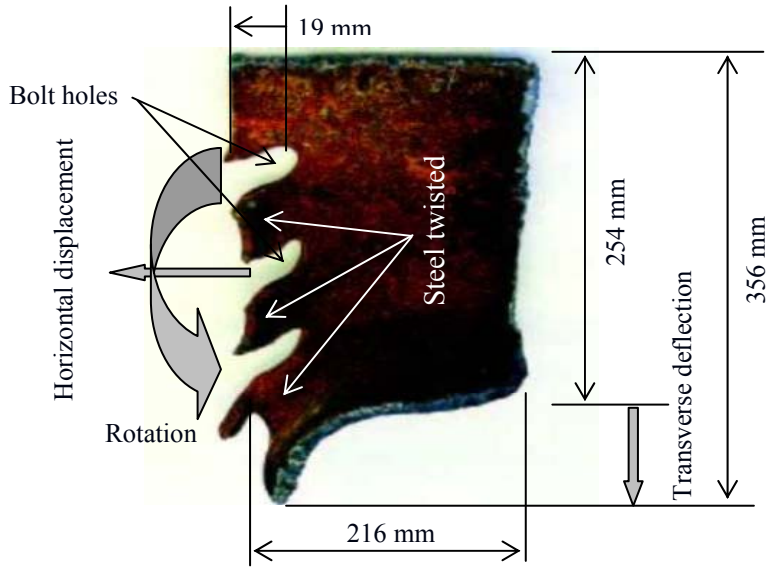

(a) Failed connection sample from the 7th floor

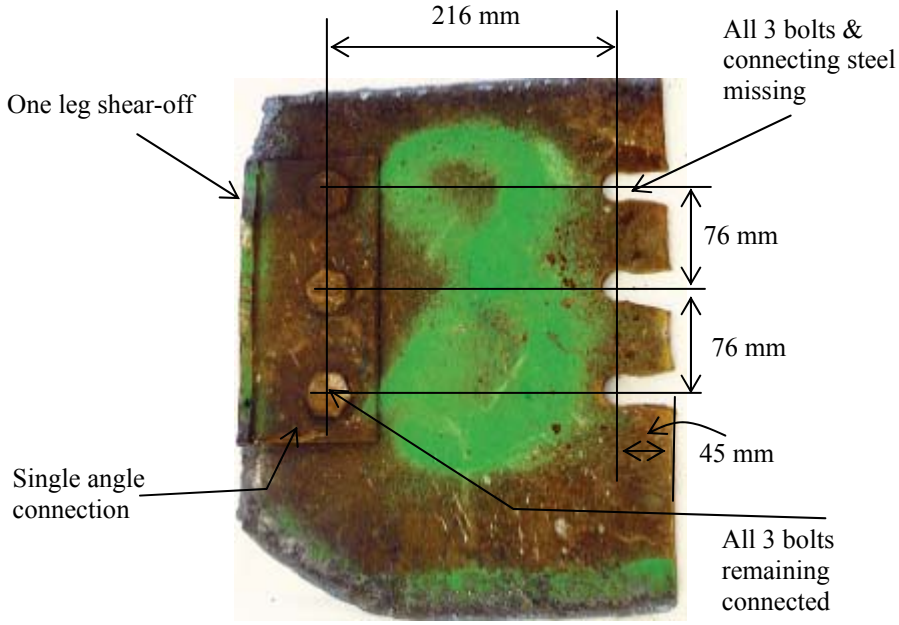

(b) Failed connection sample from the 8th floor

Figure 5.1 Connection failures from WTC 5 Building (Sept 11, 2001)

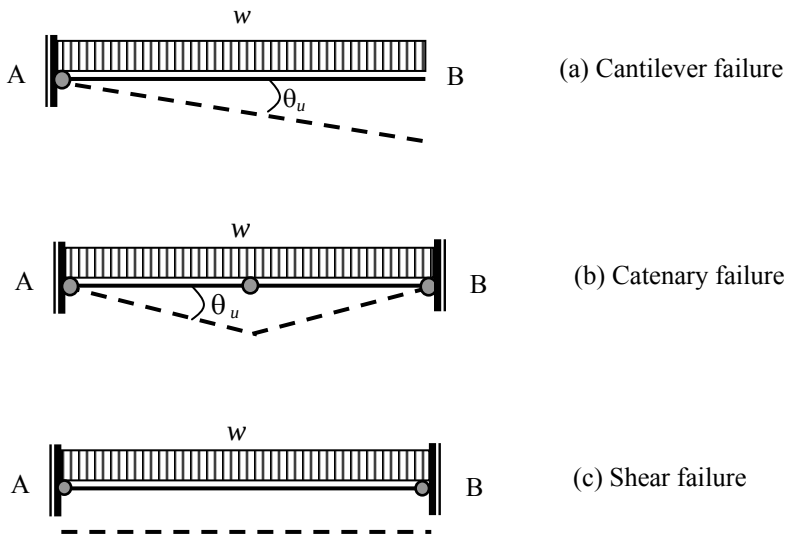

Figure 5.2 Local failure modes of members

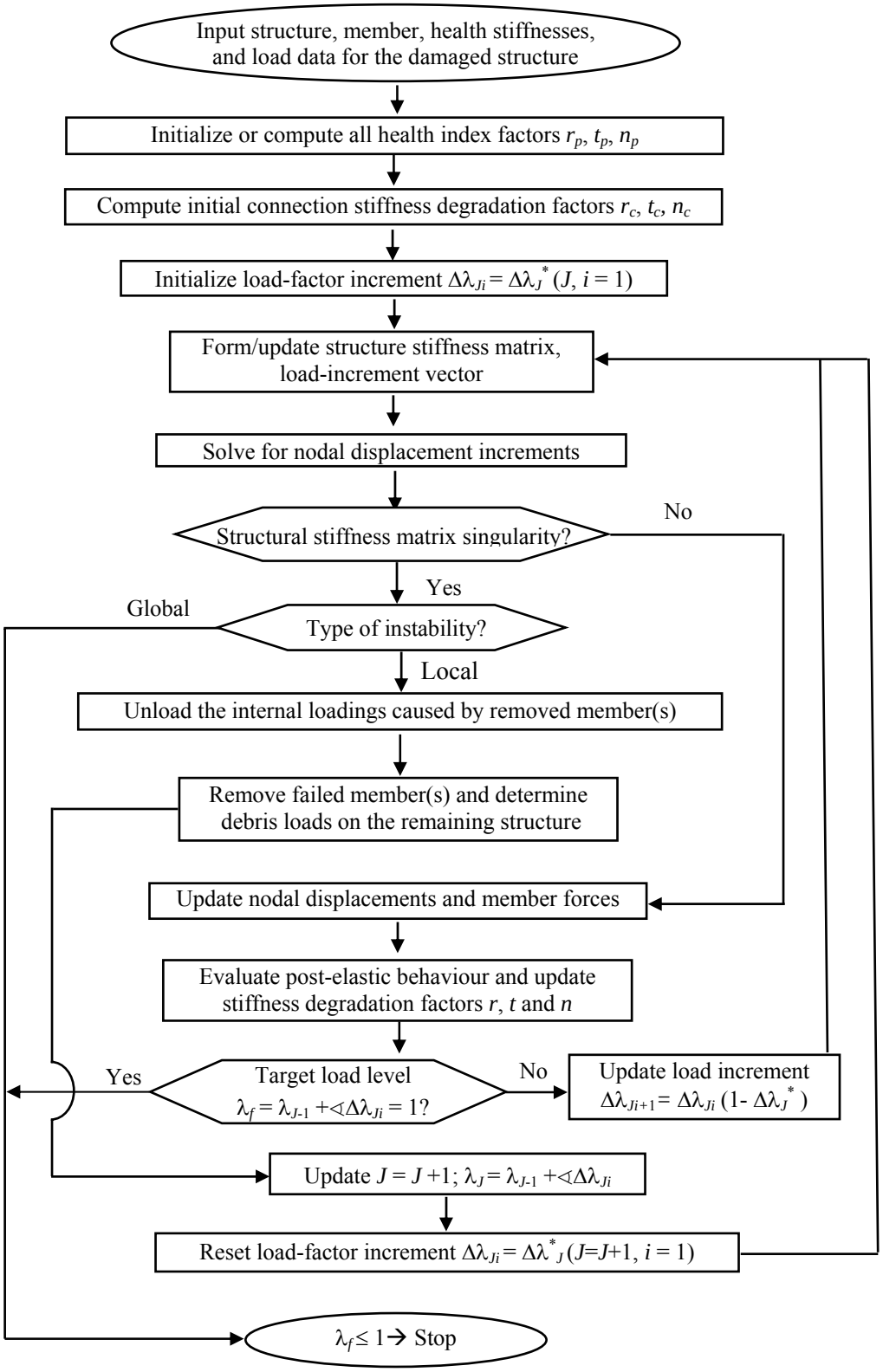

Figure 5.3 Flowchart for progressive-failure analysis

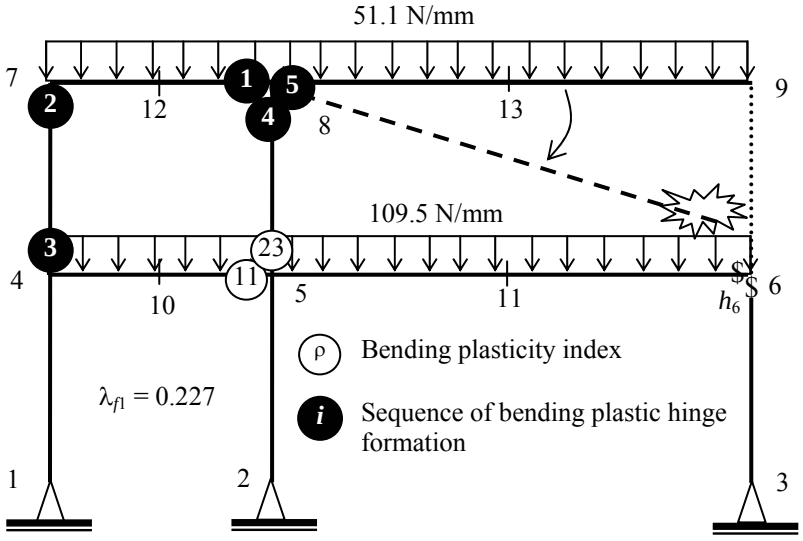

Figure 5.4 Example 1: Immediate damage propagation after failure of column C_{69} due to an initial abnormal loading event

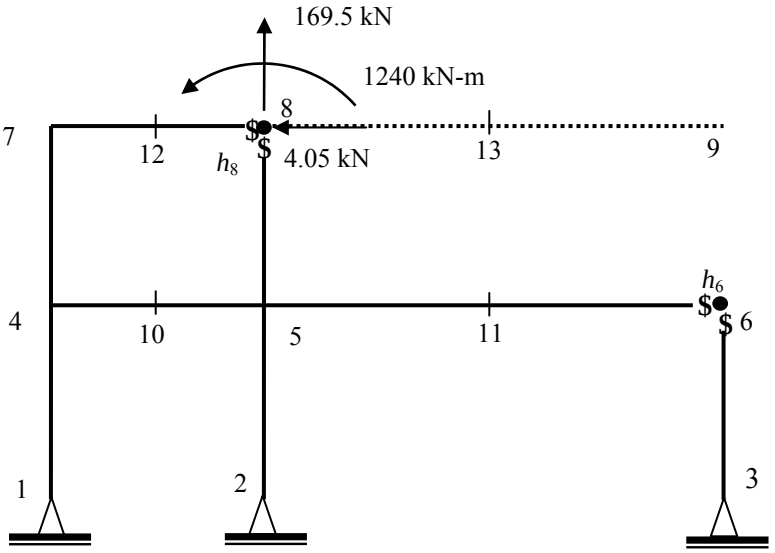

Figure 5.5 Example 1: Unloading after fracture of beam B_{89} at node 8

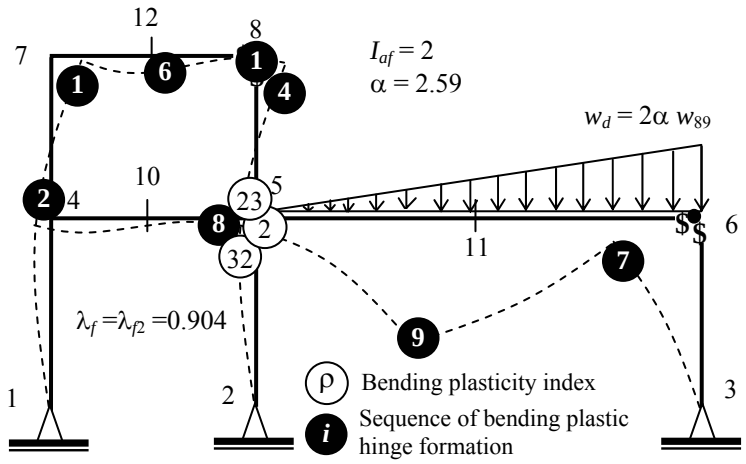

Collapse performance with h = 1

Figure 5.6 Example 1: Progressive damage propagation after failure of beam 89

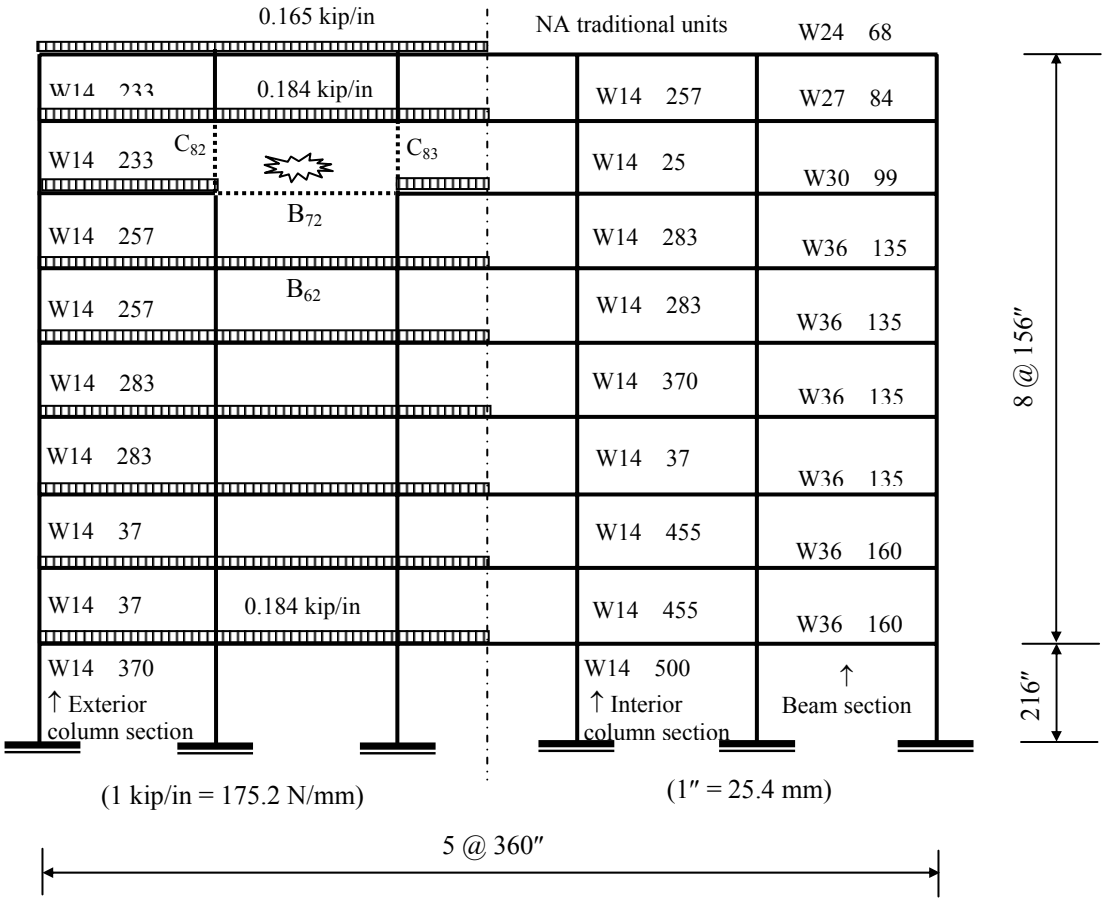

Figure 5.7 Example 2 (Los Angeles): Initial local damage due to interior explosion at 8th storey level (Stage 0)

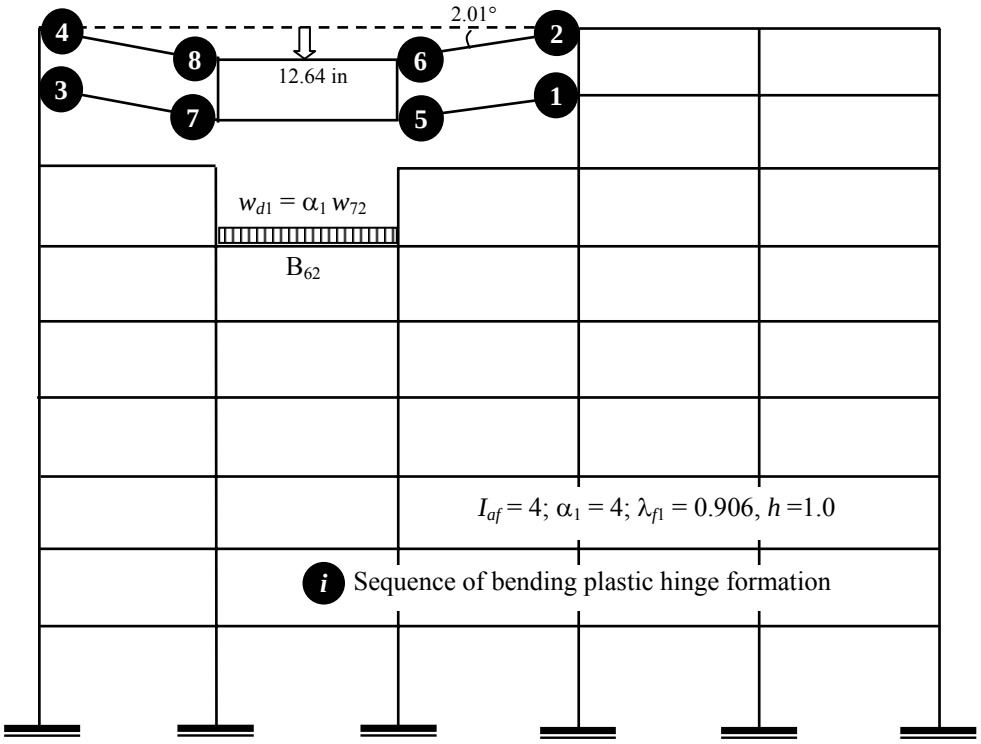

Figure 5.8 Example 2 (Los Angeles): Immediate damage propagation after initial abnormal loading (Stage 1)

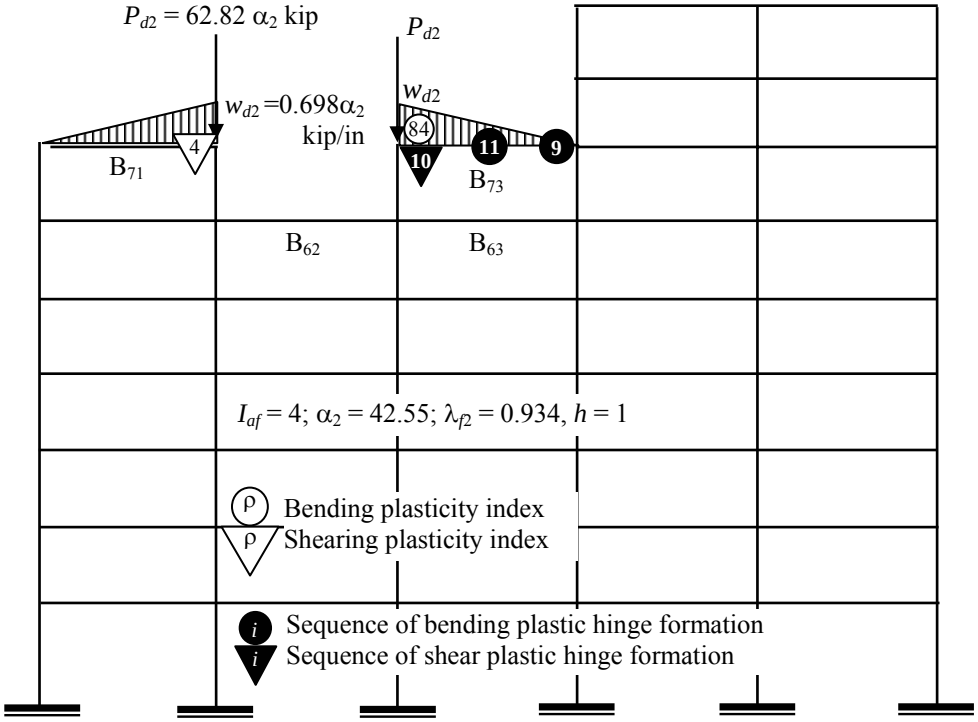

Figure 5.9 Example 2 (Los Angeles): Upper stories fall as debris loads and beam B_{73} fails (Stage 2)

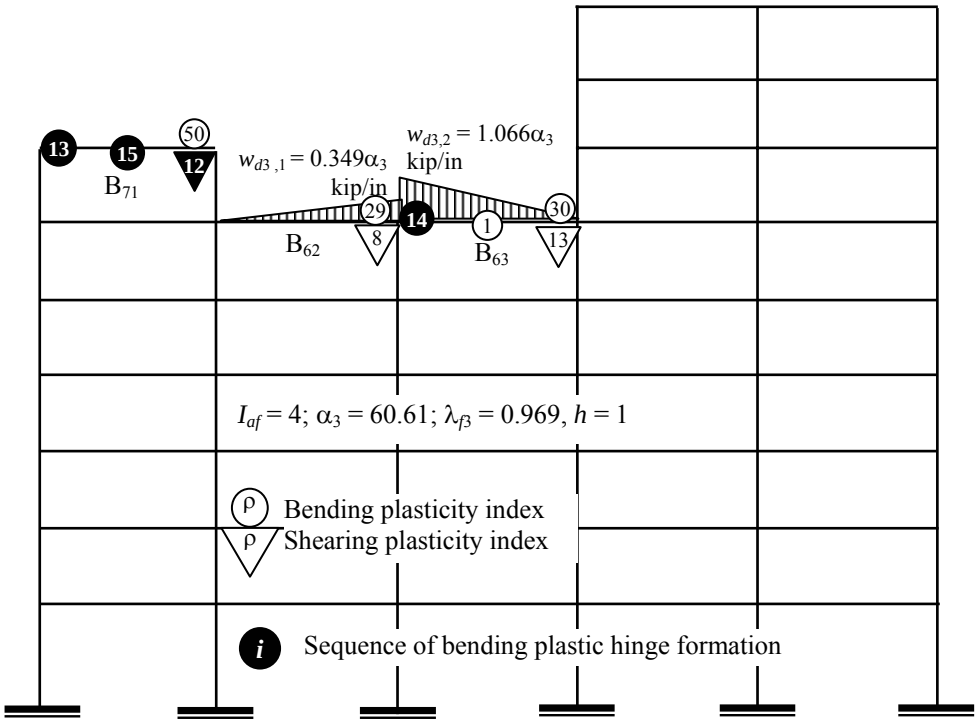

Figure 5.10 Example 2 (Los Angeles): Beam B_{73} falls as debris loading and fails beam B_{71} (Stage 3)

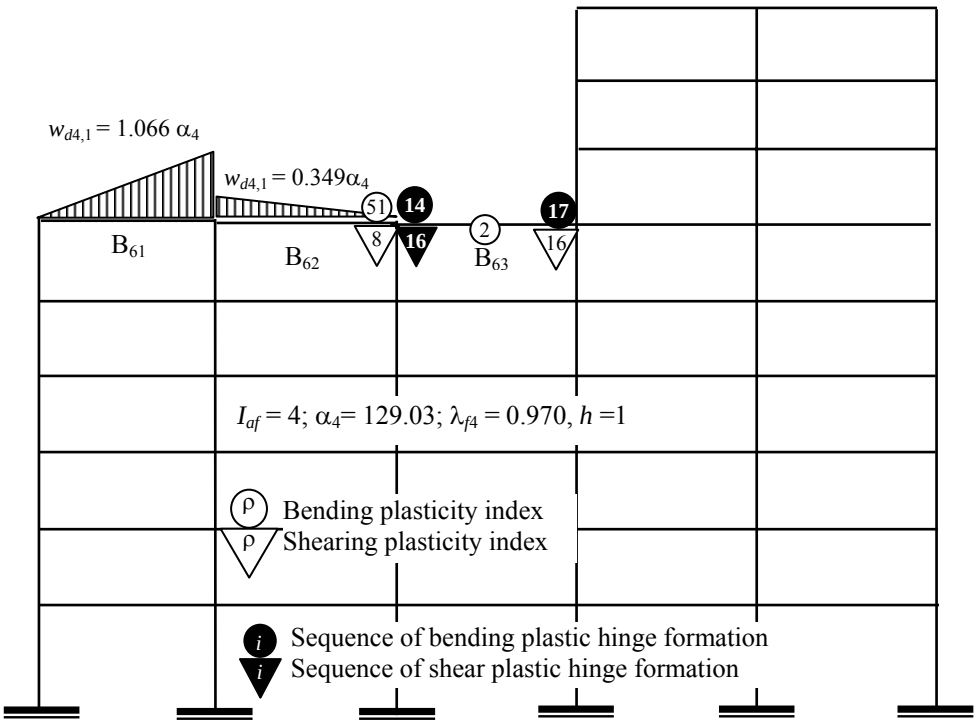

Figure 5.11 Example 2 ((Los Angeles): Beam B_7 falls as debris loads and fails beam B_{63} (Stage 4)

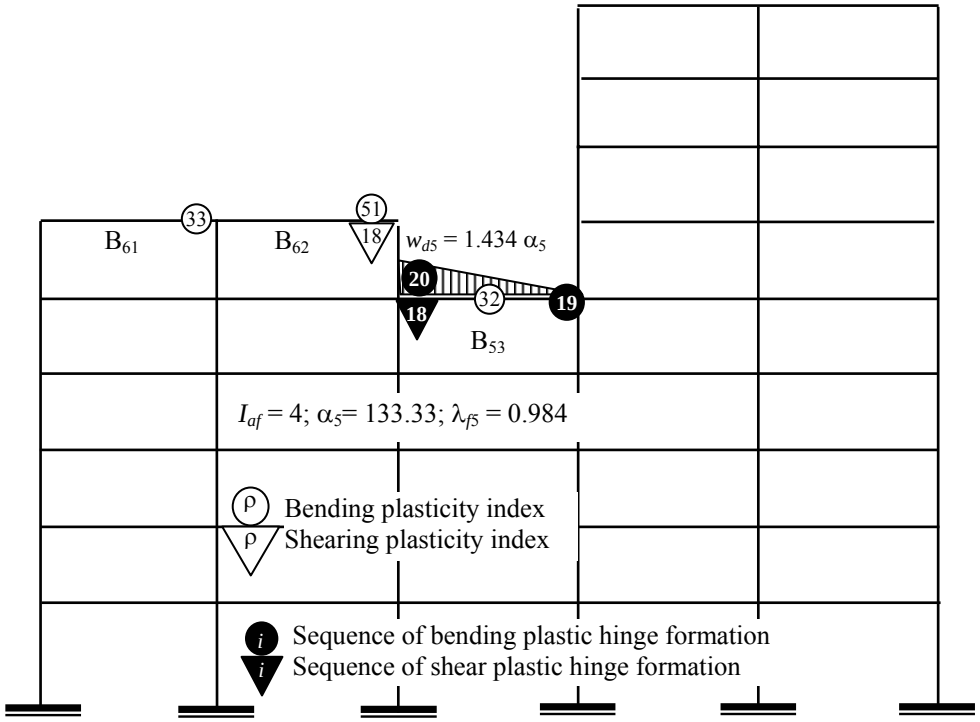

Figure 5.12 Example 2 (Los Angeles): Beam B_{63} falls as debris loads and fails beam B_{53} (Stage 5)

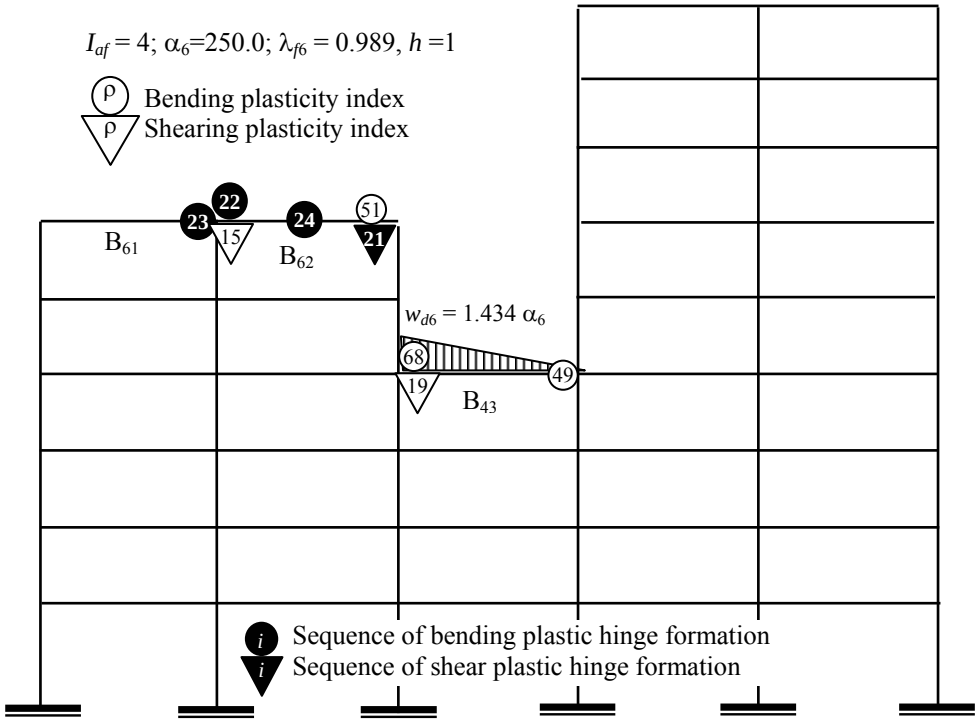

Figure 5.13 Example 2 (Los Angeles): Beam B_{53} falls as debris loads and fails beam B_{62} (Stage 6)

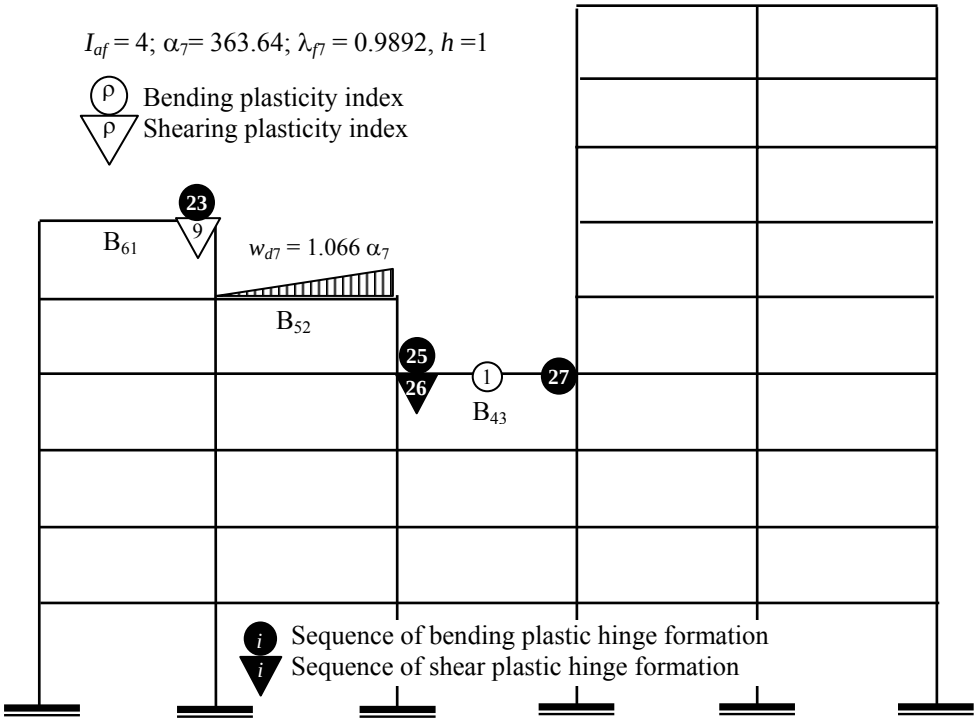

Figure 5.14 Example 2 (Los Angeles): Beam B_{62} falls as debris loads and fails beam B_{43} (Stage 7)

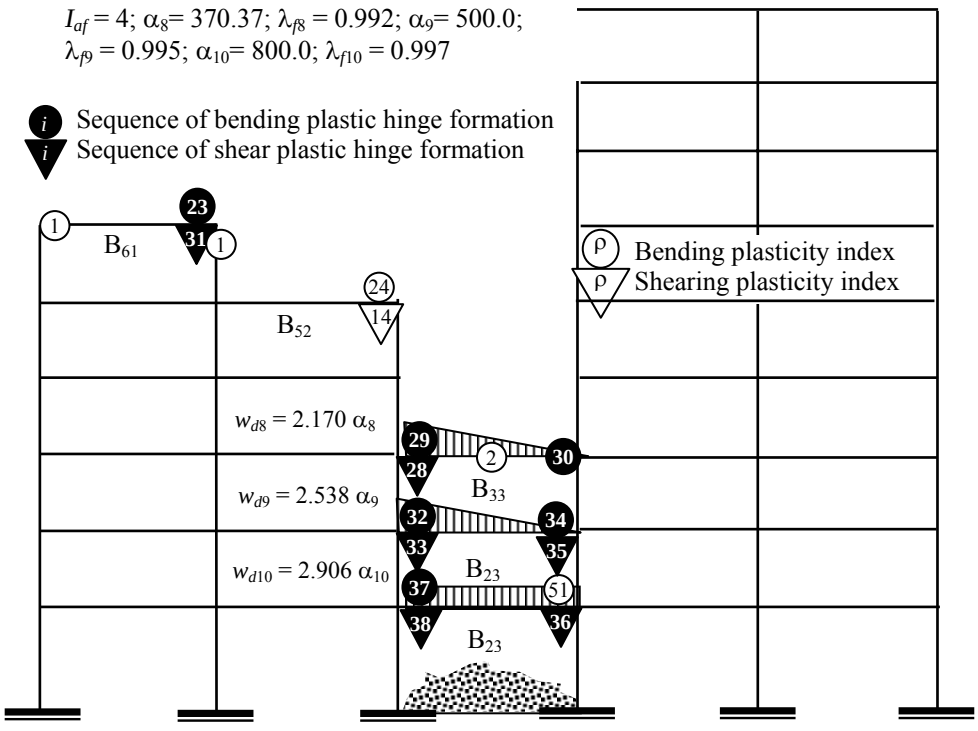

Figure 5.15 Example 2 (Los Angeles): Beams B_{33}, B_{23} and B_{13} progressively fail and fall to ground level (Stages 8, 9, and 10)

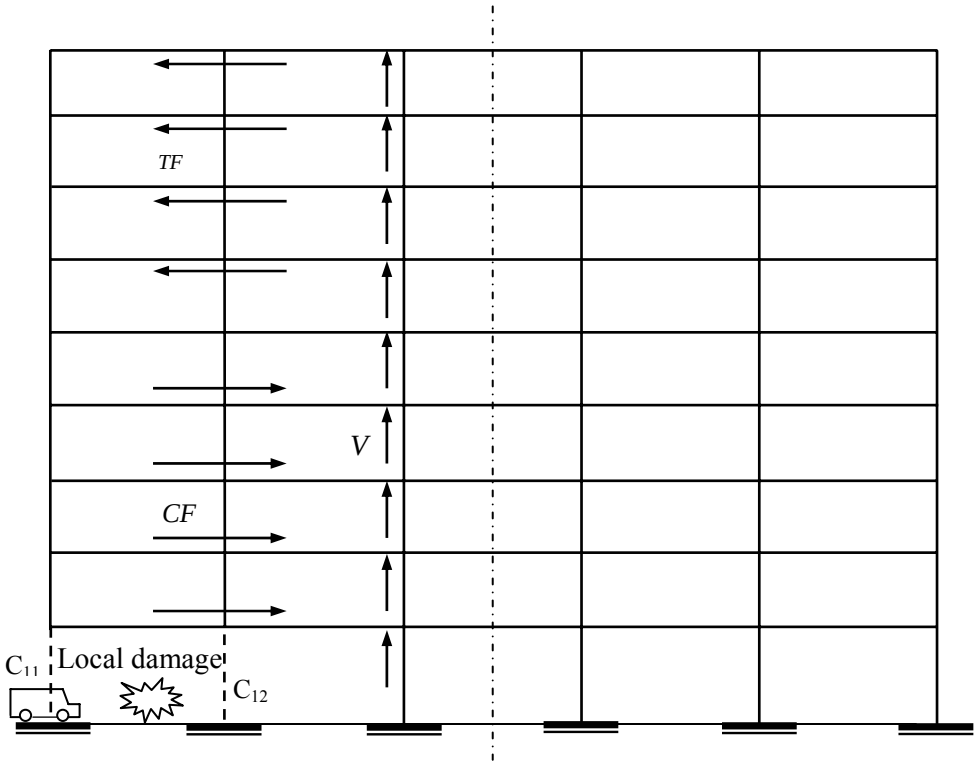

Figure 5.16 Example 3 (Los Angeles): Vehicle collision with explosion

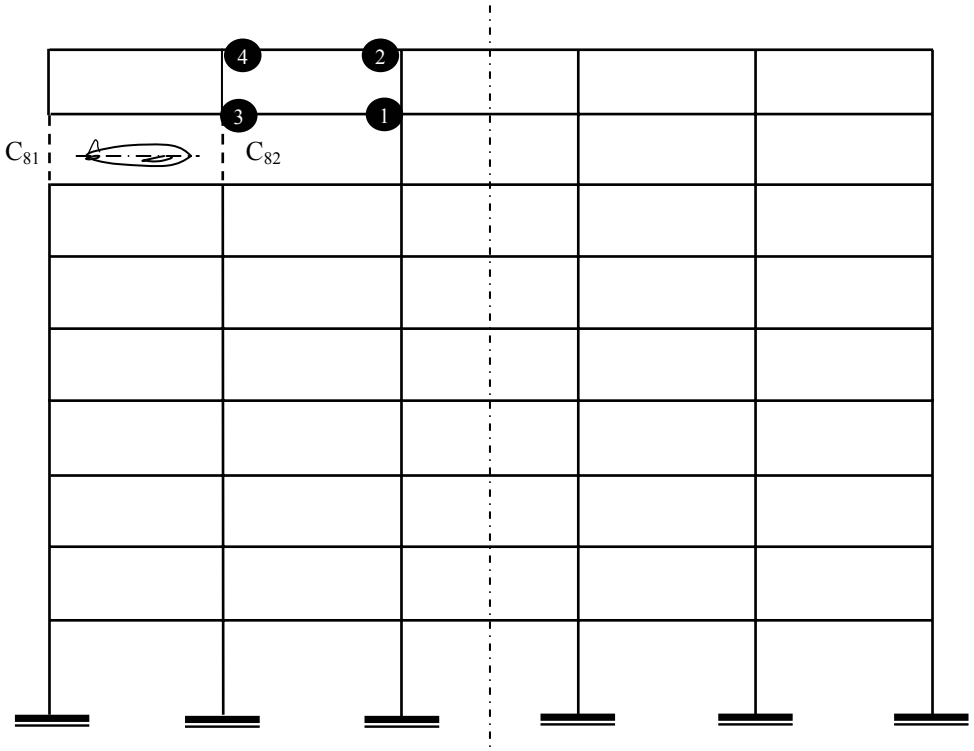

Figure 5.17 Example 4 (Los Angeles): Local damage after airplane impact

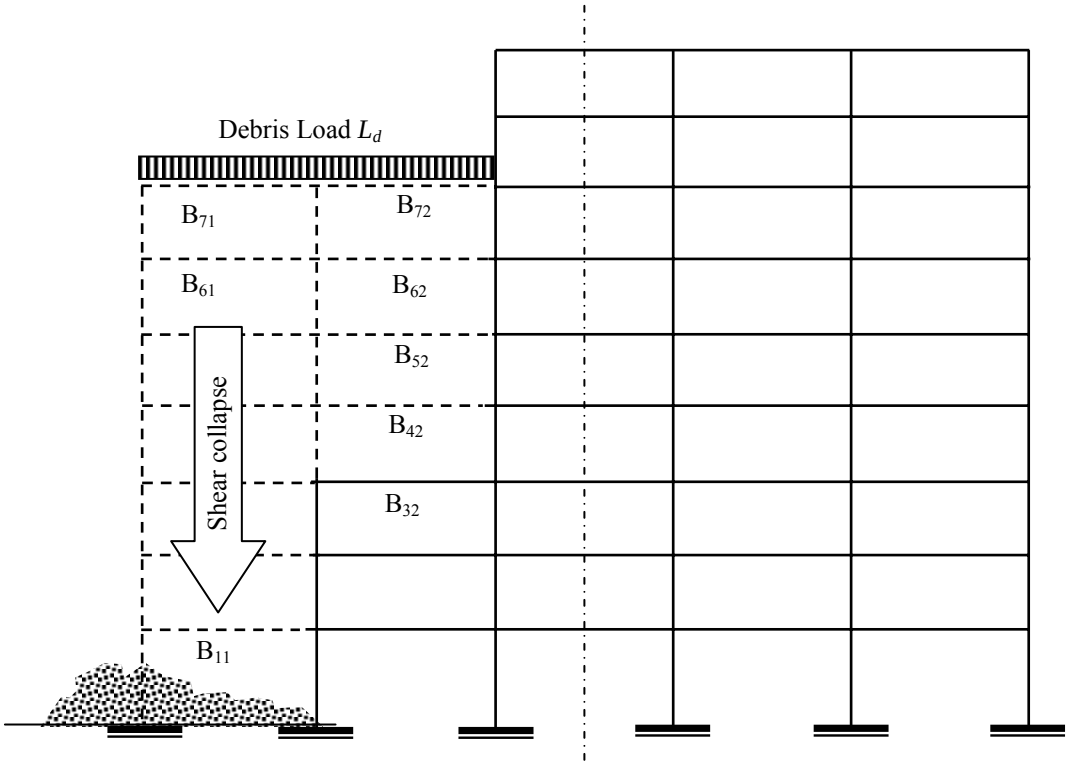

Figure 5.18 Example 4 (Los Angeles): Progressive collapse to ground level

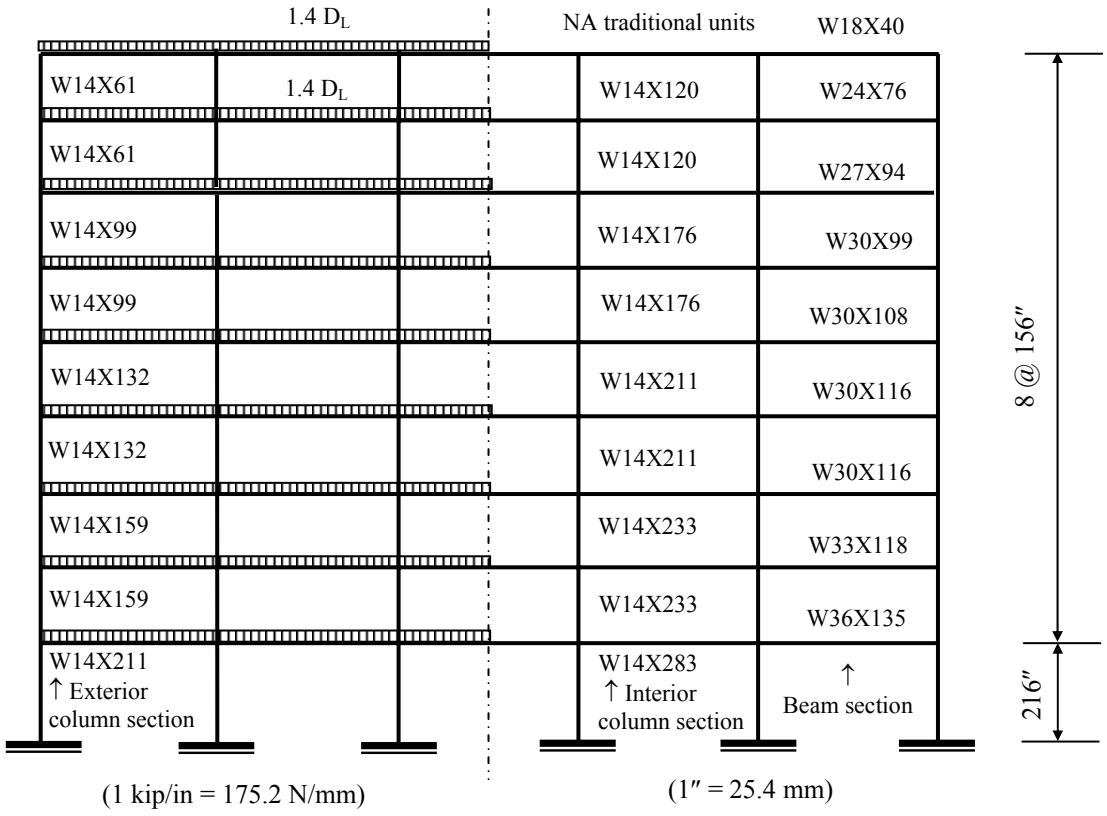

Figure 5.19 Example 5 (Boston): Cross sections of beams and columns for building (FEMA 355c, 2000)

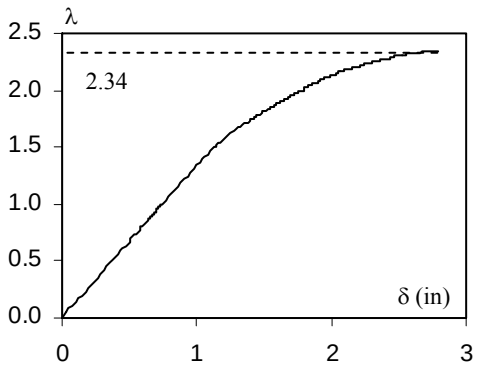

(a) Force-deflection relationship

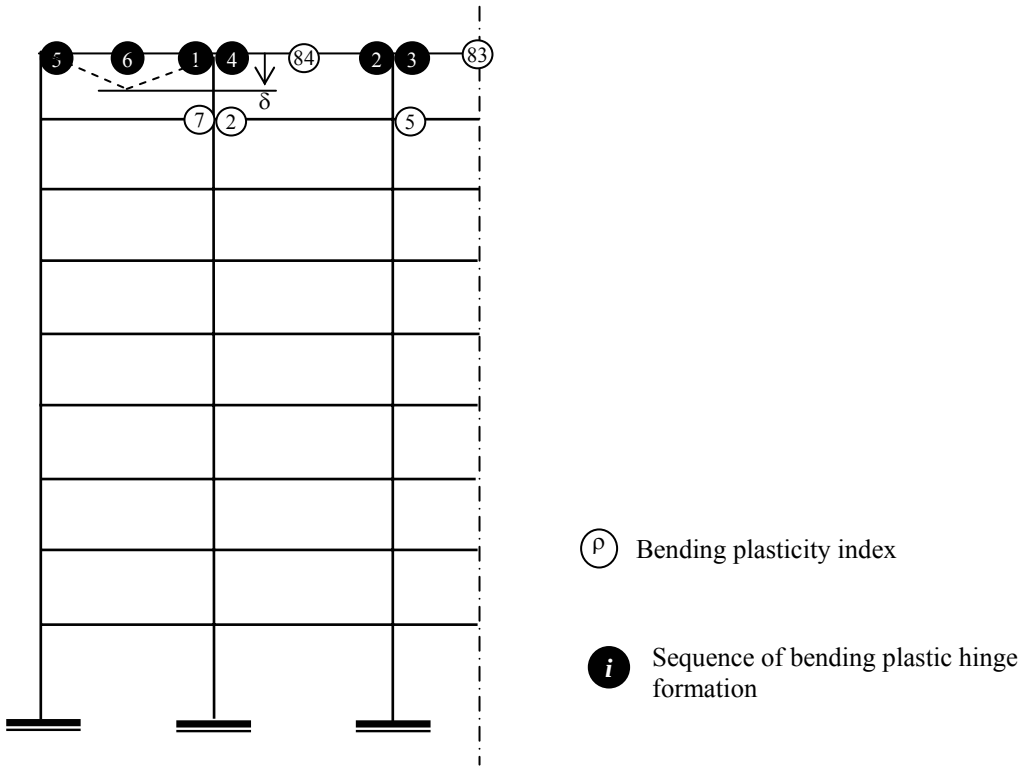

(b) Plasticity distribution

Figure 5.20 Example 5 (Boston): Results of nonlinear analysis of Boston building

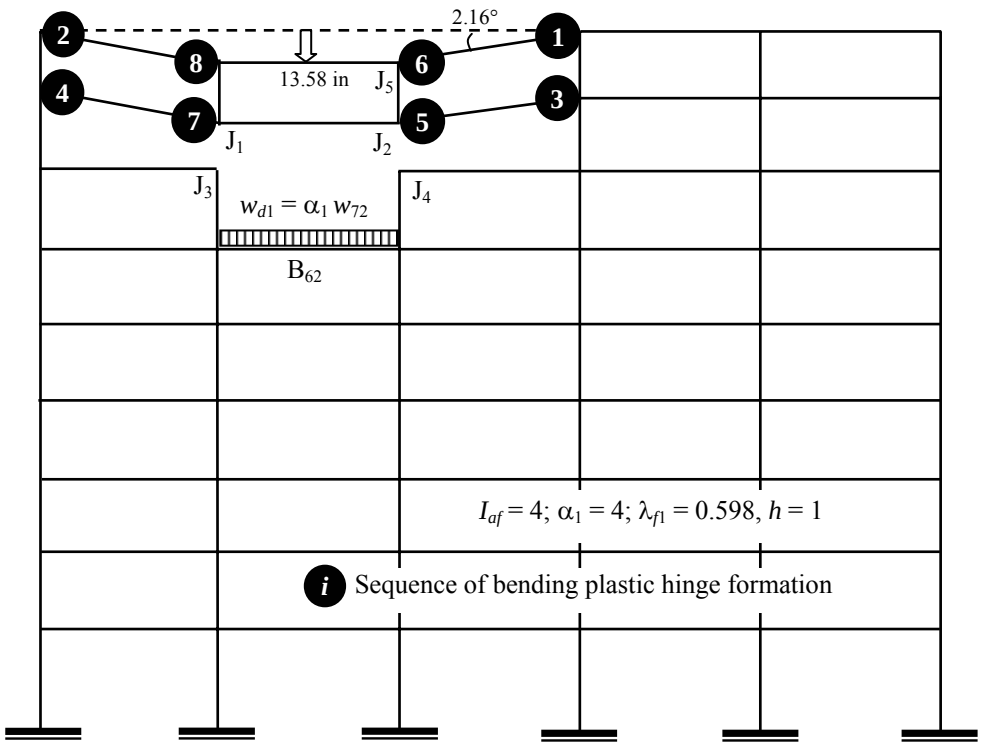

(a) Collapse mechanism

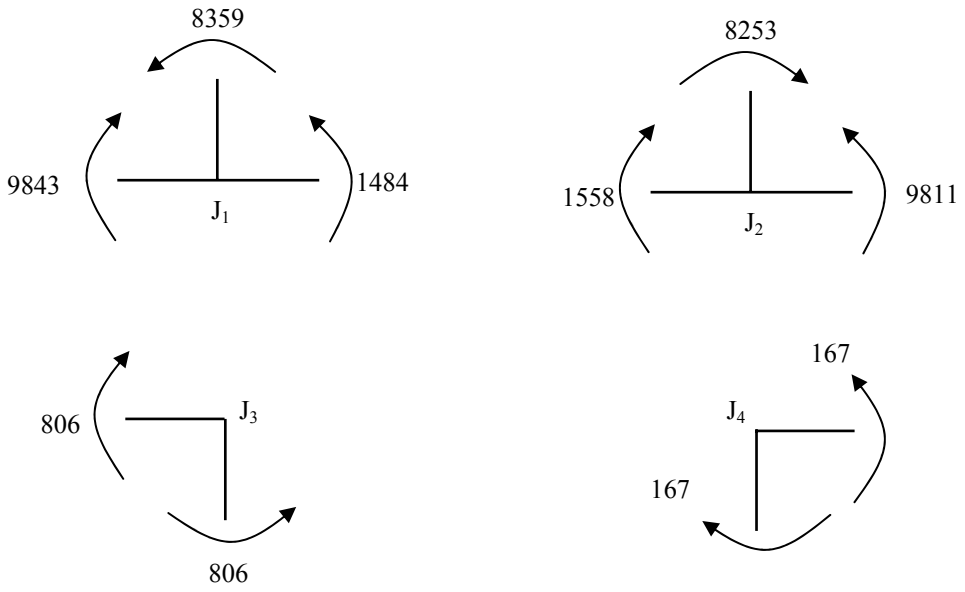

(b) Moments at the joints (kips-in)

Figure 5.21 Example 5 (Boston): Immediate damage propagation after initial abnormal loading without accounting for connection damage (Stage 1)

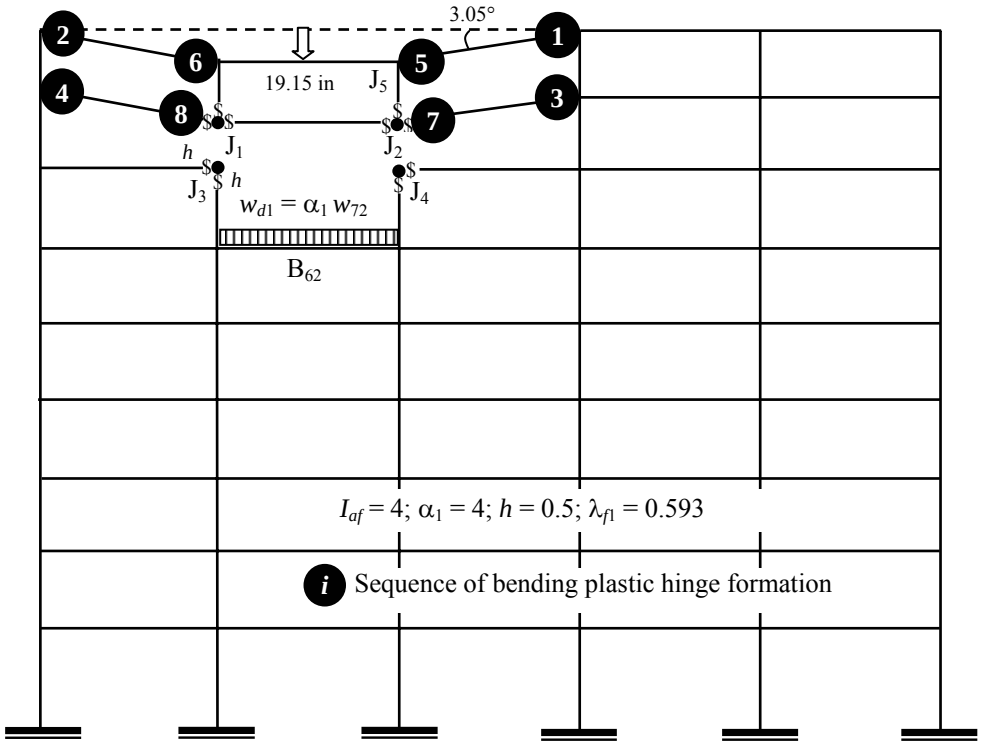

(a) Collapse mechanism

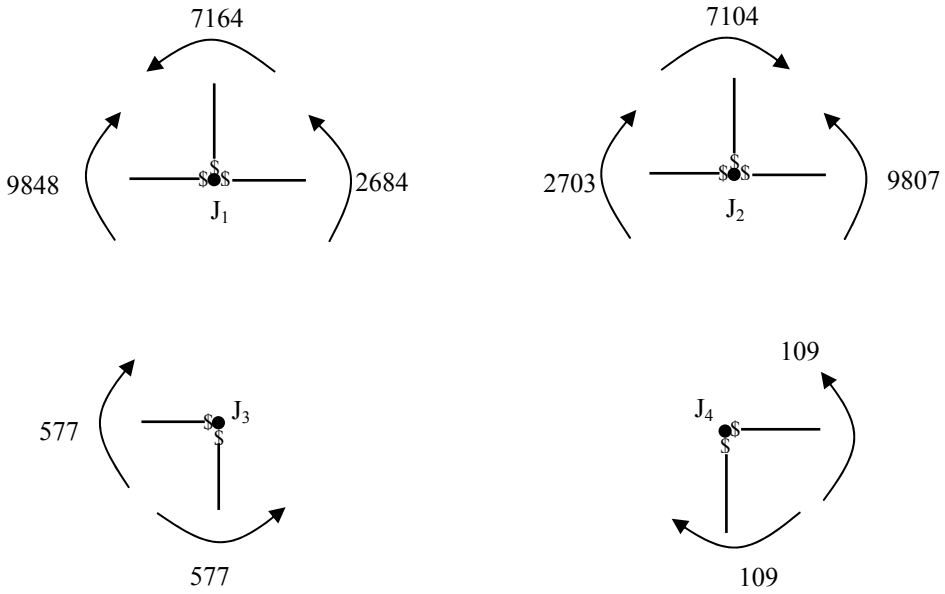

(b) Moments at the joints (kips-in)

Figure 5.22 Example 5 (Boston): Immediate damage propagation after initial abnormal loading with accounting for connection damage (Stage 1)

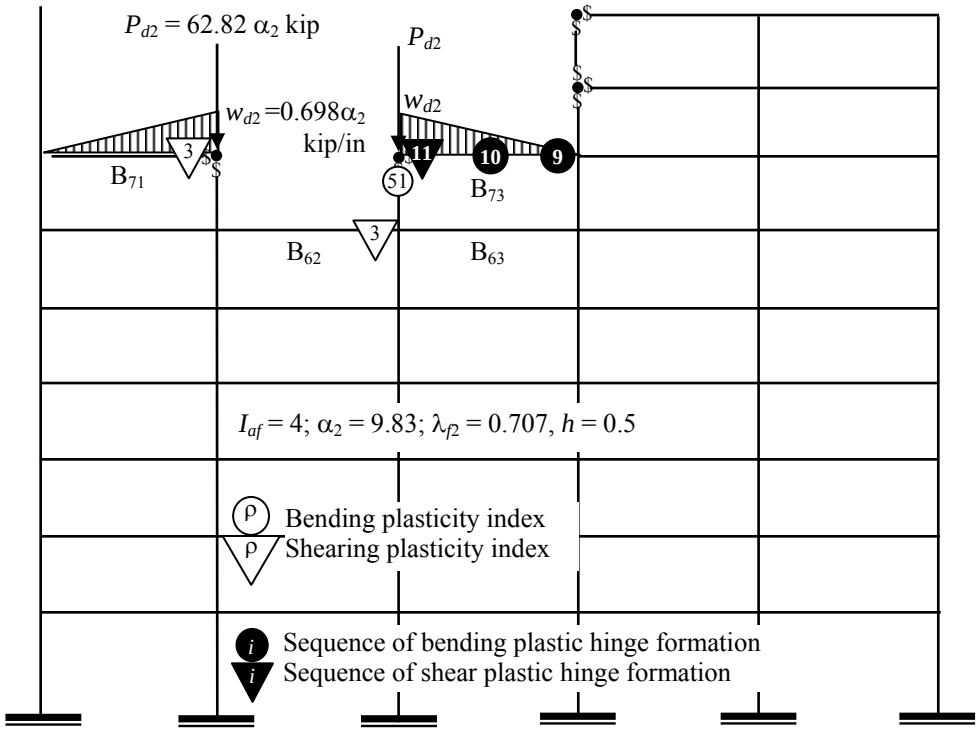

Figure 5.23 Example 5 (Boston): Upper stories fall as debris loads and beam B_{73} fails (Stage 2)

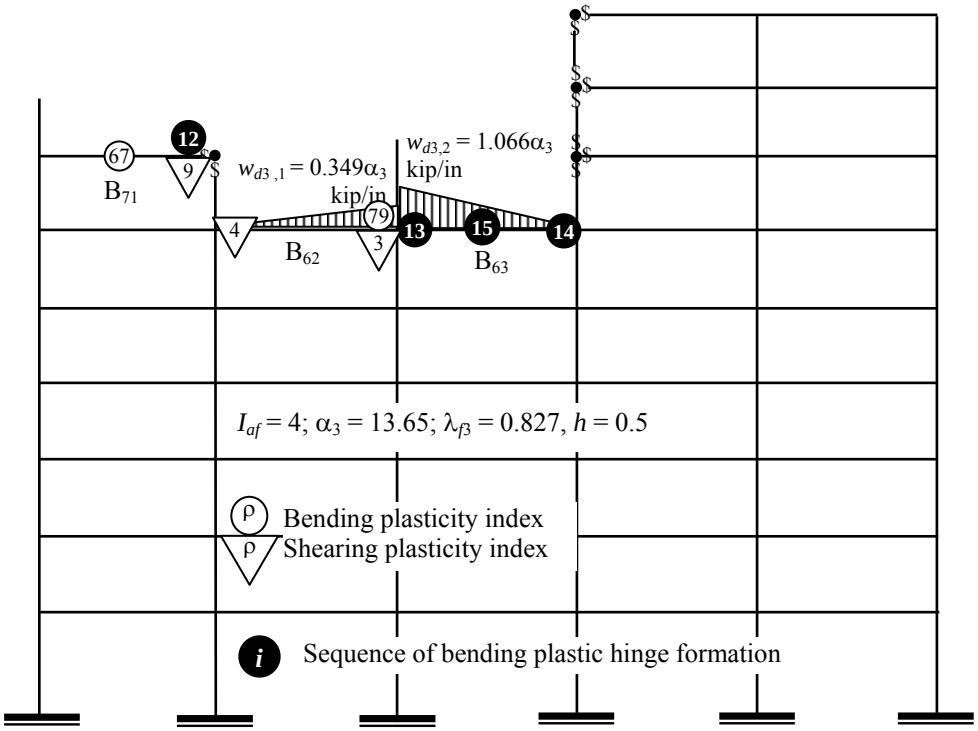

Figure 5.24 Example 5 (Boston): Beam B_{73} falls as debris loading and fails beam B_{63} (Stage 3)

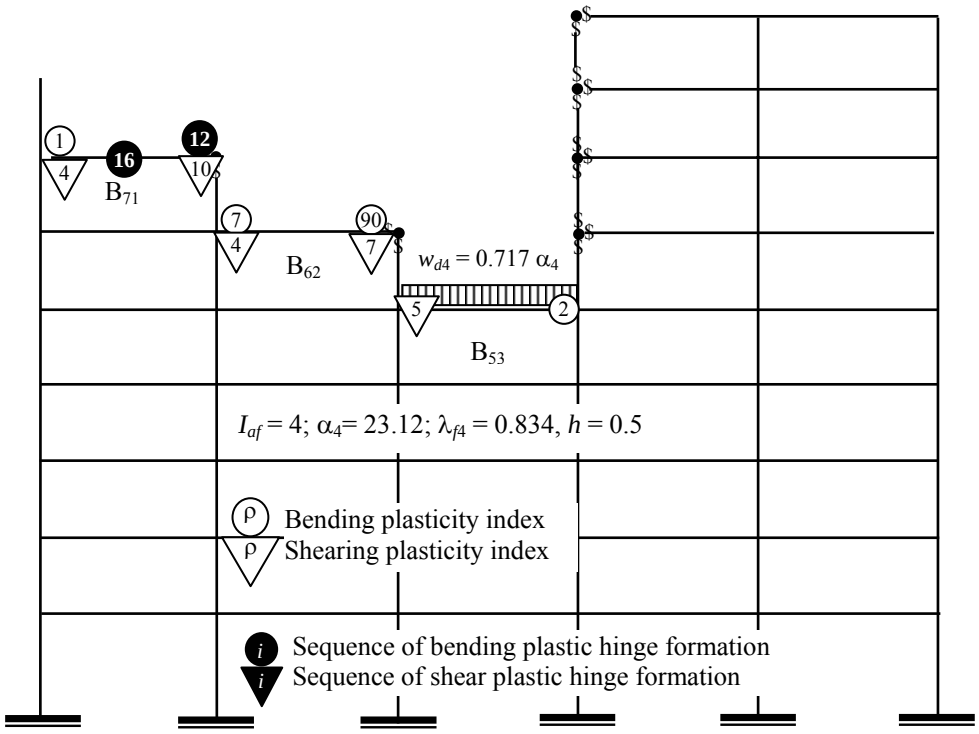

Figure 5.25 Example 5 (Boston): Beam B_{63} falls as debris loading and local instability occurs (Stage 4)

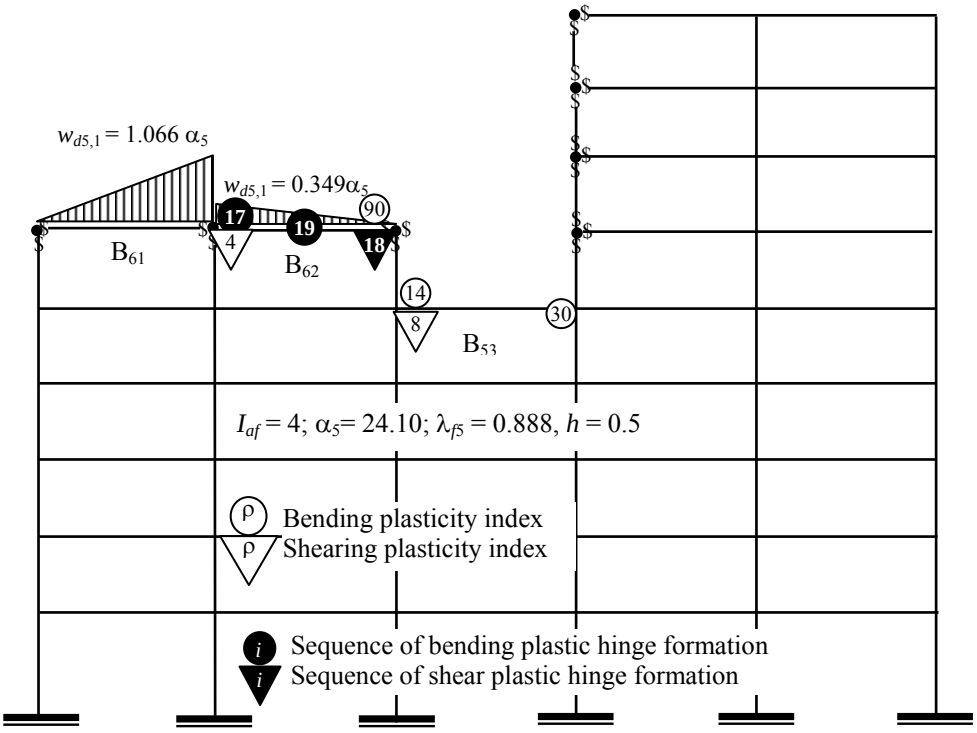

Figure 5.26 Example 5 ((Boston): Beam B_{71} falls as debris loading and beam B_{62} fails (Stage 5)

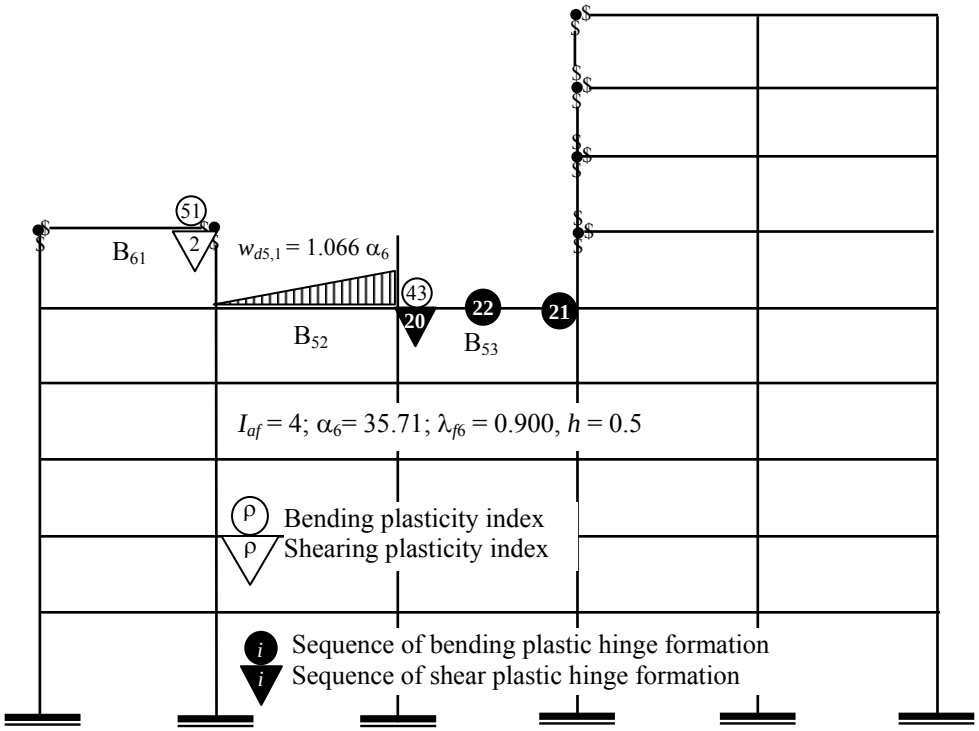

Figure 5.27 Example 5 (Boston): Beam B_{62} falls as debris loading and beam B_{53} fails (Stage 6)

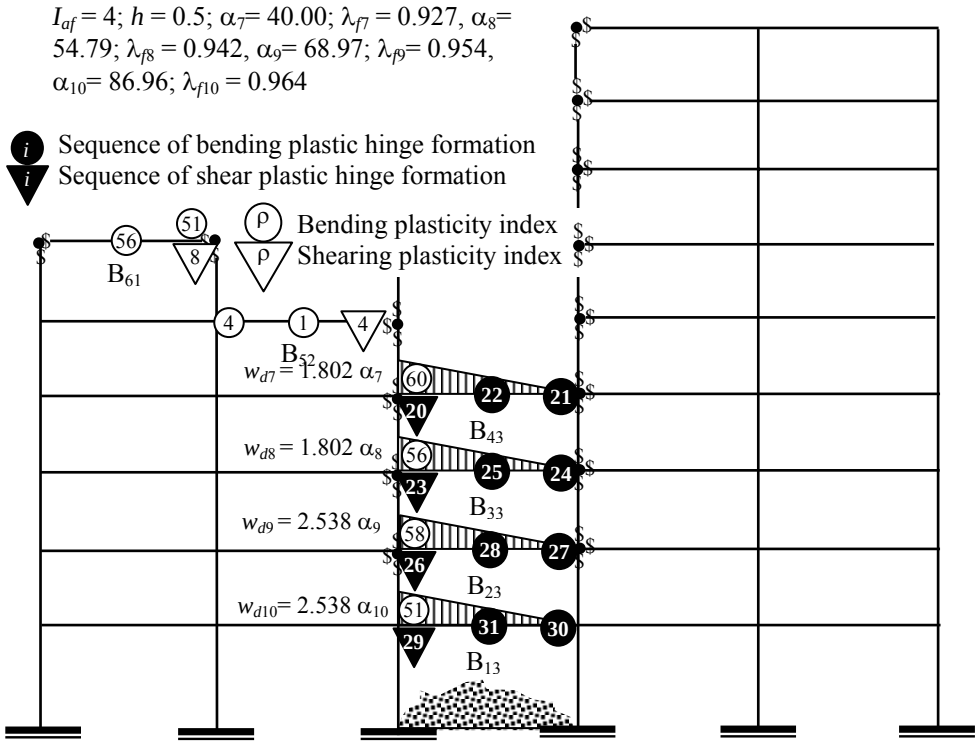

Figure 5.28 Example 5 (Boston): Beams B_{33}, B_{23} and B_{13} progressively fail and fall to ground level (Stages 7, 8, 9, and 10)

Table 5.1 Deformation limits for structural steel (DoD 2005)

Component	LLOP		M LOP and HLOP	
	Ductility	Rotation(°)	Ductility	Rotation(°)
Beams with seismic section	20	12	10	6
Beams with compact section	5	-	3	-
Beams with non-compact section	1.2	-	1	-
Columns and beam-columns	3	-	2	-
Rigid connections with a welded beam flange or cover plated	-	2.0	-	1.5
Rigid connections with reduced beam section	-	2.6	-	2.0
Semirigid connections with limit state governed by rivet shear or flexural yielding of plate, angle, or T-section	-	2.0	-	1.5
Semirigid connections with limit state governed by high strength bolt shear, tension failure of rivet or bolt, or tension failure of plate, angle, or T-section	-	1.3	-	0.9

Table 5.2 Example 1: Member forces at load level $\lambda_f = 0.227$ and $\lambda_f = 0.904$

Mem	End	Before unloading (Figure 5.4)			After unloading (Figure 5.5)			Just before collapse (Figure 5.6)		
		P (kN)	*V* (kN)	*M* (kN-m)	*P* (kN)	*V* (kN)	*M* (kN-m)	*P* (kN)	*V* (kN)	*M* (kN-m)
C_{41}	E4	41.30	-0.38	2.20	-95.26	-0.05	0.30	-311.2	3.40	58.66
C_{52}	E5	-594.9	36.67	-222.50	-314.90	22.68	-138.80	-1462.	72.87	-73.37
C_{63}	E6	-201.1	-32.18	196.50	-175.00	-22.61	137.60	-1216.	-80.19	778.20
C_{47}	E4	-35.54	20.55	44.82	80.58	20.04	44.82	186.2	14.04	44.82
C_{74}	E7	35.54	-20.55	45.14	-80.58	-20.04	45.14	-186.2	-14.04	45.14
C_{58}	E5	275.6	-24.65	760.30	-9.96	-20.05	231.00	95.5	-13.98	271.80
C_{85}	E8	-275.6	24.65	-853.40	9.96	20.05	-321.20	-95.5	13.98	-321.2
B_{45}	E4	20.17	-5.76	-47.01	19.99	14.85	-45.03	17.43	125.20	-103.4
B_{54}	E5	-20.15	157.10	-449.30	-19.97	136.80	-326.80	-17.48	478.80	-974.5
B_{56}	E5	32.17	162.10	-88.42	22.60	188.60	235.00	76.37	888.40	776.5
B_{65}	E6	-32.18	201.10	-196.50	-22.61	175.40	-138.10	-80.19	1216.00	-778.6
B_{78}	E7	-20.55	-35.54	-45.14	-20.04	80.66	-45.10	-14.04	186.30	-45.1
B_{87}	E8	20.56	106.20	-386.80	20.05	-9.90	321.20	13.98	95.56	321.2
B_{89}	E8	4.09	169.50	1240.00	-	-	-	-	-	-

Sign convention of moment *M*, shear force *V*, and axial force *P* is consistent with the local numbering system in Figure 3.1.

Table 5.3 Example 1: Nodal displacements at load level $\lambda_f = 0.227$

Joint	Before unloading (Figure 5.4)			After unloading (Figure 5.5)		
	u_x (mm)	u_y (mm)	u_z (10^{-3})	u_x (mm)	u_y (mm)	u_z (10^{-3})
J_4	2.36	0.44	0.71	-0.27	-1.02	0.19
J_5	2.33	-0.73	-4.28	-0.31	-0.38	-2.37
J_6	2.25	-0.27	3.42	-0.36	-0.23	2.71
J_7	107.40	0.77	3.32	39.32	-1.76	-9.49
J_8	107.50	-1.00	-44.76	39.39	-0.37	-18.00
J_9	107.50	-927.50	-68.94	-	-	-

Positive horizontal translation u_x is to the right; positive vertical translation u_y is upward; positive rotation u_z is counterclockwise

Table 5.4 Example 1: Effect of connection damage on load capacity (λ_f)

h_8 \ h_6	0.00	0.05	0.10	0.20	0.50	0.75	1.00
1.00	0.726	0.747	0.773	0.835	0.884	0.897	0.904
0.50	0.726	0.747	0.773	0.835	0.884	0.897	0.904
0.05	0.726	0.747	0.773	0.835	0.884	0.897	0.904

Table 5.5 Example 1: Degradation factors, internal forces, and load capacity (h = 0.5)

Member	End	First stage (λ_{f1} = 0.226)				Second stage (λ_f = 0.884)			
		r	P(kN)	V(kN)	M(kN-m)	r	P(kN)	V(kN)	M(kN-m)
C_{14}	E4	1.000	46.82	-0.92	5.16	1.000	-309.8	-0.32	17.43
C_{25}	E5	1.000	-602.3	27.85	-165.80	0.898	-1461	111.30	-601.40
C_{36}	E6	0.500	-199.0	-22.84	140.40	0.000	-1147	-115.10	759.30
C_{47}	E4	0.000	35.98	20.66	44.97	0.000	-182.8	17.20	44.97
C_{47}	E7	0.000	35.98	-20.66	45.40	0.000	-182.8	-17.20	45.40
C_{58}	E5	0.773	-276.1	-24.73	758.2	0.773	-92.65	-17.14	249.10
C_{58}	E8	0.000	-276.1	24.73	-850.8	0.000	-92.65	17.14	-320.40
B_{45}	E4	1.000	-19.75	-10.85	-50.13	1.000	-16.88	127.10	-62.32
B_{45}	E5	1.000	-19.74	162.2	-477.2	0.000	-16.93	463.60	-963.30
B_{56}	E5	1.000	-22.83	164.1	-115.3	0.990	-111.1	905.70	1316.00
B_{56}	E6	0.500	-22.84	199.0	-140.4	0.500	-115.1	1148.00	-759.50
B_{78}	E7	1.000	20.66	-35.98	-45.40	1.000	17.20	182.90	-45.36
B_{78}	E8	0.000	20.67	106.6	-389.2	0.000	17.14	92.70	320.40
B_{89}	E8	0.000	-4.062	169.5	1240	-	-	-	-

Note: h = 0.5; sign convention of internal forces follows the definition in Figure 3.1.

Table 5.6 Parameters of the connections (Kishi et al., 2004)

Connection	M_p (kN-m)	M_0 (kN-m)	R_{ce} (kN-m/rad)	R_{cp} (kN-m/rad)	γ
C1 (CF5-U10x49) (Mazroi, 1984)	387	261	893000	30300	1.18
C2 (CF6-U12x96) (Mazroi, 1984)	2773	598	1240000	56900	1.39
C3 (Test 2) (Ioannides, 1978)	387	181	632000	3320	0.83
C4 (CF5-U10x68) (Mazroi, 1984)	1240	261	893000	30300	1.18

Table 5.7 Example 1: Stiffness degradation factors for semirigid frame

Beam	End	r_{c0}	First stage (λ_{f1} = 0.226)				Second stage (λ_f = 0.863)			
			r_c	r_p	r	M	r_c	r_p	r	M
C_{14}	E4	1.000	1.000	1.000	1.000	-0.781	1.000	1.000	1.000	-8.943
C_{25}	E5	1.000	1.000	1.000	1.000	-246.2	1.000	0.680	0.680	-780.0
C_{36}	E6	1.000	1.000	1.000	1.000	208.4	1.000	0.000	0.000	785.6
C_{47}	E4	1.000	1.000	0.000	0.000	45.62	1.000	0.000	0.000	45.62
C_{47}	E7	1.000	1.000	0.000	0.000	45.58	1.000	0.000	0.000	45.58
C_{58}	E5	1.000	1.000	0.802	0.802	746.9	1.000	0.802	0.802	223.4
C_{58}	E8	1.000	1.000	0.000	0.000	-854.4	1.000	0.000	0.000	-308.8
B_{45}	E4	0.792	0.155	1.000	0.155	-44.83	0.155	1.000	0.155	-36.66
B_{45}	E5	0.792	0.136	1.000	0.136	-325.7	0.116	0.974	0.116	-521.1
B_{56}	E5	0.776	0.711	1.000	0.711	-175.0	0.140	0.993	0.140	1078
B_{56}	E6	0.776	0.701	1.000	0.701	-208.4	0.157	1.000	0.157	-785.9
B_{78}	E7	0.901	0.799	1.000	0.799	-45.58	0.799	1.000	0.799	-45.56
B_{78}	E8	0.901	0.046	0.000	0.000	-384.6	0.046	0.000	0.000	308.8
B_{89}	E8	0.878	0.197	0.000	0.000	1239	-	-	-	-
Note: $h_6 = h_8 = 1.0$, and M stands for end moment (kN-m)										

Table 5.8 Example 1: Accounting for connection damage and semi-rigid behaviour

Beam	End	r_{c0}	First stage (λ_{f1} = 0.226)				Second stage (λ_f = 0.859)			
			r_c	r_p	r	M	r_c	r_p	r	M
C_{14}	E4	1.000	1.000	1.000	1.000	2.166	1.000	1.000	1.000	8.185
C_{25}	E5	1.000	1.000	1.000	1.000	-188.1	1.000	0.680	0.680	-628.5
C_{36}	E6	1.000	1.000	0.500	0.500	150.9	1.000	0.000	0.000	744.8
C_{47}	E4	1.000	1.000	0.000	0.000	45.53	1.000	0.000	0.000	45.53
C_{47}	E7	1.000	1.000	0.000	0.000	45.78	1.000	0.000	0.000	45.78
C_{58}	E5	1.000	1.000	0.802	0.802	746.1	1.000	0.802	0.802	231.3
C_{58}	E8	1.000	1.000	0.000	0.000	-853.4	1.000	0.000	0.000	-309.0
B_{45}	E4	0.792	0.152	1.000	0.152	-47.69	0.152	1.000	0.152	-53.70
B_{45}	E5	0.792	0.131	1.000	0.131	-339.9	0.115	0.846	0.113	-677.8
B_{56}	E5	0.776	0.686	1.000	0.686	-218.0	0.140	0.979	0.139	1075
B_{56}	E6	0.776	0.366	1.000	0.366	-150.9	0.083	1.000	0.083	-744.9
B_{78}	E7	0.901	0.799	1.000	0.799	-45.78	0.799	1.000	0.799	-45.75
B_{78}	E8	0.901	0.046	0.000	0.000	-385.6	0.023	0.000	0.000	309.0
B_{89}	E8	0.878	0.197	0.000	0.000	1239	-	-	-	-

Note: $h_6 = h_8 = 0.5$, and M stands for member end moment (kN-m)

Table 5.9 Example 2 (Los Angeles): Progressive-failure analysis of 5-bay 9-storey building frame

Stage J	Load λ_{fJ}	Failure Event	Debris Loading
0	0.0	Initial abnormal loading destroys members B_{72}, C_{82}, & C_{83} [Figure 5.7].	Beam B_{72} falls on lower beam B_{62} as dynamic debris loading [Figure 5.8].
1	0.906	Eight bending plastic hinges form and catenary action causes the upper stories of the three left bays to break away from the frame at column lines 1 and 4 [Figure 5.8].	The first and third bays of the upper stories impact on beams B_{71} & B_{73} as triangular distributed debris loading, while the second bay impacts on the 7^{th}-story column lines 2 and 3 as concentrated debris loads [Figure 5.9].
2	0.934	Beam B_{73} forms a bending plastic hinge at its right end and breaks away from the frame at its left end as a shear plastic hinge forms there. It then deforms as a rigid-body cantilever mechanism before also breaking away from the frame at its right end [Figure 5.9].	Half of the second bay of the upper stories falls further as triangular distributed debris loading on lower beam B_{62}. Beam B_{73} and its previous debris loads fall on lower beam B_{63} as triangular distributed debris loading [Figure 5.10].
3	0.969	Beam B_{71} fails and breaks away from the frame in the same way that beam B_{73} does as in analysis stage 2 [Figure 5.10].	Beam B_{71} and its previous debris loads fall on lower beam B_{61} as triangular distributed debris loading, and the other half of the second bay of the upper stories further falls as triangular distributed debris loading on lower beam B_{62} [Figure 5.11].
4	0.970	Beam B_{63} forms a bending plastic hinge at its right end and breaks away from the frame at its left end as a shear plastic hinge and a bending plastic hinge form there. It then deforms as a rigid-body cantilever mechanism before breaking away completely from the frame [Figure 5.11].	Beam B_{63} and its previous debris loads fall on lower beam B_{53} as triangular distributed debris loading, [Figure 5.12].
5	0.984	Beam B_{53} fails and breaks away from the frame in the same way that beam B_{63} does as in analysis stage 4 [Figure 5.12].	Beam B_{53} and its previous debris loads fall on lower beam B_{43} as triangular distributed debris loading [Figure 5.13].
6	0.989	Beam B_{62} fails and breaks away from the frame in the same way that beam B_{71} does as in analysis stage 3 [Figure 5.13].	Beam B_{62} and its previous debris loads fall on lower beam B_{51} as triangular distributed debris loading [Figure 5.14].
7	0.9892	Beam B_{43} fails and breaks away from the frame in the same way that beam B_{53} does as in analysis stage 5 [Figure 5.14].	Beam B_{43} and its previous debris loads fall on lower beam B_{33} as triangular distributed debris loading [Figure 5.15].
8	0.992	Beam B_{33} fails and breaks away from the frame in the same way that beam B_{43} does as in analysis stage 7 [Figure 5.15].	Beam B_{33} and its previous debris loads fall on lower beam B_{23} as triangular distributed debris loading [Figure 5.15].
9	0.995	Beam B_{23} breaks away from the frame at once as bending + shear plastic hinges form at its two ends almost simultaneously [Figure 5.15].	Beam B_{23} and its previous debris loads fall on lower beam B_{13} as uniformly distributed debris loading [Figure 5.15].
10	0.997	Beam B_{13} fails and breaks away from the frame in the same way as beam B_{33} does as in analysis stage 8. The progressive collapse ends [Figure 5.15].	Beam B_{13} and all the debris loading accumulated from above fall to ground level. The progressive-failure analysis of the frame is terminated [Figure 5.15].

Table 5.10 Example 5 (Boston): Progressive-failure analysis of 5-bay 9-storey building frame

Stage J	Load λ_{fJ}	Failure Event	Debris Loading
0	0.0	Same as in Example 2, initial abnormal loading destroys members B_{72}, C_{82}, & C_{83} [Figure 5.7].	Same as in Example 2, beam B_{72} falls on lower beam B_{62} as dynamic debris loading [Figure 5.8].
1	0.598	Eight bending plastic hinges form and catenary action causes the upper stories of the three left bays to break away from the frame at column lines 1 and 4 [Figure 5.22(a)].	The first and third bays of the upper stories impact on beams B_{71} & B_{73} as triangular distributed debris loading, while the second bay impacts on the 7th story column lines 2 and 3 as concentrated debris loads [Figure 5.23].
2	0.707	Beam B_{73} forms a bending plastic hinge at its right end and breaks away from the frame at its left end as a shear plastic hinge forms there. It then deforms as a rigid-body cantilever mechanism before also breaking away from the frame at its right end [Figure 5.23].	Half of the second bay of the upper stories falls further as triangular distributed debris loading on lower beam B_{62}. Beam B_{73} and its previous debris loads fall on lower beam B_{63} as triangular distributed debris loading [Figure 5.24].
3	0.827	Beam B_{63} fails and breaks away from the frame once the three bending hinges form [Figure 5.24].	Beam B_{63} and its previous debris loads fall on lower beam B_{53} as uniformly distributed debris loading, [Figure 5.25].
4	0.834	Portal frame, including beam B_{71} and columns C_{71} and C_{72}, fails and breaks away due to local inelastic instability [Figure 5.25].	Portal frame (B_{71}, C_{71}, C_{72}) and its previous debris loads fall on lower beams B_{61} and B_{62} as triangular distributed debris loading, [Figure 5.26].
5	0.888	Beam B_{62} fails and breaks away from the frame in the same way that beam B_{73} does as in analysis stage 2 [Figure 5.26].	Beam B_{62} and its previous debris loads fall on lower beam B_{42} as triangular distributed debris loading [Figure 5.27].
6	0.900	Beam B_{53} fails and breaks away from the frame in the same way that beam B_{62} does as in analysis stage 5 [Figure 5.27].	Beam B_{53} and its previous debris loads fall on lower beam B_{52} as triangular distributed debris loading [Figure 5.28].
7	0.927	Beam B_{43} fails and breaks away from the frame in the same way that beam B_{53} does as in analysis stage 6 [Figure 5.28].	Beam B_{43} and its previous debris loads fall on lower beam B_{33} as triangular distributed debris loading [Figure 5.28].
8	0.942	Beam B_{33} fails and breaks away from the frame in the same way that beam B_{43} does as in analysis stage 7 [Figure 5.28].	Beam B_{33} and its previous debris loads fall on lower beam B_{23} as triangular distributed debris loading [Figure 5.28].
9	0.954	Beam B_{23} fails and breaks away from the frame in the same way that beam B_{13} does as in analysis stage 8 [Figure 5.28].	Beam B_{23} and its previous debris loads fall on lower beam B_{13} as uniformly distributed debris loading [Figure 5.28].
10	0.964	Beam B_{13} fails and breaks away from the frame in the same way as beam B_{23} does as in analysis in the previous stage. The progressive collapse ends [Figure 5.28].	Beam B_{13} and all the debris loading accumulated from above fall to ground level. The progressive-failure analysis of the frame is terminated [Figure 5.28].

Chapter 6
Combined M-V- P Failure Criterion (Future Research)

With a view to future extension of the research work concerning progressive collapse, this chapter derives a failure criterion for a member section that is simultaneously under combined bending, shearing and axial forces at its plastic limit state. An energy functional is employed to develop the post-elastic force-deformation relationship for the cross-section. The relationship is then utilized to determine the plastic capacity of the cross-section by using the principle of maximum potential energy. From first variation and concavity principles, the energy functional is maximized to establish the three-dimensional yield surface defining the failure criterion. The results of a numerical study of the derived yield surface are compared with other results in the literature to check the validity of the proposed failure criterion. Lastly, the 3D yield surface is utilized in a numerical example to estimate the plastic failure behaviour of a structural component under impact debris loading.

As a future extension of the research work at the University of Waterloo, it is intended that the theoretical M-V-P interaction criterion developed in this chapter will be implemented in the computer program developed by this thesis study, to investigate the effect of the 3D member failure criterion on the outcome of progressive-failure analysis of steel frameworks subjected to abnormal loading.

6.1 Introduction

The post-elastic interaction between bending moment and axial force (M+P) at the plastic limit has been long studied for beam-column components (e.g., Chen & Otsuta 1977; AISC, 2001; CISC, 2004). The similar interaction between bending moment and shear force (M+V) has also been investigated (e.g., Drucker 1956; Hodge, 1957); however, only in some special cases is this latter interaction considered (AISC, 2001; CISC, 2004) because the effect of shear force on plastic failure for slender members is negligible (Hodge, 1957). The M+P and M+V interactions have been both investigated earlier by this study in Sections 3.3.1 and 3.3.2. This chapter investigates the influence of simultaneously combined bending, shearing and axial forces (M+V+P) on the plastic failure of a member section.

For the influence of shear force, Drucker (1956) has conducted a thorough study of cantilever beams with rectangular cross-sections, and developed an empirical moment-shear plastic failure criterion. Various failure criteria and stress distributions across the member section are derived by assuming that only the web of a W-shaped cross section carries the shear force (Horne, 1951; Heyman & Dutton, 1954). Heyman and Dutton's expression has proved to be in good agreement with

experimental results (Green & Hundy, 1957). By using plane stress slip-line field methods, the upper-bound solutions of plastic collapse loads have been obtained for cantilever beams with rectangular cross- sections (Green, 1954; Ranshi et al., 1976; Chakrabarty, 2000). More general investigations of the post-elastic interaction of bending moment, shear force and axial force have also been conducted (Hodge, 1957; Ellyin & Deloin, 1972).

In certain instances, the effect of shear force should be considered in analysis and design. Darwin (2000) has suggested a cubic interaction curve to evaluate the plastic moment and shear capacities for beams with web openings. Kasai and Popov (1986) have conducted research on the eccentrically braced frames used in seismic design, where the effect of the shear forces on the behaviour of steel shear links is known to be so significant that it cannot be ignored. An experimental study of a transversely loaded two-span continuous steel beam revealed that the effect of shear force was significant even when the depth-to-span ratio was as low as 0.1025 (Driscoll & Beedle, 1957). The nonlinear analysis presented in Chapter 3 has further confirmed this conclusion. Abnormal or blast inertia loading can cause significant shear force effects in structures (Krauthammer, 1984; ASCE, 1997). The combined action of moment, axial force and shear force becomes significant when a critical column is removed, as dictated by the alternate-load-path method in design guidelines (DoD, 2005). In general, the effect of shear forces on structural behaviour may become important in the analysis and design of structures subjected to abnormal loading.

6.2 Energy Functional

A post-elastic combined stress failure criterion can be established through global-member or local-section equilibrium (Drucker, 1956). A global criterion for limit loading is based on a whole member (e.g., a cantilever), where the relationship between the external and the internal loadings are known. A local criterion for plastic limit loading, however, is for a very short length of beam between two neighbouring cross sections, where the internal forces (moments and shear forces) are assumed to be in the plastic limit state. Since internal member forces are unknown prior to the nonlinear analysis of indeterminate structures, the approach based on local-section equilibrium may be more appropriate. Using this approach, Hodge (1957) adopted a variational principle, along with the idea of convexity, to determine the interaction relationship between the moment and shear force for a beam member section. Ellyin and Deloin (1972) have extended Hodge's approach to account for the effect of axial force as well. Their variational approach to determining the plastic yield surface of a cross-section involves finding the normal stress distribution σ that minimizes shear force V, when the values of axial force P and bending moment M are given. For the previously noted variational methods,

however, the equilibrium conditions at the top and bottom boundaries of the beam section are violated, as first noted by Drucker (1956). This chapter proposes a method that combines local criteria and variational principles to obtain an M-P-V plastic yield surface for a member section, for which all boundary equilibrium conditions are satisfied.

Consider the member segment in Figure 6.1(a), that was originally adopted in Drucker's (1956) local criterion approach. The segment has a cross-section with depth *d* and a plastic zone bounded by sections 1 and 2. The forces at both sections are shown on the segment, and the segment deformations are shown in Figures 6.1(b) and (c). The assumptions of constant section rotation θ and constant average axial deformation ε in Figure 6.1(b) are adopted from Drucker's (1956) local criterion in the plastic range. But transverse shear deformation γ, however, is not assumed to be constant across the section; instead, γ varies linearly across the section in such a way that the shear strain is zero at both the top and bottom free boundaries, as depicted by the relationship $\gamma=\gamma_0(1-2|y|/d)$ in Figure 6.1(c). The distributions of normal and shear stresses σ and τ are a function of distance *y*, and the stress distributions in the plastic zone are found by solving a variational problem involving the minimization of an energy function established for the model in Figure 6.1. In the following, the energy function is derived first, and then the Euler-Lagrange differential equation is obtained by the Gâteaux variation method (Troutman, 1996). The normal stress is found by solving the differential equation, and the corresponding bending moment, axial force and shear force are found by integrating the relevant stresses.

If the distributions of normal stress σ and shear stress τ within the plastic zone are known, the resultant bending moment *M*, axial force *P* and shear force *V* applied to a section in the plastic zone can be expressed in terms of the corresponding stresses as,

$$P = \iint_A \sigma dA \tag{6.2.1a}$$

$$M = \iint_A \sigma y dA \tag{6.2.1b}$$

$$V = \iint_A \tau dA \tag{6.2.1c}$$

where the relationship between normal stress σ and shear stress τ at a point in the plastic zone is defined by the following yield condition,

$$\sigma^2 + \kappa^2 \tau^2 = \sigma_y^2 \tag{6.2.2}$$

in which σ_y is the normal material yield stress, and $\kappa^2 = 3$ or 4 for the von Mises or Tresca criterion, respectively. The Tresca yield shear stress is $\tau_y = \sigma_y/\kappa$, and therefore, $\tau_y = 0.577\sigma_y \approx 0.6\sigma_y$ for the von Mises criterion (CISC, 2004). As shown in Figures 6.1(b) and (c), axial deformation ε and bending rotation θ are assumed to be constant, whereas the transverse shear deformation γ is assumed to be linearly distributed from maximal shear strain γ_0 at the neutral axis to zero value on the upper and lower free boundaries of the section.

In the plastic zone, the total energy Π of the segment in Figure 6.1 is expressed by the following energy functional,

$$\Pi = \Pi_e + \Pi_i \tag{6.2.3}$$

where Π_e and Π_i are the external work and internal potential energy, respectively. External work Π_e is done by the forces applied to sections 1 and 2 in Figure 6.1(a) as they move through the corresponding average bending, axial, and shearing deformations θ_j, δ_{nj} and δ_{tj}, as given by (McGuire et al., 2000),

$$\Pi_e = \sum_{j=1}^{2} [M\theta + N\delta_n + V\delta_t]_j \tag{6.2.4a}$$

in which forces M_j, N_j and V_j and corresponding deformations θ_j, δ_{nj} and δ_{tj} (j=1,2) are known from the results of structural analysis of the member at a given loading level. Note that all the terms on the right-hand side of Eq. (6.2.4a) are known quantities, and therefore external work Π_e is a known constant. Internal potential energy Π_i in Eq. (6.2.3) is expressed in terms of the stresses and their corresponding strains as (McGuire et al., 2000)

$$\Pi_i = \iiint_V (\sigma\theta y + \sigma\varepsilon + \tau\gamma) dV = \Delta x \iint_A \Gamma(y, \sigma) dA \tag{6.2.4b}$$

where the integration is over all of the plastic zone. It is assumed, as in Drucker's (1956) local criterion, that length Δx of the plastic zone is small so that function Γ does not involve distance x (i.e., each cross- section within the plastic zone has the same stress distribution). Since Δx is a constant term in the energy functional, setting Δx to unity does not affect finding the maximum condition of Eq. (6.2.4b), where the integrand is an energy density function given by,

$$\Gamma(y, \sigma) = \sigma\theta y + \sigma\varepsilon + \frac{\gamma_0}{\kappa}\sqrt{\sigma_y^2 - \sigma^2}\,(1 - 2\,|\,y\,|\,/\,d) \tag{6.2.5}$$

The stress-strain relationships are nonlinear relationships in the plastic limit state, and the determination of normal stress σ in terms of moment M, shear force V, and axial force P is a variational problem that can be mathematically stated as follows (Hodge, 1957; Ellyin & Deloin,

1972): “for a plastic zone having predefined deformations, find normal stress σ such that the energy functional reaches its maximum value.” In the following development, the principle of maximum energy is used first to determine normal stress σ, and then shear stress τ is determined through Eq. (6.2.2).

6.3 Stress-Strain Relationship at Failure State

This section mathematically proves that the energy functional defined by Eq. (6.2.3) is a strictly concave function, and therefore, that normal stress σ at a stationary point corresponds to a unique maximum value of the functional. To this end, zeroing the first variation of the energy functional Eq. (6.2.3) yields the extreme condition, i.e., the Euler-Lagrange equation. Then, it is then shown that the energy functional Eq. (6.2.3) is a concave function that ensures the normal stress σ distribution can be solved from the Euler-Lagrange equation to maximize the energy.

6.3.1 Euler-Lagrange Function

The Gâteaux variation method (Troutman, 1996) is employed here to find the extreme condition of the energy functional Eq. (6.2.3). In this method, variables σ and ℵ are selected to determine the first variation, where the variable normal stress distribution ℵ is an arbitrary function of *y* that is very close to σ. For small parametric variable ν, if the following partial derivative exists (Troutman, 1996),

$$\delta\Pi(\sigma;\aleph) = \lim_{\nu\to 0}\frac{\Pi(\sigma+\nu\aleph)-\Pi(\sigma)}{\nu} = \frac{\partial}{\partial\nu}\Pi(\sigma+\nu\aleph)\,|_{\nu=0} \tag{6.3.1}$$

then a Gâteaux variation of function Π is defined at σ in the direction of ℵ. Similar to that for a normal function, an extreme value condition is reached if the first Gâteaux variation vanishes, i.e.,

$$\delta\Pi(\sigma;\aleph) = 0 \tag{6.3.2}$$

where function ℵ is within the vicinity of the extreme point of σ. To determine the stationary condition Eq. (6.3.2) for the energy function Π given in Eq. (6.2.3), it is necessary to estimate the partial derivative of function Γ(*y*, σ+νℵ) as expressed by Eq. (6.2.5). To this end, partially differentiate the expression with respect to ν to find,

$$\frac{\partial\Gamma(y,\sigma+\nu\aleph)}{\partial\nu} = \Gamma_{\sigma+\nu\aleph}\aleph \tag{6.3.3}$$

where subscript $\sigma+\nu\aleph$ represents the first partial derivative of function Γ with respect to that subscript (i.e., $\Gamma_{\sigma+\nu\aleph} = \partial\Gamma/\partial(\sigma+\nu\aleph)$). Substitute Eq. (6.2.4) into Eq. (6.2.3) and then into the first partial derivative of Eq. (6.3.3) to find,

$$\frac{\partial\Pi}{\partial\nu} = \iint_A (\Gamma_{\sigma+\nu\aleph}\aleph)dA = \int_{-d/2}^{d/2} b(y)\Gamma_{\sigma+\nu\aleph}\aleph\, dy \tag{6.3.4}$$

in which the cross-section width $b(y)$ varies over the section depth. By substituting Eq. (6.3.4) into Eq. (6.3.1) and then Eq. (6.3.2), the Gâteaux variation of function Π becomes,

$$\delta\Pi(\sigma;\aleph) = \frac{\partial}{\partial\nu}\Pi(\sigma+\nu\aleph)\,|_{\nu=0} = \int_{-d/2}^{d/2} b(y)\Gamma_\sigma\aleph\, dy \tag{6.3.5}$$

which holds for the arbitrary function $\aleph$, and therefore,

$$b(y)\Gamma_\sigma = 0 \tag{6.3.6}$$

which is the so-called Euler-Lagrange differential equation. Assuming there are no web openings, the section width function $b(y)$ cannot be zero, and Eq. (6.3.6) can be simplified to,

$$\Gamma_\sigma = \frac{\partial\Gamma}{\partial\sigma} = 0 \tag{6.3.7}$$

Substitute the energy density function expressed in Eq. (6.2.5) into Eq. (6.3.7), to find,

$$\frac{\partial\Gamma(y,\sigma)}{\partial\sigma} = \theta y + \varepsilon - \frac{\gamma_0(1-2\,|\,y\,|\,/\,d)\sigma}{\kappa\sqrt{\sigma_y^2-\sigma^2}} = 0 \tag{6.3.8}$$

which is a function that defines the distribution of normal stress σ over the cross-section depth at the plastic limit state. It is noteworthy that Eq. (6.3.2) is a necessary condition, but not a sufficient condition for function Π to attain an extreme value, and, as such, the corresponding extreme point of σ from Eq. (6.3.8) may be relevant to a maximal, minimal or saddle point of the function. Thus, if Eq. (6.3.8) is a necessary and sufficient condition to maximize function Π, then Π must be concave.

6.3.2 Concave Function

If it can be shown that the energy functional given by Eq. (6.2.3) is concave, the stress distribution defined by Eq. (6.3.8) is the true failure stress at the plastic limit state. The function Π is concave over the interval $[\sigma_b, \sigma_e]$, where subscripts b and e refer to the beginning and end points of the interval, if any line segment joining any two points on the graph of Π is never above the graph (Gradshteyn & Ryzhik, 2000). A concave function can be alternatively defined by a Gâteaux variation condition as follows: a function Π defined on interval $[\sigma_b, \sigma_e]$ is said to be strictly concave

when, for any σ and $\aleph$ belonging to the given domain, the following condition holds (Troutman, 1996),

$$\Pi(\sigma+\aleph)-\Pi(\sigma)\le\delta\Pi(\sigma;\aleph) \tag{6.3.9}$$

which is an equality if and only if $\aleph = O$, where O denotes the null function. The following presentation demonstrates how Eq. (6.3.9) is satisfied in the current analysis of a plastic limit state.

By substituting Γ_σ defined by Eq. (6.3.8) into Eq. (6.3.1), the first Gâteaux variation for the right-hand side of Eq. (6.3.9) is,

$$\delta\Pi(\sigma;\aleph)=\int_{-d/2}^{d/2} b(y)\Gamma_\sigma\aleph dy=\iint_A \Gamma_\sigma\aleph dA=In1-In2 \tag{6.3.10}$$

where integral terms $In1$ and $In2$ have the following expressions,

$$In1=\iint_A(\theta y+\varepsilon)\aleph dA \tag{6.3.11}$$

$$In2=\frac{\gamma_0}{\kappa}\iint_A(1-2|y|/d)\sigma\aleph/\sqrt{\sigma_y^2-\sigma^2}\,dA \tag{6.3.12}$$

Based on Eqs. (6.2.3), (6.2.4) and (6.2.5), the difference in the left-hand side of Eq. (6.3.9) is expressed by the following,

$$\Pi(\sigma+\aleph)-\Pi(\sigma)=In1-\frac{\gamma_0}{\kappa}\iint_A(1-\frac{2|y|}{d})\left[\sqrt{\sigma_y^2-\sigma^2}-\sqrt{\sigma_y^2-(\sigma+\aleph)^2}\right]dA \tag{6.3.13}$$

in which the term in the square brackets can be rewritten as,

$$\sqrt{\sigma_y^2-\sigma^2}-\sqrt{\sigma_y^2-(\sigma+\aleph)^2}=\frac{2\sigma\aleph(1+\aleph/\sigma)}{\sqrt{\sigma_y^2-(\sigma+\aleph)^2}+\sqrt{\sigma_y^2-\sigma^2}} \tag{6.3.14}$$

Note that interval $[\sigma_b, \sigma_e]$ can be selected in such a way that both $\aleph$ and σ have the same sign, so that $\aleph\sigma \ge 0$. If such a condition is satisfied, the following inequality holds,

$$\sqrt{\sigma_y^2/\left(1+\aleph/\sigma\right)^2-\sigma^2}\le\sqrt{\sigma_y^2-\sigma^2} \tag{6.3.16}$$

Thus, the term on the right-hand side of Eq. (6.3.14) is,

$$\frac{2\sigma\aleph(1+\aleph/\sigma)}{\sqrt{\sigma_y^2-(\sigma+\aleph)^2}+\sqrt{\sigma_y^2-\sigma^2}}\ge\frac{\sigma\aleph}{\sqrt{\sigma_y^2-\sigma^2}} \tag{6.3.16}$$

It is also observed that for the bi-axially symmetrical cross-section in Figure 6.1(a), the expression $2|y|/d \le 1$ is satisfied over the entire section depth. Thus, the term $(1\text{-}2|y|/d)$ in Eq. (6.3.13) is greater

than or equal to 0. Therefore, by substituting Eqs. (6.3.16) into Eq. (6.3.14), and then into the second term on the right-hand side of Eq. (6.3.13), we get,

$$\begin{aligned}&\frac{\gamma_0}{\kappa}\iint_A\left(1-\frac{2|y|}{d}\right)\left[\sqrt{\sigma_y^2-\sigma^2}-\sqrt{\sigma_y^2-(\sigma+\aleph)^2}\right]dA\\&\geq\frac{\gamma_0}{\kappa}\iint_A\left(1-2|y|/d\right)\sigma\aleph/\sqrt{\sigma_y^2-\sigma^2}\,dA=In2.\end{aligned}\tag{6.3.17}$$

By substituting Eq.(6.3.17) back into Eq. (6.3.13), we find,

$$\Pi(\sigma+\aleph)-\Pi(\sigma)\leq In1-In2\tag{6.3.18}$$

If Eq. (6.3.18) is compared with Eq. (6.3.10), it is observed that Eq. (6.3.9) is indeed satisfied; that is, the energy functional Π is a concave function with respect to stress σ. This indicates that a normal stress σ that satisfies the Euler-Lagrangian Eq. (6.3.8) corresponds to function Π achieving its maximum value. In other words, the distribution of normal stress σ defined in Eq. (6.3.8) holds true for the plastic zone in Figure 6.1 at the plastic limit state.

6.4 Failure Criterion Accounting for M-V-P Interaction

Once the distribution of normal stress σ in the plastic limit state is determined by Eq. (6.3.8), axial force *N* and bending moment *M* can then be, respectively, found from Eqs. (6.2.1). As the distribution of shear stress τ is expressed in terms of σ by using the von Mises or Tresca yielding criterion, defined in Eq. (6.2.2), the shear force *V* can be subsequently determined from Eq. (6.2.1c). Since all three internal forces are found in the plastic limit state, a yield surface for the plastic zone is defined. A detailed expression of the yield surface, accounting for the interaction of bending moment, shear force and axial force in the fully plastic state, is derived in the following. The yield surfaces for three typical cross sections (rectangle, narrow-flange I-section, and wide-flange W-section) are derived and compared with corresponding results obtained from other methods (Ellyin & Deloin, 1972; Kusuda & Thurlimann, 1958; Kasai & Popov, 1986).

6.4.1 Internal Forces

To facilitate the following derivation, this study introduces the following two parameters relevant to plastic flexural, translational and axial deformations,

$$\varphi=0.5\kappa\theta d/\gamma_0\tag{6.4.1a}$$

$$\zeta=\varepsilon/\gamma_0\tag{6.4.1b}$$

where κ is defined in Eq. (6.2.2), and φ and ζ represent the flexural-to-shear and axial-to-shear deformation/strain ratios at the plastic limit state, respectively. Normal stress σ at the failure state, accounting for flexural, shearing and axial deformations, are the solved for from Eq. (6.3.8) and expressed as,

$$\sigma = \frac{(\varphi\rho + \zeta)\sigma_y}{\sqrt{(\varphi\rho + \zeta)^2 + (1 - |\rho|)^2}} \tag{6.4.2}$$

where $\rho = 2|y|/d$. By incorporating the normal stress given by Eq. (6.4.2) into the failure criteria defined by Eq. (6.2.2), the following expression for the transverse shear stress at failure is obtained,

$$\tau = \frac{(1 - |\rho|)\tau_y}{\sqrt{(\varphi\rho + \zeta)^2 + (1 - |\rho|)^2}} \tag{6.4.3}$$

This study adopts the conventional assumption that any stress along the *z* axis normal to the *y* axis is as indicated in Figure 6.2. By multiplying Eq. (6.4.2) by *y*, and then integrating over the depth of the section, the expression for the bending moment at failure of the section is found as,

$$M = \iint_A \sigma y dA = \frac{d^2}{4}\sigma_y \int_{-1}^{1} \frac{b_f(\rho)\rho(\varphi\rho + \zeta)d\rho}{\sqrt{(\varphi\rho + \zeta)^2 + (1 - |\rho|)^2}} \tag{6.4.4}$$

in which the integral is dependant on the piecewise constant width function $b_f(\rho)$ for the cross-section: although conventional W-shape cross-sections are mainly illustrated in this study, the formulation derived can apply to other steel cross-section types as well; for example, the width function $b_f(\rho)$ can be for the wide-flange hollow-box section shown in Figure 6.2, Even when the cross-section is bi-axially symmetrical, the integrand of Eq. (6.4.4) is not symmetrical with respect to variable *y* or ρ due to the fact that the axial-to-shear strain ratio $\zeta \neq 0$. Therefore, the definite integral of Eq. (6.4.4) must be divided into four constant domains: $(-1, -c_1)$, $(-c_1, -0)$, $(+0, c_1)$, and $(c_1, 1)$, where the parameter $c_1 = 1-2t_f/d$. Note that finding the integral expression in Eq. (6.4.4) is a tedious process, and the expression is quite complicated. To simplify the following derivation, the anti-derivative corresponding to the integrand in Eq. (6.4.4) is presented in Appendix 6.A, where the software Mathematica-Version 3.0 (Wolfram, 1996) is employed in the derivation. Therefore, by directly using anti-derivative Eq. (6.A.8) in Appendix 6.A, the following expression can be found for the bending moment,

$$M = \frac{b_f d^2}{4}\sigma_y [I_m(1) - (1 - c_2)I_m(c_1) - c_2 I_m(0)] \tag{6.4.5}$$

where the parameter $c_2 = t_w/b_f$. The detailed expression for $I_m(c_1)$ is given in Eqs. (6.A.2) through (6.A.8) in Appendix 6.A. The expressions for $I_m(1)$ and $I_m(0)$ are determined by setting $c_1 = 1$ and $c_1 = 0$ in expression $I_m(c_1)$, to obtain,

$$\begin{aligned} I_m(1) &= \frac{(\zeta+\varphi)(2\zeta+4\varphi-\zeta\varphi^2+\varphi^3)+|\zeta-\varphi|[\zeta(\varphi^2-2)+\varphi(4+\varphi^2)]}{2(1+\varphi^2)^2} \\ &+\frac{(2\zeta+2\varphi-3\zeta^2\varphi-4\zeta\varphi^2-\varphi^3)\ln[2(\zeta+\varphi)(1+\varphi/\sqrt{1+\varphi^2})]}{2(1+\varphi^2)^{2.5}} \\ &+\frac{(2\zeta-2\varphi+3\zeta^2\varphi-4\zeta\varphi^2+\varphi^3)\ln\{2[|\zeta-\varphi|+\varphi(\zeta-\varphi)/\sqrt{1+\varphi^2})]\}}{2(1+\varphi^2)^{2.5}} \end{aligned} \tag{6.4.6}$$

and

$$\begin{aligned} I_m(0) &= \frac{(2\zeta+2\varphi-3\zeta^2\varphi-4\zeta\varphi^2-\varphi^3)\ln[2\sqrt{1+\zeta^2}+2(\zeta\varphi-1)/\sqrt{1+\varphi^2}]}{2(1+\varphi^2)^{2.5}} \\ &+\frac{(2\zeta-2\varphi+3\zeta^2\varphi-4\zeta\varphi^2+\varphi^3)\ln[2\sqrt{1+\zeta^2}+2(\zeta\varphi+1)/\sqrt{1+\varphi^2}]}{2(1+\varphi^2)^{2.5}}+\frac{3\varphi\sqrt{1+\zeta^2}}{(1+\varphi^2)^2} \end{aligned} \tag{6.4.7}$$

By integrating Eq. (6.4.3) across the section, the expression for the resultant shear force is,

$$V = \iint_A \tau dA = \frac{d}{2}\tau_y \int_{-1}^{1} \frac{b_f(\rho)(1-|\rho|)d\rho}{\sqrt{(\varphi\rho+\zeta)^2+(1-|\rho|)^2}} \tag{6.4.8}$$

Similar to the derivation of the moment, by applying the anti-derivative Eq. (6.A.12) derived in Appendix 6.A to Eq. (6.4.8), the shear force at failure is expressed as,

$$V = b_f d\tau_y[I_v(1)-(1-c_2)I_v(c_1)-c_2 I_v(0)] \tag{6.4.9}$$

where the subscript v indicates that the integral I_v refers to the shear force. The detailed expression of $I_v(c_1)$ is given in Appendix 6.A, from which the expressions $I_v(1)$ and $I_v(0)$ for $c_1 = 1$ and 0 are found to be,

$$\begin{aligned} I_v(1) &= -\frac{|\zeta-\varphi|+\zeta+\varphi}{2(1+\varphi^2)}+\frac{\varphi(\zeta+\varphi)\ln[2(\zeta+\varphi)(1+\varphi/\sqrt{1+\varphi^2})]}{2(1+\varphi^2)^{1.5}} \\ &+\frac{\varphi(\zeta-\varphi)\ln\{2[|\zeta-\varphi|+\varphi(\zeta-\varphi)/\sqrt{1+\varphi^2})]\}}{2(1+\varphi^2)^{1.5}} \end{aligned} \tag{6.4.10}$$

$$\begin{aligned} I_v(0) &= -\frac{\sqrt{1+\zeta^2}}{1+\varphi^2}+\frac{\varphi(\zeta-\varphi)\ln[2\sqrt{1+\zeta^2}+2(1+\varphi\zeta)/\sqrt{1+\varphi^2}]}{2(1+\varphi^2)^{1.5}} \\ &+\frac{\varphi(\zeta+\varphi)\ln[2\sqrt{1+\zeta^2}-2(1-\varphi\zeta)/\sqrt{1+\varphi^2}]\}}{2(1+\varphi^2)^{1.5}} \end{aligned} \tag{6.4.11}$$

Similarly, the integration of Eq. (6.4.2) for the normal stress over the section yields the following expression for the axial force,

$$P = \iint_A \sigma dA = \frac{d}{2}\sigma_y \int_{-1}^{1} \frac{b_f(\rho)(\varphi\rho + \zeta)d\rho}{\sqrt{(\varphi\rho + \zeta)^2 + (1 - |\rho|)^2}} \tag{6.4.12}$$

By using the anti-derivative Eq. (6.A.16) derived in Appendix 6.A, the axial force in Eq. (6.4.12) is expressed as,

$$P = bd\sigma_y [I_p(1) - (1 - c_2)I_p(c_1) - c_2 I_p(0)] \tag{6.4.13}$$

where the subscript p indicates that the integral I_p refers to the axial force. The detailed expression for $I_p(c_1)$ is given in Appendix 6.A, from which expressions $I_p(1)$ and $I_p(0)$ for $c_1 = 1$ and 0 are found as,

$$\begin{aligned} I_p(1) &= \frac{\zeta + \varphi - |\zeta - \varphi|}{2(1+\varphi^2)} + \frac{(\zeta + \varphi)\ln[2(\zeta + \varphi)(1 + \varphi/\sqrt{1+\varphi^2})]}{2(1+\varphi^2)^{1.5}} \\ &+ \frac{\varphi(\varphi - \zeta)\ln\{2[|\zeta - \varphi| + \varphi(\zeta - \varphi)/\sqrt{1+\varphi^2})]\}}{2(1+\varphi^2)^{1.5}} \end{aligned} \tag{6.4.14}$$

and

$$\begin{aligned} I_v(0) &= \frac{(\varphi - \zeta)\ln[2\sqrt{1+\zeta^2} + 2(1 + \varphi\zeta)/\sqrt{1+\varphi^2}]}{2(1+\varphi^2)^{1.5}} \\ &+ \frac{(\zeta + \varphi)\ln[2\sqrt{1+\zeta^2} - 2(1 - \varphi\zeta)/\sqrt{1+\varphi^2}]\}}{2(1+\varphi^2)^{1.5}} \end{aligned} \tag{6.4.15}$$

Thus far, the bending moment, shear force and axial force at failure have been derived by applying variational principles, and expressed in Eqs. (6.4.4) through (6.4.15) in terms of the two parameters ζ and φ. The three expressions Eqs. (6.4.5), (6.4.9) and (6.4.13) define the yield/failure surface for a member section under the combined action of bending moment, shear force and axial force.

6.4.2 Force-Deformation Relationships

To observe the characteristics of the three-dimensional yield surface derived in the previous section, a typical wide-flange cross section, shown in Figure 6.2 with $b_1 = 0$, is here considered to illustrate the corresponding force-deformation relationships. It is evident from Eqs. (6.4.1) that the parameter φ is the ratio of section rotation θ to transverse deformation γ_0, while the parameter ζ is the ratio of axial deformation ε to transverse deformation γ_0. As a result, the relationship between each of the three forces M, V, P and the two parameters φ, ζ represents the combined force-deformation relationship in the plastic limit state. Consider a W360X382 cross-section, and normalized axial force $p = P/P_p$,

bending moment $m=M/M_p$ and shear force $v=V/V_p$, where the normalizing factors are the axial, bending and shear capacities,

$$P_p = \sigma_y A \tag{6.4.16a}$$

$$M_p = \sigma_y Z \tag{6.4.16b}$$

$$V_p = \tau_y A \tag{6.4.16c}$$

Bending moment M, shear force V and axial force P are defined by Eqs. (6.4.5), (6.4.9) and (6.4.13), respectively. If φ is set to the values of 0, 0.5, 1, 2, and 3, while ζ assumes a value ranging from zero to four, the variations of the normalized bending moment, shear force and axial force and their corresponding deformation ratios are as shown in Figure 6.3.

It is observed from Figure 6.3 (a) that when φ tends to zero, the bending moment vanishes ($m = 0$), which corresponds to either one of two extreme cases: the flexural curvature is zero, or the shear strain becomes infinitely large in accordance with Eqs. (6.4.1). This indicates that shear failure dominates the plastic zone. When a curvature-shear deformation/strain ratio is specified, say $\varphi = 0.5$, the moment is very sensitive to the variation of the axial deformation, and its value drops considerably from its maximum value at around $\zeta = 0.5$, as shown in Figure 6.3(a). This indicates that the combined stress interaction is significant in the region close to $\varphi = \zeta = 0.5$. When the ratio φ is increased to 3, the effect of the axial loading becomes insignificant up to approximately $\zeta = 2.5$, as indicated in Figure 6.3(a), and flexural deformation dominates the failure state. Subsequently, beyond $\zeta = 2.5$, the moment quickly drops to zero as the axial loading dominates the failure. These results demonstrate that while the bending moment level at the failure state is high in deformation/strain regions exhibiting small shear or axial deformation, in some other combined deformation/strain regions involving larger axial or shear deformation, the moment capacity decreases significantly.

The relationship between the shear capacity and parameters φ and ζ is shown in Figure 6.3(b). It is evident from the figure that when parameters φ and ζ tend to zero, shear failure controls the limit state due to the extremely high level of shear force. When $\zeta = 0$ (no axial strain), the shear capacity, in particular, drops quickly with an increase of the φ value. This demonstrates that for moment-shear interaction, the bending moment plays a more significant role. If there is no flexural effect ($\varphi = 0$), the shear capacity decreases monotonically with increase of the ζ value. It is interesting that with the presence of flexural bending (say $\varphi = 0.5$), with the increase of the axial loading/deformation, the shear capacity increases to the maximum value (about 0.6) and further increase of axial loading/deformation results in the decrease of shear capacity. Furthermore, if the value of φ is

increased (such as setting φ to 1, 2, or 3), the similar humped feature shown in Figure 6.3(b) is also observed, but the peak value of *v* decreases and the flatter region, prior to the maximal shear force, continues to elongate. These results reveal that for specified ratio φ, a given shear loading level can correspond to two different ζ deformation ratios.

The relationship between the axial force capacity and combined deformations is plotted in Figure 6.3(c). It is observed that when φ = 0 (i.e., no bending moment effect), the axial capacity is quickly reached with the increase of ζ to about ζ = 1, and then the axial loading controls the failure limit state. With the increase of the φ value, say to φ = 1, the axial loading *p* increases with the increase of the ζ value. This is true when the parameter ζ reaches a certain level at which axial loading *p* jumps from a lower level to almost unity. For a given shear loading level, the lower the bending moment level, the faster the loading *p* approaches unity.

It is also important to observe the cross-section failure at the plastic state resulting from the interaction between bending moment, shear force and axial force. Although flexural failure is generally considered a key factor that contributes to local section failure, the preceding discussions clearly indicate that three-dimensional combined stress interaction should be taken into account for some extreme loading cases. Particularly for a given shear and moment loading (deformation) level (say, φ = 1), the bending moment loading in the plastic limit state dramatically changes from its maximum value to its minimum value with the increase of parameter ζ , beginning from around ζ = 1, as shown in Figure 6.3(a); normalized axial force *p* quickly increases to unity from its minimum value shown in Figure 6.3(c), indicating that the bending moment no longer dominates the local section failure.

6.4.3 M-V-P Yield-Failure Surface for Rectangular Sections

Here, a rectangular section with depth *d* and width *b* is considered. By substituting $c_1 = 0$ and $c_2 = 1$ into Eq. (6.4.5), and then normalizing by Eq. (6.4.16b), the following expression for normalized moment is found,

$$
\begin{aligned}
m = & \frac{|\zeta-\varphi|(\zeta\varphi^2-2\zeta+4\varphi+\varphi^3)+(\varphi+\zeta)(2\zeta+4\varphi-\zeta\varphi^2+\varphi^3)-6\varphi\sqrt{1+\zeta^2}}{2(1+\varphi^2)^2} \\
& + \frac{\ln\{[(\varphi\zeta+\varphi^2+(\zeta+\varphi)\sqrt{1+\varphi^2})]/(\varphi\zeta-1+\sqrt{1+\zeta^2}\sqrt{1+\varphi^2})\}}{2(1+\varphi^2)^{2.5}(2\zeta+2\varphi-3\zeta^2\varphi-4\zeta\varphi^2-\varphi^3)^{-1}} \\
& + \frac{\ln[(\varphi\zeta-\varphi^2+|\zeta-\varphi|\sqrt{1+\varphi^2})/(\varphi\zeta+1+\sqrt{1+\zeta^2}\sqrt{1+\varphi^2})]}{2(1+\varphi^2)^{2.5}(2\zeta-2\varphi+3\zeta^2\varphi-4\zeta\varphi^2+\varphi^3)^{-1}}
\end{aligned}
\tag{6.4.17}
$$

which is a parametric function with respect to variables φ and ζ . Similarly, by substituting $c_1 = 0$ and $c_2 = 1$ into Eq. (6.4.9), and then normalizing by Eq. (6.4.16c), the following expression for normalized shear force is found,

$$\begin{aligned} v = & \frac{2\sqrt{1+\zeta^2} - |\zeta - \varphi| - \zeta - \varphi}{2(1+\varphi^2)} \\ & + \frac{\varphi(\varphi+\zeta)\ln\{[(\varphi\zeta + \varphi^2 + (\zeta+\varphi)\sqrt{1+\varphi^2})]/(\varphi\zeta - 1 + \sqrt{1+\zeta^2}\sqrt{1+\varphi^2})\}}{2(1+\varphi^2)^{1.5}} \\ & + \frac{\varphi(\zeta-\varphi)\ln[(\varphi\zeta - \varphi^2 + |\zeta - \varphi|\sqrt{1+\varphi^2})/(\varphi\zeta + 1 + \sqrt{1+\zeta^2}\sqrt{1+\varphi^2})\}}{2(1+\varphi^2)^{1.5}} \end{aligned} \tag{6.4.18}$$

Finally, by substituting $c_1 = 0$ and $c_2 = 1$ into Eq. (6.4.13), and then normalizing by Eq. (6.4.16a), the following expression for normalized axial force is found,

$$\begin{aligned} p = & \frac{\varphi(\zeta + \varphi - |\zeta - \varphi|)}{2(1+\varphi^2)} \\ & + \frac{(\varphi+\zeta)\ln\{[(\varphi\zeta + \varphi^2 + (\zeta+\varphi)\sqrt{1+\varphi^2})]/(\varphi\zeta - 1 + \sqrt{1+\zeta^2}\sqrt{1+\varphi^2})\}}{2(1+\varphi^2)^{1.5}} \\ & + \frac{(\varphi-\zeta)\ln[(\varphi\zeta - \varphi^2 + |\zeta - \varphi|\sqrt{1+\varphi^2})/(\varphi\zeta + 1 + \sqrt{1+\zeta^2}\sqrt{1+\varphi^2})]}{2(1+\varphi^2)^{1.5}} \end{aligned} \tag{6.4.19}$$

Equations (6.4.17) to (6.4.19) are the parametric functions (with respect to parameters φ and ζ) that define the yield-failure surface for a rectangular cross-section. The surface can be graphically determined by the following approach. For given values of v and p, solve the system of nonlinear equations Eqs. (6.4.18) and (6.4.19) to find the corresponding values of parameters φ and ζ. Then, substitute these two parameter values into Eq. (6.4.17) to find the corresponding value of m. This is repeated for various given values of v and p to obtain sets of data points that graphically define the yield surface accounting for moment, shear and axial force interaction. For instance, if the values of v are set to 0, 0.2, 0.4, 0.6, 0.8, 0.9 and 0.95, the corresponding normalized p-m curves are the yield surface contours plotted as solid lines in Figure 6.4.When $v = 0$, the heavy solid line represents the theoretical interaction curve derived from a two-dimensional m+p analysis of a rectangular cross-section (Chen et al., 1977). When the shear loading level is low (say $v = 0.2$), neglecting the effect of the shear force is reasonable because the corresponding interaction curve almost coincides with that when $v = 0$. With an increase of the shear force (to $v = 0.4$ and beyond), the corresponding influence on the yield surface becomes much more significant. Such a shear stress effect should not be ignored, as this may lead to unsafe design in practice. This is especially true when the value of the ratio v is beyond 0.6, at which point the shear stresses affect the local plastic failure dramatically.

Note that the interaction surfaces shown as dashed lines in Figure 6.4 are derived by using the conventional assumption of constant shear strain across the section (Ellyin & Deloin, 1972). It is observed from the yield surfaces that for the values predicted by Ellyin and Deloin's method, the cross-section strengths are generally overestimated when compared with the solid-line results derived in this study. Only when shear force v is less than 0.4, is the overestimation insignificant. When the value of v is greater than 0.4, the error becomes quite substantial.

6.4.4 M-V-P Yield-Failure Surface for Wide-Flange Sections

Structural beam and column members with wide-flange cross-sections are commonly used in steel frameworks. Two typical cross-sections are now considered. The first section type, often used for beams, is an I-section with flange width-to-depth ratio $b_f/d < 0.5$. The second section type, often adopted for columns, is a W-section with $b_f/d > 0.5$.

The yield-surface contour is first investigated for a W920X253 section, for which the relevant properties are: depth d = 915 mm, flange width b_f = 305 mm, flange thickness t_f = 25.9 mm, web thickness t_w = 16.5 mm, area A = 32300 mm^2, and plastic modulus $Z = 11\times10^6$ mm^3 (CISC, 2004). It is observed that the ratio of width to depth is $b_f/d = 1/3 < 0.5$; therefore, this is a typical I-section used for beams. Unlike Eqs. (6.4.17), (6.4.18) and (6.4.19) for rectangular cross-sections, the m, v and p expressions for wide-flange cross-sections are considerably more complicated, because $c_1 \neq 0$ and $c_2 \neq 1$ in Eqs. (6.4.5), (6.4.9) and (6.4.13). By substituting parameters $c_1 = 1\text{-}2t_f/d = 0.9434$ and $c_2 = t_w/b_f = 0.0541$ into these equations for the W920X253 section, and then normalizing them through Eqs. (6.4.1), the non-dimensional expressions for the m, v and p as functions of parameters φ and ζ are derived. Then, following the same procedure employed in Section 6.4.3 for rectangular sections, the corresponding $m + p$ yield-surface contours for varying values of v from 0 to 0.95 are obtained, as shown in Figure 6.5.

By comparing Figures 6.4 and 6.5, it is evident that the corresponding normalized yield surfaces for rectangular and W-flange sections differ negligibly. Similarly, when the W-section results of this study are compared to those obtained by Ellyin and Deloin (1972), as in Figure 6.5, if the shear level is lower than v = 0.2 then, as for rectangular sections, the effect of the shear force can be reasonably ignored in the case of wide-flange sections, . However, the influence of shear force on plastic failure becomes significant when ratio v= 0.4 and beyond, which implies that yield-failure for wide-flange sections is more sensitive to shear forces than it is for rectangular sections.

The second example is a W360X382 section with the following properties: depth d = 416 mm, flange width b_f = 406 mm, flange thickness t_f = 48 mm, web thickness t_w = 29.8 mm, area A = 48700

mm^2, and plastic modulus $Z = 7970\times10^3$ mm^3 (CISC, 2004). The main feature of this section is that the flange width-to-depth ratio $b_f/d \approx 1$, which identifies a W-section typically used for columns because it has approximately equal strong-axis and weak-axial buckling capacity. For this cross-section, the two parameters $c_1 = 1\text{-}2t_f/d = 0.7692$ and $c_2 = t_w/b_f = 0.0734$. By substituting these two parameter values into Eqs. (6.4.5), (6.4.9) and (6.4.13), and then normalizing them through Eqs. (6.4.1) , the non-dimensional expressions for m, v, and p as functions of parameters φ and ζ are obtained. By using the same procedure as that for rectangular sections, the corresponding $p + m$ yield-failure surfaces found for v values of 0, 0.4, 0.6, 0.8, 0.9, and 0.95 are as shown in Figure 6.6. It is observed from the figure that for values as high as $v = 0.2$, the results predicted for the W-section by both Ellyin and Deloin (1972) and the current study are in good agreement, but that Ellyin and Deloin's results overestimate the yield-failure capacity of the section when $v > 0.2$.

It should be pointed out that it can be quite complicated to derive yield-failure surfaces as described in the previous sections, because, for a given loading level, two of the three equations defining the normalized forces m, v, and p must first be solved to find the parameters φ and ζ. In the iterative process of solving these highly nonlinear equations to obtain the yield surface contours, the computation can be extremely unstable in some cases (this topic is currently under study).

6.5 Comparisons with Experimental Results

Failure phenomena at extreme loading levels are difficult to model theoretically, because the distributions of the stresses and corresponding deformations are highly nonlinear. The correctness of a solution is directly related to the assumptions used to derive it. To verify the accuracy of the yield-failure surfaces derived in this study, the theoretical results are compared with those obtained from some experiments reported in the literature (Kusuda & Thurlimann, 1958; Kasai & Popov, 1986).

In the experiments by Kusuda and Thurlimann (1958), three specimens of length 416.25 mm (18.5 in) are designed as cantilever beams with a 10WF29 section having the following properties: depth d = 259.59 mm (10.22 in), flange width b_f = 147.32 mm (6.8 in), flange thickness t_f = 12.7 mm (0.5 in), web thickness t_w = 7.341 mm (0.289 in), area A = 5503.22 mm^2 (6.53 in^2), and plastic modulus Z = 568631 mm^3 (34.7 in^3).

The short beams have a depth-to-length ratio = 0.624 to enhance the effect of the shear force in the experiments (typically, the ratio is about 0.1 for designed beams). Based on coupon tests taken from the flange and web of the cross-section, the static yield stress σ_y = 254.93 MPa (37 ksi). Accordingly, the plastic moment capacity $M_p = \sigma_y Z$ = 144.96 kN-m, the axial plastic capacity $P_p = \sigma_y A$ = 1402.94

kN, and the shear plastic capacity $V_p = \tau_y A$ = 809.98 kN. For the monotonic loading history adopted for the experiments, the normalized axial force were assigned values of $p = P/P_p$ = 0.13, 0.19, and 0.37 for the three specimens. As the corresponding recorded load-deflection curves displayed no distinct yield-load level, Kusuda and Thurlimann (1958) determined it to be at the intersection of the tangent lines to the elastic and strain-hardening portions of the experimental curves. With this approach, the yield loads for the three specimens are those listed in the second column of Table 6.1. The values of internal axial force P in the third column are computed by multiplying P_p with given values of normalized axial force p. Also in Table 6.1, the values of internal shear force V in the fourth column and internal bending moment M in the fifth column are determined from the static equilibrium conditions. The previously noted values for P_p, V_p and M_p are used to normalize the internal yield forces to obtain the values of p, v and m shown in the last three columns of Table 6.1.

To compare the experimental results with those predicted by the method proposed in this study, the three pairs of points (m, p) in Table 6.1 from the test results are shown in Figure 6.7 as the three open circles. If normalized shear force v is selected to have values 0.26 and 0.31 listed in Table 6.1, then the two corresponding M-P interaction curves are plotted in Figure 6.7 by using the failure-surface defined by Eqs. (6.4.5), (6.4.9) and (6.4.13). Obviously, the three points from the experimental results are not located on the corresponding two predicted curves. The reason is that when v is normalized, the entire cross-section area A is used to determine V_p (= $\tau_y A$ = 809.98 kN) so that the shear capacities are overestimated. If the entire web area and only 52% (achieved after several trials) of the flange area are assumed to take shear force, the adjusted yield strength V_h becomes 542 kN. By using V_h instead of V_p to normalize the values of shear force V in Eq. (6.4.9), the non-dimensional values of v_h become as listed in Table 6.2 for the three specimens. If v_h = 0.46, the interaction curve is obtained as the dashed line in Figure 6.7. It can be seen from Table 6.2 and Figure 6.7 that the experimental results are quite close to those in the dashed line. For example, from column 5 of Table 6.2, the differences of the m values are 1.22%, 0%, and -2.82%, respectively, for the three specimens. This implies that approximately 50% of the flange area contributes to the shear loading.

Note that the effect of the shear force on the plastic yield failure cannot be ignored. When the effect is neglected by setting v = 0, the predicted m values are those in column 6 of Table 6.2. The differences of the values of m in Figure 6.7 are 0.18, 0.14 and 0.08, for the first, second, and third specimens, respectively, as indicated in column 7 of Table 6.2; the corresponding relative differences of 18.6%, 15.1% and 10.5% are listed in column 8 of Table 6.2. It can be concluded that when the ratio of the section depth-to-member length for a beam is large enough for the axial force and shear force to be of the same order of magnitude as that at the yield-failure level, the three-dimensional

yield-failure criterion accounting for the interaction of bending, shearing and axial forces should be employed for progressive-failure analysis.

As another example, the cyclical test results from an experimental investigation of the behaviour of shear links applied in seismic engineering (Kasai & Popov, 1986) are used to check the accuracy of the combined-stress failure surface derived by this study. Two link beam specimens with a W8X10 cross section are tested under combined axial force, shear force and bending moment. The ratio of the shear force to the axial force is fixed at unity during the cyclically loading process (i.e., $P = V$). The properties of the cross-section are: depth d = 202.44 mm (7.97 in), flange width b_f = 100.58 mm (3.96 in), flange thickness t_f = 5.28 mm (0.208 in), web thickness t_w = 4.32 mm (0.17 in), and area A = 1922.58 mm^2 (2.98 in^2). The two link beam lengths are 368.3 mm (14.5 in) and 444.5 mm (17.5 in), and the corresponding depth-to-length ratios are 0.55 and 0.46, respectively.

The axial, shear and moment plastic strengths P_p = 743.6 kN (167.1 kips), V_p = 205.6 kN (46.2 kips) and M_p = 56.3 kN-m (498 kips-in) for the W8X10 section were determined by cyclical dynamic tests (Kasai & Popov, 1986). To be consistent with the experimental results for the purpose of comparison, these three strength values are adopted for the model of interactive failure behaviour proposed by this study. To investigate such interaction behaviour using the failure surface defined by Eqs. (6.4.5), (6.4.9) and (6.4.13), one test data pair for the shear link from the Kasai and Popov (1986) experiments is illustrated here; specifically, for $m = M/M_p$ = 0.842 and $v_k = V/V_p$ = 0.96, where the normalized shear force v_k is found using effective shear area $A_{se} = t_w(d\text{-}t_f)$. If the entire cross-sectional area A is assumed to take the shear force, the non-dimensional shear force becomes,

$$v = \frac{V}{\tau_y A} = v_p \frac{A_{se}}{A} = 0.96 \frac{4.32(202.44 - 5.288)}{1922.58} = 0.425 \tag{6.5.1}$$

For $P = V$, from the experiments the normalized axial force is given by,

$$p = \frac{P}{\sigma_y A} = \frac{V}{\sqrt{3}\tau_y A} = \frac{0.425}{\sqrt{3}} = 0.245 \tag{6.5.2}$$

where the von Mises yield criterion is applied. The data pair (p, m) = (0.245, 0.842) is shown in Figure 6.7 as the symbol ⊕. For the W8X10 (English unit) cross-section with normalized shear force v = 0.425 at failure, the interaction curve predicted by using Eqs. (6.4.5), (6.4.9) and (6.4.13) is plotted in Figure 6.7 as the heavy solid line. It is evident that the tested point is significantly outside the predicted curve. In fact, the shear force v predicted by the method in this study should be adjusted from 0.425 to approximately 0.31, so as to match with the experimental value. If shear force V from the experiment is considered constant, according to Eq. (6.5.1), increasing the value τ_y can alone

achieve such an adjustment because the full section area A has already been accounted for. This reveals that perhaps strain hardening behaviour should be taken into account in the method proposed in this study. For instance, if the hardening shear stress is assumed to be $\tau_h = 1.05\tau_y$ and 95% of the cross-sectional area ($0.95A$) takes the shear force, the normalized shear force from Eq. (6.5.1) at failure remains at about $v = 0.425$ because $\tau_h \times (0.95A) \approx \tau_y A$. After the strain-hardening is considered, the axial force in Eq. (6.5.2) becomes $p = 0.245/1.05 = 0.233$. By substituting $v = 0.425$ and $p = 0.233$ into the corresponding normalized expressions of Eqs. (6.4.9) and (6.4.13), and then solving the two equations yields values of parameters φ and ζ, from which the value of m is found to be 0.801 from the normalized expression of Eqs. (6.4.5). The experimental point in the coordinate system then becomes $(m, p) = (0.801, 0.233)$, shown by the black in-fill circle in Figure 6.7, which is closer to the predicted curve. This result implies that the effect of strain hardening on plastic-yield failure of member sections can be significant in cyclical loading situations.

6.6 Combined Failure Model

In Chapter 3, two two-dimensional models are proposed for yield-failure surfaces, involving either the interaction of bending moment and axial force, or of bending moment and shear force. To facilitate progressive-failure analysis while accounting for the simultaneous interaction of bending, shearing and axial forces, a corresponding three-dimensional model is developed in the following.

6.6.1 Initial Yield

The initial yield of a structural steel cross-section is dependent on the distribution of the residual stresses that remain in an unloaded component, after it has been formed into a finished product. Residual stresses generally develop during the cooling stage after the rolling, welding, punching or cambering operations. Within a loading process for a structure, residual stresses tend to initiate plastic yielding at load levels lower than those predicted by stress analysis that ignores such stresses. The effect of residual normal stress has been extensively investigated (Huber & Beedle, 1954). In practice, design codes suggest that residual normal stress σ_r should be equal to approximately 30% of the full-yield stress σ_y (AISC, 2001). The effect of residual shear stress has not been extensively investigated. It is assumed that residual shear stress τ_r is about 5% of the full-yield stress τ_y (see Appendix 6.B).

Once the initial-yield normal and shear stresses are determined, the normalized initial-yield strengths are given by $m_y = M/M_y$, $v_y = V/V_y$ and $p_y = P/P_y$, where M_y, V_y and P_y have been defined in Section 3.3. The initial-yield surface for a section accounting the interaction of bending moment,

shear force and axial force is taken to be the shaded triangular plane defined by points m_y, v_y and p_y in Figure 6.8 (i.e., in one quadrant of the stress space). The initial-yield plane is expressed as,

$$m_y + v_y + p_y = 1 \tag{6.6.1}$$

6.6.2 Full Yield

To determine the extent of stiffness degradation due to plastic behaviour, a seven-domain failure model is proposed to account for the interactive influence of the bending moment, shear force and axial force This failure model is an extension of the planar *M-P* or *M-V* failure model discussed in Chapter 3.

After the initial-yield plane defined in Eq. (6.6.1) is determined, the three failure domains in each coordinate plane are defined by the corresponding six full-yield points P^*_1 through P^*_6 as shown in Figure 6.8. Points P^*_1 and P^*_2 are determined when $m = m_y$ and by using m-p (v =0) and m-v (p = 0) yield loci, respectively. The remaining four points P^*_3 to P^*_6 can be similarly obtained by using the corresponding yield loci by setting $v = v_y$ and $p = p_y$, respectively. These six points serve as a base to define the full-yield failure behaviour within the domain bounded by the three coordinate planes.

Based on the six points P^*_1 through P^*_6 , the three boundary curves on the yield surface in Figure 6.9 can be determined so that the *M-V-P* yield surface is divided into seven-failure domains. The following approach is adopted to define the seven domains. Curve P_3-P_8-P_9-P_6 in Figure 6.9 is the intersection between the yield surface and the following plane,

$$\underline{m}_y = \max\{m_{yp}, m_{yv}\} \tag{6.6.2}$$

where m_{yp} and m_{yv} are the moment values at points P^*_3 and P^*_6 in Figure 6.8, respectively. Similarly, if v_{ym}, v_{yp} , p_{ym} and p_{yv} are respectively determined from points P^*_2 , P^*_5 , P^*_1 and P^*_4, the intersections between the yield surface and the two following planes,

$$\underline{v}_y = \max\{v_{yp}, v_{ym}\} \tag{6.6.3}$$

$$\underline{p}_y = \max\{p_{ym}, p_{yv}\} \tag{6.6.4}$$

determine the curve P_1-P_7-P_8-P_4 parallel to the pm-plane, and the curve P_2-P_7-P_9-P_5, parallel to the vm-plane in Figure 6.9, respectively. Consequently, the seven failure domains are determined by the boundary curves in the figure.

For the loading path OP in Figure 6.9, point P(m_{pr}, v_{pr}, p_{pr}) on the yield surface is obtained by solving the intersection between the yield surface and the straight line OP, where subscript *pr* denotes the reduced strength due to the interaction of m, v and p. When shear force $v_{pr} \le \underline{v}_y$, one of the

following three failures occurs: flexural failure in domain D_m if $p_{pr} \le \underline{p}_y$; axial failure in domain D_p if $m_{pr} < \underline{m}_y$; or bending plus axial failure in D_{mp} domain.

When $v_{pr} > \underline{v}_y$, one of the following four failures occur: a shear failure in D_v if $p_{pr} \le \underline{p}_y$ and $m_{pr} < \underline{m}_y$; a bending plus shear failure in D_{mv} domain if $p_{pr} \le \underline{p}_y$; a shear plus axial failure in D_{vp} domain if $m_{pr} < \underline{m}_y$; otherwise, bending plus shearing plus axial failure in D_{mvp} domain.

In Figure 6.9, three types of failure domains are in the proposed seven-domain failure model. First, if any one of the three principal internal *M*, *V* or *P* forces is far more substantial than the other two, single-stress failure occurs, respectively, in the corresponding flexural, shearing or axial domain D_m, D_v or D_p defined by the hatched-grey surface in Figure 6.9. Secondly, if any two of the three internal forces are far more significant than the third force, a two-stress failure occurs in the corresponding $D_{mv,}$ D_{vp} or D_{mp} domain defined by the solid-grey surface in Figure 6.9. Thirdly, if the three internal forces all possess the same significance, a three-stress failure occurs in the D_{pvm} domain defined by the blank surface in Figure 6.9.

6.7 Example Application of M-V-P Failure Surface

Debris loading due to local damage is a serious problem under abnormal loading events. Consider the structural portion with W-shape columns C_1 and C_2 that support W-shape beams B_1 and B_2 in Figure 6.10(a). The beam-to-column connections at joint B, C and D are semirigid, while joint A is free to rotate and horizontally translate. As the abnormal loading occurs, beam B_1 disengages from the main portion at joint E. The beam rotates about point D, and its right end falls down onto beam B_2. This forms debris loading applied at a distance *x* from end B that has vertical and horizontal components *W* and λW, where λ is the ratio of the horizontal load to vertical load.

Assume the two columns are adequate to support beam B2 with the debris loads. Only the behaviour of B2 is investigated using the yield surface derived in this study. For the model in Figure 6.10 (b), reaction V_B at support B can be readily found as,

$$V = V_B = \frac{L_b - x}{L_b} W + \frac{M_c}{L_b} \tag{6.7.1}$$

where moment M_B at support B is a function of load *W*, and *V* stands for the shear force at the right-hand side of point C. If portion CB of the beam is taken as a free-body diagram, then the bending moment at point C is given by,

$$M = xV - M_c \tag{6.7.2}$$

If end A can move freely in the horizontal direction at the failure state, the axial force becomes,

$$P = \lambda W \tag{6.7.3}$$

Equations (6.7.1), (6.7.2) and (6.7.3) define the loading path during the increase of load W. Beam B2 fails when load W reaches such a level that M_B attains the connection capacity M_c and the internal forces V, M, P at section C are on the yield surface governed by Eqs. (6.4.5), (6.4.9) and (6.4.13). If the moment of Eq. (6.7.2) is normalized as $m = M/M_p$, normalized shear force v from Eq. (6.7.1) is expressed in terms of m as,

$$v = \kappa(m + m_c)\frac{d[1-(1-c_2)c_1^2]}{4x(c_1c_2+1-c_1)} \tag{6.7.4}$$

where κ is a yield criteria parameter (e.g., $\kappa^2 = 3$ for the von Mises criterion), dimension d is the section depth, parameters c_1 and c_2 for W-shape section have been discussed in section 6.4.4, and $m_c = M_c/M_p$ is the normalized moment of the connection. By solving for load W from Eq. (6.7.1) and then substituting it into Eq. (6.7.3), the following normalized axial force is obtained,

$$p = \frac{\lambda[m + m_c(1-x/L_b)]}{1-x/L_b}\frac{d[1-(1-c_2)c_1^2]}{4x(c_1c_2+1-c_1)} \tag{6.7.5}$$

To find the data pair of (m, v, p) at failure, the following procedure is adopted: (1) normalize the yield surface defined in Eq. (6.4.5), Eq. (6.4.9) and Eq. (6.4.13) to obtain $m(\varphi, \zeta)$, $v(\varphi, \zeta)$, and $p(\varphi, \zeta)$; (2) replace m, v and p in Eqs. (6.7.4) and (6.7.5) with $m(\varphi, \zeta)$, $v(\varphi, \zeta)$ and $p(\varphi, \zeta)$ to form two nonlinear equations with respect to φ and ζ; (3) solve for φ and ζ from the two equations for given values of the parameters in the expressions; (4) compute the values for $m_f = m(\varphi, \zeta)$, $v_f = v(\varphi, \zeta)$ and $p_f = p(\varphi, \zeta)$ from Eqs. (6.4.5), (6.7.4) and (6.7.5), respectively.

For the beam with cross section W920×253, length L_b is found to be 14630 mm by the use of $L^2{}_b = (L_c - x)^2 + L^2{}_c$ with L_c = 4572 mm and x = 733 mm. The dimension parameters in Eqs. (6.5.4) and (6.5.5) are $c_1 = 1\text{-}2t_f/d = 0.9393$, $c_2 = t_w/b = 0.0565$, $x/L_b = 0.0501$, and $d/x = 1.2537$. Substitute all of the previous values with designated load ratio λ and connection moment m_c into Eqs. (6.7.4) and (6.7.5), and solve them to obtain parameters φ and ζ , and in turn, intersection point (m_f, v_f, p_f) at failure by following the preceding procedure. The computation results are shown in Figure 6.11 with m_c set to 0, 0.25, 0.5 and 1, and the load factor λ ranging from zero to one.

It is seen from Figure 6.11 that if load ratio λ increases from zero to unity, axial force p_f increases significantly, but moment m_f and shear force v_f decrease slightly for a simply supported beam (m_c = 0). With the increase of connection strength m_c from zero to unity, moment m_f decreases and v_f increases considerably for a given load ratio λ. For example, if the horizontal debris loading is ignored (λ = 0) and m_c = 1, shear force v_f increases by about 60%, whereas the bending moment m_f

decreases by approximately 74% compared to that when $m_c = 0$. Especially, when $\lambda = 1$ and $m_c = 1$ the bending moment no longer dominates the plastic failure of beam B2 in Figure 6.11. These results reveal that changes of both the load ratio and end connection strength of the beam can substantially affect the interactive behaviour of moment, shear and axial forces at failure.

The loading capacities corresponding to the designated λ and m_c values are given in Table 6.3, where non-dimensional loading capacity w_f is the ratio of W_f to P_p. Here, W_f is the load P/λ at failure from Eq. (6.7.3), and P_p is the axial capacity defined in Eq. (6.4.16a). It is seen for load ratio λ that when the connection capacity m_c is increased, loading capacity w_f increases considerably. For instance, when m_c is set to 0.25, 0.5 and 1, and λ to 0, the load capacities of w_f increase 17.49% (0.4266/0.3631-1 = 0.1749), 32.25% and 53.35%, respectively, compared with those if $m_c = 0$. On the other hand, for given connection capacity m_c, the load capacity w_f decreases with the increase of vertical-to-horizontal loading ratio λ. For example, when $m_c = 0$ the load capacity w_f decreases by 9.59% (0.3283/0.3631-1 = -0.0959) from 0.3631 (when $\lambda = 0$) to 0.3283 (when $\lambda = 1$). Similarly, when m_c = 0.25, 0.5, and 1, the decreased percentages of w_f are 10.99%, 12.12% and 19.77%, respectively.

Appendix 6.A Anti-Derivatives for Evaluating Resultant Stresses

Anti-derivatives presented in this appendix are used to evaluate the axial force, bending moment, and shear force of the member cross-sections in the plastic limit state. Parameters φ and ζ represent the parametric functions, and ρ is a non-dimensional variable. The derivations in this appendix are based on Mathematica software Version 3.0 (Wolfram, 1996), and the related intermediate expressions are not included in the subsequent text. The following integral is used to evaluate the bending moment at the plastic failure of a section,

$$I_1 = \int \rho(\varphi\rho + \zeta) / \sqrt{(\varphi\rho + \zeta)^2 + (1 - |\rho|)^2}\, d\rho \tag{6.A.1}$$

When $\rho = c_1 \geq 0$, the following solution of Eq. (6.A.1) is derived,

$$I_{M+}(c_1) = \frac{[\zeta(2-\varphi^2) + \varphi(3 + c_1 + \varphi^2 c_1)] f_{1+} + [2(\zeta + \varphi) - 3\varphi\zeta^2 - 4\zeta\varphi^2 - \varphi^3] f_{2+}}{2(1+\varphi^2)^{2.5}} \tag{6.A.2}$$

where subscript of I_{M+} denotes that the anti-derivative in Eq. (6.A.1) is employed to evaluate moment M, and subscript + denotes that variable ρ of the integrand in Eq. (6.A.1) is positive and is replaced by c_1. Functions f_{1+} and f_{2+} in Eq. (6.A.2) are given by,

$$f_{1+}(c_1) = \sqrt{1+\varphi^2}\sqrt{(1-c_1)^2 + (\zeta + \varphi c_1)^2} \tag{6.A.3}$$

and

$$f_{2+}(c_1) = \ln\{2[\varphi\zeta + (\varphi^2+1)c_1 - 1 + f_{1p}]/\sqrt{\varphi^2+1}\} \tag{6.A.4}$$

When ρ is in the negative domain, term 1-|ρ| becomes 1+ρ. The following solution of Eq. (6.A.1) in the negative domain is derived,

$$I_{M-}(c_1) = \frac{[\zeta(2-\varphi^2) - \varphi(3 + c_1 + \varphi^2 c_1)]f_{1-} + [2(\varphi-\zeta) - 3\zeta^2\varphi + 4\zeta\varphi^2 - \varphi^3)]f_{2-}}{2(1+\varphi^2)^{2.5}} \tag{6.A.5}$$

where negative variable ρ is replaced by $-c_1$ ($c_1 \geq 0$), and functions f_{1-} and f_{2-} in Eq. (6.A.5) are given by,

$$f_{1-}(c_1) = \sqrt{1+\varphi^2}\sqrt{(1-c_1)^2 + (\zeta - \varphi c_1)^2} \tag{6.A.6}$$

$$f_{2-}(c_1) = \ln\{2[\varphi\zeta - (\varphi^2+1)c_1 + 1 + f_{1-}]/\sqrt{\varphi^2+1}\} \tag{6.A.7}$$

where subscript – denotes that variable ρ of the integrand in Eq. (6.A.1) is in the negative domain.

To evaluate the bending moment at the plastic failure of a rectangular or wide-flange section, the following integral expression is employed to evaluate the definite integral,

$$I_m(c_1) = I_{1p}(c_1) - I_{1n}(c_1) \tag{6.A.8}$$

where subscript *m* refers to moment.

The integral used to evaluate shear force *V* at the plastic failure of a section is,

$$I_V = \int 0.5(1-|\rho|)/\sqrt{(\varphi\rho+\zeta)^2 + (1-|\rho|)^2}\, d\rho \tag{6.A.9}$$

Similar to the discussion of the moment for positive and negative domains of variable ρ in Eq. (6.A.9), the expressions of the anti-derivatives are derived as,

$$I_{V+}(c_1) = 0.5[-f_{1+} + \varphi(\varphi+\zeta)f_{2+}]/(1+\varphi^2)^{1.5} \tag{6.A.10}$$

$$I_{V-}(c_1) = 0.5[f_{1-} + \varphi(\varphi-\zeta)f_{2-}]/(1+\varphi^2)^{1.5} \tag{6.A.11}$$

In evaluating the shear force at the plastic failure of a rectangular or wide-flange section, the expression is,

$$I_v(c_1) = I_{2p}(c_1) - I_{2n}(c_1) \tag{6.A.12}$$

where subscript *v* refers to the shear force.

Finally, the following integral is used to evaluate axial force *P* at the plastic failure of a section,

$$I_P = \int 0.5(1-|\rho|)/\sqrt{(\varphi\rho+\zeta)^2 + (1-|\rho|)^2}\, d\rho \tag{6.A.13}$$

where subscript *P* indicates the anti-derivative in Eq. (6.A.13) and is applied for evaluating axial force *P*. For the positive and negative values of ρ, the corresponding solutions of Eq. (6.A.13) are,

$$I_{P+}(c_1) = 0.5[\varphi f_{1+} + (\zeta + \varphi) f_{2+}]/(1+\varphi^2)^{1.5} \tag{6.A.14}$$

$$I_{P-}(c_1) = 0.5[\varphi f_{1-} + (\zeta - \varphi) f_{2-}]/(1+\varphi^2)^{1.5} \tag{6.A.15}$$

In evaluating the axial force at the plastic failure of a rectangular or wide-flange section, the following expression is used,

$$I_a(c_1) = I_{3p}(c_1) - I_{3n}(c_1) \tag{6.A.16}$$

where subscript *p* means the expression is applied to determine axial force *P*.

Appendix 6.B Residual Shear Stress

This appendix presents a method to derive the residual shear stress of structural steel W-sections for determining the initial yield shear stress in structural analysis. It is known that the residual normal stresses distribution across the web of a W-section can be simply represented by a bilinear distribution, as displayed in Figure 6.12 (a) (ECCS, 1984), where *h* is equal to half of the web depth. It can be inferred from the bilinear normal stress distribution that the residual shear stress distribution varies as shown in Figure 6.12 (b) based on the equilibrium conditions of resultant normal and shear stresses, where τ_s is the maximal residual shear stress (Hibbeler, 2004) The total shear stress, including the residual shear stress in Figure 6.12 (b) and the shear stress, induced by the external loads in Figure 6.12 (c), is expressed as,

$$\tau = \tau_c[1-(y/h)^2] + \tau_s y(h-y)/h^2 \tag{6.B.1}$$

where τ_c is the maximum shear stress produced by external loading. To find the maximum stress for both the residual and external loading shear stresses, Eq. (6.B.1) is differentiated with respect to the depth variable *y* as,

$$\frac{d\tau}{dy} = -2\tau_c y/h^2 + \tau_s(h-2y)/h^2 = 0 \tag{6.B.2}$$

Thus, the location of the maximum shearing stress is determined by solving Eq. (6.B.2) for *y*, and given by,

$$y_m = \frac{h}{2}\frac{\tau_s}{\tau_c + \tau_s} \tag{6.B.3}$$

which is relevant to maximum stresses τ_s and τ_c and depth *h*. By substituting Eq. (6.B.3) for y_m into Eq. (6.B.1), the maximum shear stress is,

$$\tau_{\max} = \tau_c + \frac{-0.25\tau_c\tau_s^2 + 0.5\tau_s^2(\tau_c + 0.5\tau_s)}{(\tau_c + \tau_s)^2} = \tau_c + \frac{0.25\tau_s^2}{\tau_c + \tau_s} \tag{6.B.4}$$

Obviously, during the loading process, maximum shear stress $\tau_{\max}$ in Eq. (6.B.4) achieves initial yield stress τ_y (i.e., $\tau_{\max} = \tau_y$). Therefore, from Eq. (6.B.4) the initial-yield shearing condition is determined as,

$$\tau_y - \tau_c - \frac{0.25\tau_s^2}{\tau_c + \tau_s} = 0 \tag{6.B.5}$$

Solve Eq. (6.B.5) for initial-yield shearing stress,

$$\tau_{cy} = \frac{\tau_y}{2}\left(1 - \frac{\tau_s}{\tau_y} + \sqrt{1 + 2\frac{\tau_s}{\tau_y}}\right) \tag{6.B.6}$$

which is the initial-yield shear stress under the external loading after the residual shear stress has been accounted for. The numerical values in Table 6.4 demonstrate how the residual shearing stress affects the initial-yield shear stress τ_{cy}. It is observed in the table that when the residual shear stress is ignored ($\tau_r = 0$), then τ_{cy} becomes conventional yield-stress τ_y. It is noted that if the maximal residual shear stress τ_s is as high as 50% of yield shear stress τ_y, the effect of the residual shear stress on the initial-yield shear stress τ_{cy} is only about 4.29% of yield shear stress τ_y; also the location of the initial yield occurs at 0.17*h*. Therefore, for the design and analysis of structures, it can be reasonably and conservatively assumed that effective residual shear stress $\tau_r = 0.05\tau_y$; that is, 5% of yield shear stress τ_y.

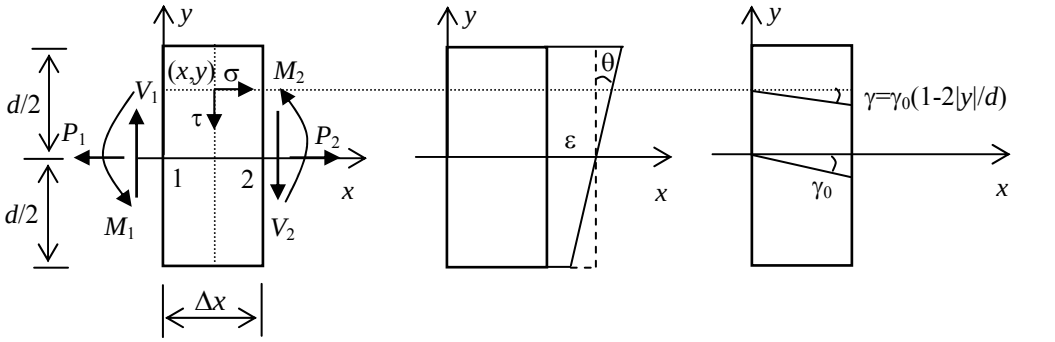

(a) Stresses and resultants (b) Rotation and axial deformation (c) Transverse deformation

Figure 6.1 Plastic zone loadings and deformations

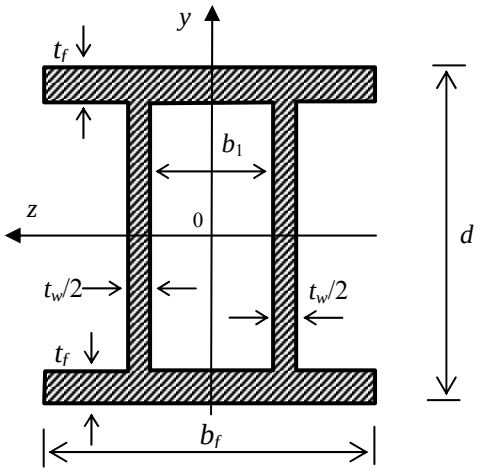

Figure 6.2 Dimensions of idealized cross-section

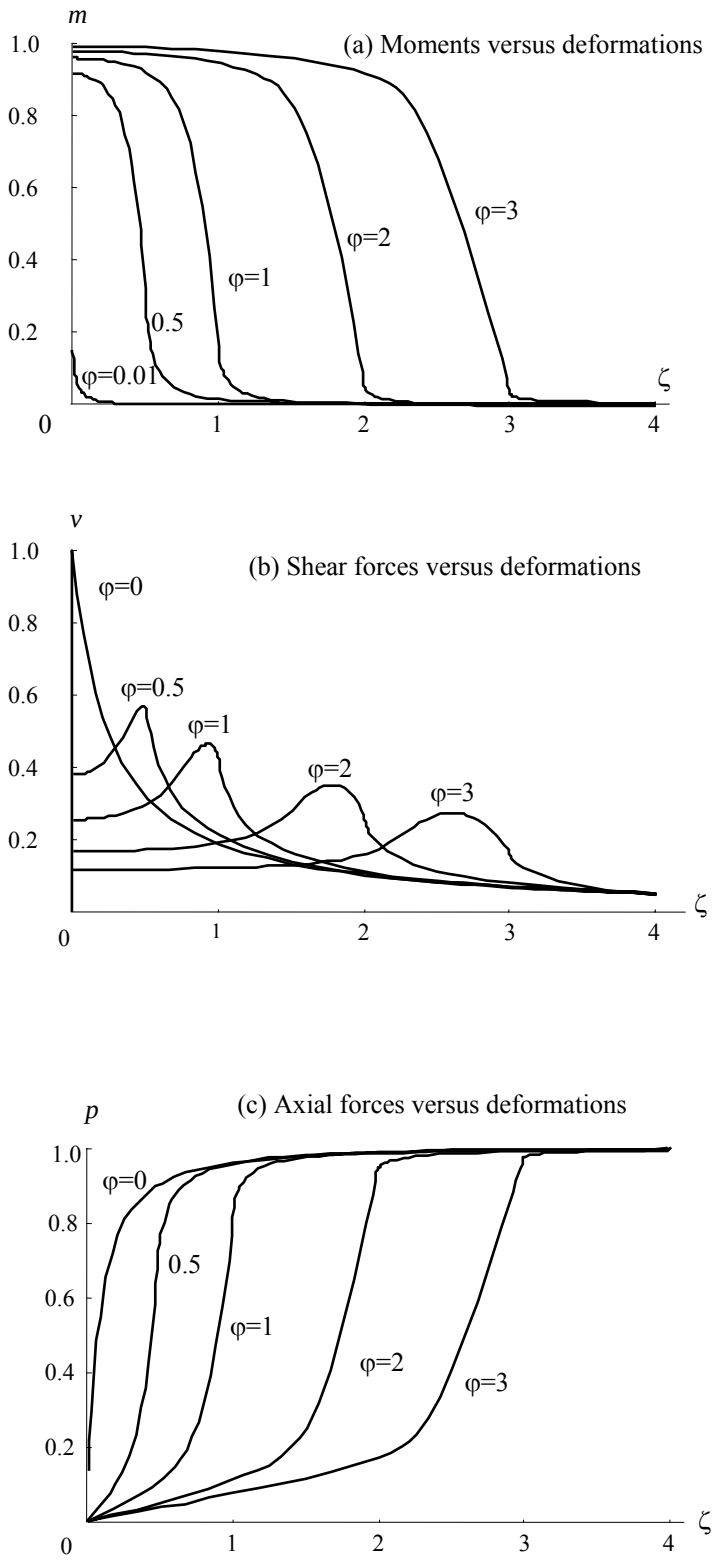

Figure 6.3 Force-deformation relationships in plastic zone

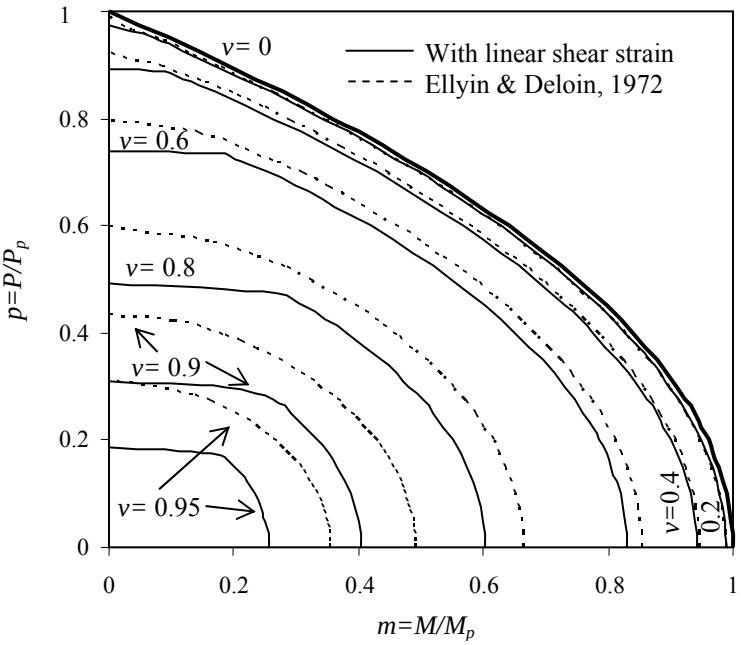

Figure 6.4 Comparison of yield-surface contours for rectangular cross section

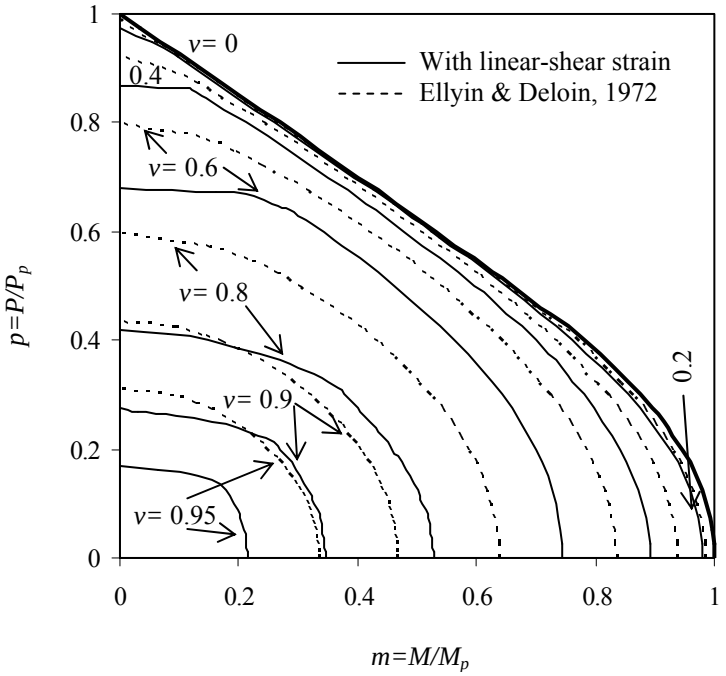

Figure 6.5 Comparison of yield-surface contours for W920X253 section

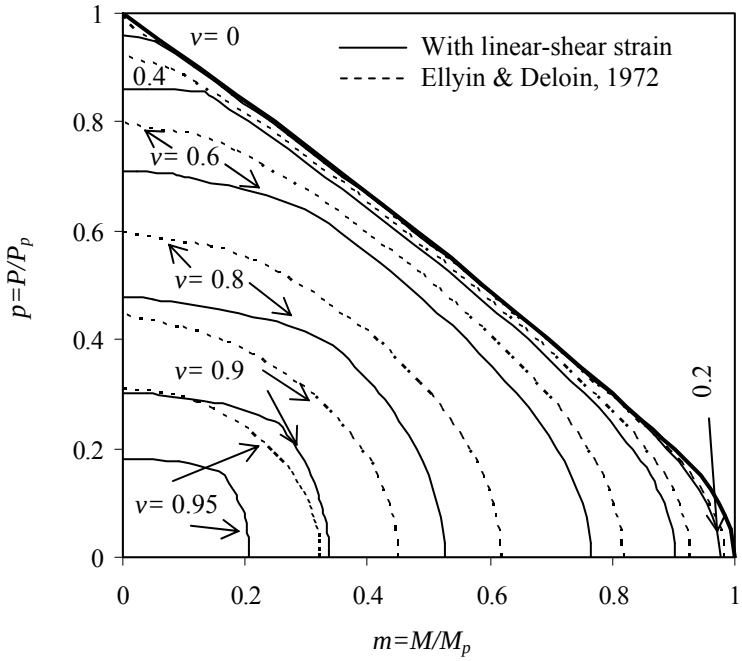

Figure 6.6 Comparison of yield-surface contours for W360X382 section

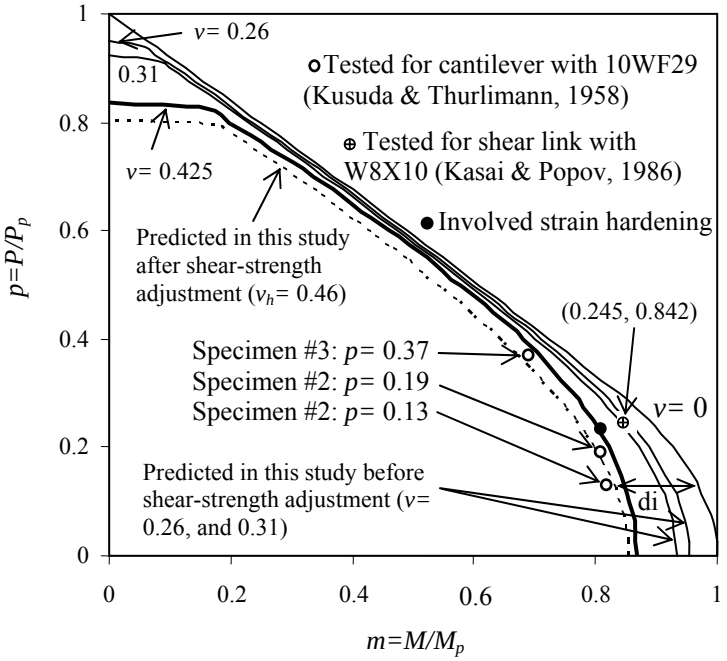

Figure 6.7 Comparison of predicted results with experimental measurements

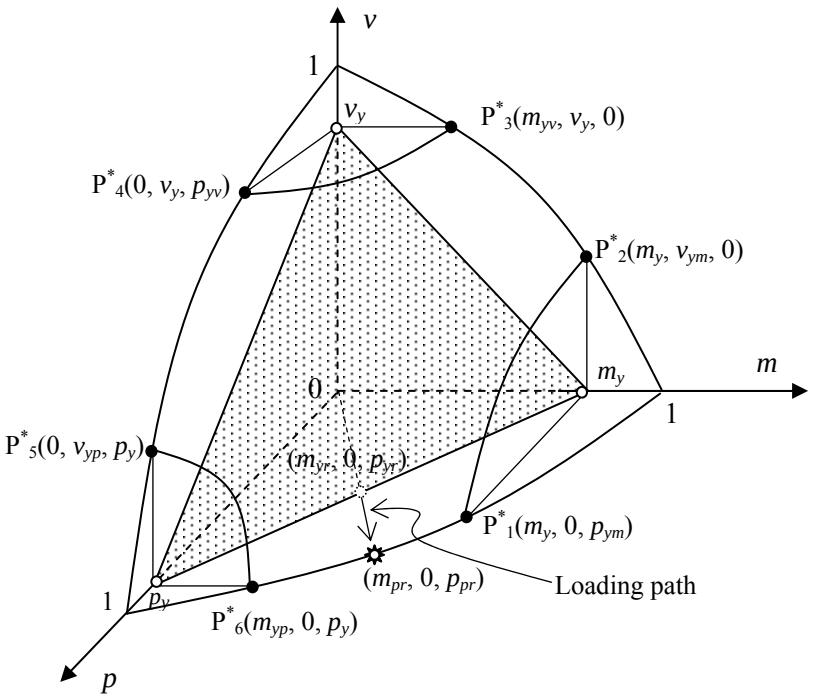

Figure 6.8 Initial-yield plane and corresponding points on full-yield surface

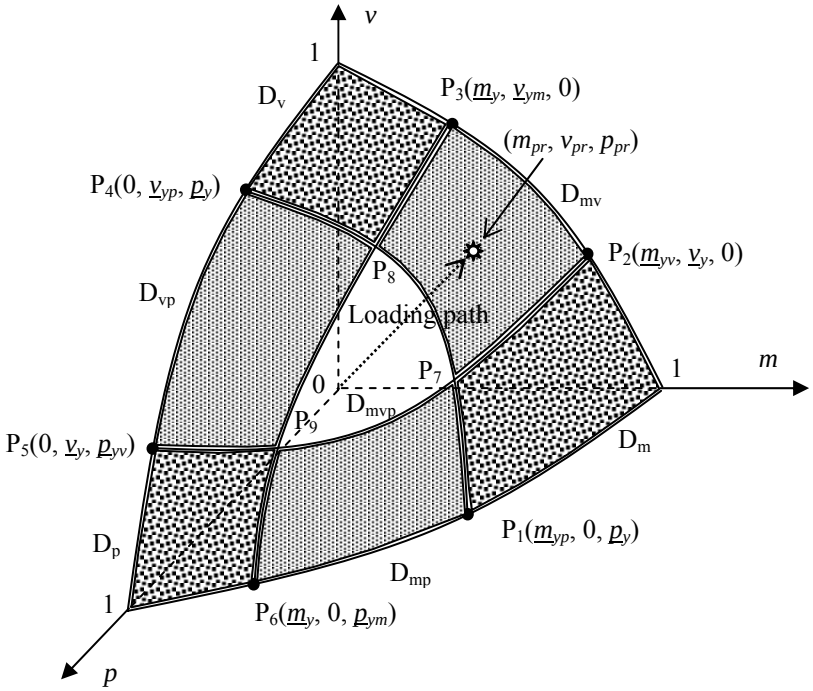

Figure 6.9 Seven-domain plastic failure model

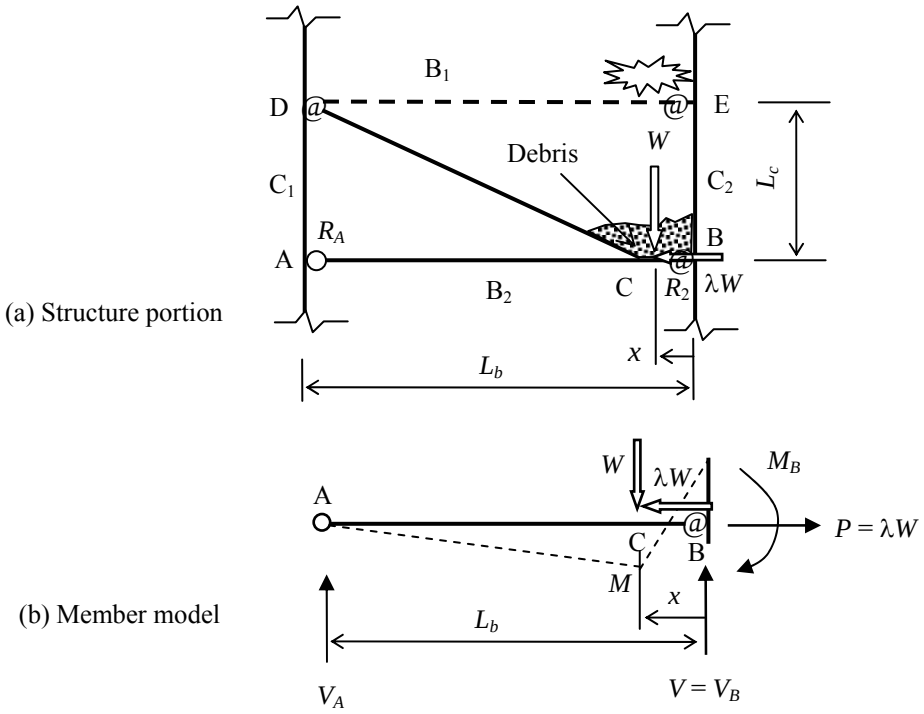

Figure 6.10 Effect of debris loading on lower-floor beam

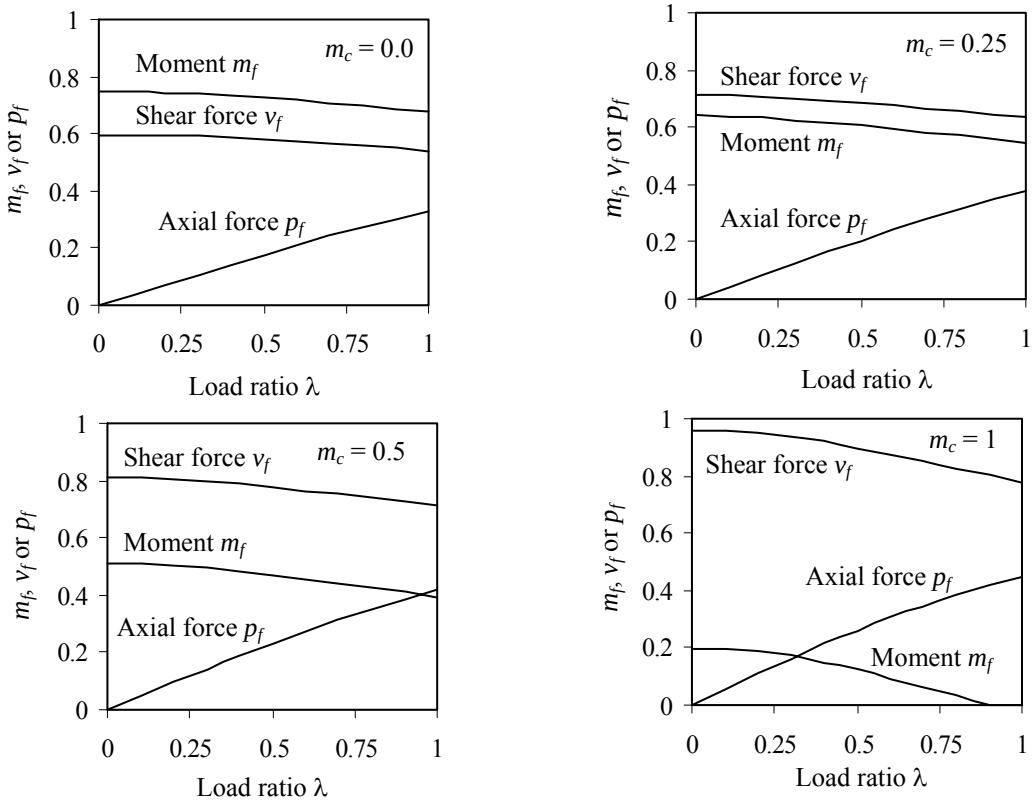

Figure 6.11 Effects of load ratio and end-connection capacity on internal forces

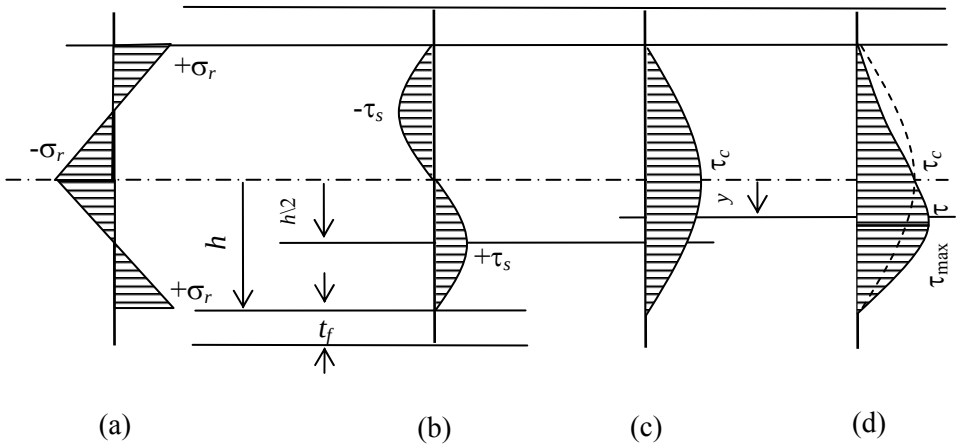

Figure 6.12 Normal and shear residual stress distributions across W-shape web section

Table 6.1 Test results accounting for M-V-P interaction (Kusuda & Thurlimann, 1958)

Specimen	Load (kN)	*P*(kN)	*V*(kN)	*M*(kN-m)	*p*	*v*	*m*
No.1	312	182	253	119	0.13	0.31	0.82
No.2	365	267	249	117	0.19	0.31	0.81
No.3	561	519	212	100	0.37	0.26	0.69

Table 6.2 Comparison of predicted results with test measurements (Kusuda et al., 1958)

Specimen	Tested *m*	v_h	Predicted *m*	Error(%)	*m*(*v*=0)	di	Error(%)
No.1	0.82	0.47	0.83	1.22	0.97	0.18	18.6
No.2	0.81	0.46	0.81	0.00	0.93	0.14	15.1
No.3	0.69	0.39	0.71	-2.82	0.76	0.08	10.5

Table 6.3 Collapse load $w_f = W_f/P_p$ for floor beam under debris loading

λ	$m_c = 0$	$m_c = 0.25$	$m_c = 0.5$	$m_c = 1$
0.0	0.3631	0.4266	0.4802	0.5568
0.1	0.3630	0.4260	0.4790	0.5560
0.2	0.3615	0.4235	0.4765	0.5530
0.3	0.3593	0.4197	0.4723	0.5463
0.4	0.3565	0.4150	0.4668	0.5345
0.5	0.3532	0.4100	0.4600	0.5216
0.6	0.3493	0.4047	0.4528	0.5077
0.7	0.3447	0.3990	0.4453	0.4931
0.8	0.3396	0.3929	0.4376	0.4781
0.9	0.3341	0.3864	0.4299	0.4626
1.0	0.3283	0.3797	0.4220	0.4467

Table 6.4 Effect of residual shear stress on initial-yield shear stress

τ_s/τ_y	0	0.1	0.2	0.3	0.4	0.5
τ_{cy}/τ_y	1	0.9977	0.9916	0.9825	0.9708	0.9571
$(1-\tau_{cy}/\tau_y)\times 100$	0	0.23	0.84	1.75	2.92	4.29
y_m/h	0	0.05	0.08	0.12	0.15	0.17

Chapter 7
Conclusions

Typically, structural failure involves progressive stiffness degradation and strength deterioration. During the failure process, structural materials can display elastic and plastic behaviour, external loads can change from being static to dynamic, and structural topology can possibly progressively change. To account for these failure phenomena, this thesis develops a progressive-failure analysis procedure to deal with the stiffness degradation and collapse performance of steel structures, due to both normal and abnormal loads. The nonlinear limit state analysis is in keeping with the requirements of current design codes (e.g., CISC, 2004; AISC, 2001). The progressive collapse analysis procedure itself is based on corresponding guidelines of GSA (2003) and DoD (2005). This chapter presents a summary and concluding remarks concerning the work completed, and suggests some research directions for future work.

7.1 Summary

Chapter 1 briefly reviewed the existing literature concerning progressive collapse under abnormal loading. A nonlinear analysis method was proposed and developed in Chapters 2 and 3 with account for geometric and material nonlinearities, and member shear deformation. The combined effects of semirigid connections and member plasticity on structural behaviour were explored in Chapter 4. A progressive-failure analysis method was developed in Chapter 5, and several example frameworks were analyzed with account for both member and connection damage. Finally, with a view to future extension of the research, Chapter 6 presented a three-dimensional failure model for member sections under simultaneous bending, shearing and axial forces.

To account for the stiffness degradation behaviour of members, the force-deformation relationship at member ends was obtained with account for the effects of both second-order geometric nonlinearities and shear deformation. The failure behaviour of a member cross-section was studied under combined moment-axial force interaction, and combined moment-shear force interaction.

A nonlinear structural analysis method based on the Euler incremental method was developed. The nonlinear analysis results for several steel frameworks were compared with those obtained from other methods to verify the accuracy of the proposed method.

A hybrid member model was introduced to include the effects of both member plasticity and semirigid connections. A four-parameter model was employed to simulate the nonlinear moment-

rotation relationship of semirigid connections. A compound stiffness degradation factor was developed as a function of semirigid connection and inelastic member stiffness degradation factors. The interactive effect of connection semi-rigidity and member inelasticity was illustrated for several semirigid frames.

A health index was introduced to quantify the degree of damage to member-end connections due to the disengagement of members during the process of progressive collapse.

The dynamic effect induced by impact debris loading during collapse was quantified by an impact amplification factor.

A progressive-failure analysis procedure was developed to predict the behaviour of building frameworks that experience initial local damage due to an abnormal loading event. The removal of critical member(s) is taken to model the initial local damage. Dead, live and other loads are as specified by design codes (e.g., ASCE 7-02), and load combinations comply with design/analysis guidelines of GSA (2003) and DoD (2005). The computer-based method predicts the progressive failure phenomenon stage by stage, over a nonlinear loading history. Inelastic degradation factors identify the failure degree of members and connections, as well as member disengagement from the main structure. An unloading analysis procedure accounts for abrupt stress reversals that have occurred when members disengage from the structure.

Several planar steel frameworks examples illustrated the progressive-failure analysis procedure. The incremental-load procedure was shown to proceed beyond loading levels at which members have broken away and/or other structural instabilities have occurred, and terminates when either a fully stable state has been reached or progressive collapse of all or part of the structure has occurred.

7.2 Conclusions

A number of specific conclusions can be drawn from the investigation described in this thesis:

- This study has developed an effective tool for conducting progressive-failure analysis of steel building frameworks. The proposed multi-stage analysis method fully traces the progressive change of structural topology during the collapse process.
- The proposed inelastic analysis procedure involving bending, shearing and axial stiffness degradation factors effectively simulates the inelastic behaviour of steel structures, including the nonlinear force-deformation behavior of framework members.
- A compound-element model has been developed that effectively simulates the combined nonlinear behaviour of both members and their connections.

- The shear failure of beams caused by impact debris loads is a significant triggering mechanism for progressive collapse.
- The damaged state of connections caused by disengaging members influences the progressive collapse of a structure. In Table 5.4, for example, a 20% difference in loading capacities is observed between that when the connection at joint 6 is not damaged (h_6 =1) and when it is fully damaged (h_6 = 0). As another example, upon comparing Table 5.5 (h=0.5) and Table 5.2 (h=1) it is observed that some internal forces have very significant differences even though the difference in loading capacities is not significant. Also, when comparing Figure 5.21 (h=1) and Figure 5.2 (h=0.5) in the first loading stage for the Boston building, both the internal forces and deflections have significant differences.

7.3 Future Work

There are a number of areas where research and developments are required in future work concerning progressive-failure analysis

- **Progressive-Failure Analysis based on the M-V-P Failure Criterion**

The M-P failure criterion and the M-V failure criterion are separately applied in the progressive-failure analysis in Chapter 5 to determine the failure of a cross-section. In future extensions of the analysis, the two failure criteria can be replaced by the M-V-P failure criterion derived in Chapter 6 in terms of implicit parametric functions. Before they can be implemented in the progressive-failure computer code, it is first necessary to establish expressions for the M-V-P failure criterion that are explicitly in terms of normalized moment m, shear force v and axial force p.

- **Spatial Structural Analysis**

The analysis and design of planar structures are important, but an actual progressive collapse is a three-dimensional failure phenomenon. The proposed analysis procedure should augmented to include lateral-torsional buckling and out-of-plane loading, so that a three-dimensional analysis may be conducted to achieve a realistic evaluation of progressive collapse under abnormal loading. Two challenging problems exist for such 3D analysis: 1) the development of an appropriate member stiffness degradation model; and 2) the establishment of a reasonable failure surface to account for each of the six internal loadings (three forces and three moments) at each member end.

- **Dynamic Analysis**

Nonlinear dynamic analysis is an important means to capture the dynamic characteristics of progressive collapse. The quasi-static method of analysis employed in this study can, with some effort, be extended to dynamic time-history analysis accounting for transient impact loading. How to

establish dynamic failure criteria and how to account for unloading due to load reversals are but two of the several challenging problems that must first be resolved to achieve this objective.

- **Experimental Verification Studies**

Verification studies for the proposed progressive-failure analysis procedure should be carried out through comparisons of predicted results with experimental results, obtained from specimens that range from components to structures, subjected to abnormal loads. These experimental results can be used to calibrate the plasticity and semirigid connection models to account for bending, shearing and axial stiffness degradations in the structural analysis. For example, the results of experimental tests of beam or slab specimens subjected to impact debris loading can be used to establish the loading model associated with impact amplification factors. As another example, a prototype two-bay by two-storey planar frame can be tested to investigate collapse behaviour when a column is suddenly removed.

- **Improvement of Analysis Techniques**

The nonlinear analysis of structures with stiffness degradation and topologic change is considerably more complicated than linear, geometrical nonlinear, or rigid-plastic analysis methods. The incremental-iterative technique should be expanded to include an unbalanced-force correction routine so that the analysis can proceed by using fewer load increments with larger step sizes to achieve the final collapse state. In addition, for both planar and spatial structures, a mechanism-based analytical technique should be developed to achieve full automation of the analysis process whenever a local collapse state is encountered during the multi-stage loading history.

- **Structures with Other Cross-Sections**

The member cross-sections considered in this study have bi-symmetric axes, such as W-shape sections. It is important to extend the failure criteria to account for the appropriate interaction relations governing post-elastic behaviour under various combinations of forces for a range of section types (e.g., T, hollow-box, etc.).

- **Effect of Shear Panel Zone**

This study demonstrates that shear failure plays an important role in progressive collapse. In addition, it is known that joint connection failure due to panel-zone shear is a significant concern in seismic design engineering. The panel-zone shear effect should also be accounted for in progressive-collapse analysis. A panel-zone model accounting for the effects of shear at a joint should be established and incorporated into the proposed analysis procedure.

- **Structures with Other Materials**

This study focuses primarily on steel building structures, but the proposed analysis procedure is readily applied to the analysis of structures comprised of concrete, wood and masonry materials. For example, for reinforced concrete building structures, it remains to introduce suitable constitutive laws governing the moment-curvature and shear-deflection relationships, crack and yield criteria, and other sectional properties.

- **Risk and Reliability Analysis**

There are many unknown factors that might lead to progressive collapse of structures. These uncertain factors can appear anytime during a structure's lifetime, from initial construction to final demolition. Abnormal loading events are random, albeit with generally low probability. Probabilistic methods of analysis should be employed to estimate structural failure probabilities, and establish acceptable risk levels in aid of the design decision-making process.

- **Other Potential Methods against Progressive Collapse**

Many methods developed in structural engineering can be employed to help prevent progressive collapse during a structure's lifetime. Passive or active structural control measures are effective in reducing and even eliminating fatal structural failure. Innovative materials and robust structural construction can improve structural performance against abnormal loading events. All the available techniques can be combined with the proposed method in this study to develop a more robust tool to deal with progressive collapse under abnormal loads.

- **Design against Progressive Collapse**

The method of nonlinear analysis developed in this study is appropriate for the analysis of planar structures. However, to be effective as a tool in aid of design some particular requirements related to stipulations in design codes should be accounted for. For instance, checking local buckling and lateral torsional buckling should be added to the current analysis procedure so that the predicted results identify compliance or violation of corresponding design requirements. In design of structures against progressive collapse, the adequacy of tie forces can be checked at the end of the first stage analysis according to the published design criteria (e.g., DoD). Further research for design should take into account interaction between abnormal loading and other loadings, such as seismic loading.

References

AASHTO. (1998). *LRFD Bridge Design Specifications*, 2nd Edition, American Association of State Highways and Transportation Officials, Washington D.C.

Acroyd, M. H. (1979), Nonlinear Inelastic Stability of Flexible-Connected Plane Steel Frame, *Ph. D Thesis*, Department of Civil Engineering, University of Colorado, Boulder, CO.

Adams, D. E. & Farrar, C. R. (2002). Identifying linear and nonlinear damage using frequency domain ARX models. *Structural Health Monitoring*, **1**(2), 185-201.

AISC. (2005). Specification for Structural Steel buildings. ANSI/AISC 360-05, *American Institute of Steel Construction*, Chicago, IL.

AISC. (2001). *Manual of Steel Construction-Load and Resistance Factor Design* (LRFD), Vol. **2**, 2nd Ed , American Institute of Steel Construction, Chicago, IL.

Allen, D. E. & Schriever, W. R. (1973). Progressive collapse, abnormal loads and building codes. Structural failures: modes, causes, responsibilities, ASCE, New York.

ANSYS. (2005). ANSYS Software, Release V10. ANSYS Inc., Southpointe, Canonsburg, PA , USA.

Areiza-Hurtado, M., Vega-Posada, C., & Aristizabal-Ochoa, J. D. (2005). Second-order stiffness matrix and loading vector of a beam-column with semirigid connections on an elastic foundation, *J. Engrg. Mech.*, ASCE, **131**(7), 725-762.

Aristizabal-Ochoa, J. D. (2004). Column stability and minimum lateral bracing: Effect of shear deformations. *J. Eng. Mech*., **130**(10), 1223-1232.

ASCE. (2005). *Minimum Design Loads for Buildings and Other Structures*. American Society of Civil Engineers, ASCE 7-05, Reston, VA.

ASCE. (2002). *Minimum Design Loads for Buildings and Other Structures*. American Society of Civil Engineers, ASCE 7-02, Reston, VA.

ASCE. (1997). Design of Blast Resistant Buildings in Petrochemical Facilities. American Society of Civil Engineers, NY, NY.

Attalla, M. R., Deierlein, G. G., & McGuire, W. (1994). Spread of plasticity: quasi-plastic-hinge approach, *J. Struct. Engrg.*, **120**(8), 2451-2473.

Aydogan, M. (1995). Stiffness-matrix formulation of beams with shear effect on elastic foundation, *J. Struct. Eng*., ASCE, **121**(9): 1265-1270.

Beedle L. S. (1958). *Plastic Design of Steel Frames*. New York: John Wiley & Sons Inc.

Bjorhovde, R., Brozzeti, J., & Colson, A. (1990). A classification system for beam to column connections. *J. Struc. Engrg.*, ASCE, **116**(11), 3059-3076.

Blandford, G. E. (1996). Progressive failure analysis of inelastic space truss structures. *Computers and Structures*, **58**(5), 981-990.

Breen, J. E., & Siess, C. P. (1979). Progressive collapse — symposium summary. *ACI Journal of American Concrete Institute*, **76**(9), 997-1004.

Burnett, E. F. P. (1975). Abnormal loading and building safety. American Society of Mechanical Engineers (Paper), 141-175. *Am Concrete Inst* (SP-48), Detroit, Mich.

Carden, E. P., & Fanning P. (2004). Vibration based condition monitoring: A review, *Structural Health Monitoring*, **3**(4), 355-377.

CEN. (2002). *Eurocode 3: Design of steel structures*, part 1.8 – Design of joints, European Standard. Brussels, Belgium.

CEN. (1994). *Eurocode 1 – Actions on structures,* part 1 – basis of design, European Pre-standard ENV 1991-1, Comite Europeen de Normalization 250, Brussels, Belgium.

Chakrabarty, J. (2000). *Applied plasticity*. Springer-Verlag Inc., New York.

Chan, S. L., & Zhou, Z. H. (2004). Elastoplastic and large deflection analysis of steel frames by one element per member. II: Three hinges along member. *J. Struct. Engrg.*, ASCE, **130**(4), 545-553.

Chen W. F., Goto Y., & Liew J. Y. R. (1996). *Stability Design of Semi-rigid Frames*. John Wiley & Sons, Inc., New York.

Chen W. F., & Toma S. (1994). *Advanced analysis of steel frames*. CRC Press: Boca Raton.

Chen, W. F., Lui, E.M. (1991), *Stability design of steel frames*, CRC Press, Inc. Boca Raton, Florida.

Chen, W. F., & Atsuta, T. (1977). *Theory of Beam-Columns, Vol. 2: Space Behaviour and Design*. McGraw-Hill, New York.

Chugh, A.K. (1977). Stiffness matrix for a beam element including transverse shear and axial force effects, *International Journal for Numerical Methods in Engineering*, **11**, 1681-1697.

CISC (Canadian Institution of Steel Construction). (2004). *Handbook of Steel Construction*. 8th Ed., Universal Offset Limited Alliston, Ontario, Canada.

Clarke M. J. (1994). Plastic-zone analysis of frames, in *Advanced Analysis of Steel Frames*, Edited by W. F. Chen & S. Toma, CRC Press, Boca Raton.

Closkey, D. J. (1988). Report of the Commissioner Inquiry Station Square Development, Burnaby, British Columbia, Canada.

CBO. (2002). *Federal Reinsurance for Disasters*, Congressional Budget Office of the United States of America, http://www.cbo.gov/showdoc.cfm?index=3787&sequence=0.

Conrath, E. J., Krauthammer, T., Marchand K. A., & Mlakar, P. F. (1999). *Structural Design for Physical Security*: *State of the Practice*, ASCE, Virginia.

Cook, N. E., Jr. (1983). *Strength and Stiffness of Type 2 Steel Frames*, Ph.D. Thesis, Department of Civil Engineering, University of Colorado, Boulder, CO.

Cross, H. (1932). Analysis of Continuous Frames by Distributing Fixed-End Moments, *Transactions* ASCE, (Paper no. 1793), **96**, 1-10.

Darwin, D. (2000). Design of composite beams with web openings. *Prog. Struct. Engng Mater.*, **2**, 157-163.

DoD. (2005). *Design of buildings to resist progressive collapse*. Unified Facilities Criteria UFC 4-023-03, Department of Defense, USA.

Driscoll G. C., & Beedle L. S. (1957). The plastic behavior of structural members and frames. *The Welding Journal*, **36**(6), 275-s.

Drucker, D. C. (1956). The effect of shear on the plastic bending of beams, *Journal of Applied Mechanics*, **23**, 509-514.

Duan, L., & Chen, W. F. (1990). A yield surface equation for doubly symmetrical sections. *Eng. Struct.*, **12**(2), 114-119.

ECCS. (1984). Ultimate limit state calculation of sway frames with rigid joints. Technical committee 8 – Structural Stability Technical Working Group 8.2., Publication No. 33. European Convention for Constructional Steelwork.

Eldukair, Z. A., & Ayyub, B. M. (1991). Analysis of recent U.S. structural and construction failures. *J. Perf. of Constr. Fac.*, ASCE, **5**(1), 57-73

Ellingwood, B. (2006). Mitigating risk from abnormal loads and progressive collapse. *J. Perform. Constr. Facil.,* **20** (4), 315-323.

Ellingwood, B., & Dusenberry, D. O. (2005). Building design for abnormal loads and progressive collapse, *Journal of Computer-Aided Civil and Infrastructure Engineering*, **20**(3), 194-205.

Ellingwood, B. (2005). Load combination requirements for fire-resistant structural design. *J. Soc. Fire Protection Engrg*. **15**(1), 43-61.

Ellingwood, B. (2005). Risk-informed condition assessment of civil infrastructure: state of practice and research issues. *J. Struct. & Infrastruct. Engrg.*, **1**(1), 7-18.

Ellingwood, B., Rosowsky, D.V., Li, Y. & Kim J. H. (2004). Fragility assessment of light-frame wood construction subjected to wind and earthquake hazards. *J. Struct. Engrg*., ASCE, **130**(12), 1921-1930.

Ellingwood, B. (2001). Acceptable risk bases for design of structures. *Progress in Struct. Engrg. and Mat.*, **3**(2), 170-179.

Ellingwood, B. & Tekie P. B. (2001). Fragility analysis of concrete gravity dams. *J. Infrastructure Systems*, ASCE, **7**(2), 41-48.

Ellingwood, B. (2001). Earthquake risk for building structures. *Reliability Engrg. & System Safety*, **74**(3), 251-262.

Ellingwood, B. (2000). LRFD: implementing structural reliability in professional practice. *Engrg. Struct*., **22**(2), 106-115.

Ellingwood, B., MacGregor, J. G., Galambos, T. V., & Cornell, C. A. (1982). Probability-based load criteria: Load factors and load combinations. *J. Struct. Div.*, ASCE, **108**(5), 978-997.

Ellingwood, B., & Leyendecker, E.V. (1978). Approaches for design against progressive collapse. *J. Struct. Div*., **104**(3), 413-423.

Ellyin, F., & Deloin, R. (1972). The effect of shear on yielding of structural members. *Int. J. Solids Structures*, **8**, 297-314.

Engel, S. J., Gilmartin, B. J., Bongort, K., & Hess A. (2000). Prognostics, the real issues involved with predicting life remaining. *The IEEE Aerospace Conference Proceedings*, **6**, 457-469.

Espion, B. (1986). Nonlinear analysis of framed structures with a plasticity mined element. *Computer and Structures*, **22**(5), 831-839.

Essa, H., & Kennedy, D. J. (1994). Station Square Revisited: Distortional Buckling Collapse. *Canadian Journal of Civil Engineering,* **21**(3), 377-381.

Faella, C., Piluso, V., & Rizzano, G. (2000). *Structural steel semirigid connections-theory, design and software*, CRC Press, Boca Raton.

Feld, J. & Carper, K. L. (1996). *Construction failure*. 2nd Edit, New York : John Wiley and Son.

FEMA-273. (1997). *Guidelines for the seismic rehabilitation of buildings*. Federal Emergency Management Agency (FEMA), USA.

FEMA-259. (1995). *Engineering principles and practices for retrofitting flood prone residential buildings*. Federal Emergency Management Agency (FEMA), USA.

FEMA-267. (1995). *Interim Guidelines:* Evaluation, repair, modification and design of steel moment frames, Report No. SAC-95-02, USA.

FEMA-316. (2000). *Design and construction guidance for community shelters*. Federal Emergency Management Agency (FEMA), USA.

FEMA-355C. (2000). Systems Performance of Steel Moment Frames Subject to Earthquake Ground Shaking. Federal Emergency Management Agency (FEMA),USA.

FEMA-403. (2002). *World Trade Center building performance study: Data collection, preliminary observations and recommendation*. Federal Emergency Management Agency (FEMA) Regin II, New York, N.Y. USA.

Fintel, M., & Schultz, D. M. (1979). Structural integrity of large panel building. *ACI Journal of American Concrete Institute*, **76**(5), 583-620.

Galambos, T.V. (1998), *Guide to Stability Design Criteria for Metal Structures*, 4th Edition, John Wiley & Son, Inc.

Galambos, T. V., Ellingwood, B., McGregor, J. G., & Cornell, C. A. (1982), Probability-based load criteria: Assessment of current design practice. *J. Struct. Div.*, ASCE, **108**(5), 957-977.

Gong, Y. (2003). Performance-based design of building frameworks under seismic loading, PhD Thesis, University of Waterloo, Canada.

Gradshteyn, I. S., & Ryzhik, I. M. (2000). *Tables of Integrals, Series, and Products,* 6th ed., San Diego, CA: Academic Press, 1132.

Green, A. P., & Hundy, B. B. (1957). Plastic yielding of I-beams—Shear loading effects analyses. *Engineering*, 1**84**, 74-76 and 112.

Grierson, D.E., Safi, M., Xu, L., & Liu, Y. (2005). Simplified Methods for Progressive-Collapse Analysis of Buildings, *Proceedings of the 2005 Structures Congress and the 2005 Forensic Engineering Symposium*, April, New York, N. Y.

Grierson, D. E., Xu, L., & Liu, Y. (2005). Progressive-failure analysis of buildings subjected to abnormal loading, *Journal of Computer-Aided Civil and Infrastructure Engineering*, **20**(3), 155-171.

Grierson, D. E. (2003), Designing Buildings Against Abnormal Loading, in *Progress in Civil and Structural Engineering Computing*, Edited by B.H.V. Topping, Saxe-Coburg Publications, Scotland, 37-62.

Grierson, E. D. (2002). *Structural Plasticity*, Civ.E. 705 Course Notes, University of Waterloo, Waterloo, On., Canada.

Grierson, D. E., & Abdel-Baset, S. B. (1977). Plastic analysis under combined stresses, *Journal of Engineering Mechanics Division*, ASCE, **103**(EM5), 837-854.

Griffiths, H., Pugsley, A., & Saunders, O. (1968). Report of the inquiry into the collapse of flats at Tonan Point, Canning Town. Her Majesty's Stationary office, London, United Kingdom.

Gross, J. L. & McGuire, W. (1983). Progressive collapse resistant design. *J. Struct. Engrg.*, **109**(1), 1-15.

GSA. (2003), Progressive collapse analysis and design guidelines for new federal office buildings and major modernization projects. Office of Chief Architect, General Services Administration, Washington, D. C.

Gupta, A., & Krawinkler, H. (1999), Seismic demands for performance evaluation of steel moment resisting frame structures. *John A. Blume Earthquake Engrg. Ctr. Rep. No. 132*, Dept. of Civil Engineering, Stanford University, Stanford, California.

Hall, W. J., & Newmark, N. M. (1957). Shear deflection of wide-flange steel beams in the plastic range. *ASCE Transactions*, **122**, 666-687.

Hamburger, R. O., Hanson, R. D., Mahoney, M., & Rojahn, C. (2002). Performance-based design: A practical approach to protecting infrastructure. *Modern Steel Construction*, June Issue.

Hartwig, R. P. (2005). September 11, 2001, One Hundred Minutes of Terror that Changed the Global Insurance Industry Forever, http://server.iii.org/yy_obj_data/binary/692822_1_0/sept11paper.doc.

Hasan, R., Xu, L., & Grierson, D. E. (2002). Push-over analysis for performance-based seismic design. *Journal of Computers & Structures*, Pergamon, **80**, 2483-2493.

Hawkins, N. M., & Mitchell, D. (1979). Progressive collapse of flat plate structures. *ACI Journal of American Concrete Institute*, **76**(7), 775-808.

Heyman J, & Dutton VL. (1954). Plastic design of plate girders with unstiffened webs. *Welding and Metal Fabrication*, **22**, 256.

Hibbeler, R. C. (2004). *Statics and mechanics of materials*, the 2nd Edition, Prentice Hall, Inc., New Jersey.

Hibbeler, R. C. (2002). *Structural analysis*, the 5th Edition, Prentice Hall, Inc., New Jersey.

Hinman, H. (1997). Lessons from the Oklahoma City Bombing: Defensive Design Techniques, ASCE, New York.

Hodge, P. G. (1959). *Plastic analysis of structures*. McGraw-Hill Book Company, Inc., New York.

Hodge, P. G. (1957). Interaction curves for shear and bending of plastic beams. *Journal of Applied Mechanics*, **24**, 453-456.

Holtz-Eakin, D. J. (2005). Macroeconomic and Budgetary Effects of Hurricanes Katrina and Rita, Congressional Budget Office: http://www.cbo.gov/showdoc.cfm?index=6684&sequence=0.

Huber A. W., & Beedle L. S. (1954). Residual stress and the compressive strength of steel. *Welding Journal*, **33**(12), 589-614.

Iffland, J. S. B., & Birnstiel, C. (1982). Stability Design Procedures for Building Frameworks, Research Report, AISC Project No. 21.62, America Institute of Steel Construction, Chicago, IL.

Jaspart, J. P. (2002). Design of structural joints in building frames. *Prog, Struct. Engng Mater.*, **4**, 18-34.

Jones, N. (1995). Quasi-static analysis of structural impact damage. *J. Construct. Steel Researc*h, **33**, 151-177.

Jones, C. P., & Nathan, N. D. (1990). Supermarket roof collapse in Burnaby, British Columbia, Canada. *Journal of Performance of Construction Facilities*, **4**(3), 142-160.

Kaewkulchai, G. & Williamson, E. B. (2006). Modeling the impact of failed members for progressive collapse analysis of frame structures. *J. Perform. Constr. Facil.*, **20** (4), 375-383.

Kaewkulchai, G., & Williamson, E. B. (2004). Beam element formulation and solution procedure for dynamic progressive collapse analysis. *Computers and Structures*, Elsevier, **82**, 639-651.

Kasai, K., & E. P. Popov (1986). General behaviour of WF steel shear link beams. *J. Struct. Engrg.*, ASCE, **112**(2), 362-382.

Khajehpour, S. & Grierson D. E. (2003). Profitability versus safety of high-rise office buildings. *Journal of Structural & Multidisciplinary Optimization*, Springer-Verlag, **25**(4), 279-293.

King, W.S., White. D. W., & Chen, W. F. (1992). Second-order inelastic analysis methods for steel-frame design. *J. Struc. Engrg*, ASCE, **118**(2), 408-428.

Kishi, N., & Chen, W. F. (1987). Moment-Rotation of Semi-Rigid Connections. Structural Engineering Report, No. CE-STR-87-29, School of Civil Engineering, Purdue University, West Lafayette, Indiana.

Kishi, N., Komuro, M., & Chen, W. F. (2004). Four-parameter power model for M-θ curves of end-plate connections, ECCS/AISC Workshop Connections in Steel Structures V: Innovative Steel Connections, June, Amsterdam, The Netherlands.

Koh, C. G., Qiao, G. Q., & Quek, S. T. (2003). Damage identification of structural members: Numerical and experimental studies. *Structural Health Monitoring*, **2**(1), 41-55.

Kusuda, T., & Thurlimann, B. (1958). Strength of Wide Flange Beams under Combined Influence of Moment, Shear and Axial Force. Frits Engineering Laboratory Report No. 248.1. Lehigh University.

Lay, M. G., & Galambos, T. V. (1964). Tests on beam and column sub-assemblages. Frits Engineering Laboratory Report No. 278.10, Lehigh University.

Leonards, G. (1982). Investigation of failures. *J. Geotech. Engrg. Div.*, ASCE, **108**(2), 185-246.

Liew, J. Y. W., Yu, C. H., Ng, Y. H., & Shanmugam, N. E. (1997). Testing of semi-rigid unbraced frame for calibration of second-order inelastic analysis. *J. Construct. Steel Res*. **41**(2/3), 159-195.

Liu, Y., & Xu, L. (2005), Storey-based stability analysis of multi-storey unbraced frames. *Structural Engineering and Mechanics – An International Journal*, **19**(6), 679-705.

Liu, Y., Xu, L., & Grierson, D. (2003). Performance of buildings under abnormal loading, Response of Structures to Extreme Loading, Toronto, Canada.

Longinow, A., & Mniszewski, K. R. (1996). Protecting buildings against vehicle bomb attacks. *Practice Periodical on Structural Design and Construction*, **1**(1), 51-54.

Lui, E. M., & Chen, W. F. (1986). Analysis and behaviour of flexibly joined frames. *Engineering Structures*, **8**(2), 107-118.

Manjoine, M. J. (1944). Influence of rate of strain and temperature on yield stress of mild steel. *J. Appl. Mech*., **11**, 211-218.

Marjanishvili, S. & Agnew, E. (2006). Comparison of various procedures for progressive collapse analysis. *J. Perform. Constr. Facil*., **20** (4), 356-374.

Marjanishvili, S. M. (2004). Progressive analysis procedure for progressive collapse. *Journal of Performance of Constructed Facilities*, ASCE, **18**(2), 79-85.

McGuire, W., Gallagher R. H., & Ziemian, R. D. (2000). *Matrix structural analysis*, 2nd Edition. John Wiley & Sons, Inc. New York.

Mlakar, P. F., Dusenberry, D. O., Harris, J. R., Haynes, G., Phan, L. T., & Sozen, M. A. (2003). The Pentagon Building Performance Report, Structural Engineering Institute, ASCE, Reston, Virginia, United States.

Monforton, G. R. & Wu, T. S. (1963). Matrix analysis of semi-rigid connected frames. *J. Struct. Div*., **89**(6), 13-42.

NAASRA. (1990). *Highway bridge design specification*, National Association of Australian State Road Authorities.

Nataraju, M., Adams, D. E., & Rigas, E. J. (2005). Nonlinear dynamical effects and observations in modeling and simulating damage evolution in a cantilevered beam. *Structural Health Monitoring*, **4**(3), 259–282.

NBS. (1970). Guide criteria for the evaluation of operation breakthrough housing systems. Accession Numbers PB-212055, 212056, 212058, National Bureau of Standards, Springfield, Va.

NRCC. (1995). National Building Code of Canada, National Research Council of Canada, Ottawa, Ont., Canada.

NRCC. (1970). Canadian structural design manual, Supplement No. 4, Publ. No. NRC 11530, National Building Code of Canada, National Research Council of Canada, Ottawa, Ont.

Orbison, J.G., McGuire, W., & Abel. J. F. (1982). Yield surface application in nonlinear steel frame analysis. *Computer Methods in Applied Mechanics and Engineering*, **33**, 1-3.

Powell, G. H. & Chen, P. F. S. (1984). 3D beam-column element with generalized plastic hinges. *J. Eng. Mech.*, ASCE, **112**(7), 627-641.

Ranshi, A. S., Chitkara, N. R., & Jonhson, W. (1973). Limit loads for the plastic bending in plane strain of cantilevers containing rectangular holes under end shear. *Int. J. Mech. Sci*., **15**(1), 15-35.

Richard, R. M. & Abbott, B. J. (1975). Versatile elastic-plastic stress-strain formula. *J. Engrg. Mech. Div*., ASCE, **101**(4), 511-515.

SA. (1998). *AS4100, Steel structures*. Standards Australia, Sydney, Australia.

SEI (Structural Engineering Institute), (2003). *The Pentagon Building Performance Report*, ASCE, Reston, Virginia, USA.

Smilowitz, R., Hapij, A., & Smilow, J. (2002). Bankers Trust Building, in World Trade Center building performance study: Data collection, preliminary observations, and recommendations, FEMA 403, FEMA and ASCE.

Tapia, C. (2001). True Loss from Sept. 11 Terrorist Attacks on U.S. is Immeasurable, As Estimates of Potential Insured, www.insurancejournal.com/magazines/west/2001/09/24/coverstory/18250.htm.

Taylor, D. A. (1975). Progressive collapse. *Can. J. Civ. Eng*., **2**(2), 571-529.

Timoshenko, S. (1955). *Strength of materials—Part I: Elementary theory and problems*, 3rd Ed. D. Van Nostrand Company, Inc., New Jersey.

Timoshenko, S. P., & Gere, J. M. (1961). *Theory of elastic stability*, New York: McGraw-Hill.

TM5-1300. (1990). *Structures to Resist the Effects of Accidental Explosions*. Department of Army, Navy and Air Force, Washington, D. C.

Troutman, J. L. (1996). Variational calculus and optimal control: optimization with elementary convexity. Springer-Verlag, Inc., New York.

UBC. (1994), Structural Engineering Design Provisions, *Uniform Building Code*, Vol. **2**, International Building Officials.

Vlassis, A. G., Izzuddin B. A., Elghazouli, A. Y., & Nethercot, D. A. (2006). Design oriented approach for progressive collapse assessment of steel framed buildings. *Journal of the International Association for Bridge and Structural Engineering*, **16**(2), 129-135.

Wada, A., Ohi, K., Suzuki, H., Kohno, M., & Sakumoto, Y. (2006). A study on the collapse control design method for high-rise steel buildings. *Journal of the International Association for Bridge and Structural Engineering*, **16**(2), 137-141.

Wang, C. M. (1995). Timoshenko Beam-Bending Solutions in Terms of Euler-Bernoulli Solutions, ASCE, *J. Engrg. Mech*., **121**(6), 763-765.

Wang, D. & Haldar, A. (1997). System identification with limited observation and without input. *J. Engrg. Mech.*, ASCE, **123**(7), 504-511.

Whittaker, A., Hamburger, R., Comartin, C., Mahoney, M., Bachman, R., & Rojahn, C. (2005). *Performance-Based Engineering of Buildings and Infrastructure for Extreme Loadings*, http://www.atcouncil.org/ATC58Technical Papers.shtml.

Wolfram, S. (1996). *The Mathematica, Version 3*, Cambridge University Press.

Xu, L. (1994). *Optimal Design of Steel Frameworks with Semirigid Connections*, PhD Thesis, University of Waterloo, Waterloo, ON., Canada.

Xu, L. (1992). Geometrical stiffness and sensitivity matrices for optimization of semi-rigid steel frameworks. *Structural Optimization*, **5**(1-2), 95-99.

Xu, L., & Liu, Y. (2002). Story-based effective length factors for unbraced PR frames. *Engineering Journal*, AISC, **39**(1), 13-29

Xu, L., Liu, Y., & Grierson, D. E. (2005). Nonlinear analysis of steel frameworks through direct modification of member stiffness properties., *Advances in Engineering Software*, **36**(5), 312-324.

Xu, L., & Liu**, Y.** (2006). Inelastic analysis of steel frames accounting for flexural and shearing stiffness degradations, *Advanced Steel Construction – An International Journal*. (Accepted)

Yau, C. Y., & Chan, S. L. (1994). Inelastic and stability analysis of flexible connected steel frames by spring-in-series model. *J. Struct. Eng.*, ASCE, **120**(10), 2803-2819.

Zalka, K. A., & Armer, G. S. T. (1992). *Stability of large structures.* Butterworth-Heinemann Ltd, Linacre House, Jordan Hill, Oxford.

Ziemian, R. D., McGuire, W., & Deierlein, G. G. (1992), Inelastic limit states design. Part I: Planar frame structures. *J. Struct. Engrg.*, ASCE, **118**(9), 2532-2549.